Anonymous Referee #1

Received and published: 14 October 2019

General Summary and Comments This manuscript describes the development and testing of UT&C, an urban canyon model that incorporates the characteristics of roof vegetation, ground vegetation, and urban trees, including the capability to represent different plant types, and their effects on the urban environment. Comparison of model output to tower flux observations indicates good performance compared to other models. Importantly, the modeling of latent heat flux, the main focus of the model formulations in the current paper, is equal to or improved compared to other models. Sensitivity simulations indicate vegetation can decrease urban canopy temperature as expected. The manuscript is well-written and thoroughly recognizes previous work in this area. The model is comprehensively presented (a detailed description is provided in the Technical Reference Material document) and simulation results are thoroughly analyzed. I recommend that this study be published after considering the minor comments listed below.

We thank the reviewer for his/her time, precise summary, and positive evaluation of the manuscript.

Specific Comments

1. Abstract: Line 9: It is stated here that the model calculates all urban hydrological fluxes. However, as mentioned in the model limitations section, snow hydrology is not accounted for. So this statement should be modified.

Yes, correct, we have modified the statement in the abstract to clarify that snow hydrology is not included in the model yet (Line 9).

2. Line 52: Change "Reasearch" to "Research".

Corrected.

3. Line 55: CLM doesn't have an explicit representation of short ground vegetation in the urban canyon. Rather it has a generic pervious canyon floor whose soil column supports evaporation.

Yes, indeed, thank you for the clarification. We have removed CLM from the list of models with short ground vegetation.

4. Line 101: Is the model restricted to an hourly time step for any reason or is it flexible enough to accommodate finer time steps. For example, meteorological forcing data may be available at ½ or ¼ hour time steps. Solution of soil moisture equations and conductive fluxes may benefit from a finer time step.

The code has been modified to accommodate shorter time steps (e.g. ½ or ¼ h) if the meteorological forcing data are available.
The soil moisture equations are internally solved at a much finer time step though, determined by an ordinary differential equation solver based on a modified Rosenbrock formula of order 2 (ode23s, Shampine and Reichelt, 1997) to ensure numerical stability. We have clarified this now in the manuscript (Line 100-102) and in Sect. "6.2 Vadose zone dynamics" in the TRM.

5. Line 173: This seems to imply that the interior building temperature is not a function of the conductive fluxes through the roof and walls and thus ignores external factors such as solar and longwave radiation impinging on roofs and walls and the transfer of that heat to building interior. Is this a reasonable assumption? Have the limitations of this assumption been explored in the cited paper (de Munck et al. 2018)? There is some reference as to the importance of this in lines 599-601, but there is no quantitative assessment of this offered.

In the current set-up, the interior building temperature is not a prognostic variable and, hence, it is not dependent on the conductive heat flux. We believe that this simplification is reasonable as building interiors are often heated or cooled when a certain temperature threshold is exceeded. In other words, inhabitants define the internal temperature, but not the amount of energy invested in cooling or heating (which is also a by-product of the UT&C model), as in the model. Furthermore, in mild-climates or in the Spring and Fall, occupants can open windows, thereby somehow setting the interior building temperature equal to the exterior air temperature or forcing air temperature.
However, the conductive heat flux is a function of all external factors (e.g., shortwave and longwave radiation) affecting the surface temperature of the roof and walls. Additionally, the conductive heat flux is a function of the interior building temperature which can influence exterior temperature. For example, the heating of building interiors in winter can influence building facade temperatures and therefore, canyon air temperature.
De Munck et al. (2018) did not further explore the limitation of fixing internal building temperature. Hence, we have now performed a sensitivity analysis for interior building temperature in Singapore where air-conditioning of building interiors is common (see TRM Sect. 5). We varied the interior building temperature and analysed the change in the air temperature at canyon reference height, and the canyon energy fluxes, if (A) the energy used for cooling is not re-emitted to the canyon air, and the energy used for cooling the building envelope is re-emitted to the canyon air with an air-conditioning coefficient of performance which is infinite (efficiency of 1) in (B), and 2.5 (De Munck et al. 2018) in (C). The air temperature at canyon reference height, the location where anthropogenic heat is emitted, increases with decreasing building temperature in the case of re-emitted anthropogenic heat. This re-emission of anthropogenic heat increases the sensible heat flux which corresponds to the increase in heat emissions caused by air-conditioning of building interiors. The further feedback of this increase in sensible heat on the forcing temperature and, therefore, urban canopy air temperature can only be analysed through a coupling with a mesoscale meteorological model.

We have clarified this now in Sect. 5 “Anthropogenic heat flux” of the TRM.

6. Table 1: Generally, “u” and “v” are used to describe the wind components. Suggest changing “Velocity u” to “Wind Velocity w”.

We have changed “Velocity u” to “Wind speed U”.
“

7. Line 560: Suggest changing “the here reported relative humidity increase” to “the relative humidity increase reported here”.

Changed.

8. Line 575: Change “fraiming” to “framing”. Or change to “helps to define reasonable expectations”.

Changed.

9. Line 618: Change “explicitely” to “explicitly”.

Changed.

10. Supplement, Line 1011: What is meant by “canyon calculation height”? Is this the height at which the air temperature calculated? Aren’t there two heights calculated?

Yes, the air temperature and humidity are calculated at two heights within the urban canyon: 1) at 2 m canyon height and 2) at canyon reference height, which is the sum of the zero-plane displacement height of the canyon and the canyon roughness length ($d_{disp,can} + z_{0,m,can}$).

We have chosen to add the anthropogenic heat at the canyon reference height. However, this could be modified depending on the exact emission location of the anthropogenic heat. The anthropogenic heat could be added at 2 m canyon height, at canyon reference height, and at roof level, or could be partitioned among these different locations.

We have now clarified in the TRM that, in the current model set up, anthropogenic heat is added at the canyon reference height ($=d_{disp,can} + z_{0,m,can}$). Modification in TRM Line 1005.

Anonymous Referee #2

Received and published: 22 October 2019

General comments

The manuscript titled "An urban ecohydrological model to quantify the effect of vegetation on urban climate and hydrology (UTC v1.0)" by Meili et al. describes a comprehensive numerical model that incorporates various urban components (grass, trees, urban facets, etc.) and their ecohydrological processes. The authors also provide a very detailed descriptive document as the technical reference manual. In the model comparison using flux tower data, simulated results using the proposed model are generally consistent with or even better than previous studies. Overall the manuscript is well written, and the study (both model development and numerical evaluation/validation) is well designed. I therefore recommend publication after resolving the issues / answering the questions below in the revision.

We thank the reviewer for his/her time, precise summary, and positive evaluation of the manuscript.

Specific comments

1. Line 97: "The anthropogenic heat flux Qf is directly added to the sensible heat budget of the canyon air." The anthropogenic heat flux should be on the LHS of Eq. (1) instead of RHS.

Thank you for your comment, we have now clarified this point in the manuscript in Eq. (1). Previously we separated the "surface budget" from the "canyon air" budget, but that was indeed confusing.

2. Line 101: "hourly time steps". Is this enough to ensure numerical stability?

The code has been modified to accommodate shorter time steps (e.g. ½ or ¼ h) if the meteorological forcing data are available (see also reply to referee 1).
Equations for which a finer temporal resolution is required to ensure numerical stability, such as the soil moisture equations, are internally solved at a much finer time step determined by an ordinary differential equation solver that is based on a modified Rosenbrock formula of order 2 (ode23s, Shampine and Reichelt, 1997). We have clarified this in the revised manuscript (Line 100-102) and in Sect. "6.2 Vadose zone dynamics" in the TRM.

3. Lines 151–152: "The air volume within the canyon is subdivided into two layers with a height of 4 m for the first layer and a height of (HCanyon - 4) m for the second layer." This geometry setting will largely limit the application of the proposed model if the height (4 m) is fixed.

Thank you for the feedback. The height of 4 m is chosen to calculate the portion of sensible heat flux from the wall that is contributing to the 2 m air temperature. In the case when the mean building height is lower than 4 m, it is assumed that the sensible heat flux from the total wall area is contributing to the air temperature at 2 m. We have now clarified this in the manuscript (Line 151-156).

4. Lines 172–173: ": : :interior building temperature Tb, which is set equal to the atmospheric forcing temperature within the range of a specified minimum Tb;min and maximum temperature Tb;max." Is there any specific reason for such setting? The interior building temperature is usually distinct from outside temperature (forcing) when H/AC is used (as mentioned in line 174).

The interior building temperature is set to a prescribed minimum temperature $T_{b,min}$ if the outdoor temperature drops below $T_{b,min}$ and building interiors are heated. Similarly, if outdoor temperatures exceed $T_{b,max}$, the interior building temperature will be fixed to $T_{b,max}$ and building interiors are air-conditioned. In between these two set-points, the interior building temperature is prescribed equal to the forcing temperature under the assumption that minimal heating or air-conditioning is applied during periods with pleasant outdoor temperatures. We believe this is a reasonable assumption as building occupants are likely to open windows during comfortable outdoor conditions. The interior building temperature can also be set to one single prescribed value T_b if the building interior is assumed temperature controlled under all outdoor conditions.
We have modified the manuscript to clarify this point in line 178-179 and TRM Line 984-985.

5. Lines 380–381: "The simulation time series length is : : : mean daily cycles averaged over the whole year". Did the authors observe any seasonal variability?

The sensitivity analysis of 2 m air temperature and relative humidity to an increase in vegetated ground cover λ_{veg}, LAI and $V_{c,max}$ is performed for the urban set-up of the eddy-covariance measurement site in Telok Kurau, Singapore. Singapore experiences a relatively uniform climate throughout the year and hence, we did not analyse seasonal variability. There is an exceptional dry period (15.2.2014 - 16.3.2014) in the modelled time series for which we have now separately analysed the mean 2 m air temperature decrease and relative humidity increase caused by the change in λ_{veg}, LAI and $V_{c,max}$. See modifications in the manuscript at line 385-388 and line 527-535.

6. Figure 5(i): Sensible heat flux is generally overestimated by the model during daytime. Please provide some possible reasons.

As shown in Figure 5, the sensible heat flux is mainly overestimated in Melbourne, while the model appears to better simulate the sensible heat fluxes in Singapore and Phoenix. As shown in Figure 5 of Coutts et al. (2007a), the spatial heterogeneity of the urban landscape combined with the variability in wind direction has an impact on the fluxes. The model lumps these heterogeneities into a handful of variables, which of course represent a simplification of the true process.
In general, uncertainties in parameter values, such as urban morphology, and thermal and radiative characteristics, can influence model performance (Demuzere et al. 2017). Additionally, uncertainties in model structure and parametrizations might also lead to simulation-observation differences. Uncertainties are also introduced in the amount of anthropogenic heat and water added to the system, and the prescribed interior building temperature used.
Furthermore, tower based eddy-covariance measurements do not close the energy budget which is attributed to the conductive heat fluxes and change in heat storage in the urban fabric as well as measurement uncertainties, since the lack of energy balance closure is also observed in the long-term averages. In other words, some difference between model simulations and observations are expected. Because the sensible heat flux is typically one of the major energy fluxes in the urban environment, model and measurement discrepancies are likely emphasized.
All of these reasons can contribute to the observed difference; however, it is hard to pinpoint the main reason with only flux-tower estimates of sensible heat and this will likely require different observations as fields of surface temperature and vertical profiles of wind speed.

7. Section 4.1.3: Probably the observed discrepancy can also be attributable to the assumption of irrigation water use.

Thank you for the comment, we have added this point to the manuscript. Modification in line 445-447 of the revised manuscript.

8. Figure 10: The dynamics of soil moisture over time are very interesting. Can this be evaluated with field measurements (of moisture)?

Unfortunately, we do not have soil moisture measurements in the ground underneath the Telok Kurau eddy-covariance site in Singapore during the simulation time period shown in the manuscript.
The evaluation with field measurements is also difficult as soil texture and soil moisture are often heterogeneous and measurements are usually performed at the point scale and, hence, unlikely representative of a larger area, while the model and the eddy-covariance measurements simulate/measure at the neighbourhood scale.

9. Lines 569–570: "Higher air temperature decrease in drier climates is often linked to urban irrigation though as shown by Broadbent et al. (2018b) in Melbourne...." and lines 30–37 about the advantages of urban vegetation: please note that using nature-based solutions for cooling should also consider the trade-off between irrigation water use and the cooling effect the urban vegetation can provide, especially in dry areas like Melbourne or Phoenix, see Yang and Wang (2017) (https://doi.org/10.1016/j.landurbplan.2017.07.014) for a regional simulation in Phoenix and Wang et al. (2019) (https://doi.org/10.1016/j.compenvurbsys.2019.101397) for a continental simulation in U.S.

Thank you for the comment which we have now included in the manuscript. Modification in line 588-590 of the revised manuscript.

Technical corrections

1. Line 81: please add "," after "accounted for".

Corrected.

2. Line 515: "The sensitivity to maximum Rubisco capacity (Vc,max), as indicative of plant photosynthetic capacity, leads to an average reduction of T2m by 0.3 °C and an increase of RH2m and ETcanyon by 1.6

Changed.

3. Figure 13: Please move the legend to the right side (outside subplot c).

Changed.

An urban ecohydrological model to quantify the effect of vegetation on urban climate and hydrology (UT&C v1.0)

Naika Meili[1,2], Gabriele Manoli[2,3], Paolo Burlando[2], Elie Bou-Zeid[4], Winston T.L. Chow[5], Andrew M. Coutts[6,7], Edoardo Daly[8], Kerry A. Nice[6,7,9], Matthias Roth[10], Nigel J. Tapper[6,7], Erik Velasco[11], Enrique R. Vivoni[12,13], and Simone Fatichi[2]

[1]ETH Zurich, Future Cities Laboratory, Singapore-ETH Centre, Singapore
[2]Institute of Environmental Engineering, ETH Zurich, Zurich, Switzerland
[3]Department of Civil, Environmental and Geomatic Engineering, University College London, London WC1E 6BT, UK
[4]Department of Civil and Environmental Engineering, Princeton University, NJ, USA
[5]School of Social Sciences, Singapore Management University, Singapore
[6]School of Earth, Atmosphere and Environment, Monash University, Clayton, Australia
[7]Cooperative Research Centre for Water Sensitive Cities, Melbourne, Australia
[8]Department of Civil Engineering, Monash University, Clayton, Australia
[9]Transport, Health, and Urban Design Hub, Faculty of Architecture, Building, and Planning, University of Melbourne, Victoria, Australia
[10]Department of Geography, National University of Singapore, Singapore
[11]Centre for Urban Greenery and Ecology, National Parks Board, Singapore
[12]School of Sustainable Engineering and the Built Environment, Arizona State University, Tempe, Arizona, USA
[13]School of Earth and Space Exploration, Arizona State University, Tempe, Arizona, USA

Correspondence: Naika Meili (meili@ifu.baug.ethz.ch)

Abstract. Increasing urbanization is likely to intensify the urban heat island effect, decrease outdoor thermal comfort and enhance runoff generation in cities. Urban green spaces are often proposed as a mitigation strategy to counteract these adverse effects and many recent developments of urban climate models focus on the inclusion of green and blue infrastructure to inform urban planning. However, many models still lack the ability to account for different plant types and oversimplify the interactions between the built environment, vegetation, and hydrology. In this study, we present an urban ecohydrological model, Urban Tethys-Chloris (UT&C), that combines principles of ecosystem modelling with an urban canopy scheme accounting for the biophysical and ecophysiological characteristics of roof vegetation, ground vegetation and urban trees. UT&C is a fully coupled energy and water balance model that calculates 2 m air temperature, 2 m humidity, and surface temperatures based on the infinite urban canyon approach. It further calculates ~~all~~ the urban hydrological fluxes in the absence of snow, including transpiration as a function of plant photosynthesis. Hence, UT&C accounts for the effects of different plant types on the urban climate and hydrology, as well as the effects of the urban environment on plant well-being and performance. UT&C performs well when compared against energy flux measurements of eddy covariance towers located in three cities in different climates (Singapore, Melbourne, Phoenix). A sensitivity analysis, performed as a proof of concept for the city of Singapore, shows a mean decrease in 2 m air temperature of 1.1 $^{\circ}\mathrm{C}$ for fully grass covered ground, 0.2 $^{\circ}\mathrm{C}$ for high values of leaf area index (LAI), and 0.3 $^{\circ}\mathrm{C}$ for high values of $V_{c,max}$ (an expression of photosynthetic ~~activity~~capacity). These reductions in temperature were combined with a simultaneous increase in relative humidity by 6.5 $\%$, 2.1 $\%$, and 1.6 $\%$, for fully grass covered ground, high values of LAI, and high values of $V_{c,max}$, respectively. Furthermore, the increase of pervious vegetated ground is able to significantly reduce surface runoff. ~~These results show that urban greening can lead to a decrease in urban air temperature and surface runoff, but this effect is limited in cities characterized by a hot, humid climate.~~

1 Introduction

More than 50 % of the world's population currently lives in cities with a predicted increase in all regions of the world (United Nations, 2014). This growing urban population, together with the projected rise in global temperature and associated higher frequency of heat waves (IPCC, 2014), is likely to exacerbate the urban heat island (UHI) effect (Li and Bou-Zeid, 2013), which can have adverse effects on outdoor thermal comfort (Mitchell et al., 2016; Mora et al., 2017), energy demand of cooling systems (Hadley et al., 2006), and urban ecology (Zhang et al., 2004; Jochner et al., 2013). At the same time, urban expansion increases impervious surface area and can enhance heavy rainfall events (Holst et al., 2016). These modifications intensify surface runoff that needs to be counteracted with greater investments in stormwater sewer systems ~~, or otherwise~~ to avoid urban flooding and damage ~~of~~ to infrastructure and valuable properties~~might result~~. Hence, the negative externalities of urbanization need to be addressed and proper mitigation strategies analysed.

Nature-based solutions, such as the increase of urban vegetation, are often encouraged to mitigate UHI and decrease surface runoff as part of a sustainable urban development (Lim and Lu, 2016; Roth, 2007; Bowler et al., 2010; Pataki et al., 2011; Li et al., 2014; Gillner et al., 2015). For instance, urban trees provide shade for pedestrians and evaporative cooling (Bowler et al., 2010; Konarska et al., 2016), while an increase in ground vegetation can further provide storm water retention (Berland et al., 2017). In addition to urban climate and water regulation, urban vegetation also provides other ecosystem services, for example, carbon storage (Nowak and Crane, 2002), enhanced biodiversity (Grimm et al., 2008), and aesthetic, cultural and health benefits (Salmond et al., 2016; Ng et al., 2018). Therefore, many ~~urban~~ policy-makers promote an increase of urban vegetation (Lim and Lu, 2016).

In this context, innovative numerical approaches are needed, given the complexity of the problem, to quantify the influence of green infrastructure on climate and water fluxes in cities and to provide guidelines for urban planners. A suitable modelling tool should resolve air temperature and humidity at the pedestrian level, surface temperatures (including mean radiant temperature), and wind speed to predict outdoor thermal comfort (OTC) (e.g. Höppe, 1999; Golasi et al., 2018). Furthermore, canopy interception and subsurface hydrology need to be included to assess surface runoff and account for potential water stress of urban vegetation. Plant biophysical and ecophysiological characteristics are also important to accurately predict the effects of plant evapotranspiration and shading on the urban climate and hydrological cycle, as well as to evaluate ~~their~~ climatic feedback on the well-being of plants and their ability to continue performing the aforementioned ecosystem services.

In recent years, a number of urban climate models started to consider the influence of vegetation on urban micrometeorology and hydrology. On the one hand, some models focus on the detailed representation of a particular process as, for example, solar irradiation (e.g. SOLWEIG: Lindberg et al., 2008; RayMan: Matzarakis et al., 2007; 2010). Methods typical of computational fluid dynamics (CFD) have been used to predict wind patterns and profiles in the urban environment (e.g. OpenFoam: Allegrini and Carmeliet, 2017; Manickathan et al., 2018; ENVI-met: Bruse and Fleer, 1998), but they usually neglect or simplify other components of the urban energy and water balance. On the other hand, mesoscale meteorological models, as for example the Weather ~~Reasearch and Forcasting~~ Research and Forecasting model (WRF) (Skamarock et al., 2008), provide a description of the large scale meteorological conditions and, when coupled with urban canopy models, can give feedback effects between

mitigation strategies and urban climate, as well as quantify the impact at different scales of the implementation. Urban canopy models solve energy and water balances and have been improved in recent years to include short ground vegetation (~~CLM: Oleson et al., 2007; 2008; 2010;~~ TEB-Veg: Lemonsu et al., 2012; PUCM: Wang et al., 2013), trees (VUCM: Park and Lee, 2008; TEB-Veg: Redon et al., 2017; PUCM: Ryu et al., 2016; BEP-Tree: Krayenhoff et al., 2014; 2015), and more detailed representations of subsurface hydrology (TEB-Hydro: Stavropulos-Laffaille et al., 2018). Further advancements allow distinguishing between deciduous and evergreen shrubs and trees (SUEWS: Ward et al., 2016), irrigated and non-irrigated vegetation (TARGET: Broadbent et al., 2018a), and plant types (VTUF-3D: Nice et al., 2018). While these studies represent significant advancements in urban geoscience, some of them still present limitations as, for example, neglecting the effects of precipitation (e.g., Broadbent et al., 2018a) or the inability to model canopy level humidity (e.g., Nice et al., 2018). Hence, while a number of urban canopy models accounting for ~~urban~~ vegetation exist, the majority of them still have a simplistic or empirical representation of plant physiological processes, and thus transpiration, or entirely neglect components of the hydrological cycle.

In this study, we combine components of the ecohydrological model Tethys-Chloris (T&C) (Fatichi et al., 2012a, b) with components of urban canopy modelling, such as the tree shading scheme of the Princeton Urban Canopy Model (Wang et al., 2013; Ryu et al., 2016), to develop the urban ecohydrological model Urban Tethys-Chloris (UT&C). UT&C accounts for detailed plant biophysical and ecophysiological characteristics and models transpiration as a function of ~~environment-plant conditions~~ (environmental conditions (e.g., soil moisture, photosynthetic active radiation, vapour pressure deficit) and plant physiological traits. Interception on plant canopy and ponding on impervious and soil surfaces, as well as urban subsurface hydrology, are accounted for. UT&C is able to simulate the influence of different configurations of green spaces (green roofs, street trees, ground vegetation), vegetation types, and plant species on the urban climate and hydrology. It is a fully coupled energy and water balance model that calculates 2 m air temperature, 2 m humidity, and skin temperatures of urban surfaces. In this article and its technical reference material (TRM) we (1) introduce UT&C and provide a detailed technical description, (2) show an evaluation of the model performance in three cities with distinctive climates, Singapore, Melbourne (Australia), and Phoenix (USA), and (3) provide proofs of concept of the model capability with a sensitivity analysis to urban vegetation cover, and plant biophysical (leaf area index, LAI) and ecophysiological (maximum Rubisco capacity, $V_{c,max}$) parameters.

2 Model design

UT&C is based on the infinite urban canyon approximation (Masson, 2000; Kusaka et al., 2001). The urban geometry is specified with a canyon height (H_{Canyon}), canyon width (W_{Canyon}), and roof width (W_{Roof}) (Fig. 1). Street directions are explicitly accounted for, resulting in one (partially) sunlit and one shaded wall (Wang et al., 2013). The ground is partitioned into impervious ($\lambda_{G,imp}$), bare soil ($\lambda_{G,bare}$), and vegetated ($\lambda_{G,veg}$) ground fractions, whereas the roof is partitioned into impervious ($\lambda_{R,imp}$) and vegetated ($\lambda_{R,veg}$) roof fractions (Wang et al., 2013). If trees are present in the urban environment, they are represented by two infinite rows of street trees described by their height (H_T), canopy radius (R_T), and distance to the nearest wall (d_T) as developed by Ryu et al. (2016).

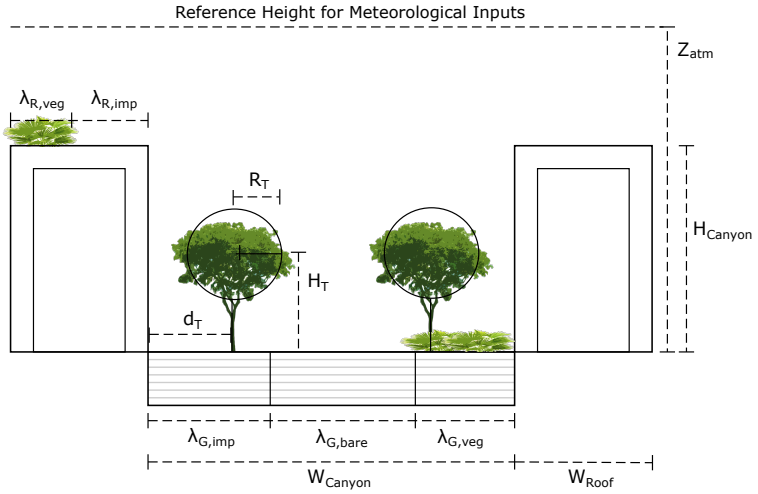

Figure 1. Geometric set-up of UT&C. Z_{atm} is the reference height for meteorological input data, H_{Canyon} the mean building height, W_{Canyon} the mean width of the urban canyon, and W_{Roof} the mean roof width. The ground is partitioned into impervious ($\lambda_{G,imp}$), bare ($\lambda_{G,bare}$), and vegetated ($\lambda_{G,veg}$) fractions. The roof is partitioned into impervious ($\lambda_{R,imp}$) and vegetated ($\lambda_{R,veg}$) fractions. The location and size of urban trees is specified by the tree height (H_T), tree radius (R_T) and tree distance to wall (d_T).

UT&C solves the energy and water budget (Fig. 2 & 3) to calculate surface temperatures of sunlit and shaded wall, tree, ground, and roof fractions. The canyon air space is subdivided into two layers. The canyon air temperature and humidity are calculated at 2 m canyon height and at canyon reference height, which is the sum of the zero-plane displacement height of the canyon and canyon roughness length (~~$d_{disp,can} + z_{0,m,can}$~~ $h_{disp,can} + z_{0,m,can}$, Fig. 2). The ~~evaporation from wall surfaces is assumed negligible. The surface energy and~~ urban energy budget for the whole atmospheric layer and the water budget are~~coupled through the evapotranspiration term E and calculated as:~~ :

$$R_n + Q_f = H + \lambda E + G \ [\mathrm{W\ m^{-2}}] \tag{1}$$

$$P + Ir = R + E + Lk + \Delta S \ [\mathrm{kg\ m^{-2} s^{-1}}] \tag{2}$$

where R_n is the net all-wave radiation, Q_f the anthropogenic heat input, H the sensible heat flux, λE the evapotranspiration E [kg m^{-2} s^{-1}] multiplied by the latent heat of vaporisation λ [J kg^{-1}], G the conductive heat flux which includes the heat storage effect of the urban fabric, P the precipitation, Ir the anthropogenic water input (irrigation), R the surface runoff, Lk the deep leakage at the bottom of the soil column, that can be regarded as a recharge term to groundwater, and ΔS the change in water storage both on the surface and in the soil. The ~~anthropogenic heat flux Q_f is directly added to the sensible heat budget of the canyon air. The heat~~ heat storage within the canyon air is not included in the current version of the model. The evaporation from wall surfaces is assumed negligible. Input data used by UT&C ~~uses as input data,~~ are observed meteorological time series of air temperature, humidity, air pressure, incoming shortwave and longwave radiation, precipitation, and wind speed at a user-specified reference height above the urban canyon and it is therefore run offline but could potentially be coupled to

mesoscale meteorological models in the future. The model runs at hourly or sub-hourly time steps and the computational speed is approximately 500 ms per time step resulting in a simulation time of one grid cell model set-up of roughly 1 h for 1 year of data (hourly time step) on a commercial laptop (Intel Core i7-6820HQ 2.7GHz, 16 GB RAM).

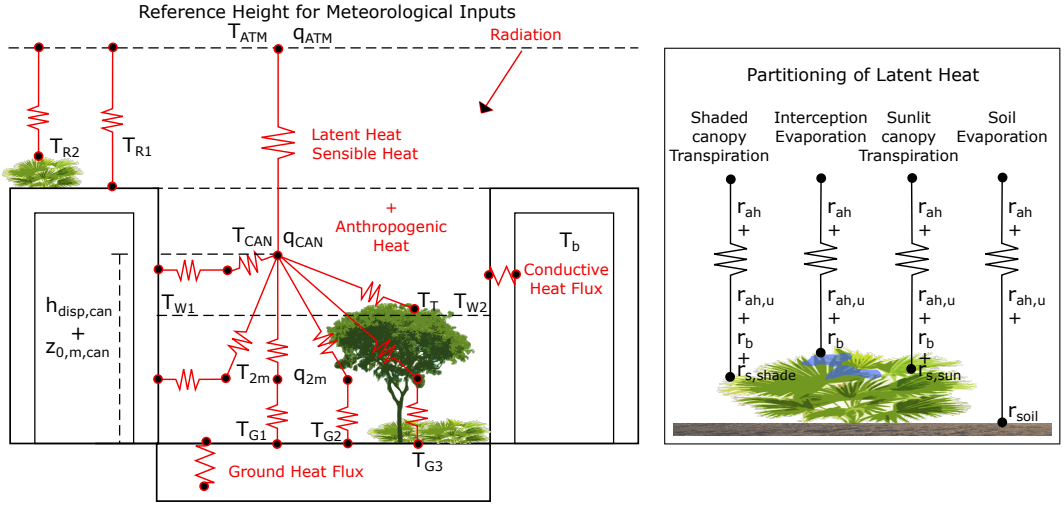

Figure 2. Modelled energy fluxes in UT&C. $T_{R,i}$, $T_{W,i}$, $T_{G,i}$, and T_T are the roof, wall, ground and tree temperatures, which are calculated solving the individual surface energy ~~balance~~balances. The canyon air is subdivided into two layers and air temperature and humidity are calculated at 2 m height (T_{2m}, q_{2m}) and at the canyon reference height (T_{can}, q_{can}) which is equal to the sum of zero-plane displacement height (~~$d_{disp,can}$~~$h_{disp,can}$) and momentum roughness length (~~$Z_{0,m,can}$~~$z_{0,m,can}$) of the canyon. T_{atm} and q_{atm} are the air temperature and humidity at the reference height for meteorological inputs, and T_b is the prescribed interior building temperature. The graph on the right shows the resistances applied to calculate shaded and sunlit canopy transpiration, evaporation from interception and soil evaporation within the urban canyon. $r_{s,shade}$ is the stomatal resistance of shaded vegetation canopy, $r_{s,sun}$ the stomatal resistance of sunlit vegetation canopy, r_b the leaf boundary resistance, r_{soil} the soil resistance, $r_{ah,u}$ the vertical aerodynamic resistance within the canyon, and r_{ah} the aerodynamic resistance above the urban canyon.

2.1 Energy budget

2.1.1 Radiative transfer

The net all-wave radiation R_n, typically referred to simply as net radiation, is the sum of net shortwave and net longwave radiation:

$$R_n = S\downarrow - S\uparrow + L\downarrow - L\uparrow \quad [\mathrm{W\ m^{-2}}] \tag{3}$$

where $S\downarrow$ is the incoming and $S\uparrow$ the reflected shortwave radiation, $L\downarrow$ the incoming longwave radiation and $L\uparrow$ the emitted and reflected longwave radiation. The incoming shortwave radiation is partitioned into direct beam and diffuse radiation using

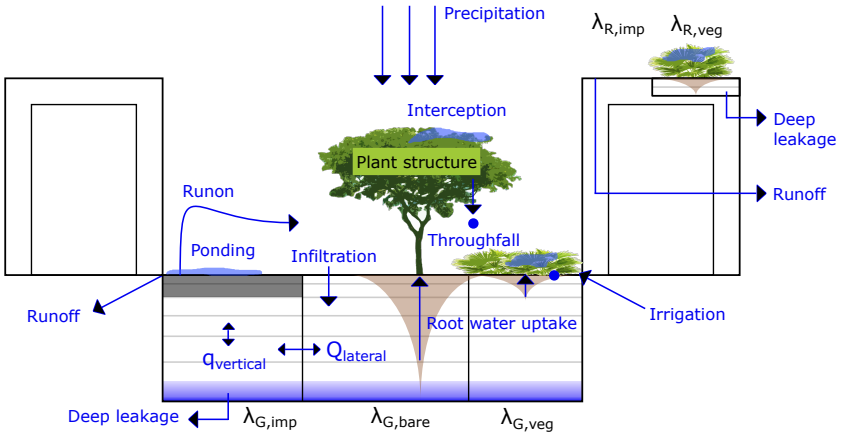

Figure 3. Modelled water fluxes in UT&C. The urban soil is subdivided into three different soil columns according to the impervious ($\lambda_{G,imp}$), bare ($\lambda_{G,bare}$), and vegetated ($\lambda_{G,veg}$) ground fraction. Vertical ($q_{vertical}$) and lateral ($Q_{lateral}$) soil water fluxes are calculated. Runoff occurs when the maximum ponding storage capacity is exceeded. An user-specified fraction of runoff can be kept in the system as runon.

a weather generator (Fatichi et al., 2011), and the absorbed shortwave radiation of surface i, $S_{n,i}$, is a function of its albedo:

$$S_{n,i} = (1-\alpha_i)(S\downarrow_i^{dir} + S\downarrow_i^{diff}) \ [\mathrm{W\ m^{-2}}] \tag{4}$$

where α_i is the albedo of surface i, and $S\downarrow_i^{dir}$ and $S\downarrow_i^{diff}$ are the direct and diffuse incoming shortwave radiation to surface i. The amount of direct shortwave radiation received by each urban surface is calculated considering shade according to established methodologies (Masson, 2000; Kusaka et al., 2001; Wang et al., 2013) if trees are absent or according to Ryu et al. (2016) if trees are present. The diffuse shortwave radiation received from the sky on each surface is calculated with the respective sky-view-factor. It is assumed that all surfaces are Lambertian with diffuse and isotropic scattering and that the different ground cover fractions are homogeneously distributed over the ground area. Following these assumptions, infinite reflections of shortwave radiation are calculated within the urban canyon with the use of view-factors (Sparrow and Cess, 1970; Harman et al., 2003; Wang, 2010, 2014). The air within the canyon does not interact in the radiative exchange, for example, the effect of airborne aerosols is neglected (Wang, 2014).

The absorbed ~~and reflected~~ longwave radiation of each surface i is calculated as:

$$L_{n,i} = \epsilon_i(L\downarrow_i - \sigma T_i^4) \ [\mathrm{W\ m^{-2}}] \tag{5}$$

where ϵ_i is the emissivity and $(1-\epsilon_i)$ the reflectivity of a surface for longwave radiation, $L\downarrow_i$ the incoming longwave radiation, $\sigma = 5.67 * 10^{-8}$ [W m^{-2} K^{-4}] is the Stefan-Boltzmann constant, and T_i [K] the surface temperature. The incoming longwave radiation $L\downarrow_i$ is calculated as a function of the emitted longwave radiation by the atmosphere and the surrounding surfaces. As with shortwave radiation, infinite reflections of longwave radiation within the urban canyon are calculated with the use of reciprocal view-factors (Harman et al., 2003). The view factors are caculated with analytically derived equations for an

urban canyon without trees (Sparrow and Cess, 1970; Masson, 2000; Harman et al., 2003; Park and Lee, 2008; Wang et al., 2013). If trees are present, the view factors are calculated with a simplified two dimensional Monte Carlo ray tracing algorithm developed and included in the UT&C code similar to the algorithms described by Wang (2014) and Frank et al. (2016). The Monte Carlo ray tracing view factors are corrected for reciprocity as to guarantee energy conservation.

The detailed description of shortwave and longwave radiation, view factor, and Monte Carlo ray tracing calculations are described in Sect. 1 of the TRM.

2.1.2 Turbulent energy fluxes

The total sensible and latent heat fluxes are calculated as the area-weighted average flux of roof and canyon area. The turbulent transport of sensible and latent heat is calculated according to a resistance parametrization (Shuttleworth, 2012) as:

$$H_i = \rho_a C_p \frac{(T_i - T_a)}{\sum r_j} \tag{6}$$

$$\lambda E_i = \lambda \rho_a \frac{(q_{sat,(T_i)} - q_a)}{\sum r_j} \tag{7}$$

where ρ_a [kg m^{-3}] is the ~~dry~~ air density, C_p [J kg^{-1} K^{-1}] the specific heat capacity of air at constant pressure, T_i [K] the temperature of surface i, T_a [K] the air temperature, $q_{sat,(T_i)}$ [$-$] the saturated specific humidity of surface i, q_a [$-$] the specific humidity of the air, and $\sum r_j$ [s m^{-1}] the sum of resistances j to the turbulent transport of sensible and latent heat. UT&C accounts for vertical aerodynamic resistance above and within the urban canyon, horizontal aerodynamic resistance within the urban canyon, leaf boundary layer resistance, stomatal resistance of sunlit and shaded leaves, and soil resistance (Fig. 2). The vertical wind speed profile is assumed logarithmic above the urban canopy, exponential within the canyon, and logarithmic again close to the canyon ground (Masson, 2000; Mahat et al., 2013). Zero-plane displacement height, ~~$d_{disp,can}$~~ $h_{disp,can}$, and momentum roughness length, $z_{0,m,can}$, of the urban canopy are calculated according to the formulations developed by Macdonald et al. (1998), which were modified by Kent et al. (2017) to include the effects of urban trees. The roughness length for heat and water vapour is assumed to be one tenth of the momentum roughness length. The aerodynamic resistance above the urban canopy, r_{ah}, is calculated according to Mascart et al. (1995) with a simplified parametrization of the Monin-Obukhov similarity theory. The vertical aerodynamic resistance within the canyon is calculated with an undercanopy resistance parametrisation, $r_{ah,u}$ (Mahat et al., 2013). The air volume within the canyon is subdivided into two layers with a height ~~of~~ equal to the minimum between 4 m and H_{Canyon} for the first layer and ~~a height of $(H_{Canyon} - 4)$~~ $H_{Canyon} - 4$ m for the second layer~~. The~~, which is not present if H_{Canyon} is less than 4 m. The total wall sensible heat flux is calculated as the area weighted average of the two layers with only the first layer contributing to the wall sensible heat flux at 2 m canyon height (TRM Sect. 2.1.4). UT&C allows for an average canyon height H_{Canyon} lower than 4 m, and, in such case, the sensible heat flux from the wall is entirely contributing to the 2 m air temperature. The horizontal aerodynamic resistance from the wall to the canyon air, $r_{ah,w}$, is calculated with the respective wind speeds at mid-height of each canyon air layer with the fomulations of Rowley et al. (1930) and Rowley and Eckley (1932). The leaf boundary layer resistance, r_b, describing the resistance imposed by a thin viscous sublayer of air around the leaf surfaces is calculated as a function of wind speed and leaf dimension (Fatichi

et al., 2012a, b; Leuning et al., 1995; Monteith, 1973; Choudhury and Monteith, 1988; Shuttleworth and Gurney, 1990). The soil resistance, r_{soil}, describes the transport of water vapour from the soil pores to the air above the soil surface boundary layer and is a function of the atmospheric condictions, ~~diffusion in the soil boundary layer, moisture transport within the soil,~~ and wetness of the surface layer (Haghighi et al., 2013; Fatichi and Pappas, 2017). The total soil resistance is the sum of the soil boundary layer resistance and internal capillary-viscous resistance (Haghighi et al., 2013; Fatichi and Pappas, 2017). The stomatal resistance, r_s, describes the transport of water vapour from the leaf interior to the air. UT&C calculates the stomatal resistance with a biochemical model as a function of photosynthetic activity as described in Sect. 2.3.1. Transpirative fluxes only occur from the vegetation canopy fraction, which is not covered by intercepted water. Evaporative fluxes occur from ground, impervious surfaces (except walls) and the canopy fraction covered by intercepted water. The fraction of vegetation canopy covered by water is calculated according to Deardorff (1978).

The detailed description of all the sensible and latent heaf fluxes, resistance parametrizations, wind profile, displacement height and roughness length calculations can be found in Sect. 2 and 3 of the TRM.

2.1.3 Conductive heat fluxes

The conductive heat fluxes of wall and roof are calculated with a numerical solution of the heat diffusion equation (Hu and Islam, 1995; Hillel, 1998; Núnez et al., 2010; Masson, 2000). UT&C considers two physical layers for vegetated roof and one physical layer for impervious roof, and sunlit and shaded wall. The numerical solution is based on three nodes (two layers) with the inner boundary condition equal to the interior building temperature T_b, which is set equal to the atmospheric forcing temperature within the range of a specified minimum $T_{b,min}$ and maximum temperature $T_{b,max}$. Below and above $T_{b,min}$ and $T_{b,max}$, the interior building temperature is fixed to $T_{b,min}$ and $T_{b,max}$ assuming air-conditioning or heating of the building interior (de Munck et al., 2018). Furthermore, UT&C is able to account for a fixed prescribed interior building temperature T_b. The outer boundary condition is given by the prognostic surface temperature and in between an internal wall and roof temperature is calculated to account for heat storage effects. The ground conductive heat flux is calculated with the force restore method (Hu and Islam, 1995; Noilhan and Planton, 1989; Fatichi et al., 2012a, b). Soil volumetric heat capacity, and soil thermal conductivity are calculated as a function of soil type and soil water content according to de Vries (1963), Farouki (1981), and Oleson et al. (2004, 2013) as described in Fatichi et al. (2012a, b). Further information on the calculation of the conductive heat fluxes can be found in Sect. 4 of the TRM.

2.1.4 Anthropogenic heat fluxes

UT&C accounts for a prescribed time series of anthropogenic heat flux, which is added to the canyon air, assuming that heat emissions mostly occur within the urban canyon. Hence, anthropogenic heat emissions caused by air conditioning, car exhaust, industry, human metabolism, or any other anthropogenic heat source need to be estimated prior to simulation, e.g. using existing approaches (Sailor and Lu, 2004; Sailor et al., 2015). Anthropogenic heat effects caused by domestic heating or cooling of building interiors are already accounted for through the conductive heat flux from building interior to canyon air that is influenced by the fixed interior building temperature as described in Sect. 2.1.3 ~~.~~and in the TRM Sect. 5. The anthropogenic

heat inputs used to assess the model performance are based on site specific values (Roth et al., 2016; Chow et al., 2014) and summarized in the TRM (Sect. 9).

2.2 Water budget

2.2.1 Interception and ponding

UT&C calculates interception of water by vegetation canopies and ponding on impervious surfaces, bare, and vegetated soils. The interception and ponding dynamics are calculated with a mass budget approach that can be written as (Rutter et al., 1971, 1975; Ivanov et al., 2008b; Fatichi et al., 2012a, b):

$$\frac{dIn}{dt} = P^* - D - E_{In} \ [\mathrm{mm\ h^{-1}}] \tag{8}$$

where In [mm] is the intercepted or ponding water, P^* [$\mathrm{mm\ h^{-1}}$] the incoming water flux from precipitation and runon, D [$\mathrm{mm\ h^{-1}}$] the canopy drainage or infiltration flux from ponding water, and E_{In} [$\mathrm{mm\ h^{-1}}$] the evaporation from intercepted and ponding water. The maximum water ponding or storage capacity of impervious surfaces is an uncertain but important parameter to accurately model the latent heat flux after rain events (Wouters et al., 2015; Ramamurthy and Bou-Zeid, 2014). UT&C accounts for a maximum impervious ponding capacity as well as runon, a fraction of runoff that is kept in the system (Sect. 2.2.3). The detailed description of interception and ponding dynamics can be found in Sect. 6.1 of the TRM and Sect. 2.3.3 for vegetation canopy. The maximum impervious ponding capacity and the fraction of runoff assigned to runon used in the model performance assessment are summarized in the TRM (Sect. 9).

2.2.2 Vadose soil moisture dynamics

The canyon ground is discretized into n vertical soil layers and three soil columns corresponding to the impervious, bare, and vegetated ground fractions (Fig. 3). The vegetated roof fraction is discretized into one column with m vertical soil layers. The first two layers of the impervious ground fraction are assumed impermeable with negligible porosity and do not participate in the vadose zone dynamics. Soil underneath buildings is not considered in the current parameterization. The 1D-Richards equation (Richards, 1931) is first solved in the vertical direction for each soil column using a finite volume approach with the methods of lines (Lee et al., 2004; Fatichi et al., 2012a, b) as:

$$d_{z,j}\frac{d\theta_j}{dt} = (q_{j-1} - q_j) - T_{tree}\, r_{tree_j} - T_{veg}\, r_{veg_j} - E_g \tag{9}$$

where $d_{z,j}$ [mm] is the soil layer thickness, and q_{j-1} and q_j [$\mathrm{mm\ h^{-1}}$] are the vertical inflow and outflow of soil layer j. The transpirative sinks of ground vegetation and trees, T_{veg} and T_{tree} [$\mathrm{mm\ h^{-1}}$], are weighted by their root biomass fraction in each soil layer, r_{veg_j} and r_{tree_j} [$-$]. The soil evaporation, E_g [$\mathrm{mm\ h^{-1}}$], is only present in the first ($j = 1$) soil layer of the bare and vegetated soil column. In a second step, the 1D-Richards equation (Richards, 1931) is solved laterally as:

$$\frac{d\theta_j}{dt} = (Q_{l,in,j} - Q_{l,out,j}) \tag{10}$$

where $Q_{l,in,j}$ and $Q_{l,out,j}$ $[\mathrm{mm\ h^{-1}}]$ are the lateral ~~in~~ inflow and outflow of soil layer j with respect to the adjacent soil columns. Exchange of soil moisture between all three soil columns is included in the model resulting in a total of six (factorial of three) lateral fluxes. The vertical q_j and lateral $Q_{l,j}$ fluxes of water in the soil are calculated according to the gradients of soil water potentials (see TRM Sect. 6.2.1). The infiltration into the first soil layer is either the maximum infiltration capacity or the water available at the surface, depending on which is limiting. The maximum infiltration capacity for bare and vegetated surfaces is calculated based on the hydraulic gradient between ponding water (if any) and water potential in the first soil layer. The maximum infiltration through the impervious ground surface is a model parameter and the infiltrated water is directly added to the third soil layer as the first two layers are not interacting with the vadose zone dynamics. The water percolating from the last soil layer n or m is called deep leakage. The formation of a shallow groundwater table is possible if soil hydraulic conditions allow or if an impermeable boundary condition is prescribed at the bottom of the soil column (Fatichi et al., 2012a, b). The soil hydraulic properties are calculated based on the soil textural composition using pedotransfer functions, and soil hydraulic conductivity and soil water retention curve can either be described with the van Genuchten (1980) or Saxton and Rawls (2006) parametrizations.

The detailed description of the vadose zone dynamics can be found in Sect. 6.2 of the TRM.

2.2.3 Runoff and runon

Runoff is generated when the maximum infiltration capacity and then interception capacity of a surface are exceeded. The total roof and ground runoff is calculated as the area averaged runoff of each surface fraction. UT&C allows users to specify a percentage of runoff that stays in the system for one time step (1 hour) and it is re-added as runon evenly to either roof or ground areas. Allowing for a runon component is important to model urban areas where excess water from one surface does not exit immediately the system but remains in place (e.g., flat roof) or is redirected to another surface as for example bioswales. Further information on the calculation of runoff and runon can be found in Sect. 6.3 of the TRM.

2.2.4 Anthropogenic water

UT&C accounts for anthropogenic water in the form of a prescribed urban irrigation time series for vegetated roof, bare ground, and vegetated ground. The irrigation can be added to the soil surface underneath vegetation to represent drip irrigation or to the vegetation surface to represent sprinkler or hose irrigation. The irrigation schemes used during the model performance assessment are described in Sect. 9 of the TRM. Urban vegetation in Phoenix is heavily dependent on irrigation year round and the irrigation time series is modelled as described by Volo et al. (2014).

2.3 Vegetation processes

2.3.1 Photosynthesis and stomata behaviour

Plants open their stomata to allow CO_2 exchange between the atmosphere and the chloroplasts inside their leaves and perform photosynthesis. This leads to an inevitable loss of water vapour from the water-saturated tissue within the plant leaves (Sellers

et al., 1997). UT&C applies a biochemical model to describe the coupling between stomatal resistance and photosynthesis (Fatichi et al., 2012a, b). The stomatal behaviour is dependent on the net CO_2 assimilation rate (i.e., photosynthesis), atmospheric vapour pressure deficit, and intercellular CO_2 concentration (Leuning, 1995). The net assimilation rate is a function of three limiting rates of enzyme kinetics: the Rubisco enzyme limited carboxylation rate, the rate of photosynthetic active radiation (PAR) captured by the leaf chlorophyll, and the limiting rate of product export and usage (Farquhar et al., 1980; Collatz et al., 1991, 1992; Fatichi et al., 2012a, b). The rates of enzyme ~~kinetic~~ kinetics are influenced by the leaf temperature. The net photosynthetic assimilation rate is further influenced by water stress that is inducing stomatal closure (e.g., Zhou et al., 2013).

The detailed mathematical formulations of the biochemical model to calculate net CO_2 assimilation rate and stomatal resistance are described in Sect. 3.6.2 and 3.6.3 of the TRM.

2.3.2 Upscaling from leaf to canopy

UT&C applies a "two big leaves" approach that divides vegetation canopy into sunlit and shaded fractions (Wang and Leuning, 1998; Fatichi et al., 2012a). The photosynthetic activity is calculated individually for the two fractions to account for the light limitation occuring in the shaded leaves, which only receive diffuse radiation. UT&C uses an exponential decay of direct beam radiation and leaf nitrogen content with leaf area throughout the vegetation canopy to scale photosynthetic capacity from leaf to canopy level (Dai et al., 2004; Ivanov et al., 2008a; Fatichi et al., 2012a). The current version of UT&C does not include a seasonally changing LAI~~yet~~, but time series of LAI can be supplied as model input if needed.

The detailed description of the leaf to canopy upscaling can be found in Sect. 3.6.1 of the TRM.

2.3.3 Canopy interception

Vegetation canopy interception is modelled using a mass budget approach and the Rutter model as described in Sect. 2.2.1. The fraction of precipitation arriving onto the canopy foliage and its throughfall is modelled as a function of the projected leaf area fraction onto the ground. The projected leaf area fraction is a function of leaf area index (LAI) and stem area index (SAI) (Mahfouf and Jacquemin, 1989). Interception excess drainage occurs if the precipitation on the canopy foliage exceeds the maximum interception capacity of the vegetation canopy. The maximum canopy interception capacity is calculated as a function of LAI and SAI according to Dickinson et al. (1993). Dripping from intercepted water on the canopy is calculated according to the Rutter model (Rutter et al., 1971; Mahfouf and Jacquemin, 1989).

Further description of the canopy interception calculations can be found in Sect. 6.1.1 of the TRM.

2.3.4 Root water uptake and root biomass distribution

The root water uptake from different soil layers is calculated according to the vertical and horizontal plant root biomass distribution. UT&C allows to distinguish between four different vertical root biomass profiles (Fatichi et al., 2012a, b): (1) an exponential vertical root profile (Arora and Boer, 2005), (2) a linear dose response root profile (Schenk and Jackson, 2002;

Collins and Bras, 2007), (3) a constant vertical root profile, and (4) a linear dose response profile with tap roots. The root biomass profile of short stature roof and ground vegetation is horizontally contained within the roof and ground vegetated areas while two different horizontal root profiles are distinguished for tree roots: (1) The tree roots are evenly distributed over the total canyon width, and (2) the tree roots are horizontally restricted to the tree canopy extent, which is assumed to be mainly located over the vegetated and bare ground fractions. The choice of horizontal tree root distribution is influenced by the patch size distribution as well as the heterogeneity of the pervious ground cover fraction and this affects soil moisture access by trees. The root water uptake can be limited by the water availability in the soil or the hydraulic resistance from the soil to the root (Fatichi et al., 2012a, b). Currently, UT&C does not include a plant hydraulic module and it is assumed that the leaf and xylem water potential are equal to the soil water potential experienced within the root zone (Fatichi et al., 2012a, b). Hence, root water uptake is equal to transpiration and water storage in plant tissue is neglected even though in certain conditions it could be significant (e.g., Mirfenderesgi et al., 2016; Huang et al., 2017).

The detailed description of vertical and horizontal root profiles, soil-to-root resistance, and root water uptake calculations can be found in Sect. 7 of the TRM.

3 Methods and data

3.1 Model performance assessment sites: Singapore, Melbourne, Phoenix

Table 1. Mean values calculated for the ~~whole~~ entire time period of the meteorological forcing data time series in Telok Kurau Singapore, Preston Melbourne, and Maryvale Phoenix.

	T_{air} (°C)	RH_{air} (%)	Precipitation (mm year^{-1})	$S\downarrow$ (W m^{-2})	$L\downarrow$ (W m^{-2})	~~Velocity u~~ Wind speed U (m s^{-1})	Data period
Singapore[(1)]	27.5	71	1840	187	420	2.2	1.5.2013 - 30.4.2014
Melbourne[(2)]	13.5	67	741	181	318	4.8	13.8.2003 - 28.11.2004
Phoenix[(3)]	24.1	28	99	236	352	2.4	17.12.2011 - 31.12.2012

[(1)] Velasco et al. (2013); Roth et al. (2016), [(2)] Coutts et al. (2007a, b), [(3)] Chow et al. (2014)

UT&C is tested to reproduce tower based eddy covariance measurements from Telok Kurau in Singapore (Velasco et al., 2013; Roth et al., 2016), Preston in Melbourne, Australia (Coutts et al., 2007a, b), and Maryvale in Phoenix, AZ (Chow et al., 2014). The measurements at all three sites have been performed according to known guidelines to ensure that the measurements are representative of the underlying surface at the neighbourhood scale, have followed accepted measurement protocols and, passed quality control checks as described in detail in Velasco et al. (2013), Roth et al. (2016), Coutts et al. (2007a, b), and Chow et al. (2014). The measurement sites will afterwards be referred to as Singapore, Melbourne, and Phoenix, respectively.

Singapore experiences a tropical rainforest climate (Köppen classification Af) with uniformly high air temperature throughout the year (data mean: 27.5 °C), high relative humidity (data mean: 71 %) and abundant rainfall (data mean: ~1840 mm y^{-1},

which is lower than the long-term mean of ∼2340 $\mathrm{mm\ y^{-1}}$) (Table 1) (Velasco et al., 2013; Roth et al., 2016). Two monsoonal wind regimes are observed, the southwest monsoon (June to September) and the northeast monsoon (December to mid-March) (Velasco et al., 2013; Roth et al., 2016). The meteorological time series used in this study is characterized by an unusual dry period from mid-January 2014 to mid-March 2014 with an almost complete absence of rainfall (Harshan et al., 2017; Demuzere et al., 2017). The Singapore measurement site is located in the Telok Kurau district (1° 18' 51" N, 103° 54' 40" E, ∼ 10 m a.s.l.) which corresponds to a 'compact low rise' local climate zone (LCZ3) (Stewart and Oke, 2012). It is a residential area with a mean building and tree height of 9.86 and 7.26 m, respectively, and an area averaged height-to-width ratio (H/W) of 0.61 (Velasco et al., 2013; Roth et al., 2016; Demuzere et al., 2017). The surface cover consists of 39 $\%$ buildings, 34 $\%$ paved and gravel, 12 $\%$ roads, 11 $\%$ trees, 4 $\%$ grass and 1 $\%$ water (Velasco et al., 2013; Roth et al., 2016). The Telok Kurau eddy covariance measurement site and set-up are described in detail in Velasco et al. (2013) and Roth et al. (2016).

Melbourne experiences a seasonal temperature cycle with warm summers and mild winters (data mean: 13.5 $^{\circ}\mathrm{C}$). The mean observed relative humidity is relatively high (data mean: 67 $\%$) while the precipitation amount is moderate (data mean: ∼741 $\mathrm{mm\ y^{-1}}$) and is evenly distributed throughout the year (Table 1). The flux tower was located in the suburb of Preston (37° 49' S, 144° 53' E, ∼ 93 m a.s.l.) (Coutts et al., 2007a, b) in a low density, moderately developed residential area classified as an 'open low rise' local climate zone (LCZ 6) (Stewart and Oke, 2012; Best and Grimmond, 2015) with mean building height of 6.4 m (Coutts et al., 2007a, b). The land surface is covered by 44.5 $\%$ buildings, 4.5 $\%$ concrete, 13 $\%$ road, 22.5 $\%$ vegetation, 15 $\%$ grass and 0.5 $\%$ bare ground or pools (Coutts et al., 2007a, b; Grimmond et al., 2011; Best and Grimmond, 2015). Further information on the Preston measurement campaign can be found in Coutts et al. (2007a, b).

Phoenix has a hot arid subtropical desert climate (Köppen classification BWh) (Chow et al., 2014). Its temperature is characterized by a yearly cycle with very high summer and cooler winter temperatures (data mean: 24.1 $^{\circ}\mathrm{C}$), and very low relative humidity (data mean: 28 $\%$) (Table 1). The yearly precipitation amount is small and occurs during winter (December-February) and in summer during the North American monsoon season (July-September) (Templeton et al., 2018). The measured time period exhibits lower than average rainfall with 99 $\mathrm{mm\ y^{-1}}$ (Table 1). The eddy covariance measurement tower was set up in the suburb of Maryvale (33° 29' 2" N, 112° 8' 35" W, 337 m a.s.l.), which corresponds to an 'open low rise' local climate zone (LCZ6) (Stewart and Oke, 2012). It is a suburban residential area with low-rise, single-family, one-story houses with a mean building and tree height of 4.5 m and 4 m respectively, and a height to width ratio (H/W) of 0.4 (Chow et al., 2014). The land cover consists of 26 $\%$ buildings, 22 $\%$ roads and asphalt, 5 $\%$ trees, 10 $\%$ grass, 37 $\%$ bare soil and <1 $\%$ water and pools (Chow et al., 2014). The landscape is mostly xeric (dry) and hose irrigation is used to water gardens. The detailed information on the Maryvale eddy covariance study site can be found in Chow et al. (2014).

The exact model parameters used in the UT&C validation in Singapore, Melbourne and Phoenix can be found in Sect. 9 of the TRM.

3.2 Model performance metrics

The UT&C assessment is based on the comparison between measured and simulated outgoing shortwave radiation $S\uparrow$, outgoing longwave radiation $L\uparrow$, net absorbed all-wave radiation R_n, sensible heat flux H, and latent heat flux λE. The comparison

is based on time series of hourly day and night time fluxes, and daily cycles of flux mean and standard deviation. Model performance is assessed considering the coefficient of determination (R^2), root mean square error (RMSE), mean absolute error (MAE), and mean bias error (MBE). Furthermore, the systematic (RMSE_s) and non-systematic (RMSE_u) components of the RMSE error (Willmott, 1982) are calculated and reported in Sect. 10 of the TRM. All model performance indices are calculated with the available data of the full time period specified for each location (Table 1, 2, and 3) including all weather conditions, except for hours with instantaneously occuring rainfall (Chow et al., 2014; Roth et al., 2016). Shortwave radiation performance is assessed only considering daytime values. ~~Seperate~~ Separate model performance is also calculated for day- and nighttime and reported in Sect. 10 of the TRM as well as for an exceptional dry period from 15.2.2014 - 16.3.2014 in Singapore (Table 3). Daytime is defined as 0800-1800 hrs LT for Singapore and as times with positive incoming shortwave radiation for Melbourne and Phoenix. Nighttime is defined as 2000-0600 hrs LT for Singapore and as times with no incoming shortwave radiation for Melbourne and Phoenix. The overall model performance results are compared to literature that validates other urban canyon models using flux tower measurements from Telok Kurau Singapore, Preston Melbourne, and Maryvale Phoenix (Table 2).

The total assessment period in Telok Kurau Singapore is one year (1.5.2013 - 30.4.2014, Table 1). The UT&C model performance results are compared to the previous studies of Demuzere et al. (2017), Harshan et al. (2017), and Liu et al. (2017), who used the same eddy-covariance measurements from Telok Kurau. Demuzere et al. (2017) analysed the model performance of four urban canopy models (SURFEX: Masson et al., 2013; CLM v4.0: Bonan et al., 2011; Lawrence et al., 2011; TERRA_URB: Wouters et al., 2015, 2016; SUEWS: Ward et al., 2016). Harshan et al. (2017) analysed the performance of one model (TEB: Masson, 2000) and Liu et al. (2017) used flux tower data to validate a coupled Noah/SLUCM model after the implementation of tree evapotranspiration. Additionally, the simulation of 2 m air temperature in Singapore is compared to the measurements (11.11.2013 - 19.4.2014) presented by Harshan et al. (2017), which were digitized for this purpose.

The total observational period in Preston Melbourne is approximately 15.5 months (13.8.2003 - 28.11.2004) (Table 1). The UT&C model performance results are compared to results from the international urban energy model comparison, Phase 2 by Grimmond et al. (2011), who analysed the performance of 32 urban land surface models with eddy-covariance measurements from Preston. The reported RMSE and MBE is the median performance of all the models with radiation budget closure, while R^2 values are determined from the reported Taylor diagrams. Furthermore, the UT&C model performance results for Melbourne are compared to the performance of VTUF-3D v1.0 (Nice et al., 2018), which also includes an ecohydrological component and was assessed against Preston eddy-covariance measurements (Nice et al., 2018).

The total assessment period in Maryvale Phoenix is approximately 1 year (17.12.2011 - 31.12.2012) (Table 1) (Chow et al., 2014). The UT&C model performance results are compared to the results of Song and Wang (2015), who assessed a single-layer urban canopy model (Wang et al., 2011, 2013) in Maryvale Phoenix (Song and Wang, 2015). Song and Wang (2015) only use a 5 day period for model performance assessment though while the UT&C model statistics are calculated for the full reported time period. Additionally, the simulation of bare ground temperature at 2 cm soil depth in Phoenix is compared with soil temperature measurements at the same depth conducted by Chow et al. (2014). Since the soil thermal profile is not a direct output of the model, the simulated bare ground surface temperature at 2 cm soil depth was calculated using the bare ground

surface temperature and a numerical solution of the heat diffusion equation with mixed boundary conditions assigning surface temperature at the top of the soil column and zero ground heat flux at 2 m depth.

3.3 Model capability and sensitivity analysis

The capability of UT&C to describe urban climate, hydrology, and vegetation is further shown through the modelled time series of soil moisture, the resulting plant water stress, and decrease in latent heat during the dry period of February 2014 in Singapore. Furthermore, the effect of changes in vegetated ground cover within the urban canyon ($\lambda_{G,veg}$), LAI, and maximum Rubisco capacity ($V_{c,max}$) on the long term 2 m air temperature, 2 m relative humidity, and the energy and water budget is shown through a sensitivity analysis using the background climate, urban fabric, and geometries of Telok Kurau in Singapore (See Sect. 9 of TRM for parameter set-up of Telok Kurau). Relative humidity is dependent on the saturation vapour pressure which is directly connected to the air temperature and therefore, relative humidity changes are also linked to temperature changes and not only the water content in the air. In this study, the analysis of relative humidity is chosen as it plays a key role in the outdoor thermal comfort of humans. The simulation time series length is one year and the results are analysed as mean changes over the whole time period, mean changes during an unirrigated dry period (15.2.2014 - 16.3.2014), and mean daily cycles averaged over the whole year, respectively. Mean changes are computed in comparison to a non-vegetated condition for the increase of $\lambda_{G,veg}$, to the flux tower baseline condition ($\lambda_{G,veg}$ = 25 $\%$ and λ_{tree} = 18 $\%$ within the urban canyon) with a LAI of 0.5 for the LAI increase, and to the flux tower baseline condition with a $V_{c,max}$ of 20 µmol CO_2 s^{-1} m^{-2} for the $V_{c,max}$ increase. $\lambda_{G,veg}$ is varied between 0 and 100 $\%$ (0 and 1), LAI between 0.5 and 5, and $V_{c,max}$ between 20 and 120 µmol CO_2 s^{-1} m^{-2} (The Figure of the schematic set-up is presented in Sect. 10 of the TRM). These ranges correspond to realistic values of biophysical and physiological parameters observed in nature (Wullschleger, 1993; Kattge et al., 2009; Iio et al., 2014; Paschalis et al., 2018; Manoli et al., 2018). Low values of $\lambda_{G,veg}$ specify a low amount of ground vegetation within the urban canyon, low values of LAI specify a thin vegetation canopy, and low values of $V_{c,max}$ specify plants with small photosynthetic and transpirative capacity. The sensitivity analysis for vegetated ground cover is performed without trees as a fully sealed ground surface with trees is not a realistic scenario. The increase of LAI and $V_{c,max}$ includes vegetated ground cover and trees and the parameters are simultaneously increased for both vegetation types.

4 Results

4.1 Model performance

4.1.1 Outgoing shortwave and longwave radiation, and net all-wave radiation

Modelled and observed $S\uparrow$ show good agreement with a high R^2 of 0.97, 0.99, and 0.98 for Singapore, Melbourne, and Phoenix, respectively (Table 2). $S\uparrow$ is generally well predicted in urban climate models with high R^2 of 0.98 or above as shown by Grimmond et al. (2011) and Demuzere et al. (2017) in their model inter comparison studies. UT&C is able to accurately simulate the mean diurnal cycle and variablilty of $S\uparrow$ (Sect. 10 of TRM), but slightly underpredicts $S\uparrow$ in all three

Table 2. Coefficient of determination (R^2), mean bias error (MBE), root mean square error (RMSE), and mean absolute error (MAE) of the UT&C model performance assessment in Singapore, Melbourne, and Phoenix, and comparison with literature values assessing urban canopy models in the same locations. The superscript * specifies a similar, ** an improved, and $^\sim$ a decreased model performance of UT&C compared to values reported in literature. The validation period specifies the total UT&C simulation period in hours (h) and the percentage of time with available eddy-covariance measurements for model performance assessment.

	UT&C					Literature		
	R^2 (−)	MBE (W m^{-2})	RMSE (W m^{-2})	MAE (W m^{-2})	Validation period % of (h)	R^2 (−)	MBE (W m^{-2})	RMSE (W m^{-2})
$S\uparrow$ (Singapore)	0.97 *	-5.5**	9.7**	6.6	84 % of 4015 h	$\sim$ 0.98 [3]	-10.6 [1]	17.0 [1]
$S\uparrow$ (Melbourne)	0.99*	-12.5$^\sim$	16.3 $^\sim$	12.8	65 % of 5747 h	>0.98 [4]	-0.5 [4]	6 [4]
$S\uparrow$ (Phoenix)	0.98	-5.9	10.7	8.1	98 % of 4539 h	-	-	-
$L\uparrow$ (Singapore)	0.93*	8.3**	23.3**	17.3	86 % of 8760 h	0.92-0.96 [3]	13.3 [1]	33.3 [1]
$L\uparrow$ (Melbourne)	0.94*	7.8*	14.8*	11.7	62 % of 11376 h	0.90-0.98 [4]	8 [4]	16 [4]
$L\uparrow$ (Phoenix)	0.98	4.9	11.5	9.2	98 % of 9144 h	-	-	-
R_n (Singapore)	>0.99*	-4.9*	20.8**	16.4	84 % of 8760 h	>0.99 [3]	-6.1 [1]	27.6 [1]
R_n (Melbourne)	>0.99*	-0.6**	9.5**	7.5	62 % of 11376 h	>0.98 [4]	-6 [4]	18 [4]
						0.99 [5]	3.0 [5]	19.0 [5]
R_n (Phoenix)	>0.99	-2.1	12.5**	9.7	98 % of 9144 h	-	-	20 [6]
H (Singapore)	0.94 *	-4*	23.5*	14.9	80 % of 8760 h	0.90-0.92 [3]	5.3 [1]	27.9 [1]
H (Melbourne)	0.90**	14.4$^\sim$	36.6**	23.6	93 % of 11376 h	0.72-0.90 [4]	4 [4]	47 [4]
						0.87 [5]	-4.0 [5]	40.2 [5]
H (Phoenix)	0.92	10.9	27.4**	20.7	78 % of 9144 h	-	-	34 [6]
λE (Singapore)	0.60*	-1.2**	28.1**	15.6	79 % of 8760 h	0.34-0.61[3]	-10.8 [1]	44.3 [1]
							-12.0 [2]	38.7 [2]
λE (Melbourne)	0.62**	1.9*	26.8**	17.8	93 % of 11376 h	0.30-0.61 [4]	-0.8 [4]	40 [4]
						0.45 [5]	-9.5 [5]	33.1 [5]
λE (Phoenix)	0.50	4.1	19.5*	11.5	78 % of 9144 h	-	-	20 [6]

Reference (Validation time series), [1] Harshan et al. (2017) (18.5.2013 - 19.4.2014), [2] Liu et al. (2017) (18.5.2013 - 19.4.2014), [3] Demuzere et al. (2017) (1.6.2013 - 17.4.2014): Taylor diagrams, [4] Grimmond et al. (2011) (August 2003 - November 2004): Coefficients of determination R^2 are determined from the Taylor diagrams and specify the performance range of the majority of models. The reported RMSE, MBE, and MAE specify the median model performance in the subset of models with radiation budget closure, [5] Nice et al. (2018) (10.2.2004 - 10.3.2004), [6] Song and Wang (2015) (12.6.2012 - 17.6.2012)

locations with a MBE of -5.5, -12.5 and -5.9 W m^{-2} for Singapore, Melbourne, and Phoenix, respectively (Table 2). UT&C shows improved modelling of $S\uparrow$ for the Singapore site with a MBE = -5.5 and RMSE = 9.7 W m^{-2} compared to TEB with MBE = -10.6 and RMSE = 17.0 W m^{-2} (Harshan et al., 2017). The MBE = -12.5 and RMSE = 16.3 W m^{-2} of the

Table 3. Same as Table 2 for the dry period (15.2.2014 - 16.3.2014) in Telok Kurau Singapore.

	UT&C					Literature		
	R^2 $(-)$	MBE $(\mathrm{W\ m^{-2}})$	RMSE $(\mathrm{W\ m^{-2}})$	MAE $(\mathrm{W\ m^{-2}})$	Validation period % of (h)	MBE $(\mathrm{W\ m^{-2}})$	RMSE $(\mathrm{W\ m^{-2}})$	MAE
$S\uparrow$ (Singapore) dry period	0.97	-13.1**	16.3**	13.3	99 % of 330 h	-19.8 (1)	26.1 (1)	20.3 (1)
$L\uparrow$ (Singapore) dry period	0.98	8.9**	23.8**	18.2	99 % of 720 h	16.7 (1)	37.1 (1)	27.1 (1)
R_n (Singapore) dry period	>0.99	-2.3*	17.0**	14.3	93 % of 720 h	-4.6 (1)	24.3 (1)	19.5 (1)
H (Singapore) dry period	0.95	-8.1*	30.0**	20.4	99 % of 720 h	11.9 (1)	35.7 (1)	21.0 (1)
λE (Singapore) dry period	0.67	2.5**	16.2**	10.5	97 % of 720 h	-20.2(1)	33.7 (1)	21.7 (1)

(1) Harshan et al. (2017) (15.2.2014 - 16.3.2014)

UT&C simulation in Melbourne lie within the range reported by Grimmond et al. (2011) but are worse than the median model (conserving radiation budget) with MBE = -0.5 and RMSE = 6 $\mathrm{W\ m^{-2}}$. Phoenix overall shows good results with MBE = -5.9 and RMSE = 10.7 $\mathrm{W\ m^{-2}}$.

Modelled and measured $L\uparrow$ show a high R^2 of 0.93, 0.94, and 0.98 for Singapore, Melbourne and Phoenix, respectively (Table 2). These values are within the range reported by Demuzere et al. (2017) in Singapore (R^2 = 0.92-0.96), and the range reported by Grimmond et al. (2011) in Melbourne (R^2=0.90-0.98). The UT&C simulation in Singapore shows an overestimation of $L\uparrow$ during the day and an underestimation of $L\uparrow$ during the night (Sect. 10 of TRM). These trends are consistent throughout the year and similar trends are also observed by Harshan et al. (2017). UT&C shows an improved modelling of $L\uparrow$ with a MBE = 8.3 and RMSE = 23.3 $\mathrm{W\ m^{-2}}$ compared to TEB in Singapore with MBE = 13.3 and RMSE = 33.3 $\mathrm{W\ m^{-2}}$ (Harshan et al., 2017) (Table 2). The MBE = 7.8 and RMSE = 14.8 $\mathrm{W\ m^{-2}}$ of the UT&C simulation in Melbourne are similar to the median model (MBE = 8 and RMSE = 16 $\mathrm{W\ m^{-2}}$) reported by Grimmond et al. (2011). The mean daily cycle and variability of $L\uparrow$ is well represented by the UT&C simulation in Phoenix with a small positive MBE = 4.9 $\mathrm{W\ m^{-2}}$ and RMSE = 11.5 $\mathrm{W\ m^{-2}}$ (Table 2 and Sect. 10 of TRM).

The net all-wave radiation R_n shows very good agreement in all three sites with a R^2 of >0.99, >0.99, and >0.99 for Singapore, Melbourne, and Phoenix, respectively (Table 2). These results agree with the high R^2 values of >0.98 reported in the literature for Singapore (Demuzere et al., 2017) and Melbourne (Grimmond et al., 2011). Similarly, the diurnal cycle, time series, and correlation plots show a good agreement between model prediction and measurement (Fig. 4). The MBE = -4.9 and RMSE = 20.8 $\mathrm{W\ m^{-2}}$ of the UT&C simulation in Singapore shows a slight improvement compared to the values of MBE = -6.1 and RMSE = 27.6 $\mathrm{W\ m^{-2}}$ reported by Harshan et al. (2017) (Table 2). The MBE = -0.6 and RMSE = 9.5 $\mathrm{W\ m^{-2}}$ of the UT&C simulation in Melbourne shows an improvement compared to the median of the models with MBE = -6 and RMSE = 18 $\mathrm{W\ m^{-2}}$ reported by Grimmond et al. (2011) and MBE = 3 and RMSE = 19 $\mathrm{W\ m^{-2}}$ reported by Nice et al. (2018) for VTUF-3D (Table 2). The RMSE = 12.5 $\mathrm{W\ m^{-2}}$ of the simulation in Phoenix shows a slight improvement compared to the RMSE = 20 $\mathrm{W\ m^{-2}}$ reported by Song and Wang (2015) (Table 2).

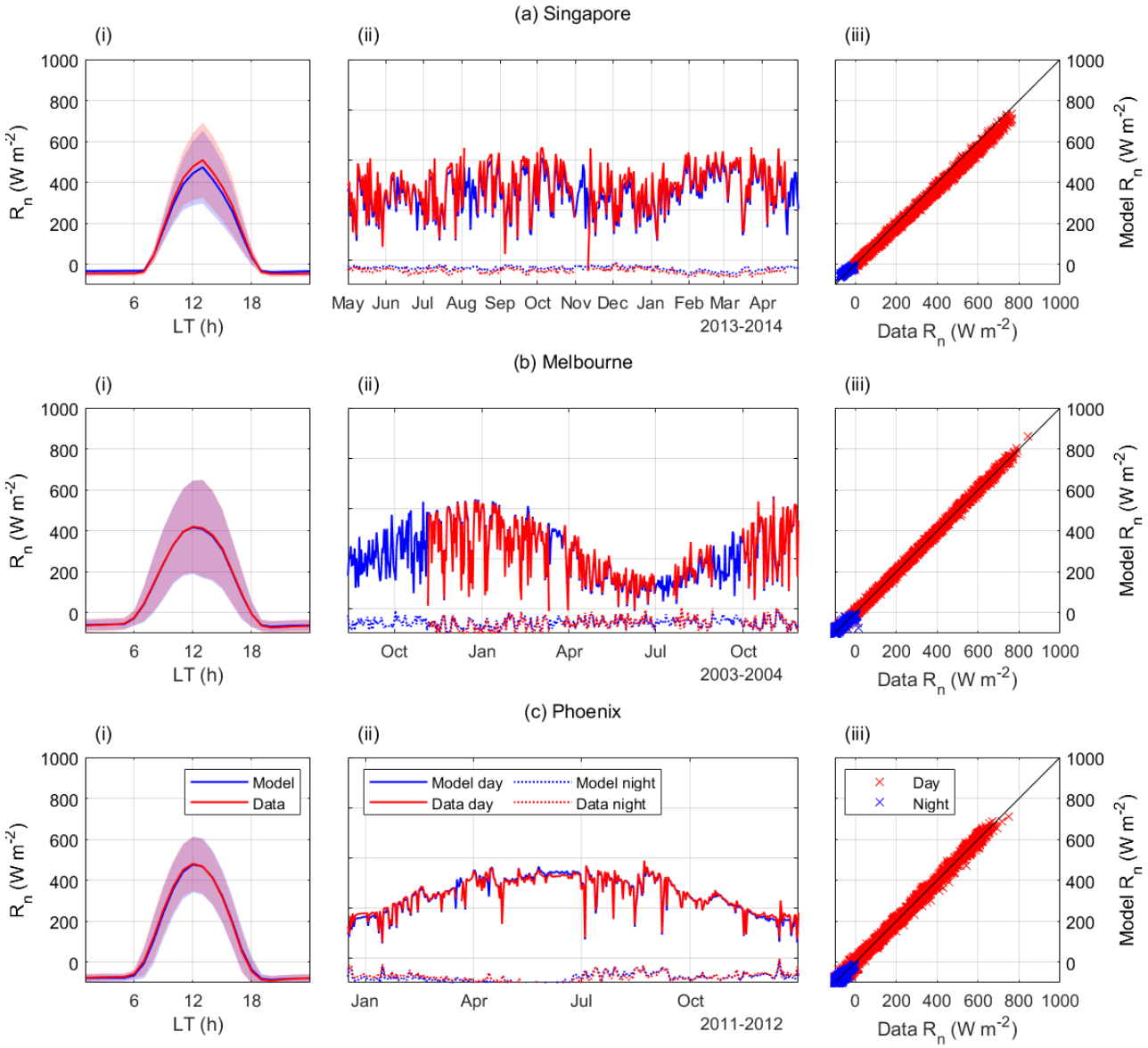

Figure 4. Comparison of modelled and measured net absorbed all-wave radiation R_n for the sites in (a) Singapore, (b) Melbourne, and (c) Phoenix. (i) ~~Ensemble~~ Average diurnal ~~variation~~ cycle (lines) +/-1 standard deviation (shaded area). (ii) Time series of mean daytime (solid lines) and nighttime (dashed lines) fluxes. (iii) Scatter plot of measurements and simulations of hourly daytime and nighttime fluxes.

4.1.2 Sensible heat flux

A relatively high R^2 between measured and simulated sensible heat flux, H, is observed with R^2=0.94, R^2=0.90, and R^2=0.92 for Singapore, Melbourne, and Phoenix, respectively (Table 2). These values lie within the range reported in the literature with R^2=0.90-0.92 for Singapore (Demuzere et al., 2017), and R^2 = 0.72-0.90 for Melbourne (Grimmond et al., 2011; Nice et al., 2018). UT&C overestimates sensible heat flux in Melbourne during daytime, while the daytime sensible heat flux in Singapore and Phoenix is well predicted (Fig. 5). The overall model performance statistics with MBE = -4.0 W m^{-2} and RMSE = 23.5 W m^{-2} for Singapore are similar to the results of MBE = 5.3 W m^{-2} and RMSE = 27.9 W m^{-2} reported by Harshan et al. (2017) (Table 2). The simulation in Melbourne shows an improvement in RMSE with a RMSE = 36.6 W m^{-2} compared to the literature values, i.e., RMSE = 47 W m^{-2} (Grimmond et al., 2011) and RMSE = 40.2 W m^{-2} (Nice et al., 2018); however, the UT&C simulation shows a larger bias with MBE = 14.4 W m^{-2} compared to MBE = 4 W m^{-2} (Grimmond et al., 2011) and MBE = - 4 W m^{-2} (Nice et al., 2018) (Table 2). Even though the mean daytime cycle is well represented, the simulation in Phoenix shows a relatively large MBE = 10.9 W m^{-2} due to a overprediction at night. The simulated RMSE = 27.4 W m^{-2} shows a slight improvement compared to the literature value of RMSE = 34 W m^{-2} (Song and Wang, 2015) (Table 2).

4.1.3 Latent heat flux

The latent heat flux λE is commonly the most difficult energy flux to predict in urban canopy modelling (Grimmond et al., 2011; Ramamurthy et al., 2014), because it is typically of lower magnitude and more variable than the other fluxes~~in cities~~, with assumptions about frequency and amount of irrigation adding further uncertainty. The R^2 values of the UT&C simulation with R^2=0.60, R^2=0.62, and R^2=0.50 for Singapore, Melbourne, and Phoenix, respectively, lie within the reported literature range of R^2=0.34-0.61 (Demuzere et al., 2017) for Singapore, and R^2=0.30-0.61 (Grimmond et al., 2011)~~and~~ , R^2=0.45 (Nice et al., 2018) for Melbourne (Table 2). The UT&C simulation is able to capture the mean daily cycle of latent heat in Singapore, Melbourne and Phoenix (Fig. 6). The variability of λE shown as standard deviation in the mean daily cycle plots is well predicted in Melbourne, whereas it is underestimated in Singapore and Phoenix (Fig. 6). During model development, it was observed that the variability of λE is heavily influenced by the maximum ponding storage capacity of impervious surfaces, which is difficult to estimate in a heterogeneous urban environment. UT&C shows an improvement of latent heat simulation in Singapore with MBE = -1.2 and RMSE = 28.1 W m^{-2} compared to the MBE = -10.8 and RMSE = 44.3 W m^{-2} reported by Harshan et al. (2017), and the MBE = -12.0 and RMSE = 38.7 W m^{-2} reported by Liu et al. (2017). Likewise, the simulation in Melbourne shows a slight improvement in RMSE with a RMSE = 26.8 W m^{-2} compared to RMSE = 40 W m^{-2} (Grimmond et al., 2011) and RMSE = 33.1 W m^{-2} (Nice et al., 2018), while the MBE = 1.9 W m^{-2} of the simulation in Melbourne shows a decrease and increase in model performance compared to the MBE = -0.8 W m^{-2} (Grimmond et al., 2011) and MBE = -9.5 W m^{-2} (Nice et al., 2018). Simulated RMSE = 19.5 W m^{-2} with UT&C and literature RMSE = 20 W m^{-2} (Song and Wang, 2015) are relatively similar for Phoenix.

Overall, UT&C shows an equal or improved ability to model the latent heat flux in comparsion to other models applied to Singapore, Melbourne, and Phoenix. Additionally, UT&C shows an improved modelling of latent heat during the dry period

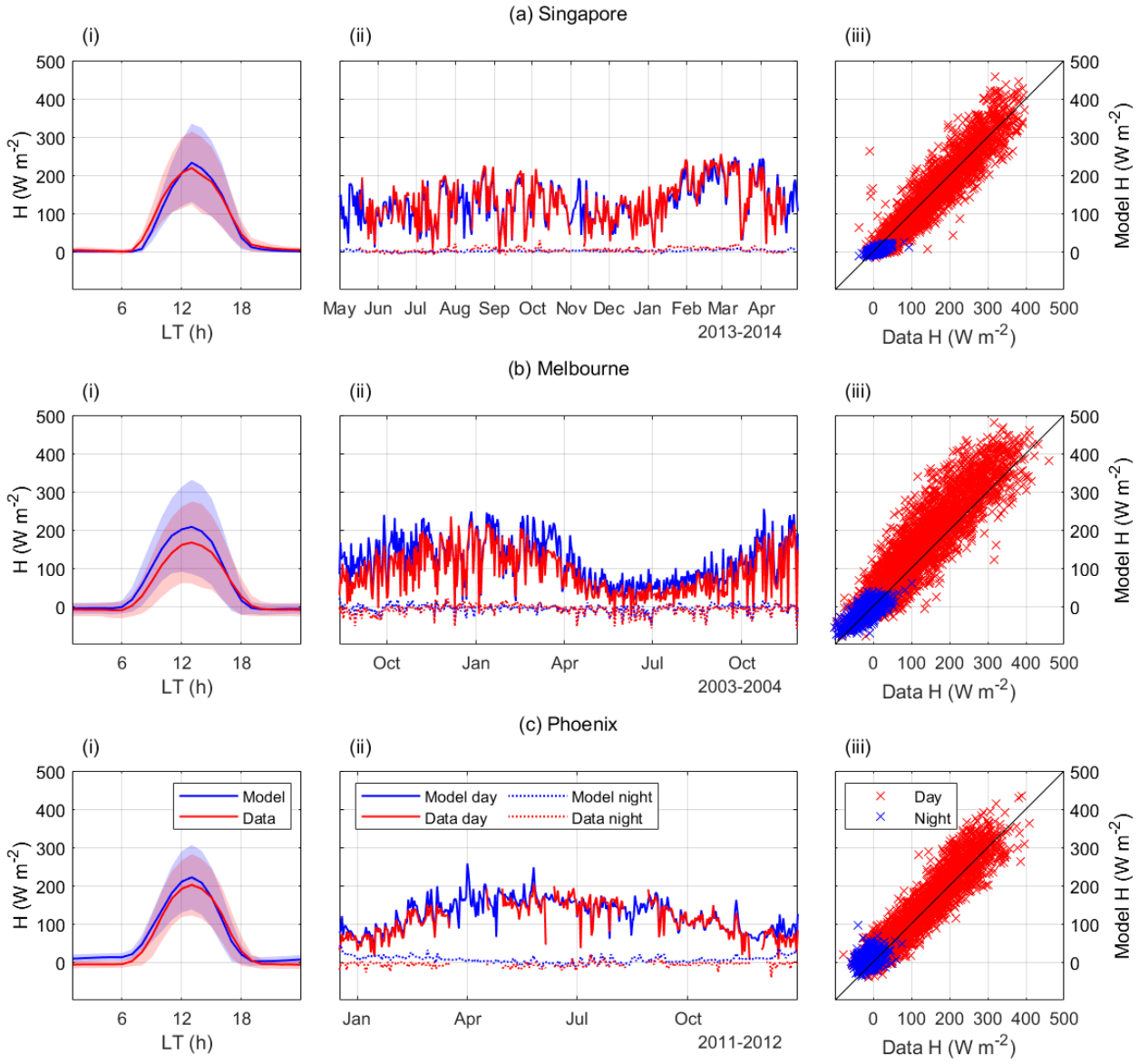

Figure 5. Comparison of modelled and measured sensible heat flux H for the sites in (a) Singapore, (b) Melbourne, and (c) Phoenix. (i) ~~Ensemble~~ Average diurnal ~~variation~~ cycle (lines) +/-1 standard deviation (shaded area). (ii) Time series of mean daytime (solid lines) and nighttime (dashed lines) fluxes. (iii) Scatter plot of measurements and simulations of hourly daytime and nighttime fluxes.

in Singapore with an R^2 value of 0.67, MBE of 2.5 W m^{-2}, RMSE of 16.2 W m^{-2} and MAE of 10.5 W m^{-2} compared to the results of Harshan et al. (2017) that show a MBE of -20.2 W m^{-2}, RMSE of 33.7 W m^{-2} and MAE of 21.7 W m^{-2}. The reason for UT&C's more accurate prediction of the latent heat flux during prolonged dry periods is its explicit representation of

soil moisture access by plant roots at different soil depths and modelling of plant response to water stress (see Sect. 4.2). The improved prediction can also be seen from mid-January to mid-March 2014 when UT&C predicts a latent heat flux comparable in magnitude to the measured latent heat flux (Fig. 6), whereas other models significantly underpredict λE during this period (Demuzere et al., 2017; Harshan et al., 2017).

4.1.4 Bare ground surface temperature (Phoenix) and 2 m air temperature (Singapore)

We compare simulated bare ground temperature at 2 cm depth with measured 2 cm soil temperature in Phoenix. Modelled and measured bare ground temperature show a high agreement with R^2 of 0.98, MBE of -0.1 °C, RMSE of 2.2 °C, and MAE of 1.7 °C. UT&C slightly underpredicts (overpredicts) ground temperature during the day (night) and shows a slight phase shift but is overall able to accurately predict bare ground temperature (Fig. 7).

UT&C overpredicts (underpredicts) 2 m air temperature in Singapore during the day (night) compared to the measurement conducted by Harshan et al. (2017). The overall mean difference (MBE) is -0.05 °C. The mean overprediction during daytime is 0.9 °C with the maximum value of 2.3 °C occuring at 1300 LT. The overall mean underprediction during nighttime is -1.2 °C with the largest negative value of -1.4 °C occuring at 0600 LT (Fig. 8). This result is not surprising and is coherent with the biases observed in Singapore for longwave radiation. Furthermore, the 2 m air temperature measured at the flux tower area, an open grass field, might not be representative of the average urban land cover based on a 500 m radius in Telok Kurau.

4.2 Ecohydrological dynamics during a dry period

UT&C is able to quantify the contribution of energy and water fluxes from different urban surfaces (impervious, bare and vegetated ground, sunlit and shaded wall, and impervious and vegetated roof) and source mechanisms (e.g. flux of water vapor from transpiration and canopy interception). The contribution of latent heat from impervious surfaces (roof and ground), bare ground, vegetated ground and trees to the overall latent heat flux for the simulation time period in Telok Kurau Singapore is analyzed and shown in Fig. 9. Latent heat from impervious surfaces is highly variable and depends on the amount of rain fallen in the previous hours. On the other hand, latent heat from vegetated ground and trees varies less and forms the baseline of the total latent heat flux. Of special interest in this study is the exceptionally dry period observed between mid-January to mid-March 2014 (Ziegler et al., 2014). During this period, rain was absent and no latent heat from impervious surfaces was observed besides a spike on 8.2.2014 related to a small rainfall event of 2.2 mm on this day. The latent heat from vegetated ground is initially high but starts to decrease as the dry period persists while the latent heat from trees remains constant and high (Fig. 9). This different behaviour of ground vegetation (grass) and trees can be explained by the water stress experienced by the different vegetation types. Plant water stress is modelled as a function of the overall soil water potential experienced by grass and tree roots (Fig. 9). In the current parametrization for Singapore, stomata closure due to plant water stress starts at a soil water potential of -0.5 MPa and -0.9 MPa for grass and trees, respectively, and stomata closure reaches 50 % at a soil water potential of -1.6 MPa and -1.7 MPa. During the dry period from mid-January to mid-March 2014, the grass experiences water stress (Fig. 9), which leads to stomata closure and a decrease in latent heat, while trees experience only moderate water stress and their transpiration continues at high ~~levels~~rates. This difference in water stress is caused by the grass and tree root

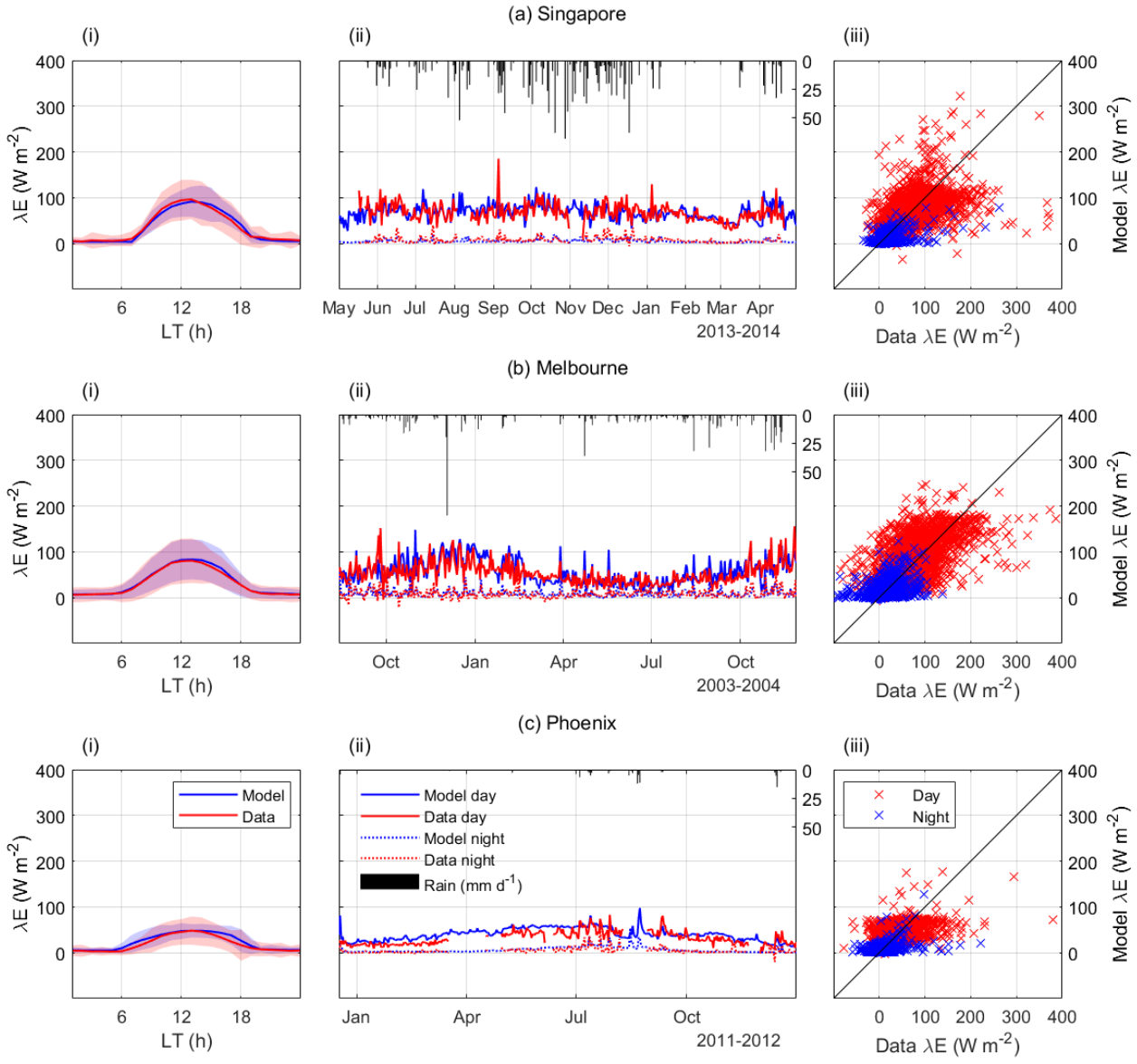

Figure 6. Comparison of modelled and measured latent heat flux λE for the sites in (a) Singapore, (b) Melbourne, and (c) Phoenix. (i) ~~Ensemble~~ Average diurnal ~~variation~~ cycle (lines) +/-1 standard deviation (shaded area). (ii) Time series of mean daytime (solid lines) and nighttime (dashed lines) fluxes. (iii) Scatter plot of measurements and simulations of hourly daytime and nighttime fluxes.

505 profiles, which allows them to access water at different soil depths. During the dry period, the upper soil layers of the vegetated soil column dry out while the deep soil layers are barely affected by the weather conditions as shown in Fig. 10. The grass has only access to the drier top soil layers (Fig. 10) as 95 % of its roots are shallower than 30 cm, while trees are able to access the

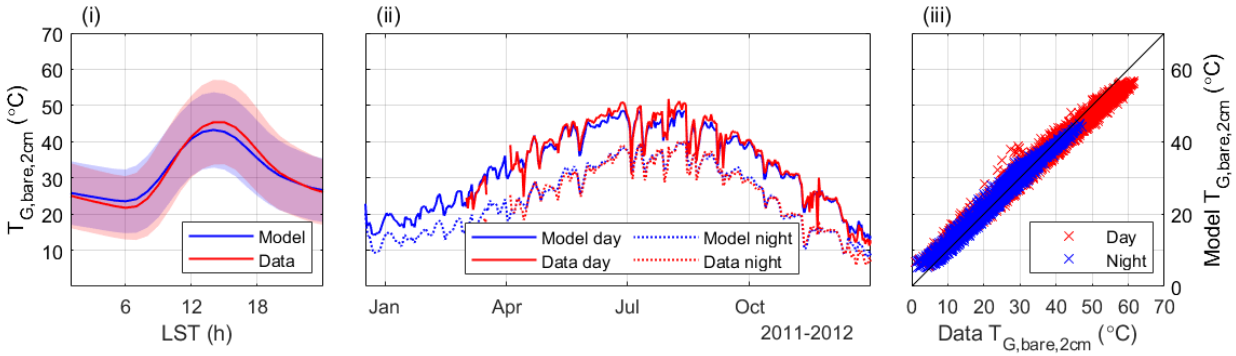

Figure 7. Comparison of modelled and measured ground temperature at 2 cm depth (T_g) for the site in Phoenix. (i) ~~Ensemble~~ Average diurnal ~~variation~~ cycle (lines) +/-1 standard deviation (shaded area). (ii) Time series of mean daytime (solid lines) and nighttime (dashed lines) ground temperature. (iii) Scatter plot of measurements and simulations of hourly daytime and nighttime temperature.

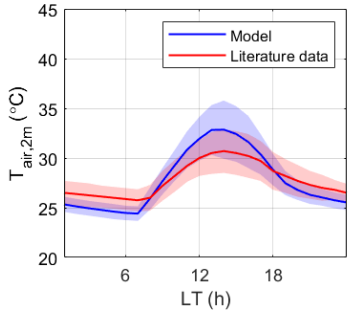

Figure 8. Comparison of modelled and measured mean ~~daily~~ diurnal cycle of 2 m air temperature ($T_{air,2m}$) in Singapore. Solid lines show hourly mean values and shaded areas +/-1 standard deviation.

wet deeper soil layers (e.g. from 70 to 175 cm depth, Fig. 10) as their roots are assumed to reach a depth of 1.5 m (Harshan et al., 2017) (ZR_{95}, Sect. 9 of TRM). This explicit representation of soil moisture in different soil layers and the vertical and horizontal root profile are important to ~~capture~~ represent the effects of climate and environment on plant performance. Furthermore, such a modelling solution improves model performance during the dry period from mid-January to mid-March 2014 in Singapore as shown in Sect. 4.1.3 and Fig. 6.

4.3 Singapore sensitivity analysis

4.3.1 Air temperature, relative humidity, evapotranspiration

The increase of vegetated ground cover ($\lambda_{G,veg}$) in Singapore from 0 to 100 % leads to an overall reduction of 2 m air temperature (T_{2m}) of 1.1 °C while relative humidity at 2 m (RH_{2m}) and canyon evapotranspiration (ET_{canyon}) are increased

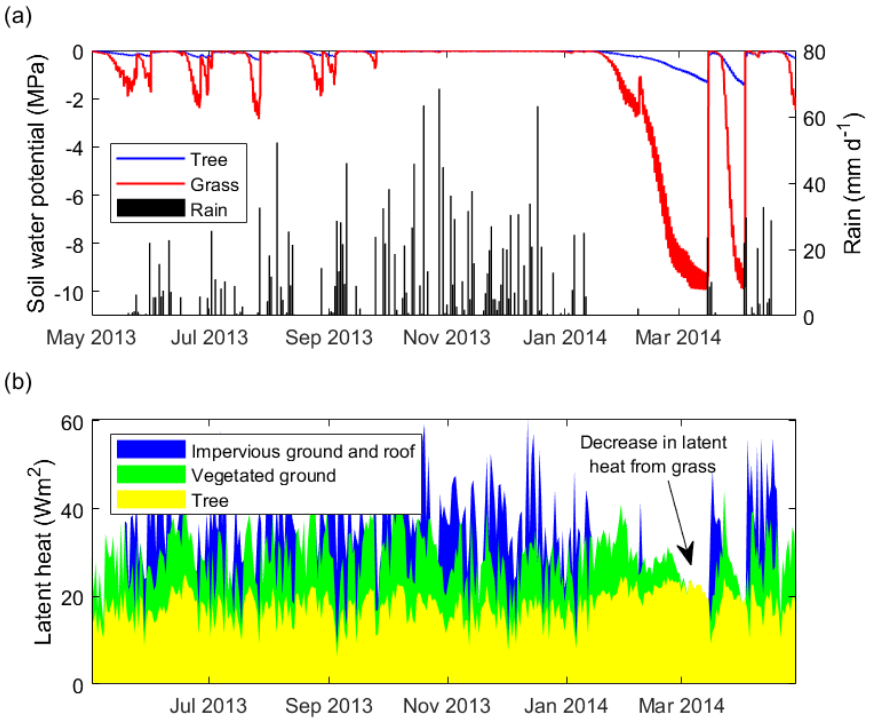

Figure 9. (a): Rain $\mathrm{mm\ d^{-1}}$ (measurement) and soil water potential averaged over the root zone (MPa) (simulation) ~~specifying~~ showing the water stress experienced by the ground vegetation (grass) and trees during the model validation in Telok Kurau Singapore. In the current parametrization, plant stomatal closure starts at a soil water potential of -0.5 MPa and -0.9 MPa for grass and trees, respectively. Stomatal closure reaches 50 % at -1.6 MPa and -1.7 MPa for grass and trees, respectively. (b) Simulated time series of latent heat from impervious surfaces, vegetated ground and trees during the model validation period in Telok Kurau Singapore. ~~Shown~~ The shown fluxes ~~are~~ correspond to the additive flux contribution from each surface to the total canyon latent heat flux.

by 6.5 % and 1.8 $\mathrm{mm\ d^{-1}}$, respectively (Fig. 11,12 and Sect. 10 of TRM). The daily cycle analysis shows a larger average decrease of T_{2m} and increase of RH_{2m} and ET_{canyon} around solar noon with maximum values of 2.2 °C (1400 LT), 12.9 % (1300 LT), and 0.33 $\mathrm{mm\ h^{-1}}$ (1300 LT), respectively (Table 4, Fig. 11,12, and Sect. 10 of TRM).

The increase of leaf area index (LAI) from 0.5 to 5 for vegetated ground and trees leads to a reduction of T_{2m} by 0.2 °C. The mean maximum decrease of T_{2m} is observed at a LAI of 2.5 while no further decrease occurs at higher values of LAI (Fig. 11). The overall increase of LAI leads to an increase of RH_{2m} and ET_{canyon} by 2.1 % and 0.7 $\mathrm{mm\ d^{-1}}$, respectively (Fig. 12 and Sect. 10 of TRM). The daily cycle analysis shows small differences in the decrease of T_{2m} and increase of RH_{2m} throughout the day with maximum values occuring during morning and evening hours of 0.3 °C (1700 LT) and 2.7 % (0800 LT), respectivley (Fig. 11 and 12). On the other hand, the maximum increase of ET_{canyon} is observed at solar noon with a magnitude of 0.07 $\mathrm{mm\ h^{-1}}$ (1300 LT) (Sect. 10 of TRM).

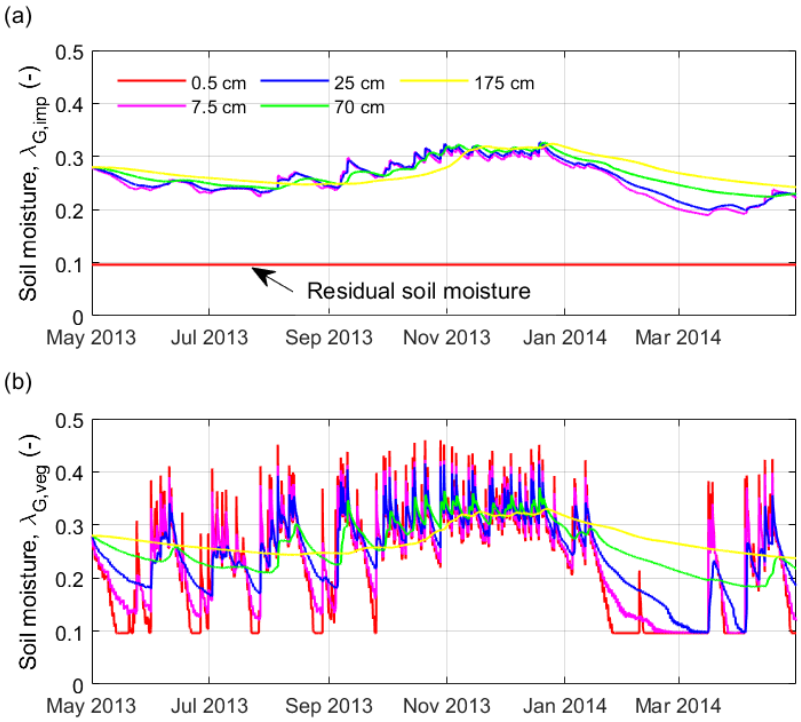

Figure 10. Simulated soil moisture in soil columns underneath impervious ground cover (a) and vegetation (b) at 0.5, 7.5, 25, 70, and 175 cm depth at Telok Kurau Singapore. Residual soil moisture is 0.096 $(-)$ and saturation soil moisture is 0.460 $(-)$. As the top soil layer of the impervious ground cover is fully sealed, it is displayed here with the residual soil moisture. The time series includes one unusually dry period from mid-January to mid-March 2014.

The sensitivity to maximum Rubisco capacity ($V_{c,max}$), as indicative of plant photosynthetic capacity, leads to an average reduction of T_{2m} by 0.3 °C ~~and~~ , an increase of RH_{2m} ~~and ET_{canyon}~~ by 1.6 % ~~and~~ , and ET_{canyon} by 0.7 $\mathrm{mm\ d^{-1}}$, respectivley (Fig. 11,12, and Sect. 10 of TRM). The daily cycle shows a larger decrease of T_{2m} and increase of RH_{2m} and ET_{canyon} around solar noon and in the late morning hours with maximum values of 0.7 °C (1300 LT), 4.2 % (1100 LT), and 0.09 $\mathrm{mm\ h^{-1}}$ (1300 LT), respectively (Table 4, Fig. 11,12, and Sect. 10 of TRM).

During the dry period (15.2.2014 - 16.3.2014), the mean decrease in T_{2m} and increase in RH_{2m} is lower than the decrease observed considering all weather conditions (Fig. 11 and 12). This is expected as no irrigation is applied and the vegetation is water stressed as described in Sect. 4.2. A stronger reduction in cooling potential is obtained when modifying LAI and $V_{c,max}$ as the cooling effect of these parameters relies on an increase in transpiration per unit of ground area, which is not possible if soil moisture is not available. At high values of $V_{c,max}$, the cooling effect even further decreases as high transpiration rates during a dry period lead to a quick depletion of soil moisture and a longer period with decreased transpiration afterwards. Increasing the vegetated ground cover ($\lambda_{G,veg}$) is only slightly less effective during the dry period than over the whole year.

This is explained by the fact that an increase in vegetated ground cover also increases the total soil moisture available for transpiration within the canyon even though soil moisture available per unit vegetated ground area does not change much.

As expected, the largest changes in T_{2m}, RH_{2m} and ET_{canyon} are observed when modifying $\lambda_{G,veg}$, while the increase of LAI and $V_{c,max}$ lead to alterations of smaller magnitudes. However, the capability of providing a mechanistically constrained quantification of these values is a non-trivial result of the UT&C application and opens the doors to test various scenarios of urban-green arrangements and types in various climates. The increase of $\lambda_{G,veg}$ and $V_{c,max}$ lead to a steady decrease of T_{2m} mostly caused by an increase in latent heat. On the other hand, the increase of LAI does not lead to a steady decrease of T_{2m}. Mechanisms such as obstruction to turbulent heat exchange with higher LAI, accounted for in the parameterization of zero plane displacement height and roughness length of the urban canopy (Sect. 3.2 of TRM), increased longwave radiation, and light limitation to photosynthesis start to counteract or limit the beneficial effects of higher LAI, such as shading and evpotranspiration. Additionally, the diurnal timing of maximal change is of interest as higher T_{2m} reduction during mid day, as for example observed with increasing $\lambda_{G,veg}$, can be especially beneficial for outdoor thermal comfort.

Table 4. Mean change over the whole simulation period and maximum change simulated ~~during~~ within the mean daily cycle in local time (LT) of 2 m air temperture (ΔT_{2m}), 2 m relative humidity (ΔRH_{2m}), and evapotranspirative fluxes (ΔET_{canyon}) at $\lambda_{G,veg}$ = 100 % compared to $\lambda_{G,veg}$ = 0 %, LAI = 5 compared to LAI = 0.5, and $V_{c,max}$ = 120 µmol CO_2 s^{-1} m^{-2} compared to $V_{c,max}$ = 20 µmol CO_2 s^{-1} m^{-2}. The hour of the day experiencing the maximum change is reported.

	Mean change			Maximum change (Mean daily cycle)		
	λ_{veg}	LAI	$V_{c,max}$	λ_{veg}	LAI	$V_{c,max}$
ΔT_{2m} [°C]	-1.1	-0.2	-0.3	-2.2 at 1400LT	-0.3 at 1700LT	-0.7 at 1300LT
ΔRH_{2m} [%]	+6.5	+2.1	+1.6	+12.9 at 1300 LT	+2.7 at 0800LT	+4.2 at 1100LT
ΔET_{canyon} [mm d^{-1}]	+1.8	+0.7	+0.7			
ΔET_{canyon} [mm h^{-1}]				+0.33 at 1300LT	+0.07 at 1300LT	+0.09 at 1300LT

4.3.2 Energy and water balance

The increase of vegetated ground cover ($\lambda_{G,veg}$) from 0 to 100 % leads to a decrease of runoff (Q) by 4.5 mm d^{-1}, while evapotranspiration (ET_{canyon}) and deep ground leakage (Lk) increase by 1.8 mm d^{-1} and 2.8 mm d^{-1}, respectively (Fig. 13, Table 5). These numbers compare with a mean daily rainfall observed during the modelling period of 5.0 mm d^{-1} (Table 1).

The increase of LAI and maximum Rubisco capacity ($V_{c,max}$) do not alter runoff significantly but slightly increase ET_{canyon} (0.7 mm d^{-1} and 0.7 mm d^{-1}) and decrease deep ground leakage (~~0.5~~ -0.5 mm d^{-1} and -0.5 mm d^{-1}) (Fig. 13, Table 5). As intuitively expected, these results indicate that plant biophysical and physiological characteristics are much less effective in modifying surface runoff production than the fraction of pervious ground. It has to be noted that these results are dependent on the soil type, in this case a sandy loam with relatively high hydraulic conductivity.

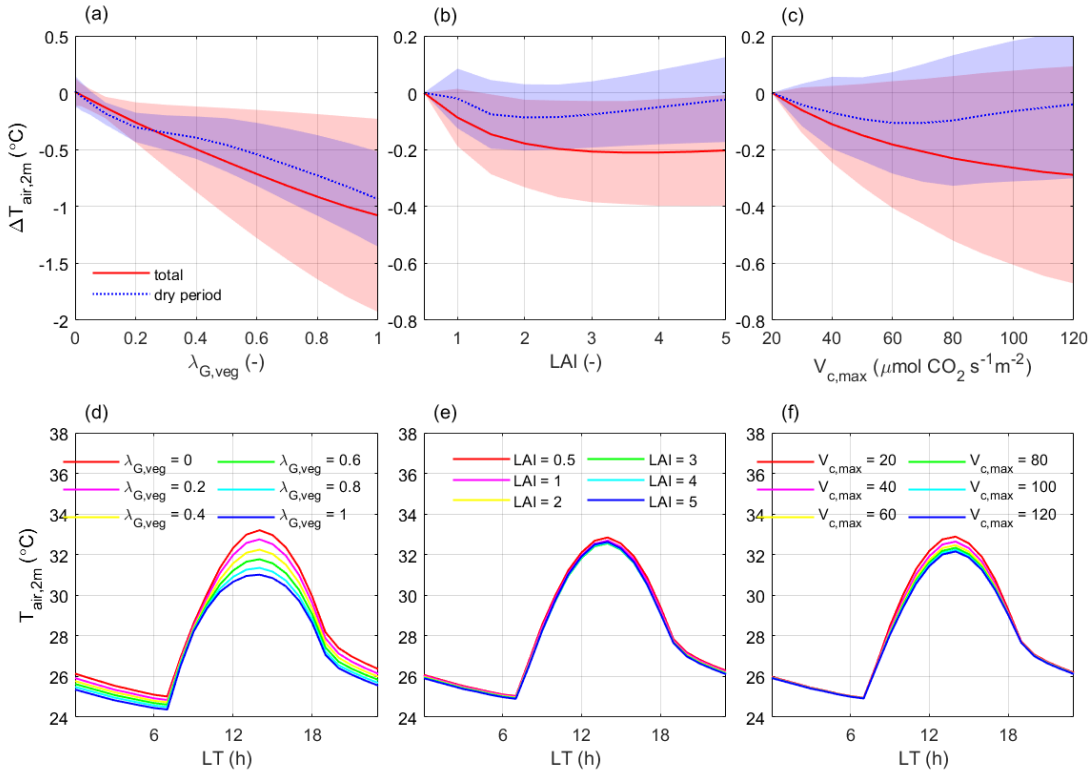

Figure 11. ~~Sensitivity analysis of~~ Change in 2 m canopy layer air temperature (T_{2m}) caused by the change in vegetated ground cover fraction ($\lambda_{G,veg}$), leaf area index (LAI), and maximum Rubisco capacity ($V_{c,max}$) in Telok Kurau Singapore. (a), (b), and (c): ~~Long term~~ Mean air temperature change considering all weather conditions (solid line) and mean air temperature change during the dry period (15.2.2014 - 16.3.2014) (dotted line) with respect to the baseline cases ~~(solid line)~~ +/-1 standard deviation (shaded area). The subplots (d), (e), and (f) ~~:~~ ~~Long~~ show long term mean daily cycle of air temperature for different values of (d) $\lambda_{G,veg}$, (e) LAI and (f) $V_{c,max}$ considering all weather conditions.

The increase of ET_{canyon} and λE caused by the increase of $\lambda_{G,veg}$, LAI and $V_{c,max}$ lead to a decrease in H, while R_n and G show very minor changes (Sect. 10 of TRM and Table 5). These results are dependent on the albedo of the vegetation for which a value of 0.27 was chosen as used by Harshan et al. (2017) (Sect. 9 of TRM), which is quite high.

5 Discussion

The model UT&C v1.0 presented in this study is among the first attempts to include in a systematic way physiological and biophysical characteristics of vegetation in the solution of the energy and water budget in the urban environment. While many

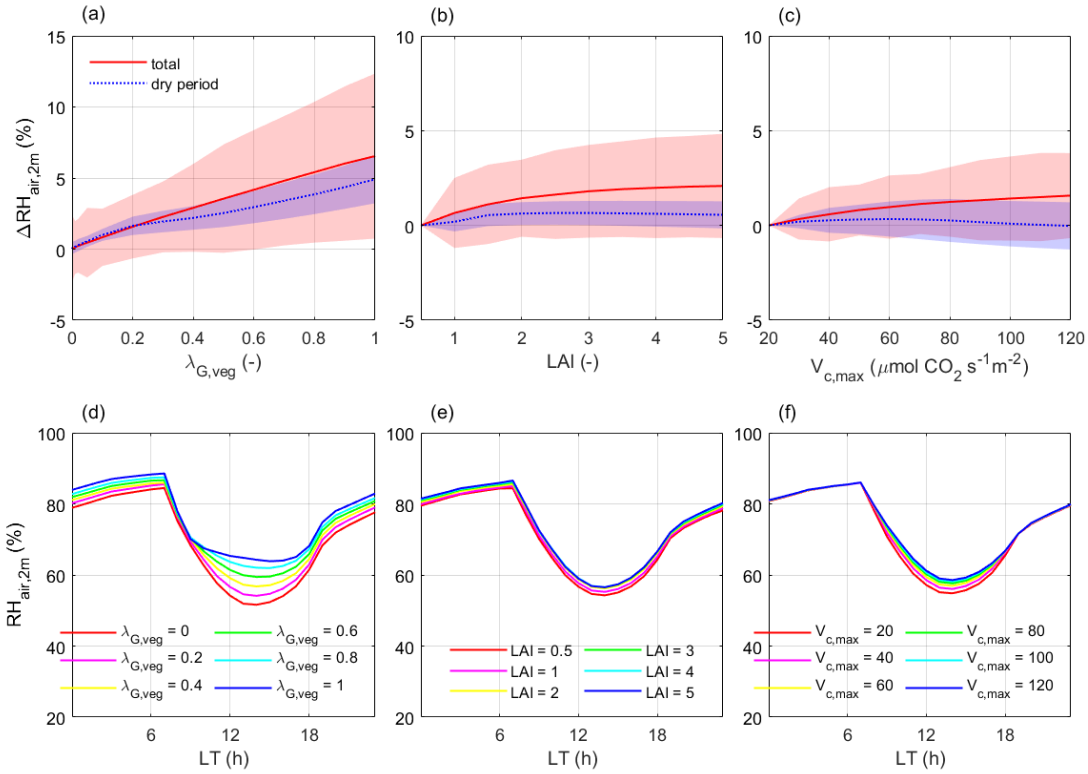

Figure 12. ~~Sensitivity analysis of~~ Change in 2 m canopy layer relative humidity (RH_{2m}) caused by the change in vegetated ground cover fraction ($\lambda_{G,veg}$), leaf area index (LAI), and maximum Rubisco capacity ($V_{c,max}$) in Telok Kurau Singapore. (a), (b), and (c): ~~Long term~~ Mean relative humidity change considering all weather conditions (solid line) and mean relative humidity change during the dry period (15.2.2014 - 16.3.2014) (dotted line) with respect to the baseline cases ~~(solid line)~~ +/-1 standard deviation (shaded area). The subplots (d), (e), and (f) ~~: Long~~ show long term mean daily cycle of ~~air temperature~~ relative humidity for different values of (d) $\lambda_{G,veg}$, (e) LAI and (f) $V_{c,max}$ considering all weather conditions.

studies have analysed the influence of vegetation on urban climate, UT&C is uniquely capable of answering the question of how different vegetation configurations and species perform in a given climate.

The inclusion of detailed plant physiological and biophysical characteristics is indeed important to quantify said effects. An example of model capability is shown through the sensitivity of simulated 2 m air temperature and 2 m relative humidity in Singapore to the vegetated ground cover fraction, LAI, and maximum Rubisco capacity. The largest decrease (increase) of air temperature (relative humidity), when compared to the case without vegetation, is observed with a fully grass covered ground that can generate a change of -2.2 °C (+12.9 %) at solar noon and an overall long-term change of mean air temperature (relative humidity) of -1.1 °C (+6.5 %). A fully vegetated ground cover might be unrealistic in a normal urban setting but is chosen in this study to demonstrate the maximum expected effect caused by this intervention and therefore, its physical limit as a heat

Table 5. Mean change over the whole simulation period of surface runoff within the canyon (ΔQ_{canyon}), ~~deep ground~~ water percolation at the bottom of the soil (ΔLk_{canyon}), change in water storage on the surface and in the soil ($\Delta(\Delta S_{canyon})$), latent heat flux ($\Delta\lambda E_{canyon}$), sensible heat flux ($\Delta H_{canyon}$), conductive heat flux into or out of buildings and ground surface (ΔG_{canyon}), net absorbed shortwave radiation ($\Delta S_{n,canyon}$), and net absorbed longwave radiaton ($\Delta L_{n,canyon}$) at $\lambda_{G,veg}$ = 100 % compared to $\lambda_{G,veg}$ = 0 %, LAI = 5 compared to LAI = 0.5, and $V_{c,max}$ = 120 µmol CO_2 s^{-1} m^{-2} compared to $V_{c,max}$ = 20 µmol CO_2 s^{-1} m^{-2}.

Mean change	λ_{veg}	LAI	$V_{c,max}$
ΔQ_{canyon} [mm d^{-1}]	-4.5	0	0
ΔET_{canyon} [mm d^{-2}]	+1.8	+0.7	+0.7
ΔLk_{canyon} [mm d^{-1}]	+2.8	-0.5	-0.5
$\Delta(\Delta S_{canyon})$ [mm d^{-1}]	-0.1	-0.2	-0.2
$\Delta\lambda E_{canyon}$ [W m^{-2}]	+52	+18	+19
ΔH_{canyon} [W m^{-2}]	-44	-15	-16
ΔG_{canyon} [W m^{-2}]	-4	-1	-1
$\Delta S_{n,canyon}$ [W m^{-2}]	-17	0	0
$\Delta L_{n,canyon}$ [W m^{-2}]	+21	+3	+2

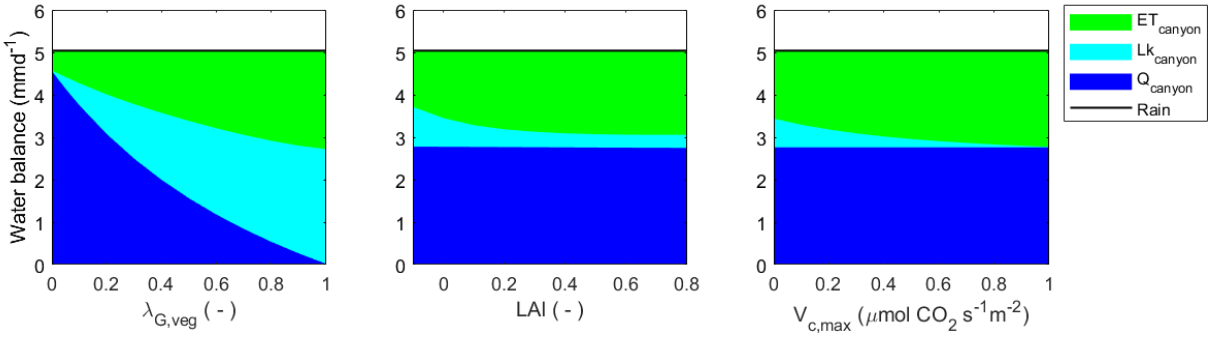

Figure 13. Water balance components in the urban canyon (ET_{canyon}: Evapotranspiration, Lk_{canyon}: Deep ground leakage, Q_{canyon}: Surface runoff) as a function of (a) vegetated ground cover fraction ($\lambda_{G,veg}$), (b) leaf area index (LAI), and (c) maximum Rubisco capacity ($V_{c,max}$) in Telok Kurau Singapore. The mean daily rainfall is 5 mm d^{-1}

575 mitigation strategy. LAI and maximum Rubisco capacity show an air temperature and relative humidity modification of much lower magnitude. It is further observed that the increase of maximum Rubisco capacity leads to a steady decrease (increase) of air temperature (relative humidity) because it does not affect plant structure. Modifying LAI triggers mechanisms, such as changes in radiation exchange, light limitations of photosynthesis within dense canopy and hindering of turbulent energy exchanges, which do not lead to a further air temperature reduction once a LAI of 2.5 is exceeded in a low rise setting in the

climate of Singapore. These results show that UT&C is sensitive and able to account for multiple effects of vegetation on the local urban climate. It has to be noted that relative humidity is dependent on the water holding capacity of air at a certain temperature and the ~~here reported~~ relative humidity increase reported here is also dependent on air temperature changes. Nevertheless, the magnitude of relative humidity is important as it influences OTC and might reduce the positive effect of decreasing air temperature.

The results ~~are~~ obtained for a low rise neighborhood of Singapore, a hot, humid, tropical city, ~~and~~ show that maximum urban greening can lead to a non-negligible decrease in air temperature at ~~screening~~ screen level (2 m) during ~~specific~~ some hours, but will unlikely be able to mitigate the UHI effect ~~significantly~~ on its own. Higher magnitudes of urban cooling due to urban vegetation are reported, for example, by Wang et al. (2018) in the contiguous ~~Unted~~ United States where tree shading reduces near surface air temperature by 3.06 °C and by Middel et al. (2015) in Phoenix where a moderate increase in tree cover can decrease average urban air temperature by 2.0 °C. This is consistent with the global analysis performed by Manoli et al. (2019) showing that the cooling potential of urban vegetation is ~~much~~ lower in the tropics. Higher air temperature decrease in drier climates is often linked to urban irrigation~~though~~ , as shown by Broadbent et al. (2018b) in ~~Melbourne~~Mawson Lakes in Adelaide, where irrigation during a heat wave can reduce average air temperture by up to 2.3 °C. In dry climates, however, the trade-off between temperature reduction potential of urban vegetation and water use through irrigation needs to be considered to fully assess the feasability of such a mitigation strategy (Yang and Wang, 2017; Wang et al., 2019).

The increase in green cover is shown to be more effective in reducing 2 m air temperature and ground surface runoff production than the change in plant types. While changes in urban ~~climate~~ air temperature and humidity caused by a change in plant physiological and biophysical characteristics are minor in the current analysis in the Singapore climate, their inclusion in urban canopy modelling is very important, as it allows quantification of the order of magnitude of predicted changes and helps ~~fraiming the right~~ to define reasonable expectations of urban planners and landscape designers using vegetation to mitigate the UHI or to improve OTC.

The explicit inclusion of ecohydrology and subsurface hydrology in urban canopy modelling leads to an improved simulation during dry down periods, as shown in Singapore. This is of particular interest as dry periods may increase in many cities in the future (Bastin et al., 2018) and allows UT&C to analyse the response of urban vegetation under different climate scenarios. Furthermore, UT&C is potentially more accurate in predicting relative humidity at pedestrian level given its more comprehensive inclusion of soil and vegetation processes. This is important to analyse the combined effects of air temperature and relative humidity alterations caused by ~~urban~~ the urban fabric and urban vegetation on the outdoor thermal comfort of city dwellers, which represent one target application of UT&C.

Future studies could focus on the application of UT&C to analyse different types of urban greening to produce guidelines for urban planners and landscape designers. Possible areas of interest are the study of the effect of urban plant types in different climates, the analysis of various urban densities, a systematic evaluation of urban irrigation practices as well as the partition of the vegetation role in shade provision versus evapotranspiration cooling in controlling OTC.

6 Model limitations

The current version of UT&C does not yet include snow hydrology and, hence, should not be used to investigate the effects of vegetation during winter in cities with snow dominated climates. Further UT&C developments can also focus on the inclusion of tree shading onto roofs, green walls, and on seasonal vegetation dynamics and vegetation phenology as in the original T&C model, rather than using a prescribed LAI as currently done.

Future model performance assessment should also focus on a more extensive use of 2 m canyon air temperature, 2 m canyon humidity, and surface temperature data as the comparison presented here with air temperature in Singapore and ground temperature in Phoenix only gives an indication of model performance as these variables are highly location specific and potentially not representative of the whole footprint areas below the flux-towers modelled here. Additionally, the validation data from low rise urban climate zones offer only a partial picture of urban conditions and further validations could focus on high-rise and dense urban settings.

A couple of notable behaviours that were observed during model development and assessment are that the prescribed interior building temperature can ~~considerably~~ influence the urban canyon air temperature, especially in narrow canyons, and, hence, realistic time series of interior building temperature are fundamental to obtain accurate results ~~.~~ (See TRM Sect. 5). Furthermore, it was observed during model development that latent heat variability and peaks are highly dependent on the maximum ponding storage capacity of the impervious surface. The maximum ponding storage capacity of impervious surfaces is difficult to estimate in the highly heterogeneous urban environment, which contains smooth surfaces but also micro-depressions due to its complex geometry and may require innovative ways of observing it to constrain model parameterizations (Wouters et al., 2015).

7 Conclusions

This study introduces the urban ecohydrological model Urban Tethys-Chloris (UT&C), and provides a technical description of its components, an assessment of model performance against three different case studies, and a sensitivity analysis to illustrate the model capabilities. UT&C is a fully coupled energy and water balance model that calculates 2 m air temperature, 2 m humidity, urban surface temperatures and all components of the energy and water balance, including surface runoff. UT&C includes a detailed representation of plant biophysical and ecophysiological characteristics. It is able to account for the effects of different plant types and urban-green typologies on the local ~~climate~~ microclimate and water fluxes. In turn, it can also provide information on how the urban environment affects plant well-being and performance.

The model was assessed against eddy covariance measurements in Singapore, Melbourne, and Phoenix, often showing better performance in terms of model validation indices compared to existing models for these three cities. UT&C shows a clear advantage in periods of water stress as it solves in detail soil hydrological dynamics and can account for different root profiles of urban vegetation and its access to soil moisture as shown for the dry-down period in Singapore.

Resolving ~~explicitely~~ explicitly subsurface hydrology, and including plant biophysical and ecophysiological characteristics allows the analysis of plant performance under water limiting conditions. Hence, UT&C is especially suited for arid and

semi-arid climates where urban irrigation is or will be applied. Furthermore, UT&C has a low computational demand and allows for analyses spanning multiple years with an hourly or sub-hourly time step, thus facilitating long-term and seasonal ~~analysis~~studies testing multiple scenarios. Hence, UT&C can assess plant performance under different existing and future climatic conditions, as for example during droughts, responses to increasing temperature, or test the effectiveness of various irrigation practices.

Code and data availability. The development of UT&C, model validation, and graphs presented in this paper were conducted in Matlab R2018b. The exact version of UT&C used to produce the results used in this paper is archived on Zenodo (Meili and Fatichi, 2019). The original source code for the ecohydrological model Tethys-Chloris was obtained from the author (Fatichi et al., 2012a, b) while the building and tree shading calculations are based on the code of Ryu et al. (2016). The tower based eddy covariance measurements used for model validation were obtained from the authors in Telok Kurau Singapore (Velasco et al., 2013; Roth et al., 2016), in Preston Melbourne (Coutts et al., 2007a, b; Nice et al., 2018), and from the Global Institute of Sustainability, Arizona State University (ASU) in Maryvale Phoenix (Chow et al., 2014; Chow, 2017).

Author contributions. NM, and SF designed the study, developed the code, conducted the analysis and wrote the manuscript with inputs from GM. MR, EV, AC, WC collected and shared their eddy-covariance measurements for the purpose of model validation. EBZ shared the code presented in Ryu et al. (2016). All authors gave commments and contributed to the final version of the manuscript.

Competing interests. The authors declare that they have no conflict of interest.

Acknowledgements. The research was conducted at the Future Cities Laboratory at the Singapore-ETH Centre, which was established collaboratively between ETH Zurich and Singapore's National Research Foundation (FI370074016) under its Campus for Research Excellence and Technological Enterprise programme. GM was supported by the "The Branco Weiss Fellowship - Society in Science" administered by ETH Zurich. EV acknowledges a research fellowship granted by the Centre for Urban Greenery and Ecology of Singapore's National Parks Board.

References

Allegrini, J. and Carmeliet, J.: Coupled CFD and building energy simulations for studying the impacts of building height topology and buoyancy on local urban microclimates, Urban Climate, 21, 278–305, https://doi.org/10.1016/j.uclim.2017.07.005, http://dx.doi.org/10.1016/j.uclim.2017.07.005, 2017.

Arora, V. K. and Boer, G. J.: A parameterization of leaf phenology for the terrestrial ecosystem component of climate models, Global Change Biology, 11, 39–59, 2005.

Bastin, J.-F., Clark, E., Elliott, T., Hart, S., van den Hoogen, J., Hordijk, I., Ma, H., Majumder, S., Manoli, G., Maschler, J., Mo, L., Routh, D., Yu, K., Zohner, C., and Crowther, T. W.: Cities of the future, visualizing climate change to inspire actions, bioRxiv, 458018, https://doi.org/http://dx.doi.org/10.1101/458018, 2018.

Berland, A., Shiflett, S. A., Shuster, W. D., Garmestani, A. S., Goddard, H. C., Herrmann, D. L., and Hopton, M. E.: The role of trees in urban stormwater management, Landscape and Urban Planning, 162, 167–177, https://doi.org/10.1016/j.landurbplan.2017.02.017, http://dx.doi.org/10.1016/j.landurbplan.2017.02.017, 2017.

Best, M. J. and Grimmond, C. S. B.: Key conclusions of the first international urban land surface model comparison project, American Meteorological Society, https://doi.org/10.1175/BAMS-D-14-00122.1, 2015.

Bonan, G. B., Lawrence, D. M., Swenson, S. C., Oleson, K. W., Jung, M., Lawrence, P. J., Levis, S., and Reichstein, M.: Improving canopy processes in the Community Land Model version 4 (CLM4) using global flux fields empirically inferred from FLUXNET data, Journal of Geophysical Research, 116, 1–22, https://doi.org/10.1029/2010jg001593, 2011.

Bowler, D. E., Buyung-Ali, L., Knight, T. M., and Pullin, A. S.: Urban greening to cool towns and cities : A systematic review of the empirical evidence, Landscape and Urban Planning, 97, 147–155, https://doi.org/10.1016/j.landurbplan.2010.05.006, http://dx.doi.org/10.1016/j.landurbplan.2010.05.006, 2010.

Broadbent, A. M., Coutts, A. M., Nice, K. A., Demuzere, M., Krayenhoff, E. S., Tapper, N. J., and Wouters, H.: The Air-temperature Response to Green/blue-infrastructure Evaluation Tool (TARGET v1.0): an efficient and user-friendly model of city cooling, Geoscientific Model Development Discussions, pp. 1–31, https://doi.org/10.5194/gmd-2018-177, 2018a.

Broadbent, A. M., Coutts, A. M., Tapper, N. J., and Demuzere, M.: The cooling effect of irrigation on urban microclimate during heatwave conditions, Urban Climate, 23, 309–329, https://doi.org/10.1016/j.uclim.2017.05.002, https://doi.org/10.1016/j.uclim.2017.05.002, 2018b.

Bruse, M. and Fleer, H.: Simulating surface-plant-air interactions inside urban environments with a three dimensional numerical model, Environmental Modelling and Software, 13, 373–384, https://doi.org/10.1016/S1364-8152(98)00042-5, 1998.

Choudhury, B. J. and Monteith, J. L.: A four-layer model for the heat budget of homogeneous land surfaces, Quarterly Journal of the Royal Meteorological Society, 114, 378–398, 1988.

Chow, W.: Eddy covariance data measured at the CAP LTER flux tower located in the west Phoenix, AZ neighborhood of Maryvale from 2011-12-16 through 2012-12-31. Environmental Data Initiative., https://doi.org/10.6073/pasta/fed17d67583eda16c439216ca40b0669, 2017.

Chow, W. T. L., Volo, T. J., Vivoni, E. R., Darrel, G., and Ruddell, B. L.: Seasonal dynamics of a suburban energy balance in Phoenix , Arizona, International Journal of Climatology, 34, 3863–3880, https://doi.org/10.1002/joc.3947, 2014.

Collatz, G. J., Ball, J. T., Grivet, C., and Berry, J. A.: Physiological and environmental regulation of stomatal conductance, photosynthesis and transpiration-A model that includes a laminar boundary-layer, Agricultural and Forest Meteorology, 54, 107–136, 1991.

Collatz, G. J., Ribas-Carbo, M., and Berry, J. A.: Coupled photosynthesis-stomatal conductance model for leaves of C4 plants, Australian Journal of Plant Physiology, 19, 519–538, 1992.

Collins, D. B. G. and Bras, R. L.: Plant rooting strategies in water-limited ecosystems, Water Resources Research, 43, doi:10.1029/2006WR005541, 2007.

Coutts, A. M., Beringer, J., and Tapper, N. J.: Characteristics influencing the variability of urban CO2 fluxes in Melbourne, Australia, Atmospheric Environment, 41, 51–62, https://doi.org/10.1016/j.atmosenv.2006.08.030, 2007a.

Coutts, A. M., Beringer, J., and Tapper, N. J.: Impact of increasing urban density on local climate: Spatial and temporal variations in the surface energy balance in Melbourne, Australia, Journal of Applied Meteorology and Climatology, 46, 477–493, https://doi.org/10.1175/JAM2462.1, 2007b.

Dai, Y., Dickinson, R. E., and Wang, Y.-P.: A two-big-leaf model for canopy temperature, photosynthesis, and stomatal conductance, Journal of Climate, 17, 2281–2299, 2004.

de Munck, C., Lemonsu, A., Masson, V., Le Bras, J., and Bonhomme, M.: Evaluating the impacts of greening scenarios on thermal comfort and energy and water consumptions for adapting Paris city to climate change, Urban Climate, 23, 260–286, https://doi.org/10.1016/j.uclim.2017.01.003, 2018.

de Vries, D. A.: Thermal Properties of Soils, in: Physics of the Plant Environment, edited by van Wijk, W., North-Holland, Amsterdam, 1963.

Deardorff, J. W.: Efficient prediction of ground surface temperature and moisture with inclusion of a layer of vegetation, Journal of Geophysical Research, 83, 1889–1903, 1978.

Demuzere, M., Harshan, S., Jaervi, L., Roth, M., Grimmond, C. S. B., Masson, V., Oleson, K. W., Velasco, E., and Wouters, H.: Impact of urban canopy models and external parameters on the modelled urban energy balance in a tropical city, Quarterly, https://doi.org/10.1002/qj.3028, 2017.

Dickinson, R. E., Henderson-Sellers, A., and Kennedy, P. J.: Biosphere-atmosphere transfer scheme (BATS) version 1E as coupled to the NCAR Community Climate Model, Tech. Rep. NCAR/TN-387+STR, Natl. Cent. for Atmos. Res., Boulder, Colorado, 1993.

Farouki, O. T.: The thermal properties of soils in cold regions, Cold Regions Science and Technology, 5, 67–75, 1981.

Farquhar, G. D., Caemmerer, S. V., and Berry, J. A.: A biochemical model of photosynthetic CO_2 assimilation in leaves of C3 species, Planta, 149, 78–90, 1980.

Fatichi, S. and Pappas, C.: Constrained variability of modeled T:ET ratio across biomes, Geophysical Research Letters, 44, 6795–6803, https://doi.org/10.1002/2017GL074041, 2017.

Fatichi, S., Ivanov, V. Y., and Caporali, E.: Simulation of future climate scenarios with a weather generator, Advances in Water Resources, 34, 448–467, https://doi.org/10.1016/j.advwatres.2010.12.013, http://dx.doi.org/10.1016/j.advwatres.2010.12.013, 2011.

Fatichi, S., Ivanov, V. Y., and Caporali, E.: A mechanistic ecohydrological model to investigate complex interactions in cold and warm water-controlled environments : 1 . Theoretical framework and plot-scale analysis, Journal of Advances in Modeling Earth Systems, 4, 1–31, https://doi.org/10.1029/2011MS000086, 2012a.

Fatichi, S., Ivanov, V. Y., and Caporali, E.: A mechanistic ecohydrological model to investigate complex interactions in cold and warm water-controlled environments : 2 . Spatiotemporal analyses, Journal of Advances in Modeling Earth Systems, 4, 1–22, https://doi.org/10.1029/2011MS000087, 2012b.

Frank, A., Heidemann, W., and Spindler, K.: Modeling of the surface-to-surface radiation exchange using a Monte Carlo method, in: Journal of Physics: Conference Series, vol. 745, https://doi.org/10.1088/1742-6596/745/3/032143, 2016.

Gillner, S., Vogt, J., Tharang, A., Dettmann, S., and Roloff, A.: Role of street trees in mitigating effects of heat and drought at highly sealed urban sites, Landscape and Urban Planning, 143, 33–42, https://doi.org/10.1016/j.landurbplan.2015.06.005, http://dx.doi.org/10.1016/j.landurbplan.2015.06.005, 2015.

Golasi, I., Salata, F., de Lieto Vollaro, E., and Coppi, M.: Complying with the demand of standardization in outdoor thermal comfort: a first approach to the Global Outdoor Comfort Index (GOCI), Building and Environment, 130, 104–119, https://doi.org/10.1016/j.buildenv.2017.12.021, https://doi.org/10.1016/j.buildenv.2017.12.021, 2018.

Grimm, N. B., Faeth, S. H., Golubiewski, N. E., Redman, C. L., Wu, J., Bai, X., and Briggs, J. M.: Global Change and the Ecology of Cities, Science, 39, 2008.

Grimmond, C. S. B., Blackett, M., Best, M. J., Baik, J., Belcher, S. E., Beringer, J., Bohnenstengel, S. I., Calmet, I., Chen, F., Coutts, A., Dandou, A., Fortuniak, K., Gouvea, M. L., Hamdi, R., Hendry, M., Kanda, M., Kawai, T., Kawamoto, Y., Kondo, H., Krayenhoff, E. S., Lee, S., Loridan, T., Martilli, A., Masson, V., Miao, S., Oleson, K., Ooka, R., Pigeon, G., Porson, A., Ryu, Y., Salamanca, F., Steeneveld, G. J., and Tombrou, M.: Initial results from Phase 2 of the international urban energy balance model comparison, International Journal of Climatology, 272, 244–272, https://doi.org/10.1002/joc.2227, 2011.

Hadley, S. W., Erickson III, D. J., Hernandez, J. L., Broniak, C. T., and Blasing, T. J.: Responses of energy use to climate change: A climate modeling study, Geophysical Research Letters, 33, 2–5, https://doi.org/10.1029/2006GL026652, 2006.

Haghighi, E., Shahraeeni, E., Lehmann, P., and Or, D.: Evaporation rates across a convective air boundary layer are dominated by diffusion, Water Resour. Res., 49, 1602–1610, doi:10.1002/wrcr.20166, 2013.

Harman, I., Best, M. J., and Belcher, S. E.: Radiative exchange in an urban street canyon, Boundary-Layer Meteorology, 110, 301–316, 2003.

Harshan, S., Roth, M., Velasco, E., and Demuzere, M.: Evaluation of an urban land surface scheme over a tropical suburban neighborhood, Theoretical and Applied Climatology, pp. 1–20, https://doi.org/10.1007/s00704-017-2221-7, 2017.

Hillel, D.: Environmental Soil Physics: Fundamentals, Applications, and Environmental Considerations, Academic Press, London, UK, 1998.

Holst, C. C., Tam, C.-y., and Chan, J. C. L.: Sensitivity of urban rainfall to anthropogenic heat flux: A numerical experiment, Geophysical Research Letters, 43, 2240–2248, https://doi.org/10.1002/2015GL067628.Received, 2016.

Höppe, P.: The physiological equivalent temperature - a universal index for the biometeorological assessment of the thermal environment, International Journal of Biometeorology, 43, 71–75, https://doi.org/10.1007/s004840050118, http://link.springer.com/10.1007/s004840050118, 1999.

Hu, Z. and Islam, S.: Prediction of ground surface temperature and soil moisture content by the force restore-method, Water Resources Research, 31, 2531–2539, 1995.

Huang, C.-W., Domec, J.-C., Ward, E. J., Duman, T., Manoli, G., Parolari, A. J., and Katul, G. G.: The effect of plant water storage on water fluxes within the coupled soil-plant system, New Phytologist, 213, 1093–1106, https://doi.org/10.1111/nph.14273, http://doi.wiley.com/10.1111/nph.14273, 2017.

Iio, A., Hikosaka, K., Anten, N. P., Nakagawa, Y., and Ito, A.: Global dependence of field-observed leaf area index in woody species on climate: A systematic review, Global Ecology and Biogeography, 23, 274–285, https://doi.org/10.1111/geb.12133, 2014.

IPCC: Climate Change 2014, Synthesis Report, Summary for Policymakers, 2014.

Ivanov, V. Y., Bras, R. L., and Vivoni, E. R.: Vegetation-hydrology dynamics in complex terrain of semiarid areas: 1. A mechanistic approach to modeling dynamic feedbacks, Water Resources Research, 44, doi:10.1029/2006WR005588, 2008a.

Ivanov, V. Y., Bras, R. L., and Vivoni, E. R.: Vegetation-hydrology dynamics in complex terrain of semiarid areas: 1. A mechanistic approach to modeling dynamic feedbacks, Water Resources Research, 44, doi:10.1029/2006WR005588, 2008b.

Jochner, S., Alves-Eigenheer, M., Menzel, A., and Morellato, L. P. C.: Using phenology to assess urban heat islands in tropical and temperate regions, International Journal of Climatology, 33, 3141–3151, https://doi.org/10.1002/joc.3651, 2013.

Kattge, J., Knorr, W., Raddatz, T., and Wirth, C.: Quantifying photosynthetic capacity and its relationship to leaf nitrogen content for global-scale terrestrial biosphere models, Global Change Biology, 15, 976–991, https://doi.org/10.1111/j.1365-2486.2008.01744.x, 2009.

Kent, C. W., Grimmond, S., and Gatey, D.: Aerodynamic roughness parameters in cities: Inclusion of vegetation, Journal of Wind Engineering and Industrial Aerodynamics, 169, 168–176, https://doi.org/10.1016/j.jweia.2017.07.016, http://dx.doi.org/10.1016/j.jweia.2017.07.016, 2017.

Konarska, J., Holmer, B., Lindberg, F., and Thorsson, S.: Influence of vegetation and building geometry on the spatial variations of air temperature and cooling rates in a high-latitude city, International Journal of Climatology, 36, 2379–2395, https://doi.org/10.1002/joc.4502, 2016.

Krayenhoff, E. S., Christen, A., Martilli, A., and Oke, T. R.: A Multi-layer Radiation Model for Urban Neighbourhoods with Trees, Boundary-Layer Meteorology, 151, 139–178, https://doi.org/10.1007/s10546-013-9883-1, 2014.

Krayenhoff, E. S., Santiago, J.-L., Martilli, A., Christen, A., and Oke, T.: Parametrization of Drag and Turbulence for Urban Neighbourhoods with Trees, Boundary-Layer Meteorology, 156, 157–189, https://doi.org/10.1007/s10546-015-0028-6, 2015.

Kusaka, H., Kondo, H., and Kikegawa, Y.: A simple single-layer urban canopy model for amtospheric models: Comparison with multi-layer and slab models, Boundary-Layer Meteorology, 101, 329–358, 2001.

Lawrence, D. M., Levis, S., Zeng, X., Flanner, M. G., Bonan, G. B., Oleson, K. W., Swenson, S. C., Lawrence, D. M., Sakaguchi, K., Slater, A. G., Yang, Z.-L., Lawrence, P. J., and Thornton, P. E.: Parameterization improvements and functional and structural advances in Version 4 of the Community Land Model, Journal of Advances in Modeling Earth Systems, 3, https://doi.org/10.1029/2011ms000045, 2011.

Lee, H. S., Matthews, C. J., Braddock, R. D., Sander, G. C., and Gandola, F.: A MATLAB method of lines template for transport equations, Environmental Modelling & Software, 19, 603–614, doi:10.1016/j.envsoft.2003.08.017, 2004.

Lemonsu, A., Masson, V., Shashua-bar, L., Erell, E., and Pearlmutter, D.: Inclusion of vegetation in the Town Energy Balance model for modelling urban green areas, Gescientific Model Development, 5, 1377–1393, https://doi.org/10.5194/gmd-5-1377-2012, 2012.

Leuning, R.: A critical appraisal of a combined stomatal- photosynthesis model for C3 plants, Plant, Cell and Environment, 18, 357–364, 1995.

Leuning, R., Kelliher, F. M., Pury, D. G. G., and Schulze, E.-D.: Leaf nitrogen, photosynthesis, conductance and transpiration: Scaling from leaves to canopies, Plant, Cell and Environment, pp. 1183–1200, 1995.

Li, D. and Bou-Zeid, E.: Synergistic Interactions between Urban Heat Islands and Heat Waves : The Impact in Cities Is Larger than the Sum of Its Parts *, Journal of Applied Meteorology and Climatology, 52, 2051–2064, https://doi.org/10.1175/JAMC-D-13-02.1, 2013.

Li, D., Bou-Zeid, E., and Oppenheimer, M.: The effectiveness of cool and green roofs as urban heat island mitigation strategies, Environmental Research Letters, 9, https://doi.org/10.1088/1748-9326/9/5/055002, 2014.

Lim, H. S. and Lu, X. X.: Sustainable urban stormwater management in the tropics : An evaluation of Singapore's ABC Waters Program, Journal of Hydrology, 538, 842–862, https://doi.org/10.1016/j.jhydrol.2016.04.063, 2016.

Lindberg, F., Holmer, B., and Thorsson, S.: SOLWEIG 1.0 - Modelling spatial variations of 3D radiant fluxes and mean radiant temperature in complex urban settings, International Journal of Biometeorology, 52, 697–713, https://doi.org/10.1007/s00484-008-0162-7, 2008.

Liu, X., Li, X.-x., Harshan, S., Roth, M., and Velasco, E.: Evaluation of an urban canopy model in a tropical city : the role of tree evapotranspiration Evaluation of an urban canopy model in a tropical city : the role of tree evapotranspiration, Environmental Research Letters, 12, 2017.

Macdonald, R. W., Griffiths, R. F., and Hall, D. J.: An improved method for the estimation of surface roughness of obstacle arrays, Atmospheric Environment, 32, 1857–1864, 1998.

Mahat, V., Tarboton, D. G., and Molotch, N. P.: Testing above- and below-canopy representations of turbulent fluxes in an energy balance snowmelt model, Water Resources Research, 49, 1107–1122, https://doi.org/10.1002/wrcr.20073, 2013.

Mahfouf, J.-F. and Jacquemin, B.: A study of rainfall interception using a land surface parameterization for mesoscale meteorological models, Journal of Applied Meteorology, 28, 1282–1302, 1989.

Manickathan, L., Defraeye, T., Allegrini, J., Derome, D., and Carmeliet, J.: Parametric study of the influence of environmental factors and tree properties on the transpirative cooling effect of trees, Agricultural and Forest Meteorology, 248, 259–274, https://doi.org/10.1016/j.agrformet.2017.10.014, http://dx.doi.org/10.1016/j.agrformet.2017.10.014, 2018.

Manoli, G., Ivanov, V. Y., and Fatichi, S.: Dry-Season Greening and Water Stress in Amazonia: The Role of Modeling Leaf Phenology, Journal of Geophysical Research: Biogeosciences, 123, 1909–1926, https://doi.org/10.1029/2017JG004282, 2018.

Manoli, G., Fatichi, S., Schläpfer, M., Yu, K., Crowther, T. W., Meili, N., Burlando, P., Katul, G. G., and Bou-Zeid, E.: Magnitude of urban heat islands largely explained by climate and population, Nature, 573, 55–60, https://doi.org/10.1038/s41586-019-1512-9, http://dx.doi.org/10.1038/s41586-019-1512-9, 2019.

Mascart, P., Noilhan, J., and Giordani, H.: A Modified Parameterization of Flux-Profile Relationships in the Surface Layer Using Different Roughness Length Values for Heat and Momentum, Boundary-Layer Meteorology, 72, 331–344, 1995.

Masson, V.: A physically-based scheme for the urban energy budget in atmospheric models, Boundary-Layer Meteorology, 94, 357–397, 2000.

Masson, V., Marguinaud, P., Decharme, B., Salgado, R., Gibelin, A.-L., Kerdraon, G., Lebeaupin Brossier, C., Boone, A., Carrer, D., Giordani, H., Brousseau, P., Alias, A., Barbu, A., Essaouini, K., Lemonsu, A., Voldoire, A., Jidane, M., Lafont, S., Martin, E., Mahfouf, J.-F., Vionnet, V., Kourzeneva, E., Donier, S., Vincendon, B., Mokhtari, M., Lafaysse, M., Masson, V., Habets, F., Le Moigne, P., Pigeon, G., Seity, Y., Morin, S., Bouyssel, F., Delire, C., Belamari, S., Tulet, P., Taillefer, F., Brun, E., Alkama, R., Tanguy, G., Calvet, J.-C., and Faroux, S.: The SURFEXv7.2 land and ocean surface platform for coupled or offline simulation of earth surface variables and fluxes, Geoscientific Model Development, 6, 929–960, https://doi.org/10.5194/gmd-6-929-2013, 2013.

Matzarakis, A., Rutz, F., and Mayer, H.: Modelling radiation fluxes in simple and complex environments - application of the RayMan model, International Journal of Biometeorology, 51, 323–334, https://doi.org/10.1007/s00484-009-0261-0, 2007.

Matzarakis, A., Rutz, F., and Mayer, H.: Modelling radiation fluxes in simple and complex environments: basics of the RayMan model, International Journal of Biometeorology, 54, 131–139, https://doi.org/10.1007/s00484-009-0261-0, 2010.

Meili, N. and Fatichi, S.: Urban Tethys-Chloris (UT&C v1.0) with the possibility of sub-houly timesteps, https://doi.org/10.5281/zenodo.3548147, 2019.

Middel, A., Chhetri, N., and Quay, R.: Urban forestry and cool roofs: Assessment of heat mitigation strategies in Phoenix residential neighborhoods, Urban Forestry and Urban Greening, 14, 178–186, https://doi.org/10.1016/j.ufug.2014.09.010, http://dx.doi.org/10.1016/j.ufug.2014.09.010, 2015.

Mirfenderesgi, G., Bohrer, G., Matheny, A., Fatichi, S., Frasson, R. P. D. M., and Schafer, K. V. R.: Tree-level hydrodynamic approach for modeling aboveground water storage and stomatal conductance illuminates the effects of tree hydraulic strategy, Journal of Geophysical Research-Biogeosciences, pp. 1792–1813, https://doi.org/10.1002/2016JG003467, 2016.

Mitchell, D., Heaviside, C., Vardoulakis, S., Huntingford, C., Masato, G., P Guillod, B., Frumhoff, P., Bowery, A., Wallom, D., and Allen, M.: Attributing human mortality during extreme heat waves to anthropogenic climate change, Environmental Research

Letters, 11, 074 006, https://doi.org/10.1088/1748-9326/11/7/074006, http://stacks.iop.org/1748-9326/11/i=7/a=074006?key=crossref.6e5075a68a4ec09357b8e361a9871511, 2016.

Monteith, J. L.: Principles of Environmental Physics, Edward Arnold, London, 1973.

Mora, C., Dousset, B., Caldwell, I. R., Powell, F. E., Geronimo, R. C., Bielecki, C. R., Counsell, C. W. W., Dietrich, B. S., Johnston, E. T., Louis, L. V., Lucas, M. P., Mckenzie, M. M., Shea, A. G., Tseng, H., Giambelluca, T. W., Leon, L. R., Hawkins, E., and Trauernicht, C.: Global risk of deadly heat, Nature Climate Change, https://doi.org/10.1038/NCLIMATE3322, 2017.

Ng, K. S. T., Sia, A., Ng, M. K., Tan, C. T., Chan, H. Y., Tan, C. H., Rawtaer, I., Feng, L., Mahendran, R., Larbi, A., Kua, E. H., and Ho, R. C.: Effects of horticultural therapy on asian older adults: A randomized controlled trial, International Journal of Environmental Research and Public Health, 15, 1–14, https://doi.org/10.3390/ijerph15081705, 2018.

Nice, K. A., Coutts, A. M., and Tapper, N. J.: Development of the VTUF-3D v1.0 urban micro-climate model to support assessment of urban vegetation influences on human thermal comfort, Urban Climate, pp. 1–25, https://doi.org/10.1016/j.uclim.2017.12.008, http://linkinghub.elsevier.com/retrieve/pii/S2212095517301141, 2018.

Noilhan, J. and Planton, S.: A simple parameterization of land surface processes for meteorological models, Monthly Weather Review, 117, 536–549, 1989.

Nowak, D. J. and Crane, D. E.: Carbon storage and sequestration by urban trees in the USA, Environmental Pollution, 116, 381–389, 2002.

Núnez, C. M., Varas, E. A., and Meza, F. J.: Modelling soil heat flux, Theoretical Applied Climatology, 100, 251–260, doi:10.1007/s00704-009-0185-y, 2010.

Oleson, K. W., Dai, Y., Bonan, G., Bosilovich, M., Dickinson, R., Dirmeyer, P., Hoffman, F., Houser, P., Levis, S., Niu, G. Y., Thornton, P., Vertenstein, M., Yang, Z. L., and Zeng, X.: Technical Description of the Community Land Model (CLM), Tech. Rep. NCAR/TN-461+STR, Natl. Cent. for Atmos. Res., Boulder, Colorado, 2004.

Oleson, K. W., Bonan, G. B., Feddema, J., Vertenstein, M., and Grimmond, C. S. B.: An Urban Parameterization for a Global Climate Model . Part I : Formulation and Evaluation for Two Cities, Journal of Applied Meteorology and Climatology, 47, 1038–1060, https://doi.org/10.1175/2007JAMC1597.1, 2007.

Oleson, K. W., Bonan, G. B., Feddema, J., and Vertenstein, M.: An Urban Parameterization for a Global Climate Model. Part II: Sensitivity to Input Parameters and the Simulated Urban Heat Island in Offline Simulations, Journal of Applied Meteorology and Climatology, pp. 1061–1076, https://doi.org/10.1175/2007JAMC1598.1, 2008.

Oleson, K. W., Bonan, G. B., Feddema, J. J., and Kluzek, E.: Technical Description of an Urban Parameterization for the Community Land Model (CLMU), NCAR Tech Note, 2010.

Oleson, K. W., Lawrence, D. M., Bonan, G. B., Drewniak, B., Huang, M., Kowen, C. D., Levis, S., Li, F., Riley, W. J., Subin, Z. M., Swenson, S. C., and Thornton, P. E.: Technical Description of version 4.5 of the Community Land Model (CLM), Tech. Rep. NCAR/TN-503+STR, Natl. Cent. for Atmos. Res., Boulder, Colorado, 2013.

Park, S.-U. and Lee, S.-H.: A Vegetated Urban Canopy Model for Meteorological and Environmental Modelling, Boundary-Layer Meteorology, 126, 73–102, https://doi.org/10.1007/s10546-007-9221-6, 2008.

Paschalis, A., Fatichi, S., Pappas, C., and Or, D.: Covariation of vegetation and climate constrains present and future T/ET variability, Environ. Res. Lett, 13, 104 012, https://doi.org/10.1088/1748-9326/aae267, https://doi.org/10.1088/1748-9326/aae267{%}0Ahttp://iopscience.iop.org/article/10.1088/1748-9326/aae267/pdf, 2018.

Pataki, D. E., Carreiro, M. M., Cherrier, J., Grulke, N. E., Jennings, V., Pincetl, S., Pouyat, R. V., Whitlow, T. H., and Zipperer, W. C.: Coupling biogeochemical cycles in urban environments: Ecosystem services, green solutions, and misconceptions, Frontiers in Ecology and the Environment, 9, 27–36, https://doi.org/10.1890/090220, 2011.

Ramamurthy, P. and Bou-Zeid, E.: Contribution of impervious surfaces to urban evaporation, Water Resources Research, 50, 2889–2902, https://doi.org/10.1111/j.1752-1688.1969.tb04897.x, 2014.

Ramamurthy, P., Bou-Zeid, E., Smith, J. A., Wang, Z., Baeck, M. L., Saliendra, N. Z., Hom, J. L., and Welty, C.: Influence of subfacet heterogeneity and material properties on the urban surface energy budget, Journal of Applied Meteorology and Climatology, 53, 2114–2129, https://doi.org/10.1175/JAMC-D-13-0286.1, 2014.

Redon, E. C., Lemonsu, A., Masson, V., Morille, B., and Musy, M.: Implementation of street trees within the solar radiative exchange parameterization of TEB in SURFEX v8.0, Geoscientific Model Development, 10, 385–411, https://doi.org/10.5194/gmd-10-385-2017, 2017.

Richards, L. A.: Capillary conduction of liquids through porous mediums, Physics, 1, 318–333, 1931.

Roth, M.: Review of urban climate research in (sub)tropical regions, International Journal of Climat, 27, 1859–1873, https://doi.org/10.1002/joc, 2007.

Roth, M., Jansson, C., and Velasco, E.: Multi-year energy balance and carbon dioxide fluxes over a residential neighbourhood in a tropical city, International Journal of Climatology, https://doi.org/10.1002/joc.4873, 2016.

Rowley, F. B. and Eckley, W. A.: Surface coefficients as affected by wind direction, ASHREA Trans., 39, 33–46, 1932.

Rowley, F. B., Algren, A. B., and Blackshaw, J.: Surface conductance as affected by air velocity, temperature and character of surface, ASHREA Trans., 36, 429–446, 1930.

Rutter, A. J., Kershaw, K. A., Robins, P. C., and Morton, A. J.: A predictive model of rainfall interception in forests. 1. Derivation of the model from observation in a plantation of Corsican pine, Agricultural Meteorology, 9, 367–384, 1971.

Rutter, A. J., Morton, A. J., and Robins, P. C.: A predictive model of rainfall interception in forests. 2. Generalization of model and comparison with observations in some coniferous and hardwood stands, The Journal of Applied Ecology, 12, 367–380, 1975.

Ryu, Y.-H., Bou-Zeid, E., Wang, Z.-H., and Smith, J. A.: Realistic Representation of Trees in an Urban Canopy Model, Boundary-Layer Meteorology, 159, 193–220, https://doi.org/10.1007/s10546-015-0120-y, 2016.

Sailor, D. J. and Lu, L.: A top-down methodology for developing diurnal and seasonal anthropogenic heating profiles for urban areas, Atmospheric Environment, 38, 2737–2748, https://doi.org/10.1016/j.atmosenv.2004.01.034, 2004.

Sailor, D. J., Georgescu, M., Milne, J. M., and Hart, M. A.: Development of a national anthropogenic heating database with an extrapolation for international cities, Atmospheric Environment, 118, 7–18, https://doi.org/10.1016/j.atmosenv.2015.07.016, http://dx.doi.org/10.1016/j.atmosenv.2015.07.016, 2015.

Salmond, J. A., Tadaki, M., Vardoulakis, S., Arbuthnott, K., Coutts, A., Demuzere, M., Dirks, K. N., Heaviside, C., Lim, S., Macintyre, H., Mcinnes, R. N., and Wheeler, B. W.: Health and climate related ecosystem services provided by street trees in the urban environment, Environmental Health, 15, https://doi.org/10.1186/s12940-016-0103-6, 2016.

Saxton, K. E. and Rawls, W. J.: Soil Water Characteristic Estimates by Texture and Organic Matter for Hydrologic Solutions, Soil Science Society of America Journal, 70, 1569–1578, doi:10.2136/sssaj2005.0117, 2006.

Schenk, H. J. and Jackson, R. B.: The global biogeography of roots, Ecological Monography, 72, 311–328, 2002.

Sellers, P. J., Dickinson, R. E., Randall, D. A., Betts, A. K., Hall, F. G., Berry, J. A., Collatz, G. J., Denning, A. S., Mooney, H. A., Nobre, C. A., Sato, N., Field, C. B., and Henderson-Sellers, A.: Modeling the Exchanges of Energy, Water and Carbon Between Continents and the Atmosphere, Science, 275, 502–509, 1997.

Shuttleworth, W. J.: Terrestrial hydrometeorology, John Wiley & Sons, Ltd, 2012.

Shuttleworth, W. J. and Gurney, R. J.: The theoretical relationship between foliage temperature and canopy resistance in sparse crops, Quarterly Journal of the Royal Meteorological Society, 116, 497–519, 1990.

Skamarock, W. C., Klemp, J. B., Dudhia, J., Gill, D. O., Barker, D. M., Duda, M. G., Huang, X.-y., Wang, W., and Powers, J. G.: A Description of the Advanced Research WRF Version 3, NCAR Tech Note, pp. 488–494, https://doi.org/10.5065/D6DZ069T, 2008.

Song, J. and Wang, Z. H.: Interfacing the Urban Land–Atmosphere System Through Coupled Urban Canopy and Atmospheric Models, Boundary-Layer Meteorology, 154, 427–448, https://doi.org/10.1007/s10546-014-9980-9, 2015.

Sparrow, E. and Cess, R. D.: Radiation Heat Transfer, Chapters 3-4, Appendices A & B, Thermal Science Series, Brooks/Cole, 1970.

Stavropulos-Laffaille, X., Chancibault, K., Brun, J.-M., Lemonsu, A., Masson, V., Boone, A., and Andrieu, H.: Improvements of the hydrological processes of the Town Energy Balance Model (TEB-Veg, SURFEX v7.3) for urban modelling and impact assessment, Geoscientific Model Development Discussions, pp. 1–28, https://doi.org/10.5194/gmd-2018-39, https://www.geosci-model-dev-discuss.net/gmd-2018-39/, 2018.

Stewart, I. D. and Oke, T. R.: Local climate zones for urban temperature studies, American Meteorological Society, https://doi.org/10.1175/BAMS-D-11-00019.1, 2012.

Templeton, N. P., Vivoni, E. R., Wang, Z. H., and Schreiner-McGraw, A. P.: Quantifying Water and Energy Fluxes Over Different Urban Land Covers in Phoenix, Arizona, Journal of Geophysical Research: Atmospheres, 123, 2111–2128, https://doi.org/10.1002/2017JD027845, 2018.

United Nations: World Urbanization Prospects, 2014.

van Genuchten, M. T.: A closed-form equation for predicting the hydraulic conductivity of unsaturated soils, Soil Science Society of America Journal, 44, 892–898, 1980.

Velasco, E., Roth, M., Tan, S. H., Quak, M., Nabarro, S. D. A., and Norford, L.: The role of vegetation in the CO 2 flux from a tropical urban neighbourhood, Atmospheric Chemistry and Physics, 13, 10 185–10 202, https://doi.org/10.5194/acp-13-10185-2013, 2013.

Volo, T. J., Vivoni, E. R., Martin, C. A., Earl, S., and Ruddell, B. L.: Modelling soil moisture, water partitioning, and plant water stress under irrigated conditions in desert Urban areas, Ecohydrology, 7, 1297–1313, https://doi.org/10.1002/eco.1457, 2014.

Wang, C., Wang, Z.-H., and Yang, J.: Cooling Effect of Urban Trees on the Built Environment of Contiguous United States, Earth's Future, pp. 1066–1081, https://doi.org/10.1029/2018EF000891, http://doi.wiley.com/10.1029/2018EF000891, 2018.

Wang, C., Wang, Z.-H., and Yang, J.: Urban water capacity: Irrigation for heat mitigation, Computers, Environment and Urban Systems, 78, 101 397, https://doi.org/10.1016/j.compenvurbsys.2019.101397, https://doi.org/10.1016/j.compenvurbsys.2019.101397, 2019.

Wang, Y.-P. and Leuning, R.: A two-leaf model for canopy conductance, photosynthesis and portioning of available energy I: Model description and comparison with a multi-layered model, Agricultural and Forest Meteorology, 91, 89–111, 1998.

Wang, Z.-h.: Geometric effect of radiative heat exchange in concave structure with application to heating of steel I-sections in fire, International Journal of Heat and Mass Transfer, 53, 997–1003, https://doi.org/10.1016/j.ijheatmasstransfer.2009.11.013, http://dx.doi.org/10.1016/j.ijheatmasstransfer.2009.11.013, 2010.

Wang, Z.-h.: Monte Carlo simulations of radiative heat exchange in a street canyon with trees, Solar Energy, 110, 704–713, https://doi.org/10.1016/j.solener.2014.10.012, http://dx.doi.org/10.1016/j.solener.2014.10.012, 2014.

Wang, Z.-h., Bou-Zeid, E., and Smith, J. A.: A Spatially-Analytical Scheme for Surface Temperatures and Conductive Heat Fluxes in Urban Canopy Models, Boundary-Layer Meteorology, 138, 171–193, https://doi.org/10.1007/s10546-010-9552-6, 2011.

Wang, Z.-h., Bou-zeid, E., and Smith, J. A.: A coupled energy transport and hydrological model for urban canopies evaluated using a wireless sensor network, Quarterly Journal of the Royal Meteorological Society, 139, 1643–1657, https://doi.org/10.1002/qj.2032, 2013.

Ward, H. C., Kotthaus, S., Järvi, L., and Grimmond, C. S.: Surface Urban Energy and Water Balance Scheme (SUEWS): Development and evaluation at two UK sites, Urban Climate, 18, 1–32, https://doi.org/10.1016/j.uclim.2016.05.001, http://dx.doi.org/10.1016/j.uclim.2016.05.001, 2016.

Willmott, C. J.: Some Comments on the Evaluation of Model Performance, Bulletin American Meteorological Society, 1982.

Wouters, H., Demuzere, M., Ridder, K. D., and Van Lipzig, N. P.: The impact of impervious water-storage parametrization on urban climate modelling, Urban Climate, 11, 24–50, https://doi.org/10.1016/j.uclim.2014.11.005, http://dx.doi.org/10.1016/j.uclim.2014.11.005, 2015.

Wouters, H., Demuzere, M., Blahak, U., Fortuniak, K., Maiheu, B., and Camps, J.: The efficient urban canopy dependency parametrization (SURY) v1 . 0 for atmospheric modelling : description and application with the COSMO-CLM model for a Belgian summer, Geoscientific Model Development, 9, 3027–3054, https://doi.org/10.5194/gmd-9-3027-2016, 2016.

Wullschleger, S. D.: Biochemical Limitations to Carbon Assimilation in C3 Plants—A Retrospective Analysis of the A/C i Curves from 109 Species, Journal of Experimental Botany, 44, 907–920, https://doi.org/10.1093/jxb/44.5.907, https://academic.oup.com/jxb/article-lookup/doi/10.1093/jxb/44.5.907, 1993.

Yang, J. and Wang, Z. H.: Planning for a sustainable desert city: The potential water buffering capacity of urban green infrastructure, Landscape and Urban Planning, 167, 339–347, https://doi.org/10.1016/j.landurbplan.2017.07.014, http://dx.doi.org/10.1016/j.landurbplan.2017.07.014, 2017.

Zhang, X., Friedl, M. A., Schaaf, C. B., Strahler, A. H., and Schneider, A.: The footprint of urban climates on vegetation phenology, Geophysical Research Letters, 31, 10–13, https://doi.org/10.1029/2004GL020137, 2004.

Zhou, S., Duursma, R. A., Medlyn, B. E., Kelly, J. W., and Prentice, I. C.: How should we model plant responses to drought? An analysis of stomatal and non-stomatal responses to water stress, Agricultural and Forest Meteorology, 182-183, 204–214, https://doi.org/10.1016/j.agrformet.2013.05.009, http://dx.doi.org/10.1016/j.agrformet.2013.05.009, 2013.

Ziegler, A. D., Terry, J. P., Oliver, G. J., Friess, D. A., Chuah, C. J., Chow, W. T., and Wasson, R. J.: Increasing Singapore's resilience to drought, Hydrological Processes, 28, 4543–4548, https://doi.org/10.1002/hyp.10212, 2014.

Technical Reference Material to:
An urban ecohydrological model to quantify the effect of vegetation on urban climate and hydrology (UT&C v1.0)

Naika Meili[1,2], Gabriele Manoli[2,3], Paolo Burlando[2], Elie Bou-Zeid[4], Winston T.L. Chow[5], Andrew M. Coutts[6,7], Edoardo Daly[8], Kerry A. Nice[6,7,9], Matthias Roth[10], Nigel J. Tapper[6,7], Erik Velasco[11], Enrique R. Vivoni[12,13], and Simone Fatichi[2]

[1]ETH Zurich, Future Cities Laboratory, Singapore-ETH Centre, Singapore
[2]Institute of Environmental Engineering, ETH Zurich, Zurich, Switzerland
[3]Department of Civil, Environmental and Geomatic Engineering, University College London, London WC1E 6BT, UK
[4]Department of Civil and Environmental Engineering, Princeton University, NJ, USA
[5]School of Social Sciences, Singapore Management University, Singapore
[6]School of Earth, Atmosphere and Environment, Monash University, Clayton, Australia
[7]Cooperative Research Centre for Water Sensitive Cities, Melbourne, Australia
[8]Department of Civil Engineering, Monash University, Clayton, Australia
[9]Transport, Health, and Urban Design Hub, Faculty of Architecture, Building, and Planning, University of Melbourne, Victoria, Australia
[10]Department of Geography, National University of Singapore, Singapore
[11]Centre for Urban Greenery and Ecology, National Parks Board, Singapore
[12]School of Sustainable Engineering and the Built Environment, Arizona State University, Tempe, Arizona, USA
[13]School of Earth and Space Exploration, Arizona State University, Tempe, Arizona, USA

Correspondence: Naika Meili (meili@ifu.baug.ethz.ch)

Contents

1 Radiation

1.1 Shortwave radiation

The direct $S^{dir}_{net,i}$ and diffuse $S^{diff}_{net,i}$ solar shortwave radiation absorbed by each urban surface ~~i~~ i [W m^{-2}] are calculated as a function of urban geometry and albedo. The urban geometry provides shade by blocking part of the incoming direct beam solar radiation. It further decreases the sky-view factor, which reduces the incoming diffuse solar radiation and traps reflected solar radiation within the urban canyon. UT&C calculates the absorbed solar shortwave radiation with the following steps:

1. (a) The direct shortwave radiation received by each urban surface is calculated as a function of solar position and shade provided by buildings and trees (Sect. 1.1.2, 1.1.3, 1.1.4).

   (b) The diffuse shortwave radiation received by each urban surface is calculated as a function of its sky-view factor (Sect. 1.1.5).

2. Infinite radiation reflections within the urban canyon are calculated using view factors and the total absorbed shortwave radiation of each urban surface ~~i~~ i is consequently calculated (Sect. 1.1.6).

It is assumed that all urban surfaces are Lambertian with isotropic scattering and reflections. The view factors are calculated analytically (Sect. 1.3.1) if there are no trees in the urban environment, and with a Monte Carlo ray tracing algorithm (Sect. 1.3.2) if trees are present. UT&C assumes no obstruction of the roof surface and the absorbed shortwave radiation is only influenced by the solar position and surface albedo (Sect. 1.1.1). UT&C further calculates the absorbed shortwave radiation due to direct beam radiation and diffuse radiation (Sect. 1.1.7), which allows to investigate the effects of shade and albedo in more detail. The energy associated with shortwave radiation is perfectly conserved (Sect. 1.1.8).

1.1.1 Absorbed shortwave radiation: Roof

The direct $S^{dir}_{net,i}$, diffuse $S^{diff}_{net,i}$, and total $S_{net,i}$ absorbed shortwave radiation of each roof surface fraction i [W m^{-2}] are calculated as:

$$S^{dir}_{net,i} = (1-\alpha_i)\, S\downarrow^{dir}\,, \tag{1}$$

$$S^{diff}_{net,i} = (1-\alpha_i)\, S\downarrow^{diff}\,, \tag{2}$$

$$S_{net,i} = (1-\alpha_i)\, (S\downarrow^{dir} + S\downarrow^{diff})\,, \tag{3}$$

where α_i [$-$] is the surface albedo of roof surface fraction i, $S\downarrow^{dir}$ [W m^{-2}] the incoming direct, and $S\downarrow^{diff}$ [W m^{-2}] the incoming diffuse shortwave radiation from the sky.

1.1.2 Incoming direct shortwave radiation: Ground and wall without trees

In the absence of trees, the direct solar radiation received by the ground facets $S^{dir}_{in,g}$, sunlit wall $S^{dir}_{in,wsun}$, and shaded wall $S^{dir}_{in,wshd}$ [W m^{-2}], are calculated according to Kusaka et al. (2001), Wang et al. (2013), and Ryu et al. (2016). The shade

positions on the ground x_0, and on the wall y_0 $[-]$ (Fig. 1) are:

$$x_0 = \max[1 - h_{can}\xi,\ 0]\ , \tag{4}$$

$$y_0 = \max[h_{can} - 1/\xi,\ 0]\ , \tag{5}$$

where h_{can} $[-]$ is the canyon height normalized by canyon width w_{can} (often referred to as height-to-width ratio), and ξ $[-]$ summarizes the influence of solar position in relation to canyon position as (Kusaka et al., 2001; Wang et al., 2013; Ryu et al., 2016):

$$\xi = \tan\theta_z \left|\sin\theta_a\right|\ , \tag{6}$$

where θ_z $[\mathrm{rad}]$ is the solar zenith angle, and θ_a $[\mathrm{rad}]$ the difference between solar azimuth angle and canyon orientation ($\theta_{azimuth}$ $[\mathrm{rad}]$ - θ_{canyon} $[\mathrm{rad}]$). The shadow length on the ground χ_{shadow} $[-]$, and on the wall η_{shadow} $[-]$, are calculated as (Kusaka et al., 2001; Wang et al., 2013; Ryu et al., 2016):

$$\chi_{shadow} = 1 - x_0\ , \tag{7}$$

$$\eta_{shadow} = y_0\, h_{can}^{-1}\ , \tag{8}$$

The direct solar radiation received by the ground $S^{dir}_{in,g}$, the sunlit wall $S^{dir}_{in,wsun}$, and the shaded wall $S^{dir}_{in,wshd}$ $[\mathrm{W\ m^{-2}}]$ are calculated as (Kusaka et al., 2001; Wang et al., 2013; Ryu et al., 2016):

$$S^{dir}_{in,g} = S\downarrow^{dir}\left[1 - \chi_{shadow}\right]\ , \tag{9}$$

$$S^{dir}_{in,wsun} = S\downarrow^{dir}\xi\left[1 - \eta_{shadow}\right]\ , \tag{10}$$

$$S^{dir}_{in,wshd} = 0\ , \tag{11}$$

where $S\downarrow^{dir}$ $[\mathrm{W\ m^{-2}}]$ is the incoming direct shortwave radiation from the sky. The shaded wall does not receive any direct solar radiation.

1.1.3 Incoming direct shortwave radiation: Ground and wall with trees

In the presence of trees, the direct solar radiation received by the ground $S^{dir}_{in,g}$, the sunlit wall $S^{dir}_{in,wsun}$, and the shaded wall $S^{dir}_{in,wshd}$ $[\mathrm{W\ m^{-2}}]$ are calculated according to Ryu et al. (2016) as:

$$S^{dir}_{in,g} = S\downarrow^{dir}\left[1 - \chi_{shadow} + \tau\chi_{tree}\right]\ , \tag{12}$$

$$S^{dir}_{in,wsun} = S\downarrow^{dir}\xi\left[h_{can} - \eta_{shadow} + \tau\eta_{tree}\right]\ , \tag{13}$$

$$S^{dir}_{in,wshd} = 0\ , \tag{14}$$

where $S\downarrow^{dir}$ $[\mathrm{W\ m^{-2}}]$ is the direct incoming solar radiation, χ_{shadow} $[-]$ the total shadow length on the ground, χ_{tree} $[-]$ the shadow length on the ground due to tree shading alone, η_{shadow} $[-]$ the total shadow length on the wall, and η_{tree} $[-]$ the

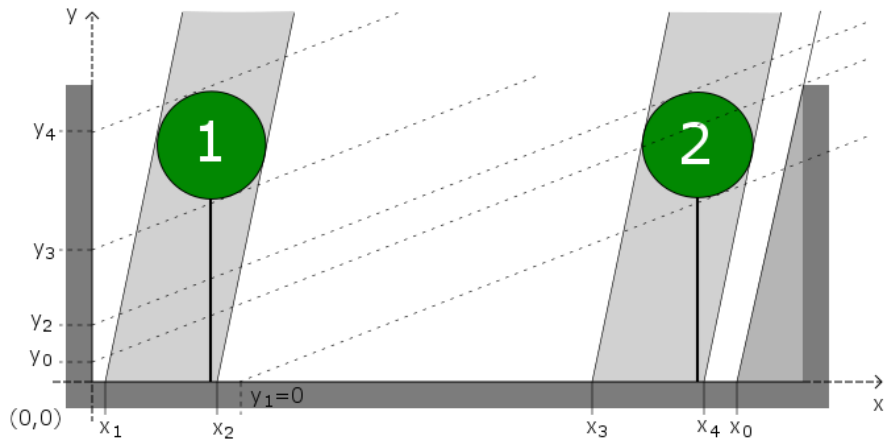

Figure 1. Shadow location on the ground and wall cast by trees and opposite wall according to Ryu et al. (2016). x_0, x_1, x_2, x_3, x_4 are the shadow locations on the ground and y_0, y_1, y_2, y_3, y_4 on the wall as described in Sect. 1.1.3.

shadow length on the wall due to tree shading alone. The variable τ $[-]$ is the tree canopy transmittance as a function of leaf area index, LAI $[-]$, and optical trasmittance factor K_{opt} $[-]$, calculated according to Maass et al. (1995) as:

$$\tau = e^{-K_{opt}\ LAI}\ , \tag{15}$$

The shaded wall does not receive any direct solar radiation. The shadow lengths χ_{shadow} $[-]$, η_{shadow} $[-]$, χ_{tree} $[-]$, and η_{tree} $[-]$ are calculated according to Ryu et al. (2016) who computes the shadow location coordinates (Fig. 1) as:

$$x_0 = \max[1 - h_{can}\xi,\ 0]\ , \tag{16}$$

$$y_0 = \max[h_{can} - 1/\xi,\ 0]\ , \tag{17}$$

$$x_1 = \max[d_t - h_t\xi - r_t\sqrt{1+\xi^2},\ 0]\ , \tag{18}$$

$$x_2 = \max[d_t - h_t\xi + r_t\sqrt{1+\xi^2},\ 0]\ , \tag{19}$$

$$x_3 = \max[1 - d_t - h_t\xi - r_t\sqrt{1+\xi^2},\ 0]\ , \tag{20}$$

$$x_4 = \max[1 - d_t - h_t\xi + r_t\sqrt{1+\xi^2},\ 0]\ , \tag{21}$$

$$y_1 = \max[h_t - (1-d_t)\xi^{-1} - r_t\sqrt{1+\xi^{-2}},\ 0]\ , \tag{22}$$

$$y_2 = \max[h_t - (1-d_t)\xi^{-1} + r_t\sqrt{1+\xi^{-2}},\ 0]\ , \tag{23}$$

$$y_3 = \max[h_t - d_t\xi^{-1} - r_t\sqrt{1+\xi^{-2}},\ 0]\ , \tag{24}$$

$$y_4 = \max[h_t - d_t\xi^{-1} + r_t\sqrt{1+\xi^{-2}},\ 0]\ , \tag{25}$$

where $x_1 < x_2 < x_3 < x_4$ and $y_1 < y_2 < y_3 < y_4$, h_t $[-]$ is the normalized tree height, r_t $[-]$ the normalized tree radius, and d_t $[-]$ the normalized tree-to-wall distance (Fig. 2). The shadow length caused by tree 1 and tree 2 on the ground, χ_{tree1} $[-]$ and χ_{tree2} $[-]$, and on the wall, η_{tree1} $[-]$ and η_{tree2} $[-]$, are:

$$\chi_{tree1} = x_2 - x_1 \ , \tag{26}$$

$$\chi_{tree2} = x_4 - x_3 \ , \tag{27}$$

$$\eta_{tree1} = y_4 - y_3 \ , \tag{28}$$

$$\eta_{tree2} = y_2 - y_1 \ , \tag{29}$$

The total shadow length caused by trees and wall on the ground χ_{shadow} $[-]$, and wall η_{shadow} $[-]$, are (Ryu et al., 2016):

$$\chi_{shadow} = \begin{cases} 1 - \min\left[x_0,\, x_3\right] + \chi_{tree1} - \max\left[x_2 - x_0,\, 0\right] & \text{if } x_0 < x_4 \\ 1 - x_0 + \chi_{tree1} + \chi_{tree2} & \text{if } x_0 \geq x_4 \end{cases} \ , \tag{30}$$

$$\eta_{shadow} = \begin{cases} \max\left[y_0,\, y_1,\, y_2,\, y_3,\, y_4\right] & \text{if } y_3 \leq \max\left[y_0,\, y_2\right] \\ \eta_{Tree1} + \max\left[y_0,\, y_2\right] & \text{if } y_3 > \max\left[y_0,\, y_2\right] \end{cases} \ , \tag{31}$$

The total shadow length caused by trees only on the ground χ_{tree} $[-]$, and wall η_{tree} $[-]$, are (Ryu et al., 2016):

$$\chi_{tree} = \begin{cases} \chi_{tree1} - \max\left[x_2 - x_0,\, 0\right] & \text{if } x_0 < x_3 \\ \chi_{tree1} + x_0 - x_3 & \text{if } x_3 \leq x_0 < x_4 \\ \chi_{tree1} + \chi_{tree2} & \text{if } x_0 \geq x_4 \end{cases} \ , \tag{32}$$

$$\eta_{tree} = \begin{cases} \eta_{tree1} + y_2 - y_0 & \text{if } y_3 > \max\left[y_0,\, y_2\right] \ \& \ y_2 > y_0 \\ \eta_{tree1} & \text{if } y_3 > \max\left[y_0,\, y_2\right] \ \& \ y_2 \leq y_0 \\ \eta_{tree1} + \eta_{tree2} & \text{if } y_3 > \max\left[y_0,\, y_2\right] \ \& \ y_1 > y_0 \\ \\ y_4 - y_0 & \text{if } y_3 \leq \max\left[y_0,\, y_2\right] \ \& \ y_2 > y_0 \\ 0 & \text{if } y_3 \leq \max\left[y_0,\, y_2\right] \ \& \ y_2 \leq y_0 \end{cases} \ , \tag{33}$$

1.1.4 Incoming direct shortwave radiation: Trees

The direct shortwave radiation received by the tree canopy $S^{dir}_{in,t}$ $[\mathrm{W\ m^{-2}\ circle\ area}]$ is calculated according to Ryu et al. (2016) as:

$$S^{dir}_{in,t} = (1 - \tau)\left(S^{dir}_{in,t1} + S^{dir}_{in,t2}\right)/2 \ , \tag{34}$$

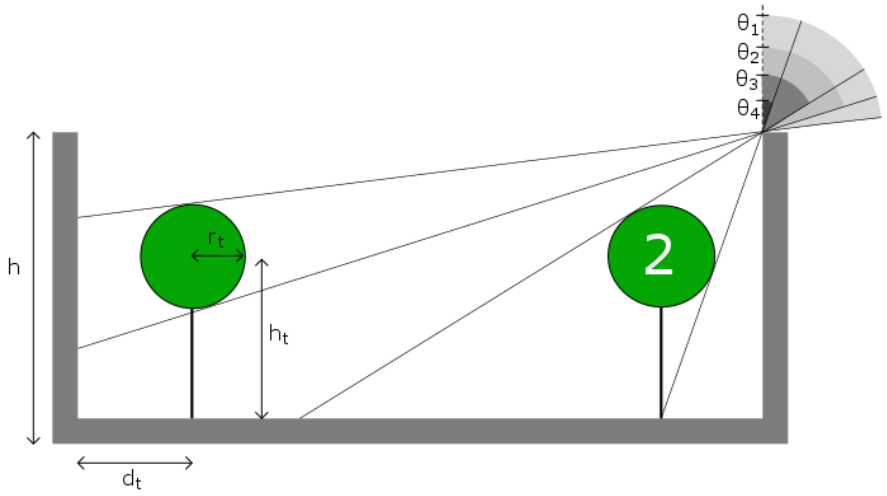

Figure 2. Urban geometry and its interaction with direct beam solar radiation according to Ryu et al. (2016). h is the normalized building height, h_t the normalized tree height, r_t the normalized tree radius, and d_t the normalized distance of tree trunk from the wall. θ_1, θ_2, θ_3, θ_4 are reference angles used to calculate radiation-tree interaction as described in Sect. 1.1.4.

where $S^{dir}_{in,t1}$ and $S^{dir}_{in,t2}$ [W m^{-2} circle area] are the direct shortwave radiation received by tree 1 and tree 2, τ [$-$] is the tree canopy transmittance (Eq. (15)). $S^{dir}_{in,t1}$ and $S^{dir}_{in,t2}$ [W m^{-2} circle area] are calculated as follows (Ryu et al., 2016):

$$S^{dir}_{in,t1} = \begin{cases} 0 & \text{if } \xi \geq \tan\theta_1 \\ S\downarrow^{dir} [r_t\sqrt{1+\xi^2} + (1-d_t) - (h_{can}-h_t)\xi]/(2\pi r_t) & \text{if } \tan\theta_2 \leq \xi < \tan\theta_1 \\ S\downarrow^{dir} [2r_t\sqrt{1+\xi^2}]/(2\pi r_t) & \text{if } \xi < \tan\theta_2 \end{cases}$$

$$S^{dir}_{in,t2} = \begin{cases} 0 & \text{if } \xi \geq \tan\theta_3 \\ S\downarrow^{dir} [r_t\sqrt{1+\xi^2} + d_t - (h_{can}-h_t)\xi]/(2\pi r_t) & \text{if } \tan\theta_4 \leq \xi < \tan\theta_3 \\ S\downarrow^{dir} [2r_t\sqrt{1+\xi^2}]/(2\pi r_t) & \text{if } \xi < \tan\theta_4 \end{cases} \quad (35)$$

where $S\downarrow^{dir}$ [W m^{-2}] is the incoming direct shortwave radiation from the sky, and d_t [$-$] the normalized tree-to-wall distance (Fig. 2).

The four reference angles θ_1, θ_2, θ_3, and θ_4 (Fig. 2) are calculated as (Ryu et al., 2016):

$$\tan\theta_1 = \frac{(1-d_t)(h_{can}-h_t) + r_t\sqrt{(1-d_t)^2 + (h_{can}-h_t)^2 - r_t^2}}{(h_{can}-h_t)^2 - r_t^2}\,, \tag{36}$$

$$\tan\theta_2 = \frac{(1-d_t)(h_{can}-h_t) - r_t\sqrt{(1-d_t)^2 + (h_{can}-h_t)^2 - r_t^2}}{(h_{can}-h_t)^2 - r_t^2}\,, \tag{37}$$

$$\tan\theta_3 = \frac{d_t(h_{can}-h_t) + r_t\sqrt{d_t^2 + (h_{can}-h_t)^2 - r_t^2}}{(h_{can}-h_t)^2 - r_t^2}\,, \tag{38}$$

$$\tan\theta_4 = \frac{d_t(h_{can}-h_t) - r_t\sqrt{d_t^2 + (h_{can}-h_t)^2 - r_t^2}}{(h_{can}-h_t)^2 - r_t^2}\,, \tag{39}$$

The relationships developed by Ryu et al. (2016) and applied in UT&C does not account for tree-on-tree shading. Hence, energy conservation is only met when trees do not shade each other. In the case of tree on tree shading, the excess or deficit of energy is added to the tree surfaces.

1.1.5 Incoming diffuse shortwave radiation: Ground, wall, trees

The diffuse shortwave radiation received by each urban surface i $S_{in,i}^{diff}$ [W m^{-2}] is a function of sky-view factors (Masson, 2000; Kusaka et al., 2001; Wang et al., 2013; Ryu et al., 2016) and is calculated as:

$$S_{in,i}^{diff} = S\downarrow^{diff} F_{is}^{(t)}\,, \tag{40}$$

where $S\downarrow^{diff}$ [W m^{-2}] is the incoming diffuse solar radiation from the sky, and $F_{is}^{(t)}$ [$-$] the respective sky-view factor of surface i either without trees (F_{is}) or with trees (F_{is}^{t}). In the absence of trees, the sky-view factors F_{is} are calculated with the analytically derived equations (Masson, 2000; Kusaka et al., 2001; Oleson et al., 2007; Park and Lee, 2008; Ryu et al., 2011; Wang et al., 2013) described in Sect. 1.3.1. In the presence of trees, the sky-view factors F_{is}^{t} are calculated with the Monte Carlo ray tracing algorithm once for each urban scene at the beginning of the simulation period (Hoff and Janni, 1989; Wang, 2014; Frank et al., 2016) as described in Sect. 1.3.2.

1.1.6 Radiation reflection and total absorbed shortwave radiation

UT&C calculates infinite reflections of shortwave radiation within the urban canyon according to the method developed by Sparrow and Cess (1970), and applied by Harman (2003), and Wang (2010, 2014).

The infinite reflection theory and its step by step application to the longwave radiative transfer in an urban canyon without trees are described in Sect. 1.2.2 and 1.2.3. The solution of shortwave radiation reflections can be derived identically under the following assumptions:

- There is no shortwave radiation generated: $\Omega_i = 0$.
- The incoming direct shortwave radiation $S_{in,i}^{dir}$ is added to each surface i.

– The reflectivity term $(1-\varepsilon_i)$ for longwave radiation is replaced by the albedo α_i.

Applying these changes and following the step by step derivation described in Sect. 1.2.3 leads to the following equation:

$$T_{ij}B_i = C_i \ , \tag{41}$$

Where B_i [W m^{-2}] is the vector of outgoing shortwave radiation from surface i, C_i [W m^{-2}] the vector of incoming direct and diffuse shortwave radiation from the sky to surface i, and T_{ij} [$-$] the matrix describing the geometric relationship between the different surfaces with their view factors. In the absence of trees, T_{ij}, B_i, and C_i are:

$$C_i = \begin{bmatrix} C_{gv}\alpha_{gv}(S^{dir}_{in,g} + F_{gs}S\downarrow^{diff}) \\ C_{gb}\alpha_{gb}(S^{dir}_{in,g} + F_{gs}S\downarrow^{diff}) \\ C_{gi}\alpha_{gi}(S^{dir}_{in,g} + F_{gs}S\downarrow^{diff}) \\ \alpha_w(S^{dir}_{wsun} + F_{ws}S\downarrow^{diff}) \\ \alpha_w F_{ws}S\downarrow^{diff} \end{bmatrix} \ , \qquad B_i = \begin{bmatrix} B_{gv} \\ B_{gb} \\ B_{gi} \\ B_{wsun} \\ B_{wshd} \end{bmatrix} \ , \tag{42}$$

$$T_{ij} = \begin{bmatrix} 1 & 0 & 0 & -C_{gv}\alpha_{gv}F_{gw} & -C_{gv}\alpha_{gv}F_{gw} \\ 0 & 1 & 0 & -C_{gb}\alpha_{gb}F_{gw} & -C_{gb}\alpha_{gb}F_{gw} \\ 0 & 0 & 1 & -C_{gi}\alpha_{gi}F_{gw} & -C_{gi}\alpha_{gi}F_{gw} \\ -C_{gv}f_{gv}\alpha_w F_{wg} & -C_{gb}f_{gb}\alpha_w F_{wg} & -C_{gi}f_{gi}\alpha_w F_{wg} & 1 & -\alpha_w F_{ww} \\ -C_{gv}f_{gv}\alpha_w F_{wg} & -C_{gb}f_{gb}\alpha_w F_{wg} & -C_{gi}f_{gi}\alpha_w F_{wg} & -\alpha_w F_{ww} & 1 \end{bmatrix} \ , \tag{43}$$

In the presence of trees, T_{ij}, B_i, and C_i are:

$$C_i = \begin{bmatrix} C_{gv}\alpha_{gv}(S^{dir}_{in,g} + F^t_{gs}S\downarrow^{diff}) \\ C_{gb}\alpha_{gb}(S^{dir}_{in,g} + F^t_{gs}S\downarrow^{diff}) \\ C_{gi}\alpha_{gi}(S^{dir}_{in,g} + F^t_{gs}S\downarrow^{diff}) \\ \alpha_w(S^{dir}_{wsun} + F^t_{ws}S\downarrow^{diff}) \\ \alpha_w F^t_{ws}S\downarrow^{diff} \\ \alpha_t(S^{dir}_{in,t} + F^t_{ts}S\downarrow^{diff}) \end{bmatrix} \ , \qquad B_i = \begin{bmatrix} B_{gv} \\ B_{gb} \\ B_{gi} \\ B_{wsun} \\ B_{wshd} \\ B_t \end{bmatrix} \ , \tag{44}$$

$$T_{ij} = \begin{bmatrix} 1 & 0 & 0 & -C_{gv}\alpha_{gv}F^t_{gw} & -C_{gv}\alpha_{gv}F^t_{gw} & -C_{gv}\alpha_{gv}F^t_{gt} \\ 0 & 1 & 0 & -C_{gb}\alpha_{gb}F^t_{gw} & -C_{gb}\alpha_{gb}F^t_{gw} & -C_{gv}\alpha_{gv}F^t_{gt} \\ 0 & 0 & 1 & -C_{gi}\alpha_{gi}F^t_{gw} & -C_{gi}\alpha_{gi}F^t_{gw} & -C_{gv}\alpha_{gv}F^t_{gt} \\ -C_{gv}f_{gv}\alpha_w F^t_{wg} & -C_{gb}f_{gb}\alpha_w F^t_{wg} & -C_{gi}f_{gi}\alpha_w F^t_{wg} & 1 & -\alpha_w F^t_{ww} & -\alpha_w F^t_{wt} \\ -C_{gv}f_{gv}\alpha_w F^t_{wg} & -C_{gb}f_{gb}\alpha_w F^t_{wg} & -C_{gi}f_{gi}\alpha_w F^t_{wg} & -\alpha_w F^t_{ww} & 1 & -\alpha_w F^t_{wt} \\ -C_{gv}f_{gv}\alpha_t F^t_{tg} & -C_{gb}f_{gb}\alpha_t F^t_{tg} & -C_{gi}f_{gi}\alpha_t F^t_{tg} & -\alpha_t F^t_{tw} & -\alpha_t F^t_{tw} & 1-\alpha_t F^t_{tt} \end{bmatrix} \ , \tag{45}$$

where C_{gv}, C_{gb}, and C_{gi} are logical factors accounting for the presence ($C_{gi} = 1$) or absence ($C_{gi} = 0$) of vegetated, bare, or impervious ground cover. α_i [$-$] is the albedo of surface i, $S^{dir}_{in,i}$ [W m^{-2}] the direct incoming radiation of surface i, $F^{(t)}_{ij}$ [$-$] the view factor from surface i to surface j, $S\downarrow^{diff}$ [W m^{-2}] the incoming diffuse shortwave radiation from the sky, f_{gv}, f_{gb}, and f_{gi} are the fraction of vegetated, bare and impervious ground, respectively. B_i [W m^{-2}] is the outgoing solar shortwave radiation from surface i. The subscripts gv, gb, gi, $wsun$, $wshd$, and t denote vegetated ground, bare ground, impervious ground, sunlit wall, shaded wall, and trees, respectively.

The outgoing shortwave radiation of surface i, B_i [W m^{-2}], is calculated with matrix inversion of Eq. (41):

$$B_i = [T_{ij}]^{-1} C_i \,, \tag{46}$$

Subsequently, the incoming shortwave radiation of surface i, Λ_i [W m^{-2}], and net absorbed shortwave radiation of surface i $S_{net,i}$ [W m^{-2}] are calculated according to Eq. (58) and (59).

1.1.7 Absorbed direct and diffuse shortwave radiation

The direct absorbed shortwave radiation of each surface $S^{dir}_{net,i}$ [W m^{-2}] is calculated as a function of the direct incoming solar radiaton to surface i $S^{dir}_{in,i}$ [W m^{-2}] and its albedo α_i [$-$] as:

$$S^{dir}_{net,i} = (1 - \alpha_i) S^{dir}_{in,i} \,, \tag{47}$$

The diffuse absorbed shortwave radiation of each surface i $S^{diff}_{net,i}$ [W m^{-2}] is calculated afterwards subtracting the absorbed direct solar radiation $S^{dir}_{net,i}$ [W m^{-2}] from the total absorbed solar radiation of surface i $S_{net,i}$ [W m^{-2}]:

$$S^{diff}_{net,i} = S_{net,i} - S^{dir}_{net,i} \,, \tag{48}$$

1.1.8 Energy conservation

UT&C is designed to conserve shortwave radiation energy. View factors are direction specific and need to fulfill a reciprocity criterion in order to conserve radiation energy. Monte Carlo Ray tracing algorithms do generally not result in reciprocal view factors due to the finite number of rays. Hence, the view factors used in UT&C are post processed to fulfill reciprocity.

Taking the directionality of the view factors into account, the shortwave radiation energy balance can be calculated from the perspective of the urban surface EB_{surf} [W m^{-2}] and from the perspective of the urban canyon EB_{can} [W m^{-2}] as:

$$EB_{surf} = \sum_i S_{in,i} \frac{f_i A_i}{A_g} - \sum_i S_{net,i} \frac{f_i A_i}{A_g} - \sum_i S_{out,i} \frac{f_i A_i}{A_g} \,, \tag{49}$$

$$EB_{can} = S\downarrow^{dir} + S\downarrow^{diff} - \sum_i S_{net,i} \frac{f_i A_i}{A_g} - \sum_i S_{out,i} f_i F^{(t)}_{si} \,, \tag{50}$$

where $S_{in,i}$ [$W\ m^{-2}$] is the incoming, $S_{out,i}$ [W m^{-2}] the outgoing, and $S_{net,i}$ [W m^{-2}] the net absorbed shortwave radiation of surface i. A_i is the surface area i, A_g the total ground area equal to the canyon width, f_i the ground cover fraction (f_i =1 for wall or tree), $F^{(t)}_{si}$ [$-$] the sky-view factor of each surface i, $S\downarrow^{dir}$ [W m^{-2}] the direct, and $S\downarrow^{diff}$ [W m^{-2}] the diffuse incoming shortwave radiation from the sky.

1.2 Longwave radiation

The absorbed longwave radiation of surface i $L_{net,i}$ [W m^{-2}] is calculated as the difference between incoming $L_{in,i}$ and emitted outgoing longwave radiation $L_{out,i}$, which is dependent on the surface temperature. As with shortwave radiation, UT&C calculates infinite reflections of longwave radiation within the urban canyon (Sparrow and Cess, 1970; Harman, 2003; Wang, 2010, 2014). Sect. 1.2.2 describes the infinite radiation reflection theory (Harman, 2003) between multiple surfaces, which is applied step by step to the urban canyon (Sect. 1.2.3). UT&C assumes no obstruction of roof surface in the calculation of longwave radiation transfer (Sect. 1.2.1). The air within the canyon does not interact in the radiative exchange. UT&C is designed to fully conserve the energy budget of longwave radiation (Sect. 1.2.4).

1.2.1 Absorbed longwave radiation: Roof

The absorbed longwave radiation of each roof surface i $L_{net,i}$ [W m^{-2}] is calculated as:

$$L_{net,i} = \varepsilon_i (L\downarrow - \sigma T_i^4) \ , \tag{51}$$

where $L\downarrow$ [W m^{-2}] is the incoming longwave radiation from the atmosphere, ε_i [$-$] the emissivity and $(1-\epsilon_i)$ the reflectivity of surface i for longwave radiation, $\sigma = 5.67 * 10^{-8}$ [W m^{-2} K^{-4}] the Stefan-Boltzmann constant, and T_i [K] the temperature of surface i.

1.2.2 Infinite radiation reflections: Theory

The incoming Λ_i [W m^{-2}], outgoing B_i [W m^{-2}], emitted Ω_i [W m^{-2}], and net absorbed Q_i [W m^{-2}] longwave radiation flux of each surface i can be described as (Sparrow and Cess, 1970; Harman, 2003; Wang, 2010, 2014) :

$$\Lambda_i = \sum_j F_{ij} B_j \ , \tag{52}$$

$$B_i = \Omega_i + (1-\varepsilon_i)\,\Lambda_i \ , \qquad \Omega_i = \begin{cases} \varepsilon_i \sigma T_i^4 & \text{for } i = g,w,t \\ L\downarrow & \text{for } i = s \end{cases} \ , \tag{53}$$

$$Q_i = \Lambda_i - B_i \ , \tag{54}$$

where F_{ij} [$-$] is the view factor from surface i to surface j, ε_i [$-$] the emissivity and $(1-\varepsilon_i)$ the longwave reflectivity of surface i, and T_i [K] the temperature of surface i.

Equations (52) and (53) are combined and solved for the emitted radiation of surface i Ω_i [W m^{-2}] as:

$$B_i = \Omega_i + (1-\varepsilon_i) \sum_j F_{ij} B_j \ , \tag{55}$$

$$\Omega_i = B_i - (1-\varepsilon_i) \sum_j F_{ij} B_j = \sum_j \Gamma_{ij} B_j \ , \tag{56}$$

$$\Gamma_{ij} = \delta_{ij} - (1-\varepsilon_i)\, F_{ij} \ , \tag{57}$$

Equation (56) shows recurrence of outgoing radiation B_i [W m^{-2}]. The geometric relationship between the surfaces is described by the view factors F_{ij} [$-$] in matrix Γ_{ij}. Γ_{ij} always has an inverse $[\Gamma_{ij}]^{-1}$ and the outgoing B_i [W m^{-2}], incoming Λ_i [W m^{-2}], and net absorbed longwave radiation flux Q_i [W m^{-2}] are calculated as:

$$B_i = \sum_j [\Gamma_{ij}]^{-1} \Omega_j \ , \qquad \Lambda_i = \frac{B_i - \Omega_i}{1 - \varepsilon_i} \ , \tag{58}$$

$$Q_i = \begin{cases} \sum_j F_{ij} B_j - \Omega_i, & \text{if } \varepsilon_i = 1 \\ \left(\varepsilon_i B_i - \Omega_i\right) / \left(1 - \varepsilon_i\right) & \text{otherwise} \end{cases} \ , \tag{59}$$

UT&C applies the above described solution for infinite reflections to the computation of longwave and shortwave radiation transfer.

1.2.3 Infinite longwave radiation reflections: Step by step

The following equations show the step by step derivation and application of the infinite reflection theory described in Sect. 1.2.2 to calculate the net absorbed longwave radiation in an urban canyon without trees.

The outgoing longwave radiation of surface i, B_i [W m^{-2}], is the sum of emitted $\Omega_i = \varepsilon_i \sigma T_i^4$ [W m^{-2}] and reflected Λ_i [W m^{-2}] longwave radiation (Eq. (53)):

$$B_{gv} = \varepsilon_{gv} \sigma T_{gv}^4 + (1 - \varepsilon_{gv}) \Lambda_{gv} \ , \tag{60}$$

$$B_{gb} = \varepsilon_{gb} \sigma T_{gb}^4 + (1 - \varepsilon_{gb}) \Lambda_{gb} \ , \tag{61}$$

$$B_{gi} = \varepsilon_{gi} \sigma T_{gi}^4 + (1 - \varepsilon_{gi}) \Lambda_{gi} \ , \tag{62}$$

$$B_{wsun} = \varepsilon_{w} \sigma T_{wsun}^4 + (1 - \varepsilon_{w}) \Lambda_{wsun} \ , \tag{63}$$

$$B_{wshd} = \varepsilon_{w} \sigma T_{wshd}^4 + (1 - \varepsilon_{w}) \Lambda_{wshd} \ , \tag{64}$$

Similarly, the incoming longwave radiation to surface i, Λ_i [W m^{-2}], can be written as (Eq. (52)):

$$\Lambda_{gv} = F_{gs} L\downarrow + F_{gw} B_{wsun} + F_{gw} B_{wshd} \ , \tag{65}$$

$$\Lambda_{gb} = F_{gs} L\downarrow + F_{gw} B_{wsun} + F_{gw} B_{wshd} \ , \tag{66}$$

$$\Lambda_{gi} = F_{gs} L\downarrow + F_{gw} B_{wsun} + F_{gw} B_{wshd} \ , \tag{67}$$

$$\Lambda_{wsun} = F_{ws} L\downarrow + f_{gv} F_{wg} B_{gv} + f_{gb} F_{wg} B_{gb} + f_{gi} F_{wg} B_{gi} + F_{ww} B_{wshd} \ , \tag{68}$$

$$\Lambda_{wshd} = F_{ws} L\downarrow + f_{gv} F_{wg} B_{gv} + f_{gb} F_{wg} B_{gb} + f_{gi} F_{wg} B_{gi} + F_{ww} B_{wsun} \ , \tag{69}$$

where B_j [W m^{-2}] is the outgoing longwave radiation from the surrounding surfaces j, and F_{ij} [$-$] the view factor from surface i to surface j. Equations (65) to (69) show that there is no direct radiative exchange between different ground covers fractions. The walls receive a weighted average of the emitted ground radiation according to the surface cover fractions (f_{gv}, f_{gb}, f_{gi}). UT&C assumes homogeneous distribution of ground cover and hence, the view factors are not ground cover specific.

Combining Eq. (60) to (64) with Eq. (65) to (69) leads to:

$$B_{gv} = \varepsilon_{gv}\sigma T_{gv}^4 + (1-\varepsilon_{gv})\left(F_{gs}L\downarrow + F_{gw}B_{wsun} + F_{gw}B_{wshd}\right), \tag{70}$$

$$B_{gb} = \varepsilon_{gb}\sigma T_{gb}^4 + (1-\varepsilon_{gb})\left(F_{gs}L\downarrow + F_{gw}B_{wsun} + F_{gw}B_{wshd}\right), \tag{71}$$

$$B_{gi} = \varepsilon_{gi}\sigma T_{gi}^4 + (1-\varepsilon_{gi})\left(F_{gs}L\downarrow + F_{gw}B_{wsun} + F_{gw}B_{wshd}\right), \tag{72}$$

$$B_{wsun} = \varepsilon_{w}\sigma T_{wsun}^4 + (1-\varepsilon_{w})\left(F_{ws}L\downarrow + f_{gv}F_{wg}B_{gv} + f_{gb}F_{wg}B_{gb} + f_{gi}F_{wg}B_{gi} + F_{ww}B_{wshd}\right), \tag{73}$$

$$B_{wshd} = \varepsilon_{w}\sigma T_{wshd}^4 + (1-\varepsilon_{w})\left(F_{ws}L\downarrow + f_{gv}F_{wg}B_{gv} + f_{gb}F_{wg}B_{gb} + f_{gi}F_{wg}B_{gi} + F_{ww}B_{wsun}\right), \tag{74}$$

Rearranging Eq. (70) to (74) leads to:

$$B_{gv} - (1-\varepsilon_{gv})(F_{gw}B_{wsun} + F_{gw}B_{wshd}) = \varepsilon_{gv}\sigma T_{gv}^4 + (1-\varepsilon_{gv})F_{gs}L\downarrow, \tag{75}$$

$$B_{gb} - (1-\varepsilon_{gb})(F_{gw}B_{wsun} + F_{gw}B_{wshd}) = \varepsilon_{gb}\sigma T_{gb}^4 + (1-\varepsilon_{gb})F_{gs}L\downarrow, \tag{76}$$

$$B_{gi} - (1-\varepsilon_{gi})(F_{gw}B_{wsun} + F_{gw}B_{wshd}) = \varepsilon_{gi}\sigma T_{gi}^4 + (1-\varepsilon_{gi})F_{gs}L\downarrow, \tag{77}$$

$$B_{wsun} - (1-\varepsilon_{w})(f_{gv}F_{wg}B_{gv} + f_{gb}F_{wg}B_{gb} + f_{gi}F_{wg}B_{gi} + F_{ww}B_{wshd}) = \varepsilon_{w}\sigma T_{wsun}^4 + (1-\varepsilon_{w})F_{ws}L\downarrow, \tag{78}$$

$$B_{wshd} - (1-\varepsilon_{w})(f_{gv}F_{wg}B_{gv} + f_{gb}F_{wg}B_{gb} + f_{gi}F_{wg}B_{gi} + F_{ww}B_{wsun}) = \varepsilon_{w}\sigma T_{wshd}^4 + (1-\varepsilon_{w})F_{ws}L\downarrow, \tag{79}$$

The system of equations (Eq. (75) to (79)) can be written in matrix notation as:

$$T_{ij}B_i = C_i, \tag{80}$$

where:

$$C_i = \begin{bmatrix} C_{gv}(\varepsilon_{gv}\sigma T_{gv}^4 + (1-\varepsilon_{gv})F_{gs}L\downarrow) \\ C_{gb}(\varepsilon_{gb}\sigma T_{gb}^4 + (1-\varepsilon_{gb})F_{gs}L\downarrow) \\ C_{gi}(\varepsilon_{gi}\sigma T_{gi}^4 + (1-\varepsilon_{gi})F_{gs}L\downarrow) \\ \varepsilon_{w}\sigma T_{wsun}^4 + (1-\varepsilon_{w})F_{ws}L\downarrow \\ \varepsilon_{w}\sigma T_{wshd}^4 + (1-\varepsilon_{w})F_{ws}L\downarrow \end{bmatrix}, \qquad B_i = \begin{bmatrix} B_{gv} \\ B_{gb} \\ B_{gi} \\ B_{wsun} \\ B_{wshd} \end{bmatrix}, \tag{81}$$

$$T_{ij} = \begin{bmatrix} 1 & 0 & 0 & & \\ 0 & 1 & 0 & & \\ 0 & 0 & 1 & & \\ -C_{gv}f_{gv}(1-\varepsilon_{w})F_{wg} & -C_{gb}f_{gb}(1-\varepsilon_{w})F_{wg} & -C_{gi}f_{gi}(1-\varepsilon_{w})F_{wg} & & \\ -C_{gv}f_{gv}(1-\varepsilon_{w})F_{wg} & -C_{gb}f_{gb}(1-\varepsilon_{w})F_{wg} & -C_{gi}f_{gi}(1-\varepsilon_{w})F_{wg} & & \end{bmatrix}$$

$$\begin{bmatrix} -C_{gv}(1-\varepsilon_{gv})F_{gw} & -C_{gv}(1-\varepsilon_{gv})F_{gw} \\ -C_{gb}(1-\varepsilon_{gb})F_{gw} & -C_{gb}(1-\varepsilon_{gb})F_{gw} \\ -C_{gi}(1-\varepsilon_{gi})F_{gw} & -C_{gi}(1-\varepsilon_{gi})F_{gw} \\ 1 & -(1-\varepsilon_{w})F_{ww} \\ -(1-\varepsilon_{w})F_{ww} & 1 \end{bmatrix}, \tag{82, 83}$$

C_{gv}, C_{gb}, and C_{gi} are logical factors accounting for the presence ($C_{gi} = 1$) or absence ($C_{gi} = 0$) of a ground cover fraction.

The outgoing longwave radiation of surface i, B_i [W m^{-2}], is calculated with matrix inversion as:

$$B_i = [T_{ij}]^{-1} C_i \,, \tag{84}$$

Subsequently, the incoming Λ_i [W m^{-2}] and net absorbed Q_i [W m^{-2}] longwave radiation are calculated according to Eq. (58) and (59).

The matrices used to describe the system of equations solving infinite longwave reflections in an urban canyon with trees are:

$$T_{ij} B_i = C_i \,, \tag{85}$$

where:

$$C_i = \begin{bmatrix} C_{gv}(\varepsilon_{gv}\sigma T_{gv}^4 + (1-\varepsilon_{gv})F_{gs}^t L\downarrow) \\ C_{gb}(\varepsilon_{gb}\sigma T_{gb}^4 + (1-\varepsilon_{gb})F_{gs}^t L\downarrow) \\ C_{gi}(\varepsilon_{gi}\sigma T_{gi}^4 + (1-\varepsilon_{gi})F_{gs}^t L\downarrow) \\ \varepsilon_w \sigma T_{wsun}^4 + (1-\varepsilon_w)F_{ws}^t L\downarrow \\ \varepsilon_w \sigma T_{wshd}^4 + (1-\varepsilon_w)F_{ws}^t L\downarrow \\ \varepsilon_t \sigma T_t^4 + (1-\varepsilon_t)F_{ts}^t L\downarrow \end{bmatrix}, \qquad B_i = \begin{bmatrix} B_{gv} \\ B_{gb} \\ B_{gi} \\ B_{wsun} \\ B_{wshd} \\ B_t \end{bmatrix}, \tag{86}$$

$$T_{ij} = \begin{bmatrix} 1 & 0 & 0 \\ 0 & 1 & 0 \\ 0 & 0 & 1 \\ -C_{gv}f_{gv}(1-\varepsilon_w)F_{wg}^t & -C_{gb}f_{gb}(1-\varepsilon_w)F_{wg}^t & -C_{gi}f_{gi}(1-\varepsilon_w)F_{wg}^t \\ -C_{gv}f_{gv}(1-\varepsilon_w)F_{wg}^t & -C_{gb}f_{gb}(1-\varepsilon_w)F_{wg}^t & -C_{gi}f_{gi}(1-\varepsilon_w)F_{wg}^t \\ -C_{gv}f_{gv}(1-\varepsilon_t)F_{tg}^t & -C_{gb}f_{gb}(1-\varepsilon_t)F_{tg}^t & -C_{gi}f_{gi}(1-\varepsilon_t)F_{tg}^t \end{bmatrix} \tag{87}$$

$$\begin{bmatrix} -C_{gv}(1-\varepsilon_{gv})F_{gw}^t & -C_{gv}(1-\varepsilon_{gv})F_{gw}^t & -C_{gv}(1-\varepsilon_{gv})F_{gt}^t \\ -C_{gb}(1-\varepsilon_{gb})F_{gw}^t & -C_{gb}(1-\varepsilon_{gb})F_{gw}^t & -C_{gv}(1-\varepsilon_{gv})F_{gt}^t \\ -C_{gi}(1-\varepsilon_{gi})F_{gw}^t & -C_{gi}(1-\varepsilon_{gi})F_{gw}^t & -C_{gv}(1-\varepsilon_{gv})F_{gt}^t \\ 1 & -(1-\varepsilon_w)F_{ww}^t & -(1-\varepsilon_w)F_{wt}^t \\ -(1-\varepsilon_w)F_{ww}^t & 1 & -(1-\varepsilon_w)F_{wt}^t \\ -(1-\varepsilon_t)F_{tw}^t & -(1-\varepsilon_t)F_{tw}^t & 1-(1-\varepsilon_t)F_{tt}^t \end{bmatrix}, \tag{88}$$

where F_{ij}^t [$-$] is the view factor from surface i to surface j for an urban canyon with trees. The subscripts $_{gv}$, $_{gb}$, $_{gi}$, $_{wsun}$, $_{wshd}$, $_t$ denote vegetated ground, bare ground, impervious ground, sunlit wall, shaded wall, and trees, respectively.

1.2.4 Energy conservation

The longwave radiation energy conservation can be calculated from the perspective of the urban surfaces $EB_{L,surf}$ [W m^{-2}] and from the perspective of the urban canyon $EB_{L,can}$ [W m^{-2}]. This directionality is important as explained in Sect. 1.1.8.

$$EB_{L,surf} = \sum_i L_{in,i} \frac{f_i A_i}{A_g} - \sum_i L_{net,i} \frac{f_i A_i}{A_g} - \sum_i L_{out,i} \frac{f_i A_i}{A_g} \ , \tag{89}$$

$$EB_{L,can} = L\downarrow - \sum_i L_{net,i} \frac{f_i A_i}{A_g} - \sum_i L_{out,i} f_i F_{si}^{(t)} \ , \tag{90}$$

where $L_{in,i}$ [W m^{-2}] is the incoming, $L_{out,i}$ [W m^{-2}] the outgoing, and $L_{net,i}$ [W m^{-2}] the net absorbed longwave radiation of surface i. A_i is the area of surface i, A_g the total ground area equal to the canyon width, f_i the ground cover fraction ($f_i = 1$ if i is wall or tree), $F_{si}^{(t)}$ [$-$] the sky-view factor of each surface i, and $L\downarrow$ [W m^{-2}] the incoming longwave radiation from the atmosphere to the urban canyon.

1.3 View factor calculation

1.3.1 Analytical solution

The view factors F_{ij} [$-$] for an infinite urban canyon without trees can be calculated with the following analytically derived equations (Sparrow and Cess, 1970; Masson, 2000; Harman, 2003; Oleson et al., 2007; Park and Lee, 2008; Ryu et al., 2011; Wang et al., 2013):

$$F_{sg} = F_{gs} = \sqrt{1 + \left(\frac{h_{can}}{w_{can}}\right)^2} - \frac{h_{can}}{w_{can}} \ , \tag{91}$$

$$F_{ww} = \sqrt{1 + \left(\frac{w_{can}}{h_{can}}\right)^2} - \frac{w_{can}}{h_{can}} \ , \tag{92}$$

$$F_{wg} = F_{ws} = 0.5\,(1 - F_{ww}) \ , \tag{93}$$

$$F_{gw} = 0.5\,(1 - F_{gs}) \ , \tag{94}$$

where w_{can} = 1 [$-$] is the normalized canyon width. The subscripts $_s$, $_g$, $_w$ denote sky, ground, and wall, respectively. The view factors F_{ij} [$-$] are directional so that the incoming flux density onto surface i $\Lambda_{i(j)}$ [$W\ m^{-2}$] originating from surface j B_j [W m^{-2}] is (Harman, 2003):

$$\Lambda_{i(j)} = F_{ij} B_j \ , \tag{95}$$

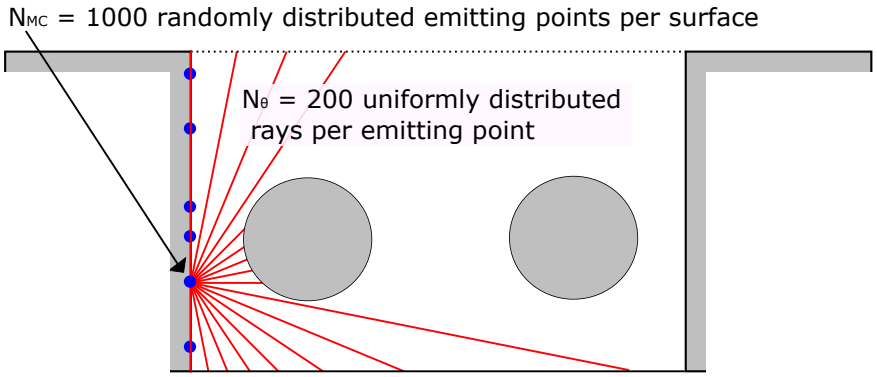

Figure 3. Representation of a 2 dimensional Monte Carlo ray tracing algorithm in an urban canyon with 2 trees.

The view factors F_{ij} $[-]$ fulfill the following three conditions (Wang, 2014): The self-view factor of a flat surface F_{ii} $[-]$ must be zero (Eq. (96)), energy must be conserved (Eq. (97)), and view factors are reciprocal (Eq. (98)).

$$F_{ii} = 0 \ , \tag{96}$$

$$\sum_{j=1}^{N} F_{ij} = 1 \ , \tag{97}$$

$$A_i F_{ij} = A_j F_{ji} \ , \tag{98}$$

A_i and A_j are the area of surface i and surface j.

1.3.2 Monte Carlo Ray Tracing

The view factors F_{ij}^{t} $[-]$ for an urban canyon with trees are calculated with a Monte Carlo ray tracing algorithm (Fig. 3). UT&C includes a simplified two dimensional Monte Carlo ray tracing code similar to the methods described by Wang (2014) and Frank et al. (2016). The Monte Carlo ray tracing algorithm does a probabilistic sampling of all rays emitted by surface i. The relative frequency of rays emitted by surface i that hit surface j is an estimation of the view factor F_{ij} (Frank et al., 2016). On each surface i, a large number N_{MC}, of randomly distributed emitting points are selected. The emitting coordinates on each canyon surface are defined as:

$$x_{g,e} = w_{can} \ R_{N_{MC}} \ , \tag{99}$$

$$z_{w,e} = h_{can} \ R_{N_{MC}} \ , \tag{100}$$

$$x_{t,e} = r_{tree} \ cos(2\pi R_{N_{MC}}) \ , \tag{101}$$

$$z_{t,e} = r_{tree} \ sin(2\pi R_{N_{MC}}) \ , \tag{102}$$

where $x_{g,e}$ is the x-coordinate of the emitting points on the ground and sky surfaces, $z_{w,e}$ the z-coordinate of the emitting points on the wall, and $x_{t,e}$ and $z_{t,e}$ are the (x,z)-coordinates of the emitting points on the circular tree surface, and $R_{N_{MC}}$ are

N_{MC} uniformly distributed random ~~variables~~ numbers in the intervall [0,1]. The direction of the emitted ray at the emitting point can be defined with the polar angle θ_{MC} [rad] as:

$$\theta_{MC} = \arcsin R_{N_\theta} \ , \tag{103}$$

where R_{N_θ} are N_θ uniformely distributed ~~variables~~ numbers in the intervall [0,1]. The polar angle θ_{MC} [rad] is defined to be zero perpendicular to the emitting surface for the ground, sky and wall and perpendicular to the tangent of the emitting point on the tree circle. The intersection of an emitted ray with a canyon surface can be calculated as the line intersection between ray and surface defining a maximum ray distance. The first surface hit by a ray is counted towards the view factor calculation. Subsequently, the view factor F_{ij}^t is calculated as:

$$F_{ij}^t = \frac{N_{rays,j}}{N_{rays,tot}} \ , \tag{104}$$

$$F_{ii}^t = 0 \ , \tag{105}$$

where $N_{rays,j}$ are the number of rays hitting surface j, and $N_{rays,tot}$ the total number of rays emitted. The self view factor is corrected to be 0 (Eq. (105)). The view factors do not necessarily fulfill the reciprocity criterion (Eq. (98)) ~~right after~~ as obtained from the Monte Carlo ray tracing, due to the finite number of rays emitted in the algorithm. In a subsequent step, the computed view factors are corrected to be reciprocal as to meet energy conservation in the infinite reflection scheme. The corrections applied in UT&C are as follows:

~~Urban canyon without trees~~

$$F_{gs} = f(Monte\ Carlo\ ray\ tracing) \ ,$$

$$F_{gw} = 0.5(1 - F_{gs}) \ ,$$

$$F_{sg} = F_{gs} \ ,$$

$$F_{sw} = F_{gw} \ ,$$

$$F_{wg} = F_{gw} w_{can}/h_{can} \ ,$$

$$F_{ws} = F_{sw} w_{can}/h_{can} \ ,$$

$$F_{ww} = 1 - F_{wg} - F_{ws} \ ,$$

~~Urban canyon~~ Urban canyon with trees

$$F_{gs}^{t} = f(Monte\ Carlo\ ray\ tracing)\ , \tag{106}$$

$$F_{gt}^{t} = f(Monte\ Carlo\ ray\ tracing)\ , \tag{107}$$

$$F_{gw}^{t} = 0.5(1 - F_{gs}^{t} - F_{gt}^{t})\ , \tag{108}$$

$$F_{st}^{t} = f(Monte\ Carlo\ ray\ tracing)\ , \tag{109}$$

$$F_{sg}^{t} = F_{gs}^{t}\ , \tag{110}$$

$$F_{sw}^{t} = 0.5(1 - F_{sg}^{t} - F_{st}^{t})\ , \tag{111}$$

$$F_{wt}^{t} = f(Monte\ Carlo\ ray\ tracing)\ , \tag{112}$$

$$F_{wg}^{t} = F_{gw}^{t} w_{can}/h_{can}\ , \tag{113}$$

$$F_{ws}^{t} = F_{sw}^{t} w_{can}/h_{can}\ , \tag{114}$$

$$F_{ww}^{t} = 1 - F_{wg}^{t} - F_{ws}^{t} - F_{wt}^{t}\ , \tag{115}$$

$$F_{ts}^{t} = F_{st}^{t} w_{can}/A_{tree}\ , \tag{116}$$

$$F_{tg}^{t} = F_{gt}^{t} w_{can}/A_{tree}\ , \tag{117}$$

$$F_{tw}^{t} = F_{wt}^{t} h_{can}/A_{tree}\ , \tag{118}$$

$$F_{tt}^{t} = 1 - F_{ts}^{t} - 2F_{tw}^{t} - F_{tg}^{t}\ , \tag{119}$$

where $A_{tree} = 2(2\pi r_{tree})$ $[-]$ is the normalized tree surface area. The Monte Carlo ray tracing algorithm implemented in UT&C is able to reproduce the analytical view factors for an urban canyon without trees (Fig. 4). The number of emitting points $N_{MC} = 1000$ and the number of emitted rays per emitting point $N_{rays} = 200$ show a sufficient approximation to the analytical solution (Fig. 4). Note that the tree canopy is assumed impermeable in the view factor calculation as well as in the calculation of infinite reflections within the urban canyon. This could lead to a slight overestimation of absorbed radiation by the tree canopy.

2 Turbulent fluxes

The total flux of sensible H_{urb} $[\mathrm{W\ m^{-2}}]$ and latent λE_{urb} $[\mathrm{W\ m^{-2}}]$ heat from the urban environment is calculated as the area weighted average of turbulent roof and canyon fluxes:

$$H_{urb} = f_r H_r + f_{can} H_{can}\ , \tag{120}$$

$$\lambda E_{urb} = f_r \lambda E_r + f_{can} \lambda E_{can}\ , \tag{121}$$

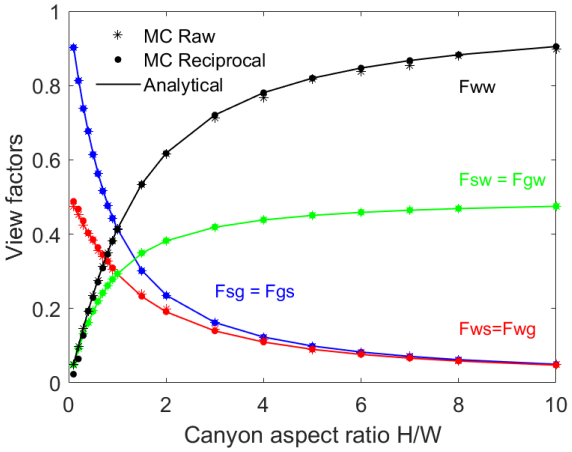

Figure 4. View factors calculated with the Monte Carlo ray tracing algorithm implemented in UT&C (MC Raw) corrected for reciprocity (MC Reciprocal) and compared with the analytical solution (Analytical) of the different canyon surfaces as a function of canyon aspect ratio H/W. The supscripts g, w and s denote ground, wall and sky, respectively.

where f_r $[-]$ is the roof plan area fraction and f_{can} $[-]$ the canyon plan area fraction. The total sensible and latent roof heat flux is calculated as:

$$H_r = f_{r,imp} H_{r,imp} + f_{r,veg} H_{r,veg} \ , \tag{122}$$

$$\lambda E_r = f_{r,imp} \lambda E_{r,imp} + f_{r,veg} \lambda E_{r,veg} \ , \tag{123}$$

where $f_{r,imp}$ $[-]$ is the impervious and $f_{r,veg}$ $[-]$ the vegetated roof fraction. The total sensible and latent canyon heat flux is calculated as:

$$H_{can} = w_{can} H_g + h_{can} H_{w,sun} + h_{can} H_{w,shd} + 4 r_{tree} H_{tree} + Q_f \ , \tag{124}$$

$$\lambda E_{can} = w_{can} \lambda E_g + h_{can} \lambda E_{w,sun} + h_{can} \lambda E_{w,shd} + 4 r_{tree} \lambda E_{tree} \ , \tag{125}$$

where Q_f $[\mathrm{W\ m^{-2}}]$ is the anthropogenic heat input. The sensible and latent heat fluxes of the tree, H_{tree} and λE_{tree}, are calculated as Watts per horizontal tree area. Therefore, H_{tree} and λE_{tree} need to be multiplied by $4 r_{tree}$ to rescale to the canyon extent. The total sensible and latent ground heat flux is calculated as:

$$H_g = f_{g,imp} H_{g,imp} + f_{g,bare} H_{g,bare} + f_{g,veg} H_{g,veg} \ , \tag{126}$$

$$\lambda E_g = f_{g,imp} \lambda E_{g,imp} + f_{g,bare} \lambda E_{g,bare} + f_{g,veg} \lambda E_{g,veg} \ , \tag{127}$$

where $f_{g,imp}$ $[-]$ is the impervious, $f_{g,bare}$ $[-]$ the bare, and $f_{g,veg}$ $[-]$ the vegetated ground fraction. The calculation of the individual sensible and latent heat fluxes are described in Sect. 2.1.1 to 2.1.5 and 2.2.1 to 2.2.5.

2.1 Sensible heat

The sensible heat flux from any surface i to a generic air mass near the surface, H_i [W m^{-2}], is calculated as (Shuttleworth, 2012):

$$H_i = \rho_a C_p \frac{(T_i - T_a)}{\sum r_j} \ , \tag{128}$$

where ρ_a [kg m^{-3}] is the air density (Eq. (130)), C_p [J kg^{-1} K^{-1}] the specific heat capacity of air at constant pressure (Eq. (129)), T_i [K] the temperature of surface i, T_a [K] the air temperature, and $\sum r_j$ [s m^{-1}] the sum of resistances j to the turbulent transport of sensible heat from the surface i to the air layer. A detailed description of the resistance calculations is described in Sect. 3.3 to 3.6. The specific heat capacity of air at constant pressure C_p [J kg^{-1} K^{-1}] is calculated as:

$$C_p = 1005 + \frac{(T_a + 23.15)^2}{3364} \ , \tag{129}$$

The air density ρ_a [kgm^{-3}] is calculated as:

$$\rho_a = \frac{P_a}{287.04 T_a}(1 - \frac{e_a}{P_a}(1 - 0.622)) \ , \tag{130}$$

where P_a [Pa] is the air pressure, and e_a [Pa] the vapour pressure.

2.1.1 Sensible heat: Roof

The sensible heat flux from the impervious $H_{r,imp}$ [W m^{-2}], and vegetated roof fraction $H_{r,veg}$ [W m^{-2}] to the air at atmospheric reference level is calculated as:

$$H_{r,imp} = \rho_a C_p \frac{(T_{r,imp} - T_{atm})}{r_{ah,r}} \ , \tag{131}$$

$$H_{r,veg} = \rho_a C_p \ \frac{(T_{r,veg} - T_{atm})}{r_{ah,r} + \frac{r_{b,r}}{2(LAI_r + SAI_r)}} \ , \tag{132}$$

where $T_{r,imp}$ [K], $T_{r,veg}$ [K], and T_{atm} [K] are the surface temperatures of the impervious and vegetated roof fraction, and the air temperature at atmospheric reference height. The resistance $r_{ah,r}$ [s m^{-1}] denotes the aerodynamic resistance from the roof to the atmospheric reference height (Sect. 3.3.1), and $r_{b,r}$ [s m^{-1}] the leaf boundary resistance of the roof vegetation (Sect. 3.4). The term LAI_r [$-$] and SAI_r [$-$] are, respectively, the leaf and stem area index of the roof vegetation. Note, both leaf sides interact in the sensible heat exchange (Fatichi et al., 2012a, b, c).

2.1.2 Sensible heat: Ground

The sensible heat flux from the impervious $H_{g,imp}$ [W m^{-2}], bare $H_{g,bare}$ [W m^{-2}], and vegetated ground fraction $H_{g,veg}$ [W m^{-2}] to the canyon air is calculated as:

$$H_{g,imp} = \rho_a C_p \frac{(T_{g,imp} - T_{can})}{r_{ah,g}} \,, \tag{133}$$

$$H_{g,bare} = \rho_a C_p \frac{(T_{g,bare} - T_{can})}{r_{ah,g}} \,, \tag{134}$$

$$H_{g,veg} = \rho_a C_p \frac{(T_{g,veg} - T_{can})}{r_{ah,g} + \frac{r_{b,g,veg}}{2(LAI_{g,veg}+SAI_{g,veg})}} \,, \tag{135}$$

where $T_{g,imp}$ [K], $T_{g,bare}$ [K], $T_{g,veg}$ [K], and T_{can} [K] are the surface tempertures of the impervious, bare and vegetated ground fraction, and the air temperature at canyon ~~calculation~~ reference height ($Z_{calc} = h_{disp,can} + z_{0m,can}$, see Sect. 3.2). The resistance $r_{ah,g}$ [s m^{-1}] denotes the aerdoynamic resistance from the ground to the canyon ~~calculation~~ reference height (Sect. 3.3.2), and $r_{b,g,veg}$ [s m^{-1}] the leaf boundary resistance of the ground vegetation (Sect. 3.4). $LAI_{g,veg}$ [$-$] is the leaf and $SAI_{g,veg}$ [$-$] the stem area index of the ground vegetation. Note, both leave sides contribute to the sensible heat exchange (Fatichi et al., 2012a, b, c).

2.1.3 Sensible heat: Trees

The sensible heat flux from the trees H_{tree} [W m^{-2} horizontal tree area] to the canyon air is calculated as:

$$H_{tree} = \rho_a C_p \frac{(T_{tree} - T_{can})}{r_{ah,tree} + \frac{r_{b,tree}}{2(LAI_{tree}+SAI_{tree})}} \,, \tag{136}$$

where T_{tree} [K] and T_{can} [K] are the tree surface temperature and the air temperature at canyon ~~calculation~~ reference height ($Z_{calc} = h_{disp,can} + z_{0m,can}$, Sect. 3.2). LAI_{tree} [$-$] is the leaf and SAI_{tree} [$-$] the stem area index of the trees. The resistance $r_{ah,tree}$ [s m^{-1}] denotes the aerdoynamic resistance from the tree to the canyon ~~calculation~~ reference height (Sect. 3.3.2), and $r_{b,tree}$ [s m^{-1}] the leaf boundary resistance of the tree (Sect. 3.4).

2.1.4 Sensible heat: Wall

The canyon air is divided into two layers and the sensible heat flux from the wall contributing to the canyon air temperature at height $Z_p = 2$ m and at height $Z_{calc} = h_{disp,can} + z_{0m,can}$ ($h_{disp,can}$ [m] is the canyon displacement height and $z_{0m,can}$ [m] the canyon roughness length, see Sect. 3.2) are calculated individually (Fig. 5). The height of the first layer is ~~$2Z_p$~~ $min(2Z_p, H_{can})$ and the height of the second layer ~~$H_{can} - 2Z_p$~~ $max(H_{can} - 2Z_p, 0)$. The total sensible heat flux from the sunlit wall $H_{w,sun}$ [W m^{-2}], and shaded wall $H_{w,shd}$ [W m^{-2}] to the canyon air is calculated as the area weighted average of the sensible heat fluxes from wall layer 1 and wall layer 2.

$$H_{w,sun} = \frac{min(2Z_p, H_{can})}{H_{can}} H_{w1,sun} + \frac{max(H_{can} - 2Z_p, 0)}{H_{can}} H_{w2,sun} \,, \tag{137}$$

$$H_{w,shd} = \frac{min(2Z_p, H_{can})}{H_{can}} H_{w1,shd} + \frac{max(H_{can} - 2Z_p, 0)}{H_{can}} H_{w2,shd} \,, \tag{138}$$

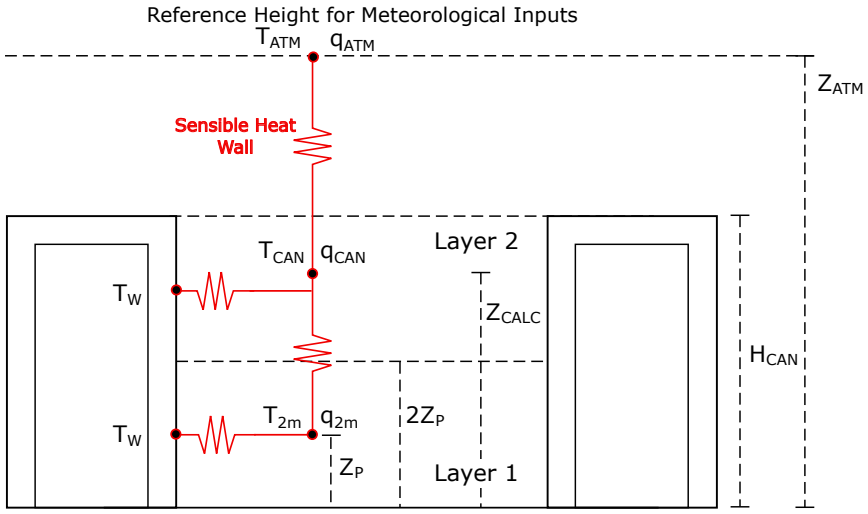

Figure 5. Sensible wall heat fluxes and canyon air layers. T_{2m} and q_{2m} are the 2 m air temperature and humidity calculated at height $Z_p = 2$ m. T_{can} and q_{can} are the air temperature and humidity at canyon ~~calculation~~ reference height Z_{calc}. The thickness of the first wall layer is ~~$2Z_p$~~ $min(2Z_p, H_{can})$ and the thickness of the second wall layer is ~~$H_{can} - 2Z_p$~~ $max(H_{can} - 2Z_p, 0)$. The variables T_{2m} and q_{2m} are calculated at mid height of the first wall layer while T_{can} and q_{can} do not necessarily correspond to the mid height of the second wall layer. The horizontal resistances from wall to canyon air for both canyon air layers are calculated at their mid heights and their subsequent vertical aerodynamic resistance is applied to reach Z_{calc}.

where $Z_p = 2$ [m] and H_{can} [m] is the canyon height. $H_{w1,sun}$ and $H_{w2,sun}$ [W m^{-2}] denote the sensible heat flux from sunlit wall layer 1 and layer 2. Similarly, $H_{w1,shd}$ and $H_{w2,shd}$ [W m^{-2}] denote the sensible heat flux from shaded wall layer 1 and layer 2. The sensible heat fluxes $H_{w1,sun}$, $H_{w2,sun}$, $H_{w1,shd}$, and $H_{w2,shd}$ are calculated as follows:

$$H_{w1,sun} = \rho_a C_p \frac{(T_{w,sun} - T_{can})}{r_{w1} + r_{ah1,w}} , \tag{139}$$

$$H_{w1,shd} = \rho_a C_p \frac{(T_{w,shd} - T_{can})}{r_{w1} + r_{ah1,w}} , \tag{140}$$

$$H_{w2,sun} = \rho_a C_p \frac{(T_{w,sun} - T_{can})}{r_{w2} + r_{ah2,w}} , \tag{141}$$

$$H_{w2,shd} = \rho_a C_p \frac{(T_{w,shd} - T_{can})}{r_{w2} + r_{ah2,w}} , \tag{142}$$

where $T_{w,sun}$ [K], $T_{w,shd}$ [K], and T_{can} [K] are the sunlit and shaded wall surface temperatures and the air temperature at canyon ~~calculation~~ reference height ($Z_{calc} = h_{disp,can} + z_{0m,can}$, Sect. 3.2). The resistances r_{w1} and r_{w2} [s m^{-1}] are the horizontal aerodynamic resistance from the wall surface to the canyon air at mid height of layer 1 and layer 2 (Sect. 3.3.3). The resistances $r_{ah1,w}$ and $r_{ah2,w}$ [s m^{-1}] are the vertical aerodynamic resistance from the mid height of layer 1 and layer 2 to the canyon air at calculation height (Sect. 3.3.2).

2.1.5 Sensible heat: Canyon

The total sensible heat flux from canyon air to atmospheric reference height H_{can} [W m^{-2}] is calculated as:

$$H_{can} = \rho_a C_p \frac{(T_{can} - T_{atm})}{r_{ah,c}} \ , \tag{143}$$

where T_{can} [K] is the canyon air temperature, T_{atm} [K] the temperature at atmospheric reference height, and $r_{ah,c}$ [s m^{-1}] the aerodynamic resistance from canyon air at calculation height to the atmospheric reference height (Sect. 3.3.1).

2.2 Latent heat

The latent heat flux from any surface i to a generic mass of air above/near the surface λE_i [W m^{-2}] is calculated as (Shuttleworth, 2012):

$$\lambda E_i = \lambda \rho_a \frac{(q_{sat,(T_i)} - q_a)}{\sum r_j} \ , \tag{144}$$

where λ [J kg^{-1}] is the latent heat of vaporization (Eq. (145)), ρ_a [kg m^{-3}] the ~~dry~~ air density (Eq. (130)), $q_{sat,(T_i)}$ [$-$] the specific humidity of surface i at saturation (Eq. (146)), q_a [$-$] the specific humdity of the air (Eq. (148)), and $\sum r_j$ [s m^{-1}] the sum of resistances j to the turbulent transport of latent heat from the surface i to the air layer. The latent heat of vaporization λ [J kg^{-1}] is calculated as (Shuttleworth, 2012):

$$\lambda = 1000(2501.3 - 2.351 T_a) \ , \tag{145}$$

where T_a [°C] is the air temperature. The specific humidity of surface i at saturation $q_{sat,(T_i)}$ [$-$] is calculated as a function of surface temperature T_i (Shuttleworth, 2012):

$$q_{sat,(T_i)} = \frac{0.622 e_{sat,(T_i)}}{P_a - 0.378 e_{sat,(T_i)}} \ , \tag{146}$$

where P_a [Pa] is the air pressure, and $e_{sat,(T_i)}$ [Pa] the saturation vapour pressure at temperature T_i [°C]. The saturation vapour pressure is calculated as (Shuttleworth, 2012):

$$e_{sat,(T_i)} = 611 e^{\frac{17.27 T_i}{237.3 + T_i}} \ , \tag{147}$$

The specific humidity of the air q_a [$-$] is calculated as a function of vapour pressure e_a [Pa] (Shuttleworth, 2012):

$$q_a = \frac{0.622 e_a}{P_a - 0.378 e_a} \ , \tag{148}$$

2.2.1 Latent heat: Roof

UT&C calculates evaporation from ponding water on impervious roof $E_{r,imp}$, evaporation from intercepted water on vegetation canopy $E_{r,veg,in}$, soil evaporation $E_{r,veg,soil}$, and transpiration from sunlit $TE_{r,veg,sun}$ and shaded $TE_{r,veg,shd}$ roof

vegetation canopy. All roof evapotranspiration fluxes have the unit of $[\mathrm{kg\ m^{-2}\ s^{-1}}]$ and are calculated from the roof level to the atmospheric reference height as:

$$E_{r,imp} = \frac{\rho_a(q_{sat,(T_{r,imp})} - q_{atm})}{r_{ah,r}} \ , \tag{149}$$

$$E_{r,veg} = E_{r,veg,int} + E_{r,veg,soil} + TE_{r,veg} \ , \tag{150}$$

$$E_{r,veg,int} = \frac{\rho_a(q_{sat,(T_{r,veg})} - q_{atm})}{r_{ah,r} + \frac{r_{b,r}}{(LAI_r + SAI_r)d_{w,r}}} \ , \tag{151}$$

$$E_{r,veg,soil} = \frac{\rho_a(\hat{\alpha}_{soil,r}\ q_{sat,(T_{r,veg})} - q_{atm})}{r_{ah,r} + r_{soil,r}} \ , \tag{152}$$

$$TE_{r,veg,sun} = \frac{\rho_a(q_{sat,(T_{r,veg})} - q_{atm})}{r_{ah,r} + \frac{r_{b,r}}{LAI_r F_{sun,r}(1-d_{w,r})} + \frac{r_{s,r,sun}}{LAI_r F_{sun,r}(1-d_{w,r})}} \ , \tag{153}$$

$$TE_{r,veg,shd} = \frac{\rho_a(q_{sat,(T_{r,veg})} - q_{atm})}{r_{ah,r} + \frac{r_{b,r}}{LAI_r F_{shd,r}(1-d_{w,r})} + \frac{r_{s,r,shd}}{LAI_r F_{shd,r}(1-d_{w,r})}} \ , \tag{154}$$

$$TE_{r,veg} = TE_{r,veg,sun} + TE_{r,veg,shd} \ , \tag{155}$$

where q_{atm} $[-]$ is the specific humidity at atmospheric reference height, $r_{ah,r}$ $[\mathrm{s\ m^{-1}}]$ the aerodynamic resistance from roof to atmospheric reference height (Sect. 3.3.1), $r_{b,r}$ $[\mathrm{s\ m^{-1}}]$ the leaf boundary layer resistance of roof vegetation (Sect. 3.4), $r_{soil,r}$ $[\mathrm{s\ m^{-1}}]$ the soil resistance (Sect. 3.5), and $r_{s,r,sun}$ and $r_{s,r,shd}$ $[\mathrm{s\ m^{-1}}]$ the stomata resistance of the sunlit and shaded vegetation canopy fraction (Sect. 3.6). The sunlit F_{sun} $[-]$ and shaded F_{shd} $[-]$ canopy fractions are calculated assuming exponential decay of direct beam radiation within the vegetation canopy where the light transmission coefficient $K_{opt} = 0.5$ is assumed constant for simplicity rather than calculated with more complex canopy radiation transfer models (Fatichi et al., 2012a, b, c):

$$F_{sun} = \frac{1}{LAI}\frac{1 - e^{(-K_{opt}LAI)}}{K_{opt}} \ , \tag{156}$$

$$F_{shd} = 1 - F_{sun} \ , \tag{157}$$

Evapotraspiration from canopy interception is calculated for the canopy fraction covered by intercepted water d_w $[-]$, whereas transpiration is calculated for the canopy fraction free of intercepted water $(1 - d_w)$ $[-]$. The canopy fraction covered by intercepted water d_w $[-]$ is calculated according to Deardorff (1978) as:

$$d_w = min\big[1, (In/In_{max})^{2/3}\big] \ , \tag{158}$$

where In [mm] is the intercepted water and In_{max} $[\mathrm{mm}]$ the maximum canopy interception capacity. The evaporation from canopy interception and ponding is eventually limited by the amount of water intercepted and ponding. The canopy transpiration and the evaporation from the first soil layer are controlled by stomata resistance and soil resistance, respectively.

2.2.2 Latent heat: Ground

UT&C calculates evaporation from ponding water on impervious ground $E_{g,imp}$, soil evaporation from bare soil $E_{g,bare,soil}$, evaporation from intercepted water on vegetation canopy $E_{g,veg,in}$, soil evaporation from ~~vegetated soil~~ soil underneath the vegetation $E_{r,veg,soil}$, and transpiration from sunlit $TE_{g,veg,sun}$ and shaded $TE_{g,veg,shd}$ ground vegetation canopy. All evapotranspiration fluxes have the unit of $[\mathrm{kg\ m^{-2}\ s^{-1}}]$ and are calculated from the ground to the canyon ~~calculation~~ reference height ($Z_{calc} = h_{disp,can} + z_{0m,can}$, Sect. 3.2) as follows:

$$E_{g,imp} = \frac{\rho_a (q_{sat,(T_{g,imp})} - q_{can})}{r_{ah,g}} \ , \tag{159}$$

$$E_{g,bare} = \frac{\rho_a (\hat{\alpha}_{soil,g}\ q_{sat,(T_{g,bare})} - q_{can})}{r_{ah,g} + r_{soil}} \ , \tag{160}$$

$$E_{g,veg} = E_{g,veg,int} + E_{g,veg,soil} + TE_{g,veg} \ , \tag{161}$$

$$E_{g,veg,int} = \frac{\rho_a (q_{sat,(T_{g,veg})} - q_{can})}{r_{ah,g} + \frac{r_{b,g,veg}}{(LAI_g + SAI_g) d_{w,g,veg}}} \ , \tag{162}$$

$$E_{g,veg,soil} = \frac{\rho_a (\hat{\alpha}_{soil}\ q_{sat,(T_{g,veg})} - q_{can})}{r_{ah,g} + r_{soil,g}} \ , \tag{163}$$

$$TE_{g,veg} = TE_{g,veg,sun} + TE_{g,veg,shd} \ , \tag{164}$$

$$TE_{g,veg,sun} = \frac{\rho_a (q_{sat,(T_{g,veg})} - q_{can})}{r_{ah,g} + \frac{r_{b,g}}{LAI_g F_{sun,g} (1 - d_{w,g})} + \frac{r_{s,g,sun}}{LAI_g F_{sun,g} (1 - d_{w,g})}} \ , \tag{165}$$

$$TE_{g,veg,shd} = \frac{\rho_a (q_{sat,(T_{g,veg})} - q_{can})}{r_{ah,g} + \frac{r_{b,g}}{LAI_g F_{shd,g} (1 - d_{w,g})} + \frac{r_{s,g,shd}}{LAI_g F_{shd,g} (1 - d_{w,g})}} \ , \tag{166}$$

where q_{can} $[-]$ is the specific humidity at canyon ~~calculation~~ reference height, $r_{ah,g}$ $[\mathrm{s\ m^{-1}}]$ the aerodynamic resistance from ground to canyon ~~calculation~~ reference height (Sect. 3.3.2), $r_{b,g}$ $[\mathrm{s\ m^{-1}}]$ the leaf boundary layer resistance (Sect. 3.4), $r_{soil,g}$ $[\mathrm{s\ m^{-1}}]$ the soil resistance (Sect. 3.5), and $r_{s,g,sun}$ and $r_{s,g,shd}$ $[\mathrm{s\ m^{-1}}]$ the stomata resistance of sunlit and shaded canopy fraction (Sect. 3.6), $\hat{\alpha}_{soil,g}$ $[-]$ the relative humidity in the soil pores (Sect. 3.5), $d_{w,g}$ $[-]$ the vegetation fraction covered by intercepted water (Eq. (158)), and $F_{sun,g}$ $[-]$ and $F_{shd,g}$ $[-]$ the sunlit and shaded vegetation canopy fraction (Eq. (156) and (157)). The evaporative fluxes from interception and ponding are eventually limited by the amount of water intercepted on the canopy and water ponding on the ground. In the case of ponding water, there is no soil resistance and the relative humidity $\hat{\alpha}$ $[-]$ is one.

2.2.3 Latent heat: Trees

UT&C calculates evaporation from intercepted water on the tree canopy $E_{tree,in}$, and transpiration from the sunlit $TE_{r,veg,sun}$ and shaded $TE_{r,veg,shd}$ tree canopy fraction. All evapotranspiration fluxes have the unit of $[\mathrm{kg\ m^{-2}\ horizontal\ tree\ area\ s^{-1}}]$

and are calculated from tree height to canyon ~~calculation~~ reference height ($h_{disp,can} + z_{0m,can}$, Sect. 3.2) as follows:

$$E_{tree} = E_{tree,int} + TE_t \ , \tag{167}$$

$$E_{tree,int} = \frac{\rho_a (q_{sat,(T_{tree})} - q_{can})}{r_{ah,t} + \frac{r_{b,t}}{(LAI_t + SAI_t) d_{w,t}}} \ , \tag{168}$$

$$TE_t = TE_{t,sun} + TE_{t,shd} \ , \tag{169}$$

$$TE_{t,sun} = \frac{\rho_a (q_{sat,(T_t)} - q_{can})}{r_{ah,t} + \frac{r_{b,t}}{LAI_t F_{sun,t} (1 - d_{w,t})} + \frac{r_{s,t,sun}}{LAI_t F_{sun,t} (1 - d_{w,t})}} \ , \tag{170}$$

$$TE_{t,shd} = \frac{\rho_a (q_{sat,(T_t)} - q_{can})}{r_{ah,t} + \frac{r_{b,t}}{LAI_t F_{shd,t} (1 - d_{w,t})} + \frac{r_{s,t,shd}}{LAI_t F_{shd,t} (1 - d_{w,t})}} \ , \tag{171}$$

where q_{can} $[-]$ is the specific humidity at canyon ~~calculation~~ reference height, $r_{ah,t}$ $[\mathrm{s\ m^{-1}}]$ the aerodynamic resistance from tree to canyon ~~calculation~~ reference height (Sect. 3.3.2), $r_{b,t}$ $[\mathrm{s\ m^{-1}}]$ the leaf boundary layer resistance (Sect. 3.4), and $r_{s,t,sun}$ and $r_{s,t,shd}$ $[\mathrm{s\ m^{-1}}]$ the stomata resistance of the sunlit and shaded tree canopy fraction (Sect. 3.6), $d_{w,t}$ $[-]$ the canopy fraction covered by intercepted water (Eq. (158)), and $F_{sun,t}$ $[-]$ and $F_{shd,t}$ $[-]$ the sunlit and shaded canopy fraction (Eq. (156) and (157)). The evaporative flux from interception is eventually limited by the amount of water intercepted on the tree canopy.

2.2.4 Latent heat: Wall

The latent heat fluxes from sunlit and shaded wall, $E_{w,sun}$ and $E_{w,sun}$, are assumed to be negligible and equal to zero ($E_{w,sun} = 0$ and $E_{w,shd} = 0$). This means that the current version of UT&C ~~does not include~~ cannot accomodate for green walls.

2.2.5 Latent heat: Canyon

The total latent heat flux from canyon air to atmospheric reference height E_{can} $[\mathrm{kg\ m^{-1}\ s^{-1}}]$ is calculated as follows:

$$E_{can} = \frac{\rho_a (q_{can} - q_{atm})}{r_{ah,c}} \ , \tag{172}$$

where q_{can} $[-]$ is the specific humidity at canyon ~~calculation~~ reference height, q_{atm} $[-]$ the specific humidity at atmospheric reference height, and $r_{ah,c}$ $[\mathrm{s\ m^{-1}}]$ the aerodynamic resistance from canyon air to the atmospheric reference height (Sect. 3.3.1).

2.3 2 m air temperature and humidity

The air temperature and canyon humidity are calculated at two heights, $Z_p = 2$ m and $Z_{calc} = h_{disp,can} + z_{0m,can}$ (Sect. 3.2). The variables T_{can} $[^\circ\mathrm{C}]$ and q_{can} $[-]$ refer to the air temperature and specific humidity at canyon ~~calculation~~ reference height Z_{calc}. The variables $T_{can,2m}$ $[^\circ\mathrm{C}]$ and $q_{can,2m}$ $[-]$ refer to the air temperature and specific humidity at a height of 2 m above the ground. A height of 2 m is often used for ~~urban~~ meteorological measurements and typically corresponds to the temperature and humidity felt by pedestrians.

T_{can} and q_{can} are calculated solving the following equations:

$$H_{can} = f_{g,imp}H_{g,imp} + f_{g,bare}H_{g,bare} + f_{g,veg}H_{g,veg} + h_1(H_{w1,sun} + H_{w1,shd}) + h_2(H_{w2,sun} + H_{w2,shd})$$
$$+ 4r_{tree}H_{tree} + Q_f \ , \quad (173)$$

$$LE_{can} = f_{g,imp}LE_{g,imp} + f_{g,bare}LE_{g,bare} + f_{g,veg}LE_{g,veg} + 4r_{tree}LE_{tree} \ , \quad (174)$$

Q_f [W m^{-2}] denotes the anthropogenic heat flux which is directly added to the energy balance of the canyon air. The calculation of T_{can} and q_{can} considers all sensible and latent heat fluxes from ground ~~fractions~~surfaces, trees, and wall layer 1 and 2.

The variables $T_{can,2m}$ and $q_{can,2m}$ are calculated solving the following equations:

$$H_{can,2m} = f_{g,imp}H_{g,imp,2m} + f_{g,bare}H_{g,bare,2m} + f_{g,veg}H_{g,veg,2m} + h_1(H_{w1,sun} + H_{w1,shd}) \ , \quad (175)$$

$$LE_{can,2m} = f_{g,imp}LE_{g,imp,2m} + f_{g,bare}LE_{g,bare,2m} + f_{g,veg}LE_{g,veg,2m} \ , \quad (176)$$

$H_{i,2m}$ and $LE_{i,2m}$ are calculated as described in Sect.2.1.2 to 2.1.5 and 2.2.2 to 2.2.5 replacing aerodynamic resistance $r_{ah,can}: \ f(h_{disp,can} + z_{0m,can})$ with aerodynamic resistance $r_{ah,2m}: \ f(2\ m)$, and T_{can} and q_{can} with $T_{can,2m}$ and $q_{can,2m}$. The heat fluxes from wall layer 2 and trees are not directly considered in the calculation of $T_{can,2m}$ and $q_{can,2m}$ but they play an indirect role through T_{can} and q_{can}.

3 Energy and mass transfer resistances

The turbulent mass and energy fluxes described in Sect. 2 to 2.3 are calculated with a set of resistances. These resistances parameterize different processes influencing the turbulent transport of water vapour and energy from the urban surface to the planetary boundary layer at reference height, Z_{atm} [m]. UT&C accounts for aerodynamic resistance r_{ah} above and within the canyon (Sect. 3.3, 3.3.1, 3.3.2 and 3.3.3), leaf boundary resistance r_b (Sect. 3.4), soil resistance r_{soil} (Sect. 3.5), and stomata resistance of sunlit and shaded leaves $r_{s,sun}$ and $r_{s,shd}$ (Sect. 3.6). The unit of resistance is the inverse of a velocity [s m^{-1}].

3.1 Wind profile

The wind speed profile $u(z)$ is assumed to be logarithmic above the urban canopy ($Z_{atm} \geq z \geq H_{can}$), exponential within the urban canyon ($H_{can} \geq z \geq Z_{can,ref}$), and logarithmic again close to the ground surface ($Z_{can,ref} \geq z$) (Masson, 2000; Mahat et al., 2013) and is calculated as (Fig. 6):

$$u(z) = \frac{1}{k}u^*_{atm}\ln\left(\frac{z - h_{d,can}}{z_{om,can}}\right) \qquad \text{for } Z_{atm} \geq z \geq H_{can} \ , \quad (177)$$

$$u(z) = u_{H_{can}}\exp\left(-\hat{\beta}(1 - \frac{z}{H_{can}})\right) \quad \text{for } H_{can} \geq z \geq Z_{can,ref} \ , \quad (178)$$

$$u(z) = \frac{1}{k}u^*_{Z_{can,ref}}\ln\left(\frac{z}{z_{om,g}}\right) \qquad \text{for } Z_{can,ref} \geq z \ , \quad (179)$$

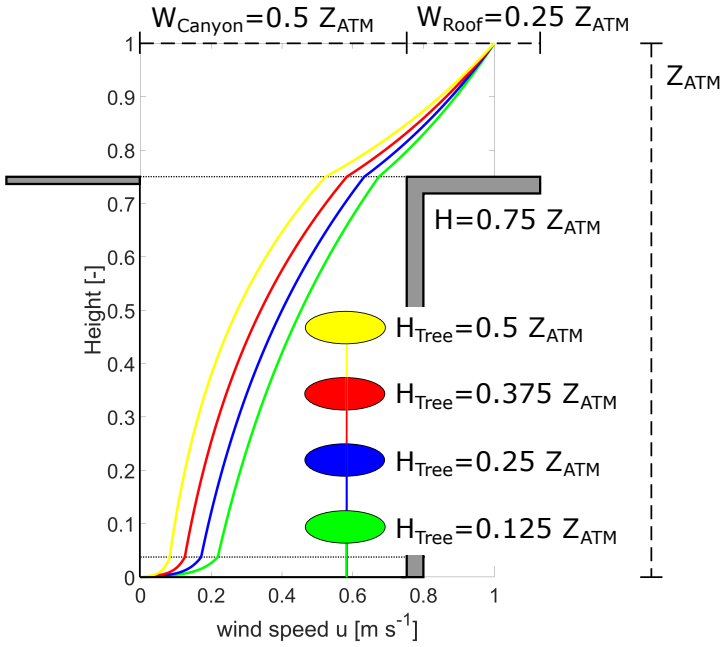

Figure 6. Vertical wind speed profile: Logarithmic above the urban canopy, exponential within the urban canyon, and logarithmic close to the canyon ground. The displayed wind speed profiles are calculated from the atmospheric reference level Z_{ATM} to the canyon ground with a canyon height of $H = 0.75\ Z_{ATM}$, a canyon width of of $W_{Canyon} = 0.5\ Z_{ATM}$, a roof width of $W_{Roof} = 0.25\ Z_{ATM}$, and varying tree heights of $H_{Tree} = 0.125\ Z_{ATM}\ to\ 0.5\ Z_{ATM}$.

where $k = 0.4$ is the von Karman constant, $\hat{\beta}$ $[-]$ an attenuation coefficient, $h_{d,can}$ $[\mathrm{m}]$ the urban canopy displacement height (Sect. 3.2), $z_{om,can}$ $[\mathrm{m}]$ the urban canopy roughness length (Sect. 3.2), $z_{om,g}$ $[\mathrm{m}]$ the ground roughness length (Sect. 3.2), u^* $[\mathrm{m\ s^{-1}}]$ the friction velocity, $u_{H_{can}} = \frac{1}{k} u^*_{atm} \ln\left(\frac{H_{can} - h_{d,can}}{z_{om,can}}\right)$ $[\mathrm{m\ s^{-1}}]$ the wind velocity at canyon height, Z_{atm} $[\mathrm{m}]$ the atmospheric reference height, H_{can} $[\mathrm{m}]$ the canyon height, and $Z_{can,ref}$ $[\mathrm{m}]$ a reference height close to the ground, typically 1.5 - 2 m, where the exponential wind profile changes to a logarithmic wind profile. The friction velocities u^*_{atm} and $u^*_{Z_{can,ref}}$ are calculated as:

$$u^*_{atm} = \frac{k\, u_{atm}}{\ln(Z_{atm} - h_{d,can})/(z_{om,can}))}\ , \tag{180}$$

$$u^*_{Z_{can,ref}} = \frac{k\, u_{Z_{can,ref}}}{\ln(Z_{can,ref})/(z_{om,g}))}\ , \tag{181}$$

where u_{atm} $[\mathrm{m\ s^{-1}}]$ is the wind velocity at atmospheric reference height, and $u_{Z_{can,ref}} = \frac{1}{k} u^*_{Z_{can,ref}} \ln\left(\frac{Z_{can,ref}}{z_{om,g}}\right)$ $[\mathrm{m\ s^{-1}}]$ the wind speed at the canyon reference height $Z_{can,ref}$. The attenuation coefficient $\hat{\beta}$ controls the vertical gradient of wind speed within the urban canyon. UT&C applies the approach developed by Fatichi et al. (2012a, b, c) for vegetated canopy which is based on a point equivalence between logarithmic and exponential wind speed profile at reference height Z_{atm} $[\mathrm{m}]$ and canopy

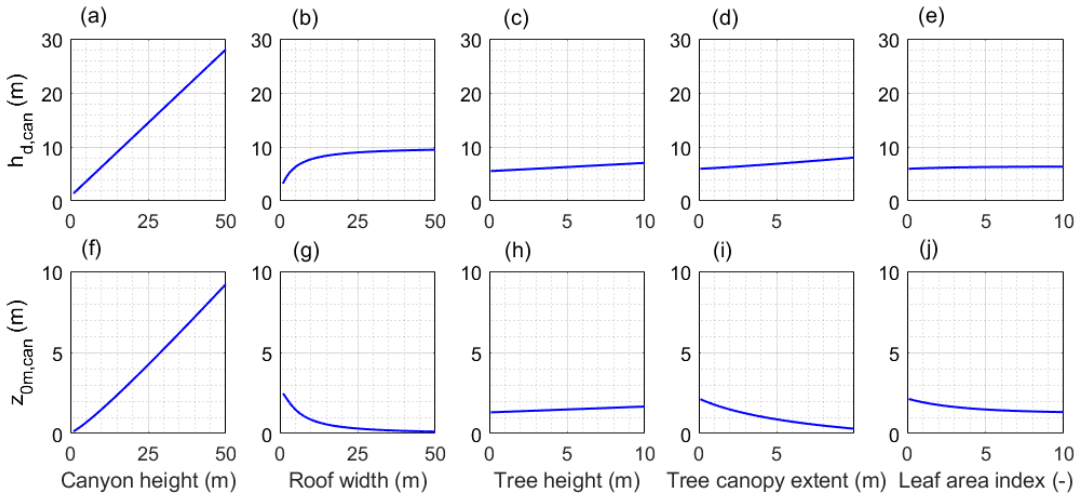

Figure 7. Sensitivity of canyon displacement height $h_{d,can}$ (Eq. (183)) and canyon roughness height $z_{0m,can}$ (Eq. (184)) as a function of canyon height, roof width, tree height, tree canopy extent, and leaf area index. The baseline scenario is a canyon height of 10 m, a canyon width of 10 m, a roof width of 5 m, a tree height of 5 m, a tree ~~extend~~ extent of 2 m, and a leaf area index of 5.

height H_{can} [m]:

$$\hat{\beta} = \frac{\ln[u_{atm}/u_{H_{can}}]}{Z_{atm}/H_{can} - 1} \,, \tag{182}$$

The mean vertical wind speed $w(z)$ [m s^{-1}] is assumed to be negligible since we do not consider three-dimensional effects. The presence of trees modifying the wind profile is considered in the canyon displacement height $h_{d,can}$ and roughness length $z_{om,can}$ as described in Sect. 3.2. The effect of ground vegetation is considered in the ground roughness length $z_{om,g}$ as described in Sect. 3.2, however displacement height of ground vegetation is considered negligible in the overall roughness parameterization of the ground, which typically include large fractions of smooth impervious surfaces.

3.2 Roughness length and zero displacement height

The urban canopy displacement height $h_{d,can}$ [m] and roughness length $z_{om,can}$ [m] are calculated according to the approach developed by Macdonald et al. (1998) which was modified by Kent et al. (2017) to include the effect of trees on the wind profile above the canyon (Fig. 7) as follows:

$$h_{d,can} = (1 + \alpha_A^{-\lambda_p}(\lambda_p - 1))\overline{H}_{urb} \,, \tag{183}$$

$$z_{om,can} = \overline{H}_{urb}\left(1 - \frac{h_{d,can}}{\overline{H}_{urb}}\right)\exp\left[-\left(\frac{1}{\kappa^2}0.5\beta_A C_{Db}\left(1 - \frac{h_{d,can}}{\overline{H}_{urb}}\right)\frac{\{A_{f,b} + (P_v)\,A_{f,v}\}}{A_{tot}}\right)^{-0.5}\right] \,, \tag{184}$$

where $\kappa = 0.4$ [−] is the von Karman constant, and $\alpha_A = 4.43$ [−], $\beta_A = 1$ [−], and $C_{Db} = 1.2$ [−] are parameter values for staggered arrays (Macdonald et al., 1998). $\overline{H}_{urb}$ [m] is the average height of the urban roughness elements, λ_p [−] the plan

area index of the urban roughness elements, $A_{f,b}$ [m] the actual frontal area of buildings, $A_{f,v}$ [m] the actual frontal area of vegetation, A_{tot} [m] the total urban plan area, and P_v [−] the ratio between vegetation drag C_{Dv} and building drag C_{Db}. The average height $\overline{H}_{urb}$ [m] and the plan area index of the urban roughness elements λ_p [−] are calculated as follows (Kent et al., 2017):

$$\overline{H}_{urb} = \frac{H_{can}\, A_{p,b} + H_{tree}\,(1 - P_{3D})\, A_{p,v}}{A_{p,b} + (1 - P_{3D})\, A_{p,v}} \,, \tag{185}$$

$$\lambda_p = \frac{A_{p,b} + (1 - P_{3D})\, A_{p,v}}{A_{tot}} \,, \tag{186}$$

where H_{can} [m] is the urban canyon height, H_{tree} [m] the tree height, $A_{p,b} = W_{roof}$ [m] the building plan area, $A_{p,v} = 4r_{tree}$ [m] the tree plan area, $A_{tot} = W_{roof} + W_{can}$ [m] the total urban plan area, and P_{3D} [−] the volumetric/aerodynamic porosity. The volumetric/aerodynamic porosity P_{3D} is calculated as a function of the optical porosity P_{2D} (Guan et al., 2003):

$$P_{3D} = {P_{2D}}^{0.40} \,, \tag{187}$$

$$P_{2D} = exp(-K_{opt} LAI) \,, \tag{188}$$

The optical porosity P_{2D} [−] is computed identically to the direct beam transmission through vegetation canopy (Sect. 1.1.3) where K_{opt} [−] is the light extinction parameter, and LAI [−] the leaf area index. The ratio P_v [−] between vegetation drag C_{Dv} and building drag C_{Db} is calculated as (Guan et al., 2000):

$$P_v = \frac{-1.251 P_{3D}^2 + 0.489 P_{3D} + 0.803}{C_{Db}} \,, \tag{189}$$

where $C_{Db} = 1.2$ [−] (Macdonald et al., 1998). The actual frontal area of buildings $A_{f,b}$ [m] and vegetation $A_{f,v}$ [m] is calculated as (Kent et al., 2017):

$$A_f = \frac{\overline{H}_{urb}}{\overline{H}_{urb} - h_{d,can}} A_f^* \,, \tag{190}$$

where A_f^* [m] is the unsheltered frontal area of buildings $A_{f,b}^* = H_{can}$ [m] and trees $A_{f,v}^* = 2r_{tree}$ [m].

The total roughness length of roof $z_{om,r}$ [m] and ground $z_{om,g}$ [m] cover are calculated as the maximum of the individual patch roughness lengths $z_{om,i}$ [m]. It is assumed that the largest roughness elements of a surface will govern the wind profile.

$$z_{om,r} = max(z_{om,r,veg},\, z_{om,r,imp}) \,, \tag{191}$$

$$z_{om,g} = max(z_{om,g,veg},\, z_{om,g,bare},\, z_{om,g,imp}) \,, \tag{192}$$

where $z_{om,r,veg}$ [m] is the roughness length of roof vegetation, $z_{om,r,imp}$ [m] of impervious roof, $z_{om,g,veg}$ [m] of ground vegetation, $z_{om,g,bare}$ [m] of bare ground, and $z_{om,g,imp}$ [m] of impervious ground. The vegetation roughness length $z_{om,veg}$ [m] and vegetation displacement height $h_{disp,veg}$ [m] are calculated as a function of the vegetation height h_{veg} [m] (Brutsaert, 1982):

$$z_{om,veg} = 0.123 h_{veg} \,, \tag{193}$$

$$z_{oh,veg} = z_{ow,veg} = 0.1 z_{om,veg} \,, \tag{194}$$

$$h_{d,veg} = 0.67 h_{veg} \,, \tag{195}$$

where h_{veg} [m] is the vegetation canopy height. The momentum roughness length of bare soil $z_{om,bare} = 0.003$ [m], road $z_{om,road} = 0.003$ [m], and impervious roof $z_{om,roof} = 0.01$ [m] are chosen according to values used by Wieringa (1993), Su (2002), and Wang et al. (2013). The roughness lengths for heat and water vapour are assumed to be one tenth of the momentum roughness length:

$$z_{oh,bare} = z_{ow,bare} = 0.1 z_{om,bare} \ , \tag{196}$$

$$z_{oh,road} = z_{ow,road} = 0.1 z_{om,road} \ , \tag{197}$$

$$z_{oh,roof} = z_{ow,roof} = 0.1 z_{om,roof} \ , \tag{198}$$

3.3 Aerodynamic resistance, r_{ah}

The aerodynamic resistance parametrizes the transport of sensible and latent heat caused by buoyancy and turbulence in the atmospheric surface layer and is based on the Monin-Obukhov similarity theory (Monin and Obukhov, 1954; Arya, 2001). Solving the complete Monin-Obukhov similarity theory is computationally demanding though and UT&C applies a simplified parametrization developed by Mascart et al. (1995) and applied by Noilhan and Mafhouf (1996), Masson (2000), Wang et al. (2013), and Fatichi et al. (2012a, b, c) (Sect. 3.3.1). The vertical aerodynamic resistance within the canyon is calculated similarly to an undercanopy resistance for a tree covered ~~landsurface~~ surface as described by Mahat et al. (2013) (Sect. 3.3.2). The horizontal aerodynamic resistance within the canyon describing the turbulent transport between wall surface and canyon air is calculated using the parametrization developed by Rowley et al. (1930) and Rowley and Eckley (1932) and applied by Masson (2000) and Wang et al. (2013) (Sect. 3.3.3). The aerodynamic resistances to the transport of heat and water vapour are assumed equal, i.e. $r_{ah} = r_{aw}$. This is a common approximation in land surface, hydrological, and urban canopy models (Viterbo and Beljaars, 1995; Sellers et al., 1996a; Noilhan and Mafhouf, 1996; Bertoldi et al., 2006; Ivanov et al., 2008a; Ryu et al., 2011; Wang et al., 2013; Ryu et al., 2016; Fatichi et al., 2012a, b, c).

3.3.1 Aerodynamic resistance: Above canyon r_{ah_r}, r_{ah_c}

The aerodynamic resistance from the roof surface r_{ah_r} [$\mathrm{m\,s^{-1}}$] and the canyon air r_{ah_c} [$\mathrm{m\,s^{-1}}$] to the atmospheric reference height Z_{atm} [m] is calculated using the simplified parametrization developed by Mascart et al. (1995) as applied in the ecohydrological model T&C (Fatichi et al., 2012a, b, c).

The aerodynamic resistance r_{ah} [$\mathrm{s\,m^{-1}}$] is calculated as a function of the neutral transport coefficient C_n and an empirical equation $F_h = f(Ri_B)$ accounting for atmospheric stability as follows:

$$r_{ah} = \frac{1}{C_n F_h(Ri_B) u_a} \ , \tag{199}$$

Where u_a [$\mathrm{m\,s^{-1}}$] is the wind speed at atmospheric reference height, and C_n and $F_h = f(Ri_B)$ are calculated as:

$$C_n = \frac{k^2}{\ln\left[(z_{atm} - d)/z_{om}\right]^2} \ , \tag{200}$$

$$F_h(Ri_B) = \left[1 - \frac{15 Ri_B}{1 + c_h\sqrt{|Ri_B|}}\right]\left[\frac{\ln[(z_{atm}-d)/z_{om}]}{\ln[(z_{atm}-d)/z_{oh}]}\right] \qquad \text{if } Ri_B \leq 0\,,$$

$$F_h(Ri_B) = \left[\frac{1}{1 + 15 Ri_B\sqrt{1+5Ri_B}}\right]\left[\frac{\ln[(z_{atm}-d)/z_{om}]}{\ln[(z_{atm}-d)/z_{oh}]}\right] \text{ if } Ri_B > 0\,, \tag{201}$$

c_h is calculated as:

$$c_h = 15{c_h}^* C_n \left[(z_{atm}-d)/z_{oh}\right]^{p_h}\left[\frac{\ln[(z_{atm}-d)/z_{om}]}{\ln[(z_{atm}-d)/z_{oh}]}\right]\,, \tag{202}$$

$${c_h}^* = 3.2165 + 4.3431\mu + 0.5360\mu^2 - 0.0781\mu^3\,, \tag{203}$$

$$p_h = 0.5802 - 0.1571\mu + 0.0327\mu^2 - 0.0026\mu^3\,, \tag{204}$$

$$\mu = \ln(z_{om}/z_{oh})\,, \tag{205}$$

where u_a [m s^{-1}] is the wind speed at the atmospheric reference height, k = 0.4 the von Karman constant, z_{atm} [m] the atmospheric reference height, d [m] the zero plane displacement, and z_{zoh} and z_{zom} [m] the roughness lengths of heat and momentum, respecivley. The bulk Richardson number Ri_B (Mascart et al., 1995; Abdella and McFarlane, 1996; van den Hurk and Holtslag, 1997) including the correction proposed by Kot and Song (1998) is calculated as:

$$Ri_B = f^2\,\frac{g(\theta_a - \theta_s)(z_{atm}-d)}{0.5(\theta_a+\theta_s){u_a}^2}\,, \tag{206}$$

$$f^2 = [1 - z_{om}/(z_{atm}-d)]^2/[1 - z_{oh}/(z_{atm}-d)]\,, \tag{207}$$

where θ_a and θ_s [K] are the potential air and surface temperature which are the temperatures corrected for the pressure gradient in the atmosphere. Note that using the potential temperature neglects the density stratification due to humidity gradients (Brutsaert, 2005). Hence, UT&C includes the option of using the virtual potential temperature which accounts for the influence of humidity on the boundary layer stability. This modification is proposed as high canyon humidity is observed during night times caused by stable boundary layer conditions. The bulk Richardson number describes the boundary layer stability condition. A stable boundary layer results in $Ri_B > 0$ and an unstable boundary layer in $Ri_B < 0$. Equation (201) for stable conditions is ~~modified from its original form (Mascart et al., 1995)~~ presented in its modified form according to Noilhan and Mafhouf (1996) and van den Hurk and Holtslag (1997).

The aerodynamic resistance formulation of Mascart et al. (1995) reaches infinity ($r_{ah} = \infty$) and prohibits turbulent transport in completely windless conditions ($u_a = 0$). This is almost never observed in reality (Kondo and Ishida, 1997) and UT&C computes the aerodynamic resistance according to Beljaars (1994) at wind speeds $u_a < 0.05$:

$$\frac{1}{r_{ah}} = 0.15\left[\frac{g\,\nu}{0.5(\theta_s+\theta_a)Pr^2}\right]^{1/3}(\theta_s - \theta_a)^{1/3}\,, \tag{208}$$

where g = 9.81 [m s^{-2}] is the gravitational acceleration, $\nu = 1.5^{-5}$ [m^2 s^{-1}] and $Pr = 0.71$.

The aerodynamic resistance above the roof r_{ah_r} is cacluated from the roof level H_{can} to the atmospheric reference height Z_{atm}. It is assumed that the area averaged roof temperature ($T_r = f_{r,veg}T_{r,veg} + f_{r,imp}T_{r,imp}$) determines boundary layer stability. The displacement height and roughness length of the roof cover is calculated as described in Sect.3.2. The aerodynamic

resistance above the canyon r_{ah_c} is calculated from the canyon ~~calculation~~ reference height Z_{calc} to the atmospheric reference height Z_{atm} using the canyon temperature T_{can} to determine boundary layer stability. The canyon ~~calculation~~ reference height is $Z_{calc} = h_{disp,can} + z_{0m,can}$ [m] (Sect. 3.2)~~for simplicity~~.

3.3.2 Aerodynamic resistance: Within canyon r_{ah_g}, r_{ah1_w}, r_{ah2_w}

The vertical aerodynamic resistances within the urban canyon, r_{ah_g}, r_{ah1_w}, and r_{ah2_w} [s m^{-1}], are calculated according to the formulation of vegetation undercanopy resistance as developed by Mahat et al. (2013) and applied by Fatichi et al. (2012a, b, c). Mahat et al. (2013) derived the vegetation undercanopy resistance applying a logarithmic wind profile above the canopy, an exponential wind profile within the canopy, and a logarithmic wind profile close to the ground surface. These wind profile assumptions match with the wind profiles commonly used in urban canopy parametrizations (Masson, 2000; Wang et al., 2013) as described in Sect. 3.1. Hence, the urban aerodynamic undercanopy resistance r'_{ah} [s m^{-1}] is derived similarly to a vegetation undercanopy resistance and is calculated as follows (Mahat et al., 2013):

$$r'_{ah} = \frac{H_{can} e^{\hat{\beta}}}{\hat{\beta} K_{H_{can}}} \left(e^{-\hat{\beta}\frac{Z_{can,ref}}{H_{can}}} - e^{-\hat{\beta}\frac{h_{d,can}+z_{om,can}}{H_{can}}} \right) + \frac{1}{k^2 u_{Z_{can,ref}}} \ln\left(\frac{Z_{can,ref}}{z_{om,g}}\right)^2 , \tag{209}$$

where H_{can} [m] is the canyon height, $\hat{\beta} = \frac{\ln[u_{atm}/u_{H_{can}}]}{Z_{atm}/H_{can}-1}$ the attenuation coefficient of the exponential wind profile (Sect. 3.1), $K_{H_{can}} = \kappa^2 u_{atm} \frac{H_{can}-h_{d,can}}{ln([Z_{atm}-h_{d,can}]/z_{om,can})}$ the eddy diffusion coefficient at canyon height (Mahat et al., 2013), $Z_{can,ref}$ [m] the selected reference height within the canyon close to the ground where exponential wind profile changes to logarithmic wind profile, $h_{d,can}$ [m] the urban canopy displacement height, $z_{om,can}$ [m] the urban canopy roughness length, $u_{Z_{can,ref}}$ [m s^{-1}] the wind speed at $Z_{can,ref}$, and $z_{om,g}$ [m] the ground roughness length. The undercanopy resistance depends on the turbulence and stability of the roughness sublayer. The following formulations are used to adjust for atmospheric stability (Choudhury and Monteith, 1988):

$$r'_{ah} = \frac{r'_{ah}}{(1-5Ri)^{3/4}} \qquad \text{if } Ri \leq 0 , \tag{210}$$

$$r'_{ah} = \frac{r'_{ah}}{(1-5Ri)^{2}} \qquad \text{if } Ri > 0 , \tag{211}$$

$$Ri = \frac{g(T_{can} - T_{s,av}) Z_{can,ref}}{(0.5(T_a + T_s) + 273.15) u^2_{Z_{can,ref}}} , \tag{212}$$

where Ri is the Richardson number within the canyon. $Ri = 0.16$ is used for $Ri > 0.16$ as Eq. (211) reaches infinity at $Ri = 0.2$. The superscript prime indicates the undercanopy quantities. The reference height within the urban canyon $Z_{can,ref}$ is assumed to be 1.5 m and the wind speed at $Z_{can,ref}$ is $u_{Z_{can,ref}} = u_{H_{can}} exp[-\hat{\beta}(1 - Z_{can,ref}/H_{can})]$. The canyon temperature T_{can} [K] and the area averaged ground surface temperature including trees $T_{s,av}$ [K] are used to account for the atmospheric stability within the urban canyon. The effect of trees and ground vegetation in modifying the undercanopy resistance are taken into account in the canyon displacement heigth $h_{d,can}$, canyon roughness length $z_{om,can}$, and ground roughness length $z_{om,g}$ (Sect. 3.2).

The aerodynamic resistance r_{ah_g} is calculated from the ground roughness length $z_{om,g}$ level to the canyon ~~calculation~~ reference height Z_{calc}. The aerodynamic resistances r_{ah1_w} and r_{ah2_w} are calculated from mid height of layer 1 and 2 to the

canyon ~~calculation~~ reference height as:

$$r_{ah1_w} = r_{ah}(z_{om,g} \rightarrow h_{d,can} + z_{om,can}) - r_{ah}(z_{om,g} \rightarrow Z_{p,w1,m}) \,, \tag{213}$$

$$r_{ah2_w} = r_{ah}(z_{om,g} \rightarrow h_{d,can} + z_{om,can}) - r_{ah}(z_{om,g} \rightarrow Z_{p,w2,m}) \,, \tag{214}$$

3.3.3 Aerodynamic resistance: Wall r_w

The horizontal aerodynamic resistance r_w [s m^{-1}] to the turbulent transport of sensible and latent heat from the wall surface to the canyon air is calculated as (Rowley et al., 1930; Rowley and Eckley, 1932; Masson, 2000; Wang et al., 2013):

$$r_w = C_p \rho_a (11.8 + 4.2\sqrt{u(Z_{p,can})^2 + w(Z_{p,can})^2})^{-1} \,, \tag{215}$$

where $u(Z_{p,can})$ [m s^{-1}] is the horizontal, and $w(Z_{p,can})$ [m s^{-1}] the vertical wind speed within the urban canyon at height $Z_{p,can}$ (Sect. 3.1). The original formulation is multiplied by the air density ρ_a [kg m^{-3}] and the specific heat capacity of air C_p [J kg^{-1} K^{-1}] to be consistent with the general resistance formulations~~and the~~. The apparent unit incongruence in Eq. (215) is due to the empirical coefficients used in Rowley et al. (1930) and Rowley and Eckley (1932). The effect of atmospheric stability on the aerodynamic resistance is not considered in the formulations of Rowley et al. (1930) and Rowley and Eckley (1932). The described horizontal aerodynamic resistance is calculated at the mid heights of layer 1 and 2.

3.4 Leaf boundary resistance, r_b

The leaf boundary resistance describes the resistance imposed by a thin layer of air around the leaf surface. UT&C calculates the one-sided leaf boundary resistance per unit leaf area r_b [s m^{-1}] as a function of leaf boundary conductance at forced turbulence $g_{b,forc}$ [m s^{-1}] and leaf boundary conductance at free convection $g_{b,free}$ [m s^{-1}] (Fatichi et al., 2012a, b, c):

$$r_b = \frac{1}{g_{b,free} + g_{b,forc}} \,, \tag{216}$$

The leaf boundary conductance at free convection $g_{b,free}$ is calculated according to Monteith (1973) and Leuning et al. (1995) if $T_s > T_a$. The leaf boundary conductance at forced turbulence ($u_a > 0$) is calculated as follows (Jones, 1983; Choudhury and Monteith, 1988; Shuttleworth and Gurney, 1990; Fatichi et al., 2012a, b, c):

$$g_{b,free} = \frac{0.5 D_h G_r^{0.25}}{d_{leaf}} \,, \tag{217}$$

$$g_{b,forc} = \left(\frac{2a}{\hat{\beta}}\right)\left(\frac{u_{H_{veg}}}{d_{leaf}}\right)^{1/2}\left[1 - e^{-\hat{\beta}/2}\right] \,, \tag{218}$$

where d_{leaf} [m] is the characteristic leaf dimension, $D_h = 1.9 \cdot 10^{-5}$ [m^2 s^{-1}] the molecular diffusivity of heat, $a = 0.01$ [m s$^{-1/2}$] an empirical coefficient (Choudhury and Monteith, 1988), $\hat{\beta}$ [$-$] the wind profile attenuation coefficient, and $G_r = 1.6 \cdot 10^8 \, (T_s - T_a) \, d_{leaf}^3$ [$-$] the Grashof number. The wind speed at vegetation canopy height $u_{H_{veg}}$ is calculated as described in Sect. 3.1. Equations (217) and (218) are derived under the assumption of a linear distribution of leaf area index over the vegetation height $L(z) = LAI/H_{veg}$ (Choudhury and Monteith, 1988) and the effects of atmospheric stability are not

considered. Note that r_b is the leaf boundary resistance for one side of the leaf. Hence, the leaf boundary resistance has to be rescaled by a factor of two to account for both leaf sides and by the LAI to account for the whole vegetation canopy. Leaf boundary resistance increases with larger leaf size and lower wind speed.

3.5 Soil resistance, r_{soil}

The soil resistance r_{soil} [s m^{-1}] describes the transport of water vapour from the soil pores to the air above the soil surface boundary layer. The transport of water vapour from the soil to the air is controlled by atmospheric conditions, diffusion in the soil boundary layer, moisture transport within the soil, and wetness of the surface soil layer. UT&C applies the expressions derived by Haghighi et al. (2013) and implemented in the ecohydrological model T&C (Fatichi et al., 2012a, b, c). Haghighi et al. (2013) calculates the soil resistance r_{soil} [s m^{-1}] as a function of soil type, soil water content in the top layer, and soil boundary layer characteristics. The total soil resistance r_{soil} [s m^{-1}] is the sum of soil boundary layer resistance r_{vbl} [s m^{-1}] and internal capillary-viscous resistance r_{sv} [s m^{-1}]:

$$r_{soil} = r_{vbl} + r_{sv} \ , \tag{219}$$

The soil internal capillary-viscous resistance r_{sv} accounts for the water vapour transport within the ~~porous media (soil)~~ soil while the soil boundary layer resistance r_{vbl} accounts for the presence of a boundary layer at the soil surface which poses a resistance to the transport of water vapour from the soil surface to the air just above the soil (Haghighi et al., 2013).

The soil internal capillary-viscous resistance r_{sv} is calculated as a function of soil water content of the surface layer θ_S and a proportionality constant γ (Haghighi et al., 2013):

$$r_{sv} = \frac{\gamma}{4K(\theta_S)} \ , \tag{220}$$

where K [m s^{-1}] is the soil hydraulic conductivity at soil water content θ_S. The proportionality constant γ [$-$] transforms the unit of capillary liquid to the unit of vapor flux (Haghighi et al., 2013):

$$\gamma = \frac{\hat{\alpha} e_{sat} - e_a}{\rho_w R_d T_g} \ , \tag{221}$$

where e_{sat} and e_a [Pa] are the saturation vapour pressure in the soil and the vapour pressure of the air, respectively, and $\hat{\alpha}$ is the relative humidity of air in the soil pores. T_g [K] is the soil surface temperture, ρ_w [kg m^{-3}] the water density, and R_d [J kg^{-1} K^{-1}] the water vapor gas constant. The relative humidity in the soil pores $\hat{\alpha}$ is calculated as Philip (1957):

$$\hat{\alpha} = \exp\left[-\frac{g\Psi_S}{R_d T_g}\right] \ , \tag{222}$$

where Ψ_S [m] is the water potential in the soil surface layer, and $g = 9.81$ [m s^{-2}] the gravity acceleration constant.

The soil boundary layer resistance r_{vbl} is calculated as (Haghighi et al., 2013):

$$r_{vbl} = \frac{\delta_m + P_{sz} f(\theta_S)}{Da} \ , \tag{223}$$

where δ_m [m] is the soil boundary layer thickness, P_{sz} [m] the pore size, and Da [m^2 s^{-1}] the molecular diffusivity of water vapour. The function $f(\theta_S)$ [$-$] describes the coupling of surface layer soil water content θ_S and diffusive resistance. The boundary layer thickness δ_m is calculated as (Shahraeeni et al., 2012):

$$\delta_m = 2.26\,10^{-3} u_a^{-0.5} \,, \tag{224}$$

where u_{ref} [m s^{-1}] is the wind speed at reference height for bare and vegetated ground (2 m on the roof, 1.5 m on the ground). The soil pore size P_{sz} [m] is correlated with the soil texture and can be computed as (Haghighi et al., 2013):

$$P_{sz} = 11.12\, n^{3.28}\, 10^{-6} \,, \tag{225}$$

where n is the pore size distribution parameter of the van-Genuchten soil water retention curve (Mualem, 1976; van Genuchten, 1980). According to Haghighi et al. (2013), $f(\theta_S)$ is calculated as follows:

$$f(\theta_s) = \frac{2}{\pi} \frac{\left[\sqrt{\frac{\pi}{4\theta_S}} - 1\right]}{\sqrt{4\theta_S}} \,, \tag{226}$$

UT&C typically considers a top soil layer with a depth of 10 [mm]. The formulation of r_{soil} proposed by Haghighi et al. (2013) and described here is mostly based on physical principles. Therefore, most uncertainty lays in the definition of soil texture and soil layer discretization (Fatichi et al., 2012a, b, c). Note that ~~the soil resistance~~ soil resistance is $r_{soil} = 0$ and the relative humidity $\hat{\alpha} = 1$ in the case of ponding water.

3.6 Stomata resistance, r_s

UT&C calculates the stomata resistance to the turbulent transport of water vapour from leaf interior to exterior air r_s [s m^{-1}] as a function of plant photosynthetic activty. Plants open their stomata to allow the transfer of CO_2 from the atmosphere to their chloroplasts inside the leaves. The open stomata lead to an inevitable loss of water vapour from the water-saturated tissue within the plants (Sellers et al., 1997). The stomata resistance is calculated individually for roof vegetation, ground vegetation, and trees. Following a two-big leaf approach, the stomata resistance for sunlit and shaded leaf area is calculated separately to account for light limitation in the shaded vegetation fraction. One single leaf temperature for sunlit and shaded vegetation canopy is used though to keep the number of prognostic temperatures small (Fatichi et al., 2012a, b, c).

3.6.1 Canopy partition and scaling from leaf to canopy

It is necessary to scale processes from leaf to canopy level due to several non-linear interactions (de Pury and Farquhar, 1997; Wang and Leuning, 1998; Dai et al., 2004; Fatichi et al., 2012a, b, c). The sunlit F_{sun} [$-$] and shaded F_{shd} [$-$] canopy fraction is calculated assuming an exponential decay of direct beam radiation within the vegetation canopy (Dai et al., 2004; Ivanov et al., 2008b; Fatichi et al., 2012a, b, c):

$$F_{sun} = \frac{1}{LAI} \frac{1 - e^{(-K_{opt} LAI)}}{K_{opt}} \,, \tag{227}$$

$$F_{shd} = 1 - F_{sun} \,, \tag{228}$$

where K_{opt} $[-]$ is the light extinction parameter, and LAI $[-]$ the leaf area index. The scaling factor for photosynthetic capacity F_N $[-]$ is calculated as in Fatichi et al. (2012a, b, c):

$$F_{N,sun} = \frac{1 - e^{-(K_N + K_{opt})\, LAI}}{K_N + K_{opt}} \,, \tag{229}$$

$$F_{N,shd} = \frac{1 - e^{-(K_N\, LAI)}}{K_N} - \frac{1 - e^{-(K_N + K_{opt})\, LAI}}{K_N + K_{opt}} \,, \tag{230}$$

where K_N $[-]$ is the canopy nitrogen decay coefficient. Subsequently, the maximum Rubisco capacity at 25°C for unit of leaf area [µmol CO_2 s^{-1} m^{-2} leaf] is calculated as (Fatichi et al., 2012a, b, c):

$$V_{max,sun} = V^T_{c,max}\, \frac{F_{N,sun}}{F_{sun} LAI} \,, \tag{231}$$

$$V_{max,shd} = V^T_{c,max}\, \frac{F_{N,shd}}{F_{shd} LAI} \,, \tag{232}$$

where $V^T_{c,max}$ [µmol CO_2 s^{-1} m^{-2}] is a model input parameter and specifies the maximum Rubisco capacity at the top of the vegetation canopy at 25°C.

The results of the photosynthetic model at leaf level need to be scaled back to the canopy level for computing the net assimilation rate $\overline{A_{nC}}$ [µmol CO_2 s^{-1} m^{-2}] and the leaf maintenance respiration $\overline{R_{dC}}$ [µmol CO_2 s^{-1} m^{-2}] (Sect. 3.6.2 and 3.6.3) (Fatichi et al., 2012a, b, c).

$$\overline{A_{nC}} = A_{nC,sun}\, F_{sun} LAI + A_{nC,shd}\, F_{shd} LAI \,, \tag{233}$$

$$\overline{R_{dC}} = R_{dC,sun}\, F_{sun} LAI + R_{dC,shd}\, F_{shd} LAI \,, \tag{234}$$

The stomata resistances, $r_{s,sun}$ and $r_{s,shd}$ $[s\ m^{-1}]$ (Sect. 3.6.2), are kept at the leaf scale as this is needed to caculate transpiration (Fatichi et al., 2012a, b, c).

3.6.2 Stomata conductance and stomata resistance

UT&C applies the biochemical model implemented in the ecohydrological model T&C (Fatichi et al., 2012a, b, c) to describe the coupling between photosynthesis and stomata resistance. The stomata resistance to water vapour r_{s,H_2O} $[m^2\ s^1\ \mu mol^{-1}\ CO_2\ ]$ is calculated as the inverse of the stomata conductance g_{s,CO_2}:

$$r_{s,H_2O} = \frac{1}{g_{s,CO_2} 1.64} \,, \tag{235}$$

where 1.64 is the ratio of stomata resistance for CO_2 and stomata resistance for H_2O ($r_{s,CO_2}/r_{s,H_2O} = 1.64$) (von Caemmerer and Farquhar, 1981). The following expression converts the resistance from biochemical units of $[m^2\ s^1\ \mu mol^{-1}\ CO_2\ ]$ to hydrological units $[s\ m^{-1}]$ (Sellers et al., 1996b):

$$r_s(s\ m^{-1}) = \frac{1}{0.0224}\, \frac{T_f\ P_{atm}}{(T + 273.15) P_{atm,0}}\, 10^6 r_{s,H_2O}(m^2\ s\ \mu mol^{-1}\, CO_2) \,, \tag{236}$$

where

P_{atm} = [Pa] is the atmospheric pressure.

$P_{atm,0}$ = 101325 [Pa] is the reference atmospheric pressure.

T_f = 273.15 [K].

T = [°C] is the leaf temperature.

r_{s,H_2O} = [m^2 s µmol^{-1} CO_2] is the resistance to convert.

Experiments have shown a relationship between stomata behaviour and net CO_2 assimilation rate A_{nC}, atmospheric vapor pressure deficit Δe, and intercellular CO_2 concentration c_i (Ball et al., 1987; Leuning, 1995; Gao et al., 2002). UT&C calculates the stomata conductance g_{s,CO_2} [µmolCO_2 m^{-2} leaf s^{-1}] according to Leuning (1990, 1995) and as implemented by Fatichi et al. (2012a, b, c) as:

$$g_{s,CO_2} = g_{0,CO_2} + a\frac{A_{nC}}{(c_c - \Gamma^*)} f(\Delta e)\, P_{atm}\ , \tag{237}$$

$$f(\Delta e) = \left(\frac{1}{1 + \Delta e/\Delta_0}\right)\ , \tag{238}$$

where

A_{nC} = [µmol CO_2 m^{-2} s^{-1}] is net CO_2 assimilation rate at leaf scale.

c_c = [Pa] is the leaf internal CO_2 concentration.

Γ^* = [Pa] is the CO_2 compensation point.

P_{atm} = [Pa] is the atmospheric pressure.

g_{0,CO_2} = [µmol CO_2 m^{-2} leaf s^{-1}] is the minimum stomatal conductance caused by cuticular conductance and imperfect stomatal closure when A_{nC} is negative.

Δe = [Pa] is the vapor pressure deficit.

Δ_0 = [Pa] is an empirical coefficient that expresses the value of vapor pressure deficit at which $f(\Delta e = \Delta_0) = 0.5$.

a = [−] is an empirical parameter connecting stomatal aperture and net assimilation.

The leaf internal CO_2 partial pressure c_c is unknown a priori and an iterative approach is needed. Equation (239 is solved iteratively to calculate resistance between leaf chloroplasts and atmosphere (Fatichi et al., 2012a, b, c):

$$A_{nC} = \frac{c_a - c_c}{P_{atm}\,(1.64 r_s + r_{mes} + 1.37 r_b + r_a)}\ , \tag{239}$$

where

A_{nC} = [µmol CO_2 m^{-2} s^{-1}] is net CO_2 assimilation rate at leaf scale.

c_c = [Pa] is the leaf internal CO_2 concentration.

c_a = [Pa] is the atmospheric CO_2 concentration at the leaf surface.

r_s = [m^2 s^1 µmol^{-1} H_2O] is the stomata resistance. $r_{s,CO_2}/r_{s,H_2O} = 1.64$ (von Caemmerer and Farquhar, 1981).

r_b = [m^2 s^1 µmol^{-1} H_2O] is the leaf boundary resistance. $r_{b,CO_2}/r_{b,H_2O} = 1.37$ (von Caemmerer and Farquhar, 1981).

r_{mes} = [m^2 s^1 µmol^{-1} CO_2] is the mesophylic resistance (Warren, 2006).

r_a = [m^2 s^1 µmol^{-1} CO_2] is the aerodynamic resistance.

3.6.3 Biochemical model of photosynthesis

The biochemical model of photosynthesis ~~(Fatichi et al., 2012a, b, c)~~ as implemented in Fatichi et al. (2012a, b, c) calculates the net and gross photosynthetic assimilation rate, A_{nC} and A^* [μmolCO_2 m^{-2} s^{-1}], as a function of three limiting rates of enzyme kinectics. The RuBP-carboxylase limited carboxylation rate J_c describes the amount and velocity of the carboxylating enzyme Rubisco. The maximum rate of photosynthetically active radiation captured by the leaf chlorophyll J_e accounts for light limitations. The export-limited (for C_3 plants) and the PEP-carboxylase limited (for C_4 plants) rate of carboxylation J_s describes the capacity of the leaf to use or export products of photosynthesis. The transition between the three rates J_c, J_e, and J_s is not abrupt. The three processes are coupled with a continous smooth function (Fatichi et al., 2012a, b, c) which is described with two quadratic equations according to Collatz et al. (1991). The gross photosynthetic assimilation rate A^* [μmol CO$_2$ m^{-2} s^{-1}] is calculated solving both quadratic equations for their smaller roots:

$$\alpha_{ce} J_p^2 - J_p(J_c + J_e) + J_e J_c = 0 \,,$$
$$\alpha_{ps} (A^*)^2 - A^*(J_p + J_s) + J_p J_s = 0 \,, \tag{240}$$

J_p = [μmol CO$_2$ m^{-2} s^{-1}] is the smoothed minimum of J_c and J_e.

A^* = [μmol CO$_2$ m^{-2} s^{-1}] is the gross assimilation rate for unit leaf before accounting for soil moisture stress.

α_{ce} = is a coupling coefficients (Sellers et al., 1996a; Bonan et al., 2011) where $\alpha_{ce} = 0.98$ for C_3 species and $\alpha_{ce} = 0.80$ for C_4 species.

α_{ps} = is a coupling coefficients (Sellers et al., 1996a; Bonan et al., 2011) where $\alpha_{ps} = 0.95$.

Subsquently, the net assimilation rate at leaf scale A_{nC} [μmol CO$_2$ m^{-2} s^{-1}] is calculated as the difference between gross assimilation rate corrected for water stress A_C and leaf maintenance respiration R_{dC} (Fatichi et al., 2012a, b, c):

$$A_{nC} = A_C - R_{dC} \,, \tag{241}$$
$$A_C = \beta_S \, A^* \,, \tag{242}$$

where

A_C = [μmol CO$_2$ m^{-2} s^{-1}] is the gross assimilation rate.

R_{dC} = [μmol CO$_2$ m^{-2} s^{-1}] is the leaf maintenance respiration assumed to be equal to the leaf dark respiration, which is a coarse approximation for respiration during daytime (Villar et al., 1995; Atkin et al., 1997).

β_S = [$-$] is a water stress factor limiting canopy photosynthesis based on leaf water potential Ψ_L [MPa].

The leaf maintenance respiration R_{dC} [μmol CO$_2$ m^{-2} s^{-1}] is estimated as (Collatz et al., 1991, 1992; Bonan et al., 2011):

$$R_{dC} = 0.015 \, V_{c,max} \exp\left[\frac{H_a(T_v - T_{ref})}{(T_{ref} \, R T_v)}\right] \frac{1 + exp\left(\frac{T_{ref}\Delta S - H_d}{T_{ref} \, R}\right)}{1 + exp\left(\frac{T_v \Delta S - H_d}{T_v \, R}\right)} \quad \text{for } C_3 \,, \tag{243}$$

$$R_{dC} = 0.025 \, V_{c,max} \, 2.0^{0.1(T_v^C - 25)} \left[1 + e^{1.3\,(T_v^C - 55)}\right]^{-1} \quad \text{for } C_4 \,, \tag{244}$$

where

$V_{c,max}$ = [µmol CO_2 s^{-1} m^{-2}] is the maximum Rubisco capacity.
T_v = [K] is the leaf temperature.
T_v^C = [°C] is the leaf temperature.
T_{ref} = 273.15 [K].
R = 8.314 [J mol^{-1} K^{-1}] is the universal gas constant.
H_a = 46.39 [kJ mol^{-1}].
H_d = 150.65 [kJ mol^{-1}].
ΔS = 0.490 [kJ mol^{-1} K^{-1}].

The water stress factor β_S, limiting canopy photosynthesis, is based on the leaf water potential Ψ_L [MPa] and calculated as:

$$\beta_S = 1 - \frac{1}{1 + \exp(p_S \Psi_L + q_S)} \ , \tag{245}$$

where

Ψ_L = [MPa] is the leaf water potential.
p_s = f($\Psi_{S,00}$, $\Psi_{S,50}$ [MPa]).
q_S = f($\Psi_{S,00}$, $\Psi_{S,50}$ [MPa]).
$\Psi_{S,00}$ = [MPa] is the water potential threshold where stomata closure begins (2% of closure).
$\Psi_{S,50}$ = [MPa] is the water potential threshold where stomata closure reaches 50%%.

UT&C does not include plant hydraulics (Tuzet et al., 2003; Buckley et al., 2003; Katul et al., 2003; Bohrer et al., 2005; Verbeeck et al., 2007; Vico and Porporato, 2008; Feddes et al., 2001; Sperry et al., 2003; Kirkham, 2005; Sack and Holbrook, 2006; Nobel, 2009) and the leaf water potential Ψ_L is equal to the soil water potential Ψ_{sR} experienced by the plant in the root zone. Note that the maximum Rubisco capacity at 25°C $V_{c,max}$ [µmol CO_2 m^{-2} s^{-1}] is an important parameter in the biochemical model and it is ~~plant~~ species specific.

RUBISCO LIMITED CARBOXYLATION RATE

The RuBP-carboxylase limited carboxylation rate is calculated as (Fatichi et al., 2012a, b, c):

$$J_c = V_m \left[\frac{c_c - \Gamma^*}{c_c + K_c(1 + O_i/K_o)} \right] \quad \text{for } C_3 \ , \tag{246}$$

$$J_c = V_m \quad \text{for } C_4 \ , \tag{247}$$

where

c_c = [Pa] is the partial pressures of CO_2 in the leaf chloroplasts.

O_i = [Pa] is the partial pressures of O_2 in the leaf chloroplasts.

V_m = [μmol CO_2 s^{-1} m^{-2}] is the temperature dependent Rubisco capacity at the leaf scale for C3 species $V_{m,C3}$, and C4 species $V_{m,C4}$.

K_c = [Pa] is the temperature dependent Michaelis-Menten constants for CO_2.

K_o = [Pa] is the temperature dependent Michaelis-Menten constants for O_2.

Γ^* = [Pa] is the temperature dependent CO_2 compensation point.

The temperature dependence of the maximum catalytic Rubisco capacity for C3 species $V_{m,C3}$ [μmol CO_2 s^{-1} m^{-2}] (Kattge and Knorr, 2007), and for C4 species $V_{m,C4}$ [μmol CO_2 s^{-1} m^{-2}] (Sellers et al., 1996b; Dai et al., 2004; Bonan et al., 2011) is calculated as:

$$V_{m,C3} = V_{c,max} \exp\Big[\frac{H_a(T_v - T_{ref})}{(T_{ref}\, R T_v)}\Big] \frac{1 + exp\left(\frac{T_{ref}\Delta S - H_d}{T_{ref}\, R}\right)}{1 + exp\left(\frac{T_v \Delta S - H_d}{T_v\, R}\right)}\,, \tag{248}$$

$$V_{m,C4} = V_{c,max}\, \left[2.1^{0.1(T_v^C - 25)}\right] \left[\frac{1}{1 + \exp[0.3(T_v^C - 40)]}\right] \left[\frac{1}{1 + \exp(0.2(15 - T_v^C))}\right]\,, \tag{249}$$

The temperature dependence of the Michaelis-Menten constant for CO_2, K_c [Pa] and O_2, K_o [Pa], and the CO_2 compensation point Γ^* [Pa] are calculated as (Bonan et al., 2011):

$$K_c = K_{c,25} \exp\Big[\frac{79.43(T_v - T_{ref})}{(T_{ref}\, R T_v)}\Big]\,, \tag{250}$$

$$K_o = K_{o,25} \exp\Big[\frac{36.38(T_v - T_{ref})}{(T_{ref}\, R T_v)}\Big]\,, \tag{251}$$

$$\Gamma^* = \Gamma^*_{25} \exp\Big[\frac{37.83(T_v - T_{ref})}{(T_{ref}\, R T_v)}\Big]\,, \tag{252}$$

where

$V_{c,max}$ = [µmol CO_2 m^{-2} s^{-1}] is the maximum Rubisco capacity at 25 °C.

H_a = [kJ mol^{-1}] is the species dependent activation energy with a typical range of $H_a = 45 - 95$ [kJ mol^{-1}]. A reference value of $H_a = 72$ [kJ mol^{-1}] is used if no paramter is provided (Kattge and Knorr, 2007).

H_d = 200 [kJ mol^{-1}] is the constant deactivation energy describing the rate of decrease above the optimum temperature.

ΔS = [kJ mol^{-1} K^{-1}] is the species dependent "entropy factor" with a typical range of $\Delta S = 0.625 - 0.665$ [kJ mol^{-1} K^{-1}]. A reference value of $\Delta S = 0.649$ [kJ mol^{-1} K^{-1}] is used if no paramter is provided (Kattge and Knorr, 2007).

R = 8.314 [J mol^{-1} K^{-1}] is the universal gas constant.

T_{ref} = 273.15 [K].

T_v = [K] is the leaf temperature.

T_v^C = [°C] is the leaf temperature.

$K_{c,25}$ = 404.9 10^{-6} P_{atm} [Pa] is the reference value of the Michaelis-Menten constants for CO_2 at 25 °C (Bonan et al., 2011).

$K_{o,25}$ = 278.4 10^{-3} P_{atm} [Pa] is the reference value of the Michaelis-Menten constants for O_2 at 25 °C (Bonan et al., 2011).

RATE LIMITED BY PHOTOSYNTHETIC ACTIVE RADIATION (PAR) CAPTURED BY LEAF CHLOROPHYLL

The maximum rate of photosynthetically active radiation captured by the leaf chlorophyll is calculated as (Farquhar et al., 1980; Collatz et al., 1991, 1992; Bonan et al., 2011; Fatichi et al., 2012a, b, c):

$$J_e = J \left[\frac{c_c - \Gamma^*}{c_c + 2\Gamma^*} \right] \qquad \text{for } C_3 \text{ ,} \tag{253}$$

$$J_e = PPFD^* \qquad \text{for } C_4 \text{ ,} \tag{254}$$

where

c_c = [Pa] is the partial pressures of CO_2 in the leaf chloroplasts.

Γ^* = [Pa] is the temperature dependent CO_2 compensation point.

$PPFD^*$ = [µmol CO_2 s^{-1} m^{-2}] is the effective photosynthetic photon flux density of photosystem II.

J is the smaller root of the following quadratic equation:

$$\alpha_J J^2 - (PPFD^* + \frac{J_m}{4}) J + PPFD^* \frac{J_m}{4} = 0 \text{ ,} \tag{255}$$

with

$$PPFD^* = \epsilon\,\beta_Q\,PAR_{abs}\ , \tag{256}$$

$$PAR_{abs} = \frac{PAR_{abs,sun}}{F_{sun}LAI} \qquad \text{for sunlit leaves}\ , \tag{257}$$

$$PAR_{abs} = \frac{PAR_{abs,shd}}{F_{shd}LAI} \qquad \text{for shaded leaves}\ , \tag{258}$$

where

J_m = [µmol equivalent s^{-1} m^{-2}] is the temperature dependent electron transport capacity at leaf scale.

α_J = 0.7 [−] is a shape parameter (Bonan, 2002).

ϵ = [µmol CO_2 µmol^{-1} photons] is the intrinsic quantum efficiency depending on the photosynthesis pathway (C_3 or C_4). $\epsilon = 0.081$ [µmol CO_2 µmol^{-1} photons] for C_3 plants, $\epsilon = 0.040$ [µmol CO_2 µmol^{-1} photons] for C_4 plants (Farquhar et al., 1980; Collatz et al., 1991, 1992; Singsaas et al., 2001).

β_Q = 4.57 [µmol photons J^{-1}] is a quanta-to-energy conversion factor between the measurement units (Dye, 2004).

PAR_{abs} = [W m^{-2}] is the absorbed photosynthetically active radiation at leaf scale.

F_{sun} = [−] is the fraction of sunlit leaves.

F_{shd} = [−] is the fraction of shaded leaves.

LAI = [−] is the leaf area index.

The maximum electron transport capacity J_m [µmol equivalent s^{-1} m^{-2}] as a function of temperature is calculated as (Kattge and Knorr, 2007):

$$J_m = J_{max}\,\exp\Big[\frac{H_a(T_v - T_{ref})}{(T_{ref}\,R\,T_v)}\Big]\,\frac{1 + exp\left(\frac{T_{ref}\Delta S - H_d}{T_{ref}\,R}\right)}{1 + exp\left(\frac{T_v\Delta S - H_d}{T_v\,R}\right)}\ , \tag{259}$$

$$J_{max} = r_{jv}\,V_{c,max}\ , \tag{260}$$

where

J_{max} = [µmol equivalent s^{-1} m^{-2}] is the maximum electron transport capacity at 25 °C.

$V_{c,max}$ = [µmol CO_2 s^{-1} m^{-2}] is the maximum Rubisco capacity.

r_{jv} = [µmol equivalent µmol CO_2^{-1}] is a scaling factor between $V_{c,max}$ and J_{max} with a typical range $r_{jv} = 1.6 - 2.6$.

H_a = 50 [kJ mol^{-1}] (Kattge and Knorr, 2007).

H_d = 200 [kJ mol^{-1}] (Kattge and Knorr, 2007).

ΔS = 0.646 [kJ mol^{-1} K^{-1}] (Kattge and Knorr, 2007).

R = 8.314 [J mol^{-1} K^{-1}] is the universal gas constant.

T_{ref} = 273.15 [K].

T_v = [K] is the leaf temperature.

965 PRODUCT EXPORT AND USAGE LIMITED RATE

The export-limited rate of carboxylation (for C_3 plants) and the PEP-carboxylase limited rate of carboxylation (for C_4 plants) are calculated as:

$$J_s = 3TPU \qquad \text{for } C_3\ , \tag{261}$$

$$J_s = k_e \frac{c_c}{P_{atm}} \qquad \text{for } C_4\ , \tag{262}$$

970 where

$TPU = [\mu\text{mol equivalent s}^{-1}\ \text{m}^{-2}]$ is the temperature dependent triose phosphate utilization at leaf scale.
$k_e = [\mu\text{mol equivalent s}^{-1}\ \text{m}^{-2}]$ is the PEP Carboxylase coefficient.
$c_c = [\text{Pa}]$ is the partial pressures of CO_2 in the leaf chloroplasts.
$P_{atm} = [\text{Pa}]$ is the atmospheric pressure.

The Triose Phosphate Utilization TPU [μmol equivalent $\text{s}^{-1}\ \text{m}^{-2}$] and the PEP Carboxylase coefficient k_e [μmol equivalent $\text{s}^{-1}\ \text{m}^{-2}$] are calculated as (Bonan et al., 2011):

$$TPU = TPU_{25}\ \exp\left[\frac{H_a(T_v - T_{ref})}{(T_{ref}\,R T_v)}\right] \frac{1 + exp\left(\frac{T_{ref}\Delta S - H_d}{T_{ref}\,R}\right)}{1 + exp\left(\frac{T_v \Delta S - H_d}{T_v\,R}\right)}\ , \tag{263}$$

975 $$TPU_{25} = 0.1182 V_{c,max}\ , \tag{264}$$

$$k_e = k_{e,25}\left[2.1^{0.1(T_v - 25)}\right]\ , \tag{265}$$

$$k_{e,25} = 20000\, V_{c,max}\ , \tag{266}$$

where

$TPU_{25} = [\mu\text{mol equivalent s}^{-1}\ \text{m}^{-2}]$ is the triose phosphate utilization at 25 °C computed as a function of $V_{c,max}$.
$H_a = 53.1\ [\text{kJ mol}^{-1}]$.
$\Delta S = 0.490\ [\text{kJ mol}^{-1}\ \text{K}^{-1}]$.
$H_d = 150.65\ [\text{kJ mol}^{-1}]$.
$T_v = [^\circ\text{C}]$ is the leaf temperature.
$k_{e,25} = [\mu\text{mol equivalent s}^{-1}\ \text{m}^{-2}]$ is the PEP Carboxylase coefficient at 25 °C.

980 ## 4 Conductive heat flux

4.1 Conductive heat flux: Building envelope

The conductive heat flux into and out of the building envelope (wall and roof) is calculated with a numerical solution of the heat diffusion equation (Hu and Islam, 1995; Hillel, 1998; Núnez et al., 2010; Masson, 2000; Wang et al., 2011; Park and Lee,

2008):

$$\frac{\partial T_k}{\partial t} = k_k \frac{\partial^2 T_k}{\partial z^2} \,, \tag{267}$$

where T_k [°C] is the temperature of wall or roof layer k, and $k_k = \lambda_k / cv_k$ [m^2 s^{-1}] the heat diffusivity of the wall or roof material. UT&C considers two physical layers for the vegetated roof and one physical layer for the impervious roof, and sunlit and shaded wall. The numerical solution is based on three nodes (two numerical layers) with the inner boundary condition equal to the interior building temperature T_b and the outer boundary condition equal to the prognostic surface temperature T_i. The conductive heat flux of wall and roof layer 1 and 2, $G_1(t,z)$ and $G_2(t,z)$ [W m^{-2}], are calculated as:

$$G_1(t,z) = -\lambda_1 \frac{(T_{int}(t) - T_i(t))}{\Delta z_1} \,, \tag{268}$$

$$G_2(t,z) = -\lambda_2 \frac{(T_b(t) - T_{int}(t))}{\Delta z_2} \,, \tag{269}$$

where λ_1 and λ_2 [J K^{-1} m^{-1} s^{-1}] are the heat conductivity of numerical layer 1 and 2, and Δz_1 and Δz_2 the thickness of layer 1 and 2. An internal wall and roof temperature T_{int} is calculated to account for heat storage effects inside the wall or roof. The interior building air temperature T_b is prescribed equal to the air temperature at atmospheric reference height if the air temperature is between a ~~set~~ minimum value $T_{b,min}$ and a ~~set~~ maximum value $T_{b,max}$. In the case of higher or lower air temperature, the interior building temperature T_b is prescribed equal to $T_{b,min}$ or $T_{b,max}$ assuming that heating or cooling of building interior is occuring (de Munck et al., 2018). Furthermore, UT&C is able to account for an a priori defined interior building temperature time series T_b.

4.2 Conductive heat flux: Ground

The conductive heat flux into and out of the ground is calculated applying the force restore method, which approximates the heat diffusion equation with a single ordinary differential equation as (Hu and Islam, 1995):

$$\frac{dT_g}{dt} = C_1 G - C_2 (T_g - T_d) \,, \tag{270}$$

where T_g [K] is the ground surface temperature, and T_d [K] the ground temperature at dampening depth d. C_1 [m^2 K J^{-1}] and C_2 [s^{-1}] are coefficients of the method. UT&C uses the Deardorff (1978) force restore method as implemented in the ecohydrological model T&C (Fatichi et al., 2012a, b, c):

$$G(t) = \frac{1}{C_1} \left[C_2 [T_g(t) - T_d(t)] + \frac{T_g(t) - T_g(t-1)}{dt} \right] \,, \tag{271}$$

$$C_1 = 2/(cv_s d) = 2\sqrt{\pi / (\lambda_s cv_s \tau_{day})} \,, \tag{272}$$

$$C_2 = \omega_1 = \frac{2\pi}{\tau_{day}} \,, \tag{273}$$

where λ_s [J K^{-1} m^{-1} s^{-1}] is the bulk ground heat conductivity, cv_s [J K^{-1} m^{-3}] the bulk ground volumetric heat capacity, and $\tau_{day} = 86400$ [s]. The dampening temperature T_d is calculated as (Noilhan and Planton, 1989):

$$dT_d/dt = (T_g - T_d)/\tau_{day} \,, \tag{274}$$

4.3 Soil thermal properties

The soil volumetric heat capacity cv_s and the soil thermal conductivity λ_s are calculated as a function of soil type and soil water content according to de Vries (1963), Farouki (1981), and Oleson et al. (2004, 2013) as described in Fatichi et al. (2012a, b, c).

5 Anthropogenic heat flux

The current UT&C parametrization allows for a prescribed time series of anthropogenic heat flux ~~, which is added to the canyon air at the canyon calculation height .~~ that contributes to the sensible heat flux from the canyon reference height (= $h_{disp,can} + z_{0,m,can}$) to the atmospheric reference height. The anthropogenic heat flux is a model input timeseries. Hence, anthropogenic heat emissions caused by air conditioning, car exhaust, industry, human metabolism, or any other additional source need to be estimated a priori, e.g. using existing approaches (Sailor and Lu, 2004; Sailor et al., 2015). The conductive anthropogenic heat flux caused by heating of building interiors is represented with a prescribed interior building temperature if air temperature falls below the set value $T_{b,min}$ (See Sect. 4.1). On the other hand, the conductive anthropogenic heat flux due to air conditioning of building interiors produces a negative anthropogenic heat effect, ~~which could be counteracted by adding air conditioning heat emission input~~ cooling the canyon. However, when the heat waste of air conditioning is re-emitted to the canyon air as described above, there is a positive anthropogenic heat effect, which counteract the cooling coming from heat conduction. Future developments of UT&C could focus on the inclusion of anthropogenic heat emissions due to the air conditioning of buildings by adding the value of the total conductive heat flux into the building envelope back into the urban canyon air or above the roof (depending on location of ~~airconditioning~~ air-conditioning units), with an appropriate adjustement for efficiency ~~.~~ and potentially even a coupling with a mesoscale meteorological model. Figure 8 and 9 show the effect of a change in fixed interior building temperature T_b on the air temperature at canyon reference height and the canyon energy fluxes without coupling to a mesoscale meteorological model for the Singapore eddy-covariance site. Results are presented for the case of no re-emission of the anthropogenic heat used for cooling, re-emission without adjustment for air-conditioning efficiency (infinite coefficient of performance), and re-emission with an air-conditioning coefficient of performance of 2.5 (de Munck et al., 2018). The air temperature at canyon reference height, the location where anthropogenic heat is emitted, increases with decreasing building temperature in the case of re-emitted anthropogenic heat while decreases if no heat is re-emitted in the canyon. The further feedback of this increase in sensible heat on the forcing temperature and, therefore, urban canopy air temperature could be analysed only through a coupling with a mesoscale meteorological model.

6 Urban hydrological model

UT&C solves the urban water mass balance as:

$$\frac{dS}{dt} = P + Q_f - E - R\,, \tag{275}$$

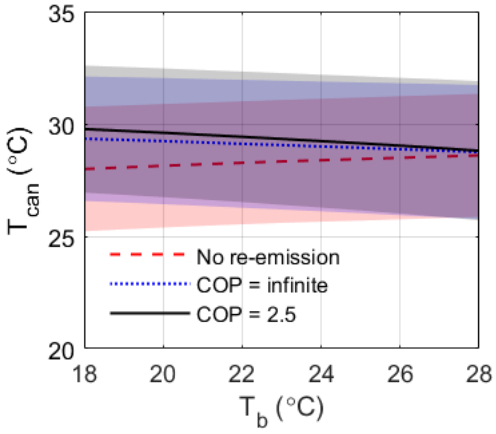

Figure 8. Air temperature at canyon reference height T_{can} for the Singapore eddy-covariance site as a function of prescribed interior building temperature T_b if no anthropogenic heat used for cooling is re-emitted, the anthropogenic heat used for cooling is re-emitted to the canyon air withouth adjustement for air-conditioning efficiency (coefficient of performance (COP) = infinite), and the anthropogenic heat used for cooling is re-emitted to the canyon air with an air-conditioning COP of 2.5 (de Munck et al., 2018).

where P $[\mathrm{mm\ h^{-1}}]$ is the incoming precipitation, Q_f $[\mathrm{mm\ h^{-1}}]$ the anthropogenic water input, E $[\mathrm{mm\ h^{-1}}]$ the total evapotranspiration, R $[\mathrm{mm\ h^{-1}}]$ the total runoff plus deep leakage from the soil column, and dS/dt $[\mathrm{mm\ h^{-1}}]$ the change of water storage S in the system. P and Q_f are both model input timeseries, and E and R are calculated within UT&C as described in Sect. 2.2 to 2.2.5 and 6.3. The total water storage S consists of intercepted water, ponding water, and water stored in the soil column. The water mass balance is calculated individually for roof and canyon. It is assumed that the total roof runoff and the soil water leakage of green roofs is directed towards the sewer system and does not affect the canyon water budget anymore. It is further assumed that soil moisture changes slowly in comparison to energy fluxes to reduce the complexity of the system and to facilitate faster computation. Hence, the energy balance is solved first for a given time step t and the evapotranspiration is constrained by the water availability at the previous timestep (t-1). The obtained evapotranspiration E_t $[\mathrm{kg\ m^{-2}\ s^{-1}}]$ is then used as an input to solve the water mass balance.

6.1 Interception and ponding

UT&C considers interception on vegetation canopy (Sect. 6.1.1), ponding on impervious surfaces (Sect. 6.1.2) and ponding on bare soil or soil underneath vegetation (Sect. 6.1.3). The interception and ponding storage dynamics are calculated according to a mass conservation equation as:

$$\frac{dIn}{dt} = P^* - D - E_{In}\ , \tag{276}$$

where In $[\mathrm{mm}]$ is the intercepted or ponding water, P^* $[\mathrm{mm\ h^{-1}}]$ the incoming water flux from precipitation and runon , D $[\mathrm{mm\ h^{-1}}]$ the canopy drainage or soil infiltration, and E_{In} $[\mathrm{mm\ h^{-1}}]$ the evaporation from intercepted or ponding water.

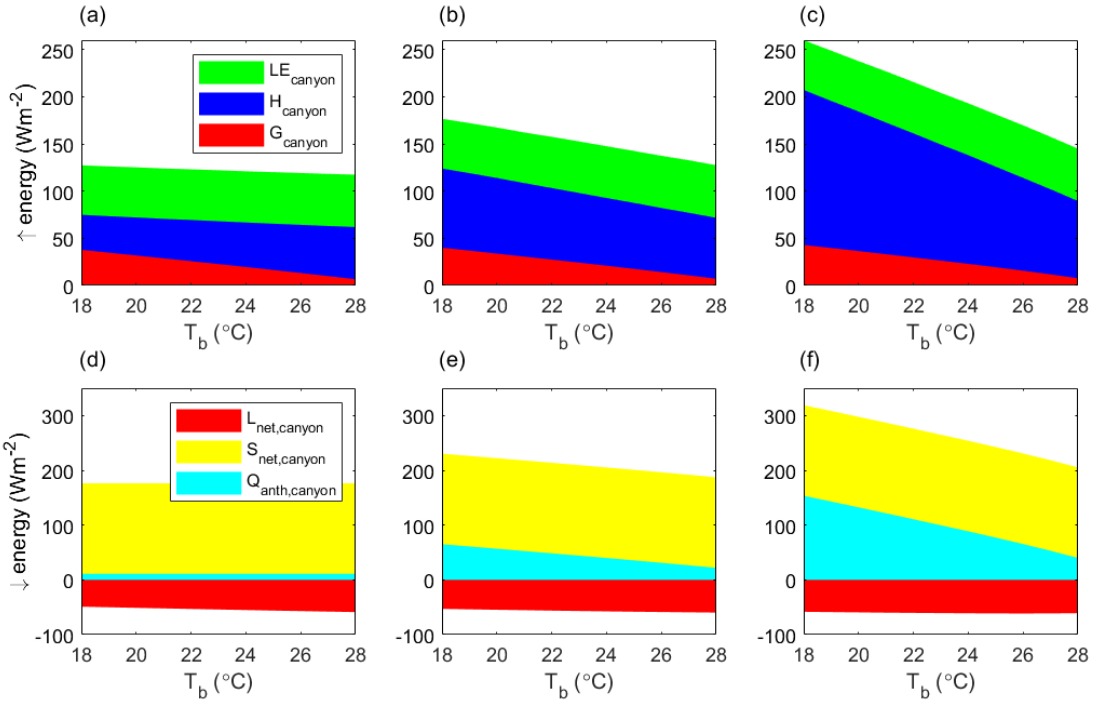

Figure 9. Energy fluxes for the Singapore eddy-covariance site as a function of prescribed interior building temperature T_b if (a) & (d) no anthropogenic heat used for cooling is re-emitted, (b) & (e) the anthropogenic heat used for cooling is re-emitted to the canyon air withouth adjustement for air-conditioning efficiency (infinite coefficient of performance), (c) & (f) the anthropogenic heat used for cooling is re-emitted to the canyon air with an air-conditioning coefficient of performance of 2.5 (de Munck et al., 2018).

A finite difference approximation is used to solve Eq. (276) as suggested by Fatichi et al. (2012a, b, c) where the effects of evaporation and precipitation are considered first and the canopy drainage or infiltration are substracted subsequently:

$$In_t(t) = In(t - \Delta t) + P^*(t)\Delta t - E_{In}(t)\Delta t \ , \tag{277}$$

$$In(t) = In_t(t) - Dr(t)\Delta t \ , \tag{278}$$

where $\Delta t = 1$ [h] is the time step of the calculation.

6.1.1 Interception: Plant canopy

The canopy interception is calculated according to the Rutter model (Rutter et al., 1971, 1975; Mahfouf and Jacquemin, 1989; Eltahir and Bras, 1993; Ivanov et al., 2008b) as:

$$\frac{dIn}{dt} = P_{fol} - Dr - E_{In} \ , \tag{279}$$

The precipitation onto the canopy foilage P_{fol} [mm h^{-1}] and the throughfall $P_{through}$ [mm h^{-1}] are calculated as a function of projected leaf area fraction onto the ground C_{fol} as follows (Mahfouf and Jacquemin, 1989):

$$P_{fol} = P\, C_{fol} \ , \tag{280}$$

$$P_{through} = P\,(1 - C_{fol}) \ , \tag{281}$$

$$C_{fol} = 1 - e^{-\kappa(LAI+SAI)} \ ,, \tag{282}$$

where P [mm h^{-1}] is the incoming precipitation, LAI [$-$] and SAI [$-$] the leaf and stem area index, and $\kappa = 0.75$ (Ramírez and Senarath, 2000). $C_{fol} = [0-1]$ [m^2 obstructed area m^{-2} VEG area] represents the projected leaf area onto the ground, which is active in the interception process.

The canopy drainage Dr [mm h^{-1}] is calculated as:

$$Dr = Dr_s + Dr_d \ , \tag{283}$$

where Dr_s [mm h^{-1}] is the saturation excess drainage, and Dr_d [mm h^{-1}] the canopy dripping. Dr_s and Dr_d are calculated as (Fatichi et al., 2012a, b, c):

$$Dr_s = \frac{(In_t - In^{Max})}{dt} (In > In^{Max}) \ , \tag{284}$$

$$Dr_d = K_c e^{g_c(In_t - In^{Max})} \ , \tag{285}$$

where In^{Max} [mm] is the maximum interception capacity of the vegetation canopy, $K_c = 0.06$ [mm h^{-1}] the drainage rate coefficient (Rutter et al., 1971; Mahfouf and Jacquemin, 1989), and $g_c = 3.7$ [mm^{-1}] the exponential decay paramter (Rutter et al., 1971; Mahfouf and Jacquemin, 1989). The total intercepted water In [mm] must always be smaller than the maximum interception capacity In^{Max} (Fatichi et al., 2012a, b, c). The maximum interception capacity of the vegetation canopy In^{Max} [mm] is calculated as (Dickinson et al., 1993):

$$In^{Max} = S_{p,In}(LAI + SAI) \ , \tag{286}$$

where $S_{p,In}$ [mm] is a model input parameter and a function of vegetation type.

The fraction of precipitation reaching the layer below the vegetation P_{down} [mm] is calculated as:

$$P_{down} = P(1 - A_{veg}) + DrA_{veg} \ , \tag{287}$$

where A_{veg} is the vegetation canopy area in relation to the underlying ground area. It is assumed that the vegetated roof and canyon ground fraction f_{veg} [$-$] are completely covered by vegetation leading to $A_{veg} = 1$. The impervious, bare and vegetated ground cover fraction underneath trees are homogeneously distributed leading to $A_{veg,tree} = 4r_{tree}$.

6.1.2 Ponding: Impervious surface

Ponding on impervious surfaces is calculated according to a water mass budget as:

$$\frac{dIn}{dt} = P_{imp} - Lk - E_{In} \ , \tag{288}$$

The incoming water flux to the impervious roof fraction $P_{r,imp}$ and the impervious ground fraction $P_{g,imp}$ are calculated as follows:

$$P_{r,imp} = P + q_{roof} \ , \tag{289}$$

$$P_{g,imp} = P_{down} + q_{ground} \ , \tag{290}$$

where P_{down} [mm h^{-1}] is the precipitation plus dripping reaching the ground level within the canyon accounting for tree canopy interception, and q_{roof} and q_{ground} are the roof and ground runon which represent the runoff fluxes that did not leave the system in the previous time step (Sect. 6.3).

The leakage of the impervious roof fraction Lk_r [mm h^{-1}] is zero, since the roof is considered perfectly impermeable, whereas the leakage of the impervious ground fraction Lk_g [mm h^{-1}] is modelled with a prescribed hydraulic conductivity $K_{g,imp}$, typically a small value corresponding to asphalt or other pavements which is a model input parameter.

The maximum storage capacity of the impervious roof $In^M_{r,imp}$ [mm] and ground $In^M_{g,imp}$ [mm] is a model input parameter and it depends on the roof and ground cover roughness and micro-depressions. Ponding water exceeding the maximum interception capacity is leaving the system as runoff or can remain in the system and becomes runon in the following time step (Sect. 6.3).

6.1.3 Ponding: Soil surface

Ponding and water logging on bare soil surfaces is calculated with the water budget equation:

$$\frac{dIn}{dt} = P_{soil} - I_{f\ soil} - E_{In} \ , \tag{291}$$

where P_{soil} [mm h^{-1}] is the incoming water flux to the soil, $I_{f\ soil}$ [mm h^{-1}] the soil infiltration rate (Sect. 6.2.2), and E_{In} [mm h^{-1}] the evaporation from ponding water on the soil. The incoming water flux to the roof $P_{r,soil}$ and ground $P_{g,soil}$ soil fractions is calculated as follows:

$$P_{r,soil} = P_{down} + q_{roof}(t-1) \ , \tag{292}$$

$$P_{g,bare,soil} = P_{down,tree} + q_{ground}(t-1) \ , \tag{293}$$

$$P_{g,veg,soil} = P_{down,tree,veg} + q_{ground}(t-1) \ , \tag{294}$$

where P_{down} [mm h^{-1}] is the precipitation reaching the soil level underneath the roof vegetation canopy accounting for canopy interception (Sect. 6.1.1), $P_{down,tree}$ [mm h^{-1}] is the precipitation reaching the canyon ground accounting for tree canopy interception, $P_{down,tree,veg}$ [mm h^{-1}] is the precipitation reaching the soil level underneath the ground vegetation canopy accounting for both tree and ground vegetation canopy interception. Finally, $q_{roof}(t-1)$ and $q_{ground}(t-1)$ are the roof and ground runon, i.e., the ponding water remaining in the system from the previous time step (Sect. 6.3).

6.2 Vadose zone dynamics

The urban soil and its vertical and horizontal $\theta(z,x)$ soil moisture profile directly influence water and energy fluxes in the urban environment. UT&C divides the urban soil into three soil columns beneath the impervious, bare, and vegetated ground cover fractions and one soil column for the vegetated roof fraction (Fig. 10). Soil underneath buildings is not considered in the current model formulation. The first two soil layers of the impervious ground soil column are assumed largely impermeable and do not participate in the water exchanges.

6.2.1 Vertical and horizontal soil moisture profile

The soil moisture and soil water content is calculated according to the 1D-Richards equation (Richards, 1931) describing the flow of water in variably saturated soils subjected to capillary and gravity forces in the vertical direction z (positive downward) as:

$$\frac{\partial \theta}{\partial t} = \frac{\partial}{\partial z}\left[K_v(\theta)\frac{\partial \Psi_S(\theta)}{\partial z} + K_v(\theta)\right] - S \ , \tag{295}$$

where θ $[-]$ is the soil water content, $K_v(\theta)$ $[\mathrm{mm\ h^{-1}}]$ the vertical hydraulic conductivity as a function of soil moisture, and $\Psi_S(\theta)$ $[\mathrm{mm}]$ the soil water potential. The sink term S $[\mathrm{h^{-1}}]$ accounts for lateral fluxes, soil evaporation, and root water uptake for transpiration.

The 1D-Richards equation is first solved in vertical direction for each soil column (impervious, bare, vegetated) using a finite volume approach with the method of lines (Lee et al., 2004), discretizing the spatial domain and reducing the partial differential equation to a system of ordinary differential equations in time as described by Fatichi et al. (2012a, b, c). Each soil column is subdivided into $j = 1, ..., n$ layers with varying layer thickness $d_{z,j}$ $[\mathrm{mm}]$. Soil layer depth z is increasing downwards (Fig. 10) and the top soil layer is soil layer 1. For each soil layer, the ordinary differential equation describing the change in soil moisture over time can be written as (Fatichi et al., 2012a, b, c):

$$d_{z,j}\frac{d\theta_j}{dt} = (q_{j-1} - q_j) + (Q_{l,in,j} - Q_{l,out,j}) - T_H\, r_{H_j} - T_L\, r_{L_j} - E_g \ , \tag{296}$$

where q_{j-1} and q_j $[\mathrm{mm\ h^{-1}}]$ are the vertical fluxes in and out of soil layer j, and $Q_{l,in,j}$ and $Q_{l,out,j}$ $[\mathrm{mm\ h^{-1}}]$ are the lateral fluxes in and out of soil layer j from and into the adjacent soil columns. The soil evaporation E_g $[\mathrm{mm\ h^{-1}}]$ is assumed to be only present in the first ($j = 1$) soil layer of the bare and vegetated soil column.

The transpirative sinks of high and low vegetation, T_H and T_L $[\mathrm{mm\ h^{-1}}]$, are weighted according to their root biomass fraction in each soil layer, r_{H_j} and r_{L_j} $[-]$. In the absence of trees or ground vegetation, T_H and T_L are zero. The calculation of root biomass fraction in each soil layer, r_{H_j} and r_{L_j} $[-]$, is described in Sect. 7.1 and 7.2.

The vertical water flow associated with soil layer j is calculated as:

$$q_j = \overline{K_{v,j}}\left(1 + \frac{\Psi_{S,j} - \Psi_{S,j+1}}{Dz_{j+1}}\right) \ , \tag{297}$$

where $\Psi_{S,j}$ $[\mathrm{mm}]$ is the soil water potential of layer j, $\overline{K_{v,j}}$ $[\mathrm{mm\ h^{-1}}]$ the vertical unsaturated hydraulic conductivity arithmetically averaged between soil layers j and j+1, and Dz_{j+1} $[\mathrm{mm}]$ the distance between the center of soil layer j and j+1.

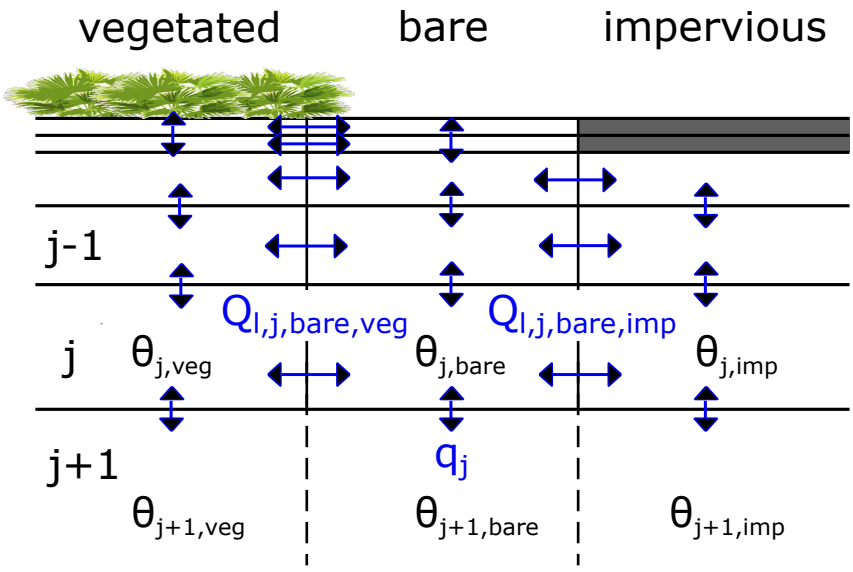

Figure 10. Soil layer (j) and soil column (vegetated, bare, and impervious) discretization. $Q_{l,j,bare,veg}$ and $Q_{l,j,bare,imp}$ denote the lateral water fluxes between bare and vegetated soil column and bare and impervious soil column in layer j and q_j the vertical water flux between soil layers.

The vertical inflow to the first soil layer is the infiltration $q_0 = I_f$ [mm h^{-1}] as calculated in Sect. 6.2.2. The outflow of the last soil layer is the deep leakage $q_n = L_{kb}$ [mm h^{-1}]. It is possible that soil layers become saturated for example when an impermeable bottom is defined. In this case, a shallow water table depth is calculated and the excess water is transported to the soil layers above. This mechanism can lead to a saturated zone within the soil column (Fatichi et al., 2012a, b, c).

The lateral water inflow to soil layer j in soil column k from the adjacent soil column i, $Q_{l,in,j,i\rightarrow k}$ [mm h^{-1}], with k and i denoting vegetated, bare, or impervious soil column, is calculated as:

$$Q_{l,in,j,i\rightarrow k} = a_r \left[K_{v,j,\overline{ik}} \left(\frac{\Psi_{S,j,i} - \Psi_{S,j,k}}{Dy} \right) \right] \left(\frac{d_{z,j}}{f_k \, W_{can}} \right) , \tag{298}$$

where $a_r = K_h/K_v$ [$-$] is an anisotropy factor accounting for the difference in horizontal, K_h, and vertical hydraulic conductivity, K_v (Garrote and Bras, 1995; Assouline and Or, 2006), $K_{v,j,\overline{ik}}$ [mm h^{-1}] is the arithmetic average of the vertical hydraulic conductivity of soil layer j in soil column i and k, and $\Psi_{S,j,k}$ and $\Psi_{S,j,i}$ [mm] are the soil water potential of layer j in soil column k and i, respectively. $Dy = 1000$ [mm] is a selected characteristic length scale on which soil moisture differences will affect the unsaturated lateral water exchange and it is a model input parameter. The factor $d_{z,j}/(f_k \, W_{can})$ rescales the horizontal water flux over the layer depth $d_{z,j}$ [mm] to the vertical water flux over the column width where f_k [$-$] is the ground cover fraction of column k and W_{can} [mm] the total canyon width. Note that the scaling factors of the lateral soil water fluxes vary depending on the extent of the soil columns origin and destination ~~soil columns~~ to garantuee mass conservation.

The soil moisture profile is numerically resolved in a mesh with n vertical layers and i = 1, 2, or 3 columns (Fig. 10) with width specified by the ground cover fractions (impervious, bare and vegetated) and roof cover fraction. A typical vertical soil layer parametrization includes n=10-30 ground layers and n=1-5 roof layers. The vertical mesh has a higher resolution near the surface and coarser resolution near the bottom with soil layer depths varying from 10 to 500 [mm] (Fatichi et al., 2012a, b, c).

The first two soil layers of the impervious soil column are considered impervious and do not interact with the vertical and lateral soil water transport. A small infiltration capacity can be prescribed for the impervious soil column and the infiltrated water will be directly added to the third soil layer. The lateral soil water exchange is calculated among all ground soil columns resulting in 3 ~~1~~ lateral fluxes. No lateral soil water exchange is calculated for the vegetated roof fraction.

The solution of the system of ordinary differential equations (Eq. 296 and 298) is carried out with a modified Rosenbrock formula of order 2 (Shampine and Reichelt, 1997).

6.2.2 Infiltration

The actual infiltration into the bare and vegetated soil column is calculated as the minimum between infiltration capacity I_f^C $[\mathrm{mm\ h^{-1}}]$ and water availability at the soil surface q_{ins} $[\mathrm{mm\ h^{-1}}]$ (Fatichi et al., 2012a, b, c):

$$I_f = \min\left(q_{ins}, I_f^C\right) , \tag{299}$$

The infiltration capacity I_f^C, as the upper limit to infiltration, is calculated as a soil hydraulic conductivity applying a Dirichlet boundary condition at the soil surface which assumes a soil water potential of zero (Fatichi et al., 2012a, b, c) and using the actual water potential of the first soil layer. The hydraulic conducitivity is calculated from the water potential with the pedotransfer functions described in Sect. 6.4. ~~UT&C does not yet account for soil crust mechanisms and soil surface sealing.~~

Similarly, a maximum impervious infiltration capacity $I_{f,imp}^C$ $[\mathrm{mm\ h^{-1}}]$ is prescribed for the impervious soil column. $I_{f,imp}^C$ is typically very small when compared to the permeability of natural surfaces.

6.3 Runoff and runon

Runoff R $[\mathrm{mm\ h^{-1}}]$ is generated as infiltration excess runoff (Hortonian runoff) when the available water at the ground surface exceeds the maximum infiltration capacity I_f^C $[\mathrm{mm\ h^{-1}}]$ and the maximum allowed ponding depth over bare and vegetated surfaces In^{Max} $[\mathrm{mm\ h^{-1}}]$ is overcome (Fatichi et al., 2012a, b, c). Runoff can further be generated as saturation excess runoff when a soil column becomes saturated and the shallow water table reaches the surface as described in Sect. 6.2.1.

The total roof and ground runoff are calculated as the area weighted average of the runoff generated by each surface fraction:

$$R_r = \sum f_{r,i} R_{r,i} , \tag{300}$$

$$R_g = \sum f_{g,i} R_{g,i} , \tag{301}$$

where $f_{r,i}$ and $f_{g,i}$ $[-]$ are the roof and ground cover fractions, and $R_{r,i}$, and $R_{g,i}$ $[\mathrm{mm\ h^{-1}}]$ are the roof and ground runoff of each surface fraction. It is assumed that roof runoff does not interact with the ground but rather enters into a sewer system.

A fraction of the total roof and ground runoff can be kept in the system and becomes runon in the next time step $R_{on}(t+1)$ $[\mathrm{mm\ h^{-1}}]$:

$$R_{on}(t+1) = \lambda_{R_{on}}\, R_i\ , \tag{302}$$

where $\lambda_{R_{on}} = [0-1]$ $[-]$ is the fraction of runoff kept in the system and and R_i $[\mathrm{mm\ h^{-1}}]$ is the total roof or ground runoff. The runon is distributed homogeneously over either the roof or ground and is put back into the system at the next time step. A runon fraction larger than zero ($\lambda_{R_{on}} > 0$) can account for microdepressions and surface exchanges between the various surfaces in the urban environment before the water reaches the sewer system. For example, it can account for runoff from impervious area that is redirected to infiltrate in vegetated areas in the roof or as for example in bioswales.

6.4 Soil hydraulic properties

UT&C can either use the van Genuchten (1980) or the Saxton and Rawls (2006) parameterization to calculate the soil hydraulic conductivity $K(\theta)$ $[\mathrm{mm\ h^{-1}}]$ and the soil water retention curve $\Psi_s = f(\theta)$ $[\mathrm{MPa}]$ which are a function of soil moisture content θ $[\mathrm{mm^3\ mm^{-3}}]$. Soil hydraulic properties are calculated according to the soil textural composition specified as fraction of clay, sand, and organic material in the soil. The hydraulic conductivity at field capacity is set to 0.2 $[\mathrm{mm\ h^{-1}}]$ and the soil water potential at residual water content to -10 $[\mathrm{MPa}]$. Further description on the calculation of soil hydraulic properties can be found in Fatichi et al. (2012a, b, c).

7 Plant water and biophysical relations

7.1 Horizontal root distribution

UT&C assumes that ground and roof vegetation can only access the soil moisture of the vegetated ground and roof fraction. Two possible horizontal tree root distributions are implemented that specify the abilty of the tree to reach different soil columns: (1) the trees have even access to the impervious, bare, and vegetation ground columns, and (2a) the trees have only access to the vegetated and bare ground columns, if the tree canopy is smaller than the combined vegetated and bare ground area, or (2b) the trees fully accesses the vegetated and bare soil columns and parts of the impervious soil column if the tree canopy is bigger than the combined vegetated and bare ground area.

7.2 Vertical root distribution and root soil moisture access

The fraction of root biomass within each soil layer r_j $[-]$ with $j = 1...n_s$, n_s being the last soil layer accessed by the roots, is calculated assuming a vertical root biomass profile (Fatichi et al., 2012a, b, c). Four different root biomass profiles can be specified in UT&C: (1) an exponential root profile (Arora and Boer, 2005; Ivanov et al., 2008a), (2) a linear dose response root profile (Schenk and Jackson, 2002; Collins and Bras, 2007), (3) a constant root profile, and (4) a linear dose response profile with tap roots (Fatichi et al., 2012a, b, c). The described root profiles are specified by the rooting depth containing 50 $\%$ and

95 % of the fine root biomass $Z_{R,50}$ and $Z_{R,95}$ [mm], and by the maximum rooting depth $Z_{R,max}$ [mm]. $Z_{R,50}$, $Z_{R,95}$, and $Z_{R,max}$ are model input parameters. Note that the maximum rooting depth $Z_{R,max}$ and the rooting depth containing 95 % of the fine roots $Z_{R,95}$ need to be smaller than the total soil depth as the soil profile is not resolved underneath (Fatichi et al., 2012a, b, c). The detailed description of the root biomass fraction calculation can be found in Fatichi et al. (2012a, b, c).

The average water content available to the roots of a given plant type θ_R [−] is calculated according to Fatichi et al. (2012a, b, c) as:

$$\theta_R = \sum_{j=1}^{n_s} r_j \theta_j \ , \tag{303}$$

where r_j [−] is the fraction of root biomass in soil layer j, θ_j [−] the soil moisture of soil layer j, and n_s the total number of soil layers. The average water content available to the roots θ_R [−] is used to calculate the soil water potential felt by the plant roots Ψ_{sR} [MPa] and the resulting water stress β [−] (Sect. 3.6.3).

7.3 Plant hydraulics

Plant hydraulics is currently not implemented in UT&C. It is assumed that leaf water potential Ψ_L [MPa] and xylem water potential Ψ_X [MPa] are equal to the soil water potential felt by the plant Ψ_{sR} [MPa] (Fatichi et al., 2012a, b, c).

7.4 Plant water uptake

The plant-water uptake J_{sx} [mm h^{-1}] is assumed to be equal to the transpirative flux T [mm h^{-1}] since there is no plant hydraulic component implemented in UT&C (Sect. 7.3). The plant water uptake and transpirative flux can be limited by the soil water availability and maximum root-water uptake capacity RWU_{max} [mm h^{-1}] and are calculated as:

$$J_{sx} = T = min(T_{\text{“}pot''}, soil\ water, RWU_{max}) \ , \tag{304}$$

The plant-water uptake J_{sx} is distributed within the different soil layers according to the root biomass fractions r_j [−]. The soil-to-root conductance in each soil layer j $g_{sr,j}$ [mmol H_20 s^{-1} MPa^{-1} m^{-2} ground] parameterizes the hydraulic resistance between soil and root and is calculated as (Newman, 1969; Deckmyn et al., 2008; Fatichi et al., 2012a, b, c):

$$g_{sr,j} = \kappa K_v(\theta_j)\, R_{L,j}\, 2\pi \log\left[\frac{r_{cyl}}{r_{root}}\right] \ , \tag{305}$$

where $\kappa = 5.66 \cdot 10^9$ is an unit conversion factor, $K_v(\theta_j)$ [m s^{-1}] the unsaturated hydraulic conductivity as a function of soil water content in layer j, $R_{L,j} = r_j R_L$ [m root m^{-2} ground] the root length density in a given soil layer for a given vegetation type, $r_{root} = 0.5$ mm the average radius of fine roots, and $r_{cyl} = 2.0$ mm the average radius to which roots have soil access. The root length density R_L [m root m^{-2} ground] is a model input parameter.

The maximum root-water uptake capacity in each soil layer $RWU_{max,j}$ [mm h^{-1}] is calculated with the soil-to-root conductance $g_{sr,j}$ [mmol H_20 s^{-1} MPa^{-1} m^{-2} ground] as described in Fatichi et al. (2012a, b, c):

$$RWU_{max,j} = \tilde{\kappa} g_{sr,j} |\Psi_{s,j} - \Psi_{min}| \ , \tag{306}$$

where $\tilde{\kappa} = 0.0648$ is a unit conversion factor (Fatichi et al., 2012a, b, c), $\Psi_{s,j}$ [MPa] the soil water potential in soil layer j, and $\Psi_{min} = \min(\Psi_{X,50}, \Psi_{L,50})$ [MPa] the minimum water potential experienced by the leaf $\Psi_{L,50}$ [MPa] or xylem $\Psi_{X,50}$ [MPa] before a 50 % reduction of hydraulic conductivty occurs. Ψ_{min} represents a lower limit for plant water extraction. Furthermore, low values of soil-to-root conductance prevent plant water uptake.

8 Anthropogenic water

UT&C accounts for prescribed timeseries of anthropogenic water Q_f [$\mathrm{mm\ h^{-1}}$] to the vegetated roof, bare ground, and vegetated ground. The anthropogenic water can either be added above the vegetation canopy or on the soil underneath to represent sprinkler and hose irrigation or drip irrigation.

9 Model input parameters

The following tables summarize the model input parameters used in the model performance assessment for Singapore, Melbourne and Phoenix. Specifically, they specify the urban geometry, radiation and conductive heat flux parameters (Table 1), vegetation parameters (Table 2), soil, interception and runoff parameters (Table 3), location parameters, as well as anthropogenic heat forcings (Table 4), and irrigation time series (Table 5).

Table 1. Urban Geometry, radiation, and conductive heat flux parameters used for the model validation in Singapore (SG), Melbourne (MB), and Phoenix (PH).

Parameter	Description	SG	MB	PH
H_{can}	Height of urban canyon (m)	9.86$^{(1,2)}$	6.4$^{(4,5)}$	4.5$^{(7)}$
W_{can}	Ground width of urban canyon (m)	16.16$^{(1,2,3)*}$	15.2$^{(4,5)*}$	11.3$^{(7)*}$
W_{roof}	Roof width of urban canyon (m)	10.33$^{(1,2,3)*}$	12.2$^{(4,5)*}$	4$^{(7)*}$
H_{tree}	Tree height (m)	7.26$^{(1,2)}$	4.2	4$^{(7)}$
R_{tree}	Tree radius (=1/4 $f_{g,tree}$ *W_{can}) (m)	0.73$^{(1,2,3)*}$	1.5$^{(4,5)*}$	0.19$^{(7)*}$
D_{tree}	Distance of wall to tree trunk (m)	3$^{(a)}$	2$^{(a)}$	2$^{(a)}$
N_{tree}	Absence (0) or presence (1) of trees $(-)$	1$^{(1,2)}$	1$^{(6)}$	1$^{(7)}$
$f_{r,imp}$	Fraction of impervious roof $(-)$ $^{(+)}$	1$^{(a)}$	1$^{(a)}$	1$^{(a)}$
$f_{r,veg}$	Fraction of vegetated roof $(-)$ $^{(+)}$	0$^{(a)}$	0$^{(a)}$	0$^{(a)}$
$f_{g,imp}$	Fraction of impervious ground $(-)$ $^{(+)}$	0.75$^{(1,2)}$	0.53$^{(4,5)}$	0.32$^{(7)}$
$f_{g,bare}$	Fraction of bare ground $(-)$ $^{(+)}$	0$^{(1,2)}$	0.02$^{(4,5)}$	0.53$^{(7)}$
$f_{g,veg}$	Fraction of vegetated ground $(-)$ $^{(+)}$	0.25$^{(1,2)}$	0.45$^{(4,5)}$	0.15$^{(7)}$
α_r	Albedo roof [imp, veg] $(-)$	[0.2$^{(8)}$, -]	[0.15$^{(6)}$, -]	[0.16$^{(10)}$, -]
α_g	Albedo ground [imp, bare, veg] $(-)$	[0.08$^{(8)}$, 0.2$^{(a)}$, 0.27$^{(8)}$]	[0.1$^{(6)}$, 0.2$^{(a)}$, 0.27]	[0.15$^{(9)}$, 0.2$^{(a)}$, 0.27]
α_w	Albedo wall $(-)$	0.5$^{(8)}$	0.3$^{(6)}$	0.5$^{(8)}$
α_t	Albedo tree canopy $(-)$	0.27$^{(8)}$	0.27	0.27
ϵ_r	Emissivity roof [imp, veg] $(-)$	[0.9$^{(8)}$, -]	[0.92$^{(6)}$, -]	[0.95$^{(9)}$, -]
ϵ_g	Emissivity ground [imp, bare, veg] $(-)$	[0.94$^{(8)}$, 0.95$^{(a)}$, 0.97$^{(8)}$]	[0.92$^{(6)}$, 0.973$^{(5)}$, 0.97$^{(8)}$]	[0.95$^{(9)}$, 0.98$^{(11)}$, 0.97$^{(8)}$]
ϵ_w	Emissivity wall $(-)$	0.9$^{(8)}$	0.88$^{(6)}$	0.95$^{(9)}$
ϵ_t	Emissivity tree canopy $(-)$	0.97$^{(8)}$	0.97$^{(8)}$	0.97$^{(8)}$
$\lambda_{r,imp}$	Thermal conductivity of impervious roof $(\mathrm{W\ K^{-1}\ m^{-1}})$	0.406$^{(3)*}$	0.773$^{(5)*}$	0.6$^{(9)}$
$\lambda_{g,imp}$	Thermal conductivity of impervious ground $(\mathrm{W\ K^{-1}\ m^{-1}})$	1.552$^{(3)*}$	2.682$^{(5)*}$	1.2$^{(9)}$
λ_w	Thermal conductivity of wall $(\mathrm{W\ K^{-1}\ m^{-1}})$	0.75$^{(3)*}$	0.342$^{(5)*}$	1.3$^{(9)}$
$Cv_{r,imp}$	Volumetric heat capacity of impervious roof $(\mathrm{MJ\ K^{-1}\ m^{-3}})$	0.577$^{(3)*}$	0.813$^{(5)*}$	1.9$^{(9)}$
$Cv_{g,imp}$	Volumetric heat capacity of impervious ground $(\mathrm{MJ\ K^{-1}\ m^{-3}})$	1.552$^{(3)*}$	1.3413$^{(5)*}$	1.1$^{(9)}$
Cv_w	Volumetric heat capacity of wall $(\mathrm{MJ\ K^{-1}\ m^{-3}})$	1.357$^{(3)*}$	0.9035$^{(5)*}$	1.5$^{(9)}$
dz_r	Thickness of roof layers [1, 2] (m)	[0.106, 0.106]$^{(8)*}$	[0.057, 0.057]$^{(5)*}$	[0.075, 0.075]$^{(a)}$
dz_w	Thickness of wall layers [1, 2] (m)	[0.098, 0.098]$^{(8)*}$	[0.074, 0.074]$^{(5)*}$	[0.075, 0.075]$^{(a)}$

* Calculated from literature values, $^{(a)}$ Assumption, $^{(1)}$ Velasco et al. (2013), $^{(2)}$ Roth et al. (2016), $^{(3)}$ Demuzere et al. (2017), $^{(4)}$ Coutts et al. (2007a, b), $^{(5)}$ Grimmond et al. (2011), $^{(6)}$ Nice et al. (2018), $^{(7)}$ Chow et al. (2014), $^{(8)}$ Harshan et al. (2017), $^{(9)}$ Song and Wang (2015), $^{(10)}$ Yang et al. (2015), $^{(11)}$ Park and Lee (2008); $^{(+)}$ land cover fractions reported in literature were rescaled by the canyon and roof fraction so that $f_{r,imp}$+$f_{r,veg}$ = 1 and $f_{g,imp}$+$f_{g,bare}$+$f_{g,veg}$ = 1.

Table 2. Vegetation parameters* used for the model validation in Singapore (SG), Melbourne (MB), and Phoenix (PH). Seperate parameters for roof vegetation [r_{veg}], ground vegetation [g_{veg}], and trees [$_{tree}$] are specified for each location in this respective order.

Parameter	Description	SG $[r_{veg}, g_{veg}, tree]$	MB $[r_{veg}, g_{veg}, tree]$	PH $[r_{veg}, g_{veg}, tree]$
h_c	Canopy height (m)	[-, 0.05, 7.26]	[-, 0.1, 4.2]	[-, 0.1, 4]
d_{leaf}	Leaf dimension (cm)	[-, 2, 5]	[-, 2, 3]	[-, 0.8, 1.5]
LAI	Leaf area index $(-)$	[-, 2.5, 3$^{(2)}$]	[-, 3, 3]	[-, 1.5, 1.8]
SAI	Stem area index $(-)$	[-, 0.001, 0.2]	[-, 0.001, 0.1]	[-, 0.001, 0.1]
S_{LAI}	Specific leaf area $(\mathrm{m^2\ LAI\,g\ C^{-1}})$	[-, 0.025, 0.02]	[-, 0.016, 0.009]	[-, 0.022, 0.015]
K_{opt}	Canopy light extinction coefficient $(-)$	[-, 0.5, 0.5]	[-, 0.5, 0.5]	[-, 0.5, 0.5]
$VCASE_{root}$	Vertical root profile (1, 2, 3, 4)	[-, 1, 1]	[-, 1, 1]	[-, 1, 1]
$HCASE_{root}$	Type of root profile of tree (1, 2)	2	2	2
ZR_{50}	Root depth, 50^{th} percentile (mm)	[-, -, -]	[-, -, -]	[-, -, -]
ZR_{95}	Root depth, 95^{th} percentile of vegetation (mm)	[-, 300, 1500$^{(1)}$]	[-, 200, 1000]	[-, 250, 1000]
RI_{root}	Root length index $(\mathrm{m\ root\ m^{-2}\ PFT})$	[-, 4000, 2200]	[-, 4500, 5000]	[-, 2000, 1200]
$\psi_{Sto_{00}}$	Soil water potential at the beginning of stomatal closure (MPa)	[-, -0.5, -0.9]	[-, -0.6, -0.7]	[-, -0.5, -0.9]
$\psi_{Sto_{50}}$	Soil water potential at 50 % stomatal closure (MPa)	[-, -1.6, -1.7]	[-, -2, -1.5]	[-, -3, -2]
ψ_{L50}	Water potential at 50 % of leaf hydraulic conductivity (MPa)	[-, -2, -2.8]	[-, -2.5, -2.5]	[-, -2.5, -1.2]
ψ_{X50}	Water potential at 50 % of xylem hydraulic conductivity and limit for water extraction from soil (MPa)	[-, -5.5, -4.5]	[-, -9.5, -9]	[-, -3.5, -4]
ϕ_p	Photosynthesis pathway (C_3, C_4, or CAM)	[-, 4, 3]	[-, 3, 3]	[-, 3, 3]
K_N	Canopy nitrogen decay coefficient $(-)$	[-, 0.3, 0.4]	[-, 0.3, 0.15]	[-, 0.2, 0.25]
$V_{c,max}$	Maximum Rubisco capacity at 25 °C leaf scale $(\mu\mathrm{mol\ CO_2\ m^{-2}\ s^{-1}})$	[-, 54, 49]	[-, 54, 45]	[-, 58, 45]
g_{0,CO_2}	Minimum/cuticular stomatal conductance $(\mathrm{mol\ CO_2\ m^{-2}\ leaf\ s^{-1}})$	[-, 0.01, 0.01]	[-, 0.01, 0.01]	[-, 0.01, 0.01]
a_1	Empirical parameter linking net assimilaton A_{nC} to stomatal conductance g_{s,CO_2} $(-)$	[-, 5, 9]	[-, 7, 8]	[-, 6, 9]
r_{jv}	Scaling factor between J_{max} and $V_{c,max}$ $(\mu\mathrm{mol\ equivalent\ \mu mol^{-1}\ CO_2})$	[-, 2.1, 2.2]	[-, 2.1, 2.0]	[-, 2.2, 2.0]
ϵ_{FI}	Intrinsec quantum efficency $(\mu\mathrm{mol\ CO_2\ \mu mol^{-1}\ photons})$	[-, 0.04, 0.081]	[-, 0.081, 0.081]	[-, 0.081, 0.081]
$\Delta_{0,r}$	Empirical coefficient that expresses the value of vapor pressure deficit at which $f(\Delta e) = 0.5$ (Pa)	[-, 2000, 2000]	[-, 1000, 1200]	[-, 2000, 2000]

* (Fatichi and Pappas, 2017), $^{(1)}$ Harshan et al. (2017), $^{(2)}$ Liu et al. (2017)

Table 3. Soil, interception, and runoff parameters used for the model validation in Singapore (SG), Melbourne (MB), and Phoenix (PH).

Parameter	Description	SG	MB	PH
$Z_{s,r}$	Roof soil layer discretization (mm)	-	-	-
$Z_{s,g}$	Ground soil layer discretization (mm)	[0 ... 2000]	[0 ... 2000]	[0 ... 2000]
$F_{r,soil}$	Roof soil composition [f_{clay}, f_{sand}, $f_{organic}$] $(-)$	-	-	-
$F_{g,soil}$	Ground soil composition [f_{clay}, f_{sand}, $f_{organic}$] $(-)$	[0.20, 0.40, 0.025]	[0.20, 0.40, 0.025]	[0.20, 0.40, 0.025]
K_{imp}	Hydraulic conductivity of impervous surface [$_{roof}$, $_{ground}$] $(\mathrm{mm\ h^{-1}})$	[-, 0.001]	[-, 0.001]	[-, 0.001]
K_{bot}	Hydraulic conductivity of at the bottom of the last soil layer [$_{roof}$, $_{ground}$] $(\mathrm{mm\ h^{-1}})$	[-, free drainage]	[-, free drainage]	[-, free drainage]
$SPAR$	Soil parameter type, 1-VanGenuchten or 2-Saxton-Rawls [$_{roof}$, $_{ground}$] $(-)$	[-, 2]	[-, 2]	[-, 2]
In_{imp}^{max}	Maximum interception capacity of impervious surfaces [$_{roof}$, $_{ground}$] (mm)	[0.25, 0.5]	[0.25, 0.5]	[0.25, 0.5]
In_{soil}^{max}	Maximum interception capacity on top of soil [$_{r,veg}$, $_{g,bare}$, $_{g,veg}$] (mm)	[-, 10, 10]	[-, 10, 10]	[-, 10, 10]
$S_{P,In}^{max}$	Specific water retained by vegetation surface [$_{r,veg}$, $g_{g,veg}$, $_{tree}$] $(\mathrm{mm\ m^2\ PFT\ area\ m^{-2}\ leaf\ area})$	[-, 0.2, 0.1]	[-, 0.2, 0.1]	[-, 0.2, 0.1]
λ_r	Percentage of runoff that leaves the system [$_{roof}$, $_{ground}$] $(-)$	[1, 0.5]	[1, 0.5]	[1, 0.5]

Table 4. Location and measurement parameters, and anthropogenic heat used for the model validation in Singapore (SG), Melbourne (MB), and Phoenix (PH).

Parameter	Description	SG	MB	PH
ϕ_{data}	Latitude (positive north) $(^\circ)$	1.31[1,2]	-37.81[6]	33.48[8]
λ_{data}	Longitude (positive east) $(^\circ)$	103.91[1,2]	144.88[6]	-112.14[8]
θ_{canyon}	Canyon orientation [direction 1, direction 2] $(^\circ)$	[78, 157][10]	[98, 189][10]	[90, 180][10]
Δ_{GMT}	difference of LT with Greenwich Meridian Time (h)	8[2]	10	-7
Z_{atm}	Atmospheric forcing/reference height (m)	23.7[3,4,5]	40[6,7]	22.1[8]
$T_{b,min}$	Minimum interior building temperature $(^\circ\mathrm{C})$	20	18	18
$T_{b,max}$	Maximum interior building temperature $(^\circ\mathrm{C})$	25	27	28
$Q_{f,roof}$	Anthropogenic heat input on top of roof $(\mathrm{W\ m^{-1}})$	0	0	0
$Q_{f,can}$	Anthropogenic heat input within canyon $(\mathrm{W\ m^{-1}})$	11[2]	0	23.25[9]

[1] Velasco et al. (2013), [2] Roth et al. (2016), [3] Demuzere et al. (2017), [4] Harshan et al. (2017), [5] Liu et al. (2017), [6] Coutts et al. (2007a, b), [7] Grimmond et al. (2011), [8] Chow et al. (2014), [9] average calculated from values reported by Chow et al. (2014), [10] estimated from GoogleEarth.

Table 5. Timeseries of urban irrigation applied during model performance assessment of UT&C in Singapore, Melbourne, and Phoenix. In short, no irrigation is applied in Singapore, while plants receive irrigation during summer and autumn time in Melbourne, and there is hose irrigation year-round with higher values during summer time in Phoenix (Volo et al., 2014).

	Time (h)	Vegetated roof ($\mathrm{mm\ h^{-1}}$)	Bare ground ($\mathrm{mm\ h^{-1}}$)	Vegetated ground ($\mathrm{mm\ h^{-1}}$)
Singapore				
1^{st} of January - 31^{st} of December	00:00-23:00	-	0	0
Melbourne				
15^{th} of November - 29^{th} of February	00:00-23:00	-	0	0.125
1^{st} of March - 15^{th} of April	00:00-23:00	-	0	0.083
16^{th} of April - 14^{th} of November	00:00-23:00	-	0	0
Phoenix				
January	06:00 - 17:00	-	0	0.0365
February	06:00 - 17:00	-	0	0.0437
March	06:00 - 17:00	-	0	0.1313
April	06:00 - 17:00	-	0	0.4375
May	06:00 - 17:00	-	0	1.0646
June	06:00 - 17:00	-	0	1.1812
July	06:00 - 17:00	-	0	1.2396
August	06:00 - 17:00	-	0	0.2625
September	06:00 - 17:00	-	0	0.1604
October	06:00 - 17:00	-	0	0.1167
November	06:00 - 17:00	-	0	0.0729
December	06:00 - 17:00	-	0	0.0219

10 Additional Figures and model performance results

The following Tables ~~?? and ??~~ 6 to 10 provide additional model performance results for the total time periods~~as well as~~ , daytime and nighttime fluxes~~.~~, and different seasons. In Singapore, the model performance is analysed for a dry period (15.2.2014 - 16.3.2014) and a wet period (16.11.2013 - 17.12.2013) as defined by Harshan et al. (2017). In Melbourne, the model performance is analysed for spring (23^{rd} of September to 21^{nd} of December), summer (22^{rd} of December to 19^{th} of March), autumn (20^{th} of March to 20^{th} of June), and winter (21^{st} of June to 22^{nd} of September) time. Similarly, model performance is analysed in Phoenix for spring (20^{th} of March to 20^{th} of June), summer (21^{st} of June to 22^{nd} of September), autum (23^{rd} of September to 21^{nd} of December), and winter (22^{rd} of December to 19^{th} of March) time.

The following figures show the validation of shortwave radiation (Fig. 11), and longwave radiation (Fig. 12) in Singapore, Melbourne, and Phoenix as an addition to the validation of net all wave radiation presented in the main article. Figure 14 and 15 show the sensitivity of evapotranspiration and the energy fluxes to the change in vegetated ground cover ($\lambda_{G,veg}$), leaf area index (LAI), and maximum Rubisco capacity ($V_{c,max}$) in Singapore as an addition to the sensitivity of 2 m air temperature, 2 m humidity and the water fluxes presented in the main article.

Table 6. Coefficient of determination (R^2), mean bias error (MBE), root mean square error (RMSE), systematic root mean square error (RMSE_s), unsystematic root mean square error (RMSE_u), and mean absolute error (MAE) of the UT&C model performance assessment in Singapore, Melbourne and Phoenix ~~split in daytime and nighttime values~~ for the ~~radiative fluxes~~outgoing shortwave radiation ($S\uparrow$). The validation period specifies the total UT&C simulation period in hours (h) and the percentage of time with available eddy-covariance measurements for model performance assessment.

	R^2 (−)	MBE ($\mathrm{W\ m^{-2}}$)	RMSE ($\mathrm{W\ m^{-2}}$)	RMSE_s ($\mathrm{W\ m^{-2}}$)	RMSE_u ($\mathrm{W\ m^{-2}}$)	MAE ($\mathrm{W\ m^{-2}}$)	Validation period % of (h)
$S\uparrow$ (Singapore), full period, daytime	0.97	-5.5	9.7	7.6	6	6.6	84 % of 4015 h
$S\uparrow$ (Singapore), dry period, daytime	0.97	-13.1	16.3	15.1	6.1	13.3	99 % of 330 h
$S\uparrow$ (Singapore), wet period, daytime	0.99	1.7	3.6	1.7	3.1	2.6	86 % of 352 h
$S\uparrow$ (Melbourne), full period, daytime	0.99	-12.5	16.3	15.9	3.4	12.8	65 % of 5747 h
$S\uparrow$ (Melbourne), spring, daytime	0.99	-14.3	17.8	17.5	3.2	14.4	68 % of 2110 h
$S\uparrow$ (Melbourne), summer, daytime	0.99	-15.6	19.1	18.8	3.6	15.8	86 % of 1200 h
$S\uparrow$ (Melbourne), autumn, daytime	0.98	-8	11.4	10.8	3.5	8.8	84 % of 977 h
$S\uparrow$ (Melbourne), winter, daytime	0.98	-7.7	10.5	10.1	2.8	8.2	30 % of 1460 h
$S\uparrow$ (Phoenix), full period, daytime	0.98	-5.9	10.7	8.8	6.1	8.1	98 % of 4539 h
$S\uparrow$ (Phoenix), spring, daytime	0.99	-11.6	14.6	13.8	4.7	12.3	97 % of 1242 h
$S\uparrow$ (Phoenix), summer, daytime	0.99	-6.8	9.6	8.2	4.9	7.6	99 % of 1251 h
$S\uparrow$ (Phoenix), autumn daytime	0.96	-1.9	8.6	4.7	7.2	6.4	99 % of 1001 h
$S\uparrow$ (Phoenix), winter, daytime	0.97	-2.1	8	5.6	5.7	5.5	97 % of 1045 h

Table 7. Same as Table 6 for outgoing longwave radiation ($L\uparrow$).

	R^2 (−)	MBE (W m^{-2})	RMSE (W m^{-2})	$RMSE_s$ (W m^{-2})	$RMSE_u$ (W m^{-2})	MAE (W m^{-2})	Validation period % of (h)
$L\uparrow$ (Singapore), full period	0.93	8.3	23.3	20.4	11.4	17.3	86 % of 8760 h
$L\uparrow$ (Singapore), full period, daytime	0.93	28.2	33.4	31.6	10.6	28.4	84 % of 4015 h
$L\uparrow$ (Singapore), full period, nighttime	0.79	-8.3	9.3	8.4	3.9	8.6	88 % of 4015 h
$L\uparrow$ (Singapore), dry period	0.98	8.9	23.8	22.8	6.9	18.2	99 % of 720 h
$L\uparrow$ (Singapore), dry period, daytime	0.98	29.7	33.8	33.1	7	29.7	99 % of 330 h
$L\uparrow$ (Singapore), dry period, nighttime	0.94	-9	9.4	9.1	2	9	100 % of 330 h
$L\uparrow$ (Singapore), wet period	0.94	8.9	22.9	21	9.1	16.1	89 % of 768 h
$L\uparrow$ (Melbourne), full period	0.94	7.8	14.8	8.6	12	11.7	62 % of 11376 h
$L\uparrow$ (Melbourne), full period, daytime	0.95	15.2	18.8	15.5	10.7	16	64 % of 5747 h
$L\uparrow$ (Melbourne), full period, nighttime	0.91	-0.1	8.6	6.1	6	7	61 % of 5629 h
$L\uparrow$ (Melbourne), spring	0.93	8.3	16.4	9.9	13.1	12.7	63 % of 3768 h
$L\uparrow$ (Melbourne), summer	0.96	3.7	14.8	9.9	11	11.8	86 % of 2136 h
$L\uparrow$ (Melbourne), autumn	0.93	9.5	13.3	10	8.8	10.5	84 % of 2232 h
$L\uparrow$ (Melbourne), winter	0.91	10.9	13.2	11.4	6.7	11.1	30 % of 3240 h
$L\uparrow$ (Phoenix), full period	0.98	4.9	11.5	5.4	10.2	9.2	98 % of 9144 h
$L\uparrow$ (Phoenix), full period, daytime	0.98	8.2	13.5	8.6	10.5	11.2	98 % of 4539 h
$L\uparrow$ (Phoenix), full period, nighttime	0.99	1.6	9.1	8	4.3	7.3	98 % of 4605 h
$L\uparrow$ (Phoenix), spring	0.97	3.3	11.9	4	11.3	8.7	97 % of 2232 h
$L\uparrow$ (Phoenix), summer	0.96	1.4	13	4.5	12.2	10.5	98 % of 2256 h
$L\uparrow$ (Phoenix), autumn	0.98	4.6	9.1	4.7	7.9	7.1	99 % of 2280 h
$L\uparrow$ (Phoenix), winter	0.98	10	11.8	10.4	5.5	10.4	98 % of 2376 h

Table 8. Same as Table 6 for net absorbed radiation (R_n).

	R^2 (−)	MBE ($W\ m^{-2}$)	RMSE ($W\ m^{-2}$)	$RMSE_s$ ($W\ m^{-2}$)	$RMSE_u$ ($W\ m^{-2}$)	MAE ($W\ m^{-2}$)	Validation period % of (h)
R_n (Singapore), full period	>0.99	-4.9	20.8	19	8.4	16.4	84 % of 8760 h
R_n (Singapore), full period, daytime	>0.99	-22.8	28	26.2	10	23.4	84 % of 4015 h
R_n (Singapore), full period, nighttime	0.91	11.3	12.2	11.8	3.1	11.4	84 % of 4015 h
R_n (Singapore), dry period	>0.99	-2.3	17	15.2	7.5	14.3	93 % of 720 h
R_n (Singapore), dry period, daytime	>0.99	-16.6	21.1	19	9.2	17.6	99 % of 330 h
R_n (Singapore), dry period, nighttime	0.87	12.1	12.4	12.2	2.4	12.1	87 % of 330 h
R_n (Singapore), wet period	>0.99	-8.8	24.5	23.8	5.8	18	89 % of 768 h
R_n (Melbourne), full period	>0.99	-0.6	9.5	1.5	9.4	7.5	62 % of 11376 h
R_n (Melbourne), full period, daytime	>0.99	-2.7	9.4	3	8.9	7.5	64 % of 5747 h
R_n (Melbourne), full period, nighttime	0.94	1.7	9.6	6.9	6.6	7.5	61 % of 5629 h
R_n (Melbourne), spring	>0.99	0.6	9.8	2.3	9.5	7.7	63 % of 3768 h
R_n (Melbourne), summer	>0.99	5.7	10.2	6.3	8	7.9	86 % of 2136 h
R_n (Melbourne), autumn	>0.99	-5.1	8.8	5.8	6.6	7.1	84 % of 2232 h
R_n (Melbourne), winter	>0.99	-6.6	8.6	6.8	5.2	7.1	30 % of 3240 h
R_n (Phoenix), full period	>0.99	-2.1	12.5	2.1	12.3	9.7	98 % of 9144 h
R_n (Phoenix), full period, daytime	>0.99	-2.3	15	2.3	14.8	11.9	98 % of 4539 h
R_n (Phoenix), full period, nighttime	0.8	-1.9	9.4	4.3	8.3	7.4	98 % of 4605 h
R_n (Phoenix), spring	>0.99	3.1	13.9	4.4	13.2	10.6	97 % of 2232 h
R_n (Phoenix), summer	>0.99	2.4	12.2	6.8	10.1	9.7	98 % of 2256 h
R_n (Phoenix), autumn	>0.99	-4	11	5	9.8	7.8	99 % of 2280 h
R_n (Phoenix), winter	>0.99	-9.2	12.7	9.4	8.5	10.6	98 % of 2376 h

Table 9. Same as Table ~~??~~ 6 for sensible heat fluxes (H)~~and latent (λE) heat fluxes~~.

	R^2 (−)	MBE ($W\ m^{-2}$)	RMSE ($W\ m^{-2}$)	$RMSE_s$ ($W\ m^{-2}$)	$RMSE_u$ ($W\ m^{-2}$)	MAE ($W\ m^{-2}$)	Validation period % of (h)
H (Singapore), full period	0.93	-3.3	25.6	3.3	25.3	15.4	82 % of 8760 h
H (Singapore), full period, daytime	0.87	-3.3	37	3.3	36.8	26.6	80 % of 4015 h
H (Singapore), full period, nighttime	0.35	-3	8.2	7.5	3.2	5.9	84 % of 4015 h
H (Singapore), dry period	0.95	-8.1	30	8.2	28.9	20.4	99 % of 720 h
H (Singapore), dry period, daytime	0.89	-10.5	43.1	13.8	40.8	35.2	98 % of 330 h
H (Singapore), dry period, nighttime	0.62	-5.2	8.9	8.4	3	7.2	100 % of 330 h
H (Singapore), wet period	0.91	-1.3	20.3	1.9	20.2	12.8	89 % of 768 h
H (Melbourne), full period	0.9	14.4	36.6	17.2	32.3	23.6	93 % of 11376 h
H (Melbourne), full period, daytime	0.86	25.5	49.8	26.3	42.3	37.2	93 % of 5747 h
H (Melbourne), full period, nighttime	0.48	2.9	13.1	8.2	10.2	9.7	92 % of 5629 h
H (Melbourne), spring	0.9	16	41.8	18.7	37.4	27.2	92 % of 3768 h
H (Melbourne), summer	0.93	8.5	38.4	16.4	34.7	25.2	97 % of 2136 h
H (Melbourne), autumn	0.9	12.1	28.8	17.5	22.9	18	93 % of 2232 h h
H (Melbourne), winter	0.84	18.1	33.6	20	27	22.2	90 % of 3240 h h
H (Phoenix), full period	0.92	10.9	27.4	11.6	24.9	20.7	78 % of 9144 h
H (Phoenix), full period, daytime	0.88	7.6	33.8	8.2	32.8	26.3	77 % of 4539 h
H (Phoenix), full period, nighttime	0.1	14	19.2	15.6	11.2	15.1	78 % of 4605 h
H (Phoenix), spring	0.94	11.9	32.3	13	29.6	22.9	51 % of 2232 h
H (Phoenix), summer	0.94	1.5	26	4.8	25.6	18.4	78 % of 2256 h
H (Phoenix), autumn	0.89	11	24.8	12.7	21.3	18.8	83 % of 2280 h
H (Phoenix), winter	0.89	17.3	28	18.4	21	22.8	98 % of 2376 h

Table 10. Same as Table 6 for latent heat fluxes (λE).

	R^2 (−)	MBE ($W\ m^{-2}$)	RMSE ($W\ m^{-2}$)	$RMSE_s$ ($W\ m^{-2}$)	$RMSE_u$ ($W\ m^{-2}$)	MAE ($W\ m^{-2}$)	Validation period % of (h)
λE (Singapore), full period	0.58	-0.6	28.7	13.8	25.2	15.9	81 % of 8760 h
λE (Singapore), full period, daytime	0.27	1.4	39.8	27	29.3	26.7	80 % of 4015 h
λE (Singapore), full period, nighttime	0.25	-2.1	12.9	11.7	5.5	6.2	81 % of 4015 h
λE (Singapore), dry period	0.67	2.5	16.2	7	14.7	10.5	97 % of 720 h
λE (Singapore), dry period, daytime	0.24	4.8	22.5	18	13.5	17.2	98 % of 330 h
λE (Singapore), dry period, nighttime	0.03	0.2	6.2	5.8	2.2	3.9	95 % of 330 h
λE (Singapore), wet period	0.54	-4.9	32.6	19.6	26.1	18.3	88 % of 768 h
λE (Melbourne), full period	0.62	1.9	26.8	9.4	25.1	16.8	93 % of 11376 h
λE (Melbourne), full period, daytime	0.48	3.5	34.3	14.9	30.9	23.5	93 % of 5747 h
λE (Melbourne), full period, nighttime	0.15	0.2	15.6	11.6	10.5	10	92 % of 5629 h
λE (Melbourne), spring	0.62	1.6	32.6	13.9	29.4	20.7	92 % of 3768 h
λE (Melbourne), summer	0.64	6.8	29.6	9	28.2	19.4	97 % of 2136 h
λE (Melbourne), autumn	0.57	-0.1	17	5.7	16	10.8	93 % of 2232 h
λE (Melbourne), winter	0.47	0.2	22.3	9.5	20.2	14.7	90 % of 3240 h h
λE (Phoenix), full period	0.5	4.1	19.5	11.3	16	11.5	78 % of 9144 h
λE (Phoenix), full period, daytime	0.3	7.1	25.2	19.5	15.9	17.8	77 % of 4539 h
λE (Phoenix), full period, nighttime	0.16	1.2	11.7	10.1	5.8	5.3	78 % of 4605 h
λE (Phoenix), spring	0.61	8.1	19.5	11.2	16	13.8	51 % of 2232 h
λE (Phoenix), summer	0.38	2.4	28.3	21.4	18.5	18.1	78 % of 2256 h
λE (Phoenix), autumn	0.4	3.1	17.8	10.4	14.4	9.6	83 % of 2280 h
λE (Phoenix), winter	0.62	4.3	11	4.3	10.1	6.8	98 % of 2376 h

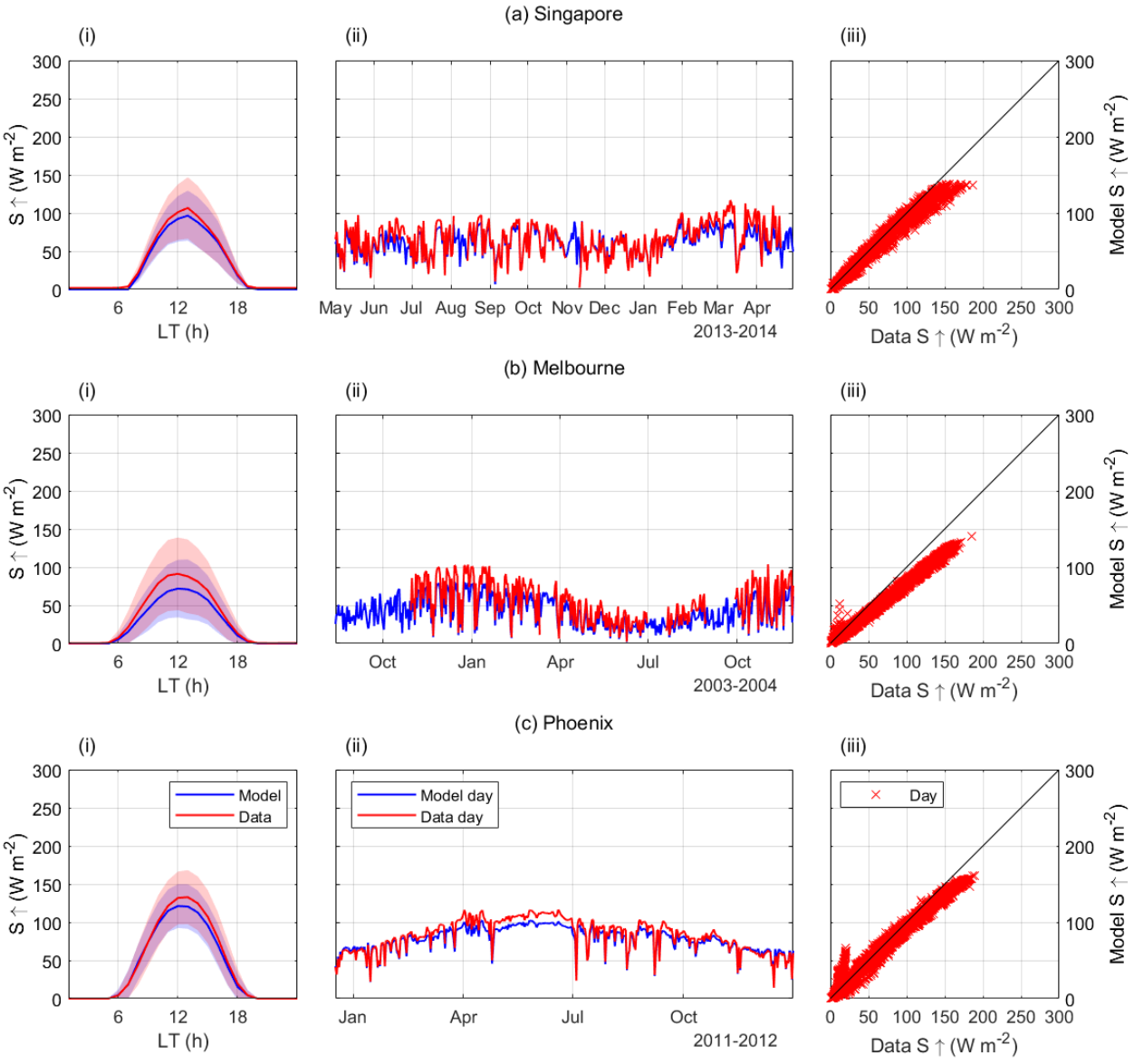

Figure 11. Comparison of modelled and measured outgoing shortwave radiation $K\uparrow$ for the validation sites in a) Singapore, b) Melbourne, and c) Phoenix. (i): Mean ~~daily~~ diurnal cycle (lines) +/-1 standard deviation (shaded area). (ii): Time series of mean daytime fluxes. (iii): Correlation of hourly daytime measurements and simulations.

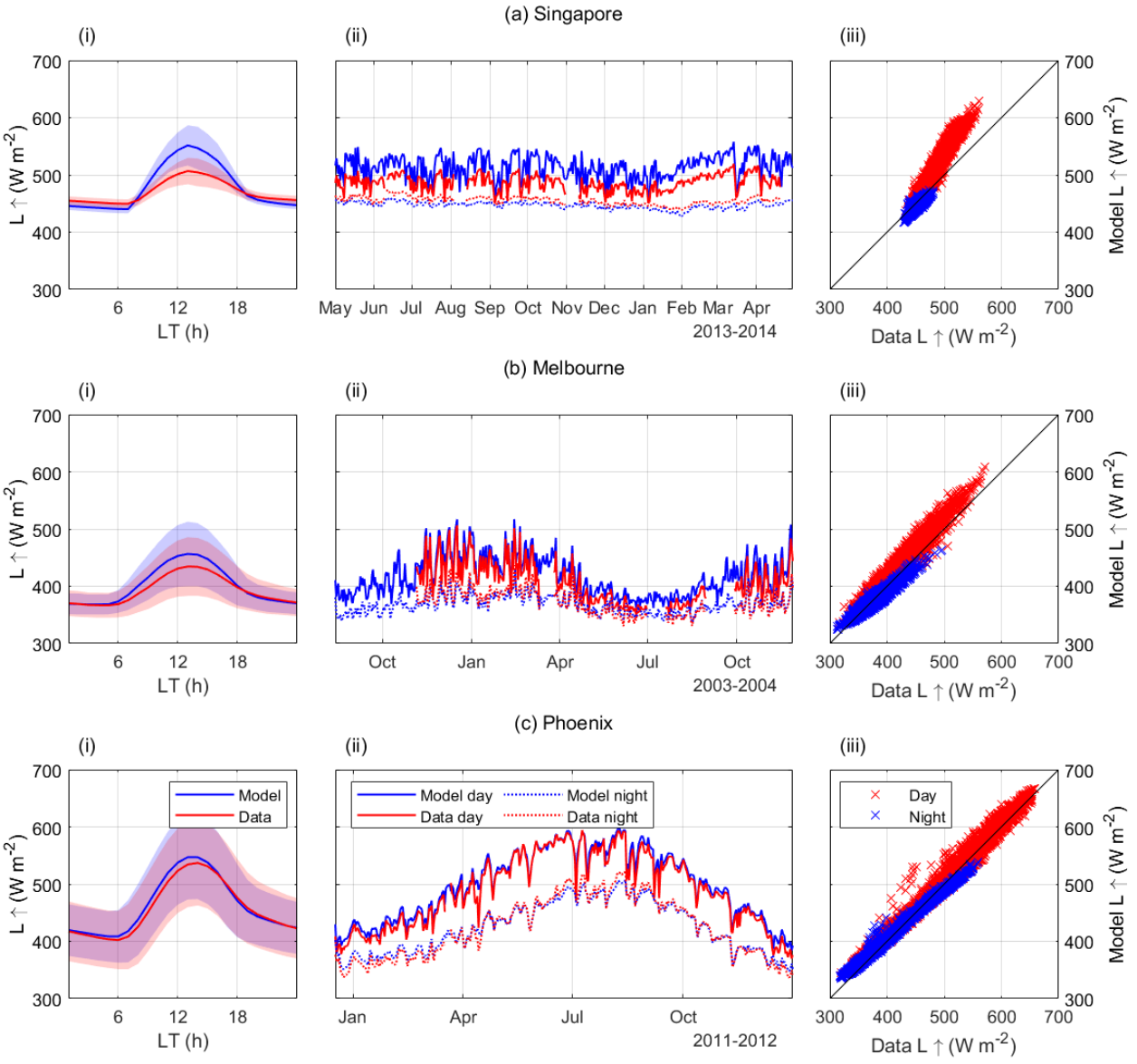

Figure 12. Comparison of modelled and measured outgoing longwave radiation $L\uparrow$ for the validation sites in a) Singapore, b) Melbourne, and c) Phoenix. (i): Mean ~~daily~~ diurnal cycle (lines) +/-1 standard deviation (shaded area). (ii): Time series of mean daytime (solid lines) and nighttime (dashed lines) fluxes. (iii): Correlation of hourly daytime/nighttime measurements and simulations.

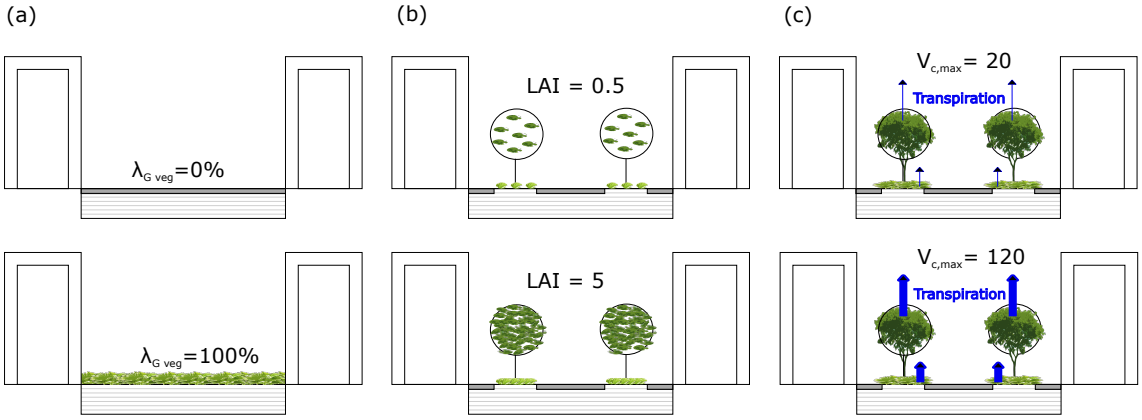

Figure 13. Geometric set-up of the urban scene in Telok Kurau Singapore for the sensitivity analysis of the vegetated ground fraction ($\lambda_{G,veg}$), LAI and maximum Rubisco capacity ($V_{c,max}$). $\lambda_{G,veg}$ is varied between 0 and 100 $\%$ (0 and 1), LAI between 0.5 and 5, and $V_{c,max}$ between 20 and 120 µmol CO_2 $s^{-1}m^{-2}$. The urban scene is defined by the parameter set of Telok Kurau (Sect. 9 of TRM).

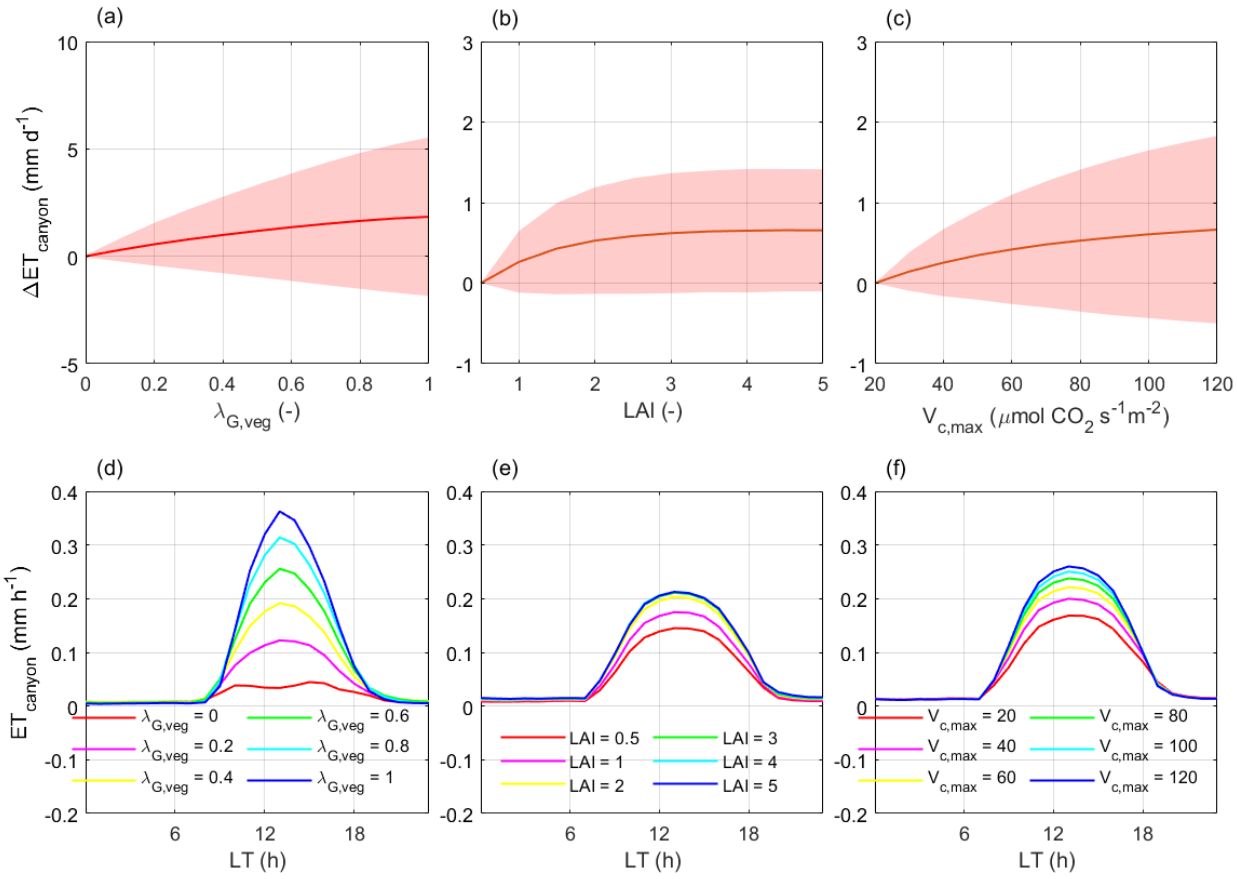

Figure 14. ~~Sensitivity analysis of~~ Change in canyon evapotranspiration (ET_{canyon}) caused by the change in vegetated ground cover fraction (λ_{veg}), leaf area index (LAI), and maximum Rubisco capacity ($V_{c,max}$) in Telok Kurau Singapore. (a), (b), and (c): ~~Long term mean~~ Mean evapotranspiration change ~~with respect to the baseline case of no-vegetation~~ considering all weather conditions (solid line) +/-1 standard deviation (shaded area). The subplots (d), (e), and (f) ~~: Long~~ show long term mean daily cycle of evapotranspiration ~~.~~ for different values of (d) λ_{veg} ~~is increased from 0 to 1~~, (e) LAI ~~is increased from 0.5 to 5~~, and (f) $V_{c,max}$ ~~is increased from 20 to 120.~~ considering all weather conditions.

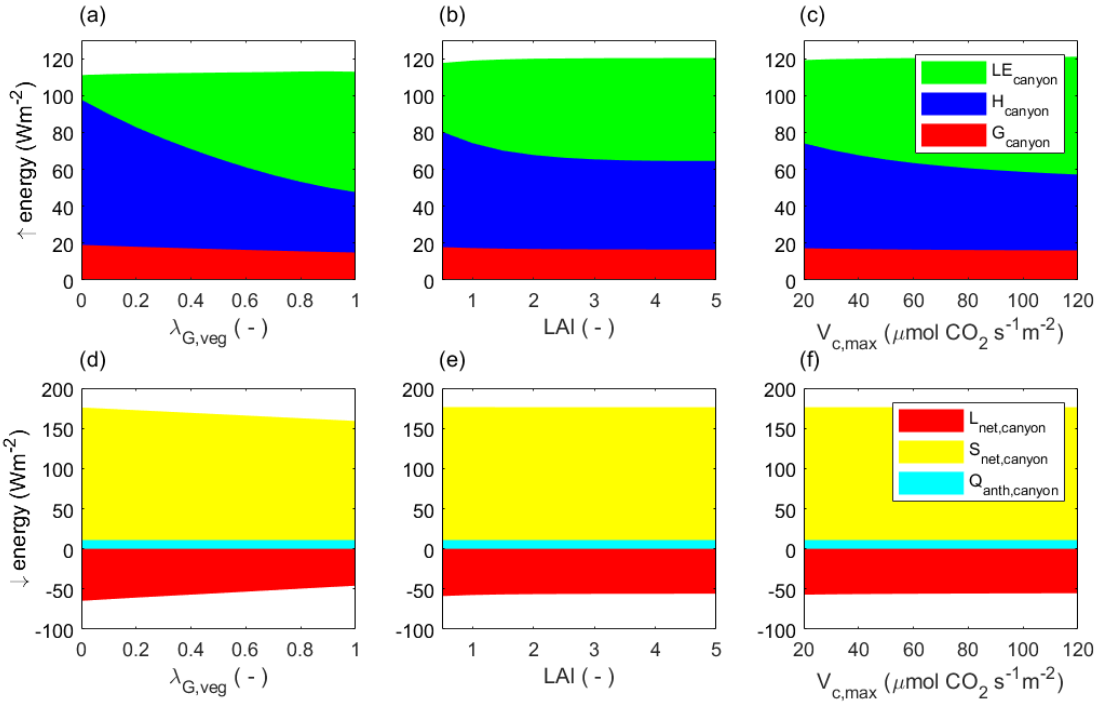

Figure 15. Energy balance components of the urban canyon (LE_{canyon}: Latent heat, H_{canyon}: Sensible heat, G_{canyon}: Conductive heat flux) as a function of (a) vegetated ground cover fraction ($\lambda_{G,veg}$), (b) leaf area index (LAI), and (c) maximum Rubisco capacity ($V_{c,max}$) in Telok Kurau Singapore. Absorbed longwave radiation ($L_{net,canyon}$), absorbed shortwave radiation ($S_{net,canyon}$), and anthropogenic heat flux ($Q_{anth,canyon}$) in the urban canyon as a function of (d) vegetated ground cover fraction ($\lambda_{G,veg}$), (e) leaf area index (LAI), and (f) maximum Rubisco capacity ($V_{c,max}$) in Telok Kurau Singapore. The overall conductive heat flux G_{canyon} comprises ground heat fluxes as well as conductive fluxes into buildings which in Singapore often have airconditioned interiors resulting in an overall positive G_{canyon} .

Code and data availability. The development of UT&C, model validation, and graphs presented in this paper were conducted in Matlab R2018b. The exact version of UT&C used to produce the results used in this paper is archived on Zenodo (Meili and Fatichi, 2019). The original source code for the ecohydrological model Tethys-Chloris was obtained from the author (Fatichi et al., 2012a, b) while the building and tree shading calculations are based on the code of Ryu et al. (2016). The tower based eddy covariance measurements used for model validation were obtained from the authors in Telok Kurau Singapore (Velasco et al., 2013; Roth et al., 2016), in Preston Melbourne (Coutts et al., 2007a, b; Nice et al., 2018), and from the Global Institute of Sustainability, Arizona State University (ASU) in Maryvale Phoenix (Chow et al., 2014; Chow, 2017).

Author contributions. NM, and SF designed the study, developed the code, conducted the analysis and wrote the manuscript with inputs from GM. MR, EV, AC, WC collected and shared their eddy-covariance measurements for the purpose of model validation. EBZ shared the code presented in Ryu et al. (2016). All authors gave commments and contributed to the final version of the manuscript.

Competing interests. The authors declare that they have no conflict of interest.

Acknowledgements. The research was conducted at the Future Cities Laboratory at the Singapore-ETH Centre, which was established collaboratively between ETH Zurich and Singapore's National Research Foundation (FI370074016) under its Campus for Research Excellence and Technological Enterprise programme. GM was supported by the "The Branco Weiss Fellowship - Society in Science" administered by ETH Zurich. EV acknowledges a research fellowship granted by the Centre for Urban Greenery and Ecology of Singapore's National Parks Board.

References

Abdella, K. and McFarlane, N. A.: Parameterization of the surface-layer exchange coefficients for atmospheric models, Boundary-Layer Meteorology, 80, 223–248, 1996.

Arora, V. K. and Boer, G. J.: A parameterization of leaf phenology for the terrestrial ecosystem component of climate models, Global Change Biology, 11, 39–59, 2005.

Arya, S. P.: Introduction to Micrometeorology, Academic Press, 2nd edn., 2001.

Assouline, S. and Or, D.: Anisotropy factor of saturated and unsaturated soils, Water Resour. Res., 42, W12 403, doi:10.1029/2006WR005001, 2006.

Atkin, O. K., Westbeek, M. H. M., Cambridge, M. L., Lambers, H., and Pons, T. L.: Leaf respiration in light and darkness. A comparison of slow- and fast-growing Poa species, Plant Physiology, 113, 961–965, 1997.

Ball, J. T., Woodrow, I. E., and Berry, J. A.: A model predicting stomatal conductance and its contribution to the control of photosynthesis under different environmental conditions, in: Progress in photosynthesis research, edited by Biggins, pp. 221–224, Martinus Nijhoff, Netherlands, 1987.

Beljaars, A. C. M.: The parametrization of surface fluxes in large-scale models under free convection, Q. J . R. Meteorol. Soc., 121, 255–270, 1994.

Bertoldi, G., Rigon, R., Tamanini, D., and Zanotti, F.: GEOtop version 0.875: Technical description and programs guide, Tech. Rep. dica-06-001, University of Trento E-Prints, 2006.

Bohrer, G., Mourad, H., Laursen, T. A., Drewry, D., Avissar, R., Poggi, D., Oren, R., and Katul, G. G.: Finite element tree crown hydrodynamics model (FETCH) using porous media flow within branching elements: A new representation of tree hydrodynamics, Water Resources Research, 41, doi:10.1029/2005WR004181, 2005.

Bonan, G.: Ecological Climatology: Concept and Applications, Cambridge Univ. Press, New York, 2002.

Bonan, G. B., Lawrence, P. J., Oleson, K. W., Levis, S., Jung, M., Reichstein, M., Lawrence, D. M., and Swenson, S. C.: Improving canopy processes in the Community Land Model version 4 (CLM4) using global flux fields empirically inferred from FLUXNET data, Journal of Geophysical Research, 116, doi:10.1029/2010JG001593, 2011.

Brutsaert, W.: Evaporation into the atmosphere, D. Reidel, 1982.

Brutsaert, W.: Hydrology. An Introduction, Cambridge University Press, Cambridge, UK, 2005.

Buckley, T. N., Mott, K. A., and Farquhar, G. D.: A hydromechanical and biochemical model of stomatal conductance, Plant, Cell and Environment, 26, 1767–1785, 2003.

Choudhury, B. J. and Monteith, J. L.: A four-layer model for the heat budget of homogeneous land surfaces, Quarterly Journal of the Royal Meteorological Society, 114, 378–398, 1988.

Chow, W.: Eddy covariance data measured at the CAP LTER flux tower located in the west Phoenix, AZ neighborhood of Maryvale from 2011-12-16 through 2012-12-31. Environmental Data Initiative., https://doi.org/10.6073/pasta/fed17d67583eda16c439216ca40b0669, 2017.

Chow, W. T. L., Volo, T. J., Vivoni, E. R., Darrel, G., and Ruddell, B. L.: Seasonal dynamics of a suburban energy balance in Phoenix , Arizona, International Journal of Climatology, 34, 3863–3880, https://doi.org/10.1002/joc.3947, 2014.

Collatz, G. J., Ball, J. T., Grivet, C., and Berry, J. A.: Physiological and environmental regulation of stomatal conductance, photosynthesis and transpiration-A model that includes a laminar boundary-layer, Agricultural and Forest Meteorology, 54, 107–136, 1991.

Collatz, G. J., Ribas-Carbo, M., and Berry, J. A.: Coupled photosynthesis-stomatal conductance model for leaves of C4 plants, Australian Journal of Plant Physiology, 19, 519–538, 1992.

Collins, D. B. G. and Bras, R. L.: Plant rooting strategies in water-limited ecosystems, Water Resources Research, 43, doi:10.1029/2006WR005541, 2007.

Coutts, A. M., Beringer, J., and Tapper, N. J.: Characteristics influencing the variability of urban CO2 fluxes in Melbourne, Australia, Atmospheric Environment, 41, 51–62, https://doi.org/10.1016/j.atmosenv.2006.08.030, 2007a.

Coutts, A. M., Beringer, J., and Tapper, N. J.: Impact of increasing urban density on local climate: Spatial and temporal variations in the surface energy balance in Melbourne, Australia, Journal of Applied Meteorology and Climatology, 46, 477–493, https://doi.org/10.1175/JAM2462.1, 2007b.

Dai, Y., Dickinson, R. E., and Wang, Y.-P.: A two-big-leaf model for canopy temperature, photosynthesis, and stomatal conductance, Journal of Climate, 17, 2281–2299, 2004.

de Munck, C., Lemonsu, A., Masson, V., Le Bras, J., and Bonhomme, M.: Evaluating the impacts of greening scenarios on thermal comfort and energy and water consumptions for adapting Paris city to climate change, Urban Climate, 23, 260–286, https://doi.org/10.1016/j.uclim.2017.01.003, 2018.

de Pury, D. G. G. and Farquhar, G. D.: Simple scaling of photosynthesis from leaves to canopies without the errors of big-leaf models, Plant, Cell and Environment, 20, 537–557, 1997.

de Vries, D. A.: Thermal Properties of Soils, in: Physics of the Plant Environment, edited by van Wijk, W., North-Holland, Amsterdam, 1963.

Deardorff, J. W.: Efficient prediction of ground surface temperature and moisture with inclusion of a layer of vegetation, Journal of Geophysical Research, 83, 1889–1903, 1978.

Deckmyn, G., Verbeeck, H., de Beeck, M. O., Vansteenkiste, D., Steppe, K., and Ceulemans, R.: ANAFORE: A stand-scale process-based forest model that includes wood tissue development and labile carbon storage in trees, Ecological Modelling, 215, 345–368, doi:10.1016/j.ecolmodel.2008.04.007, 2008.

Demuzere, M., Harshan, S., Jaervi, L., Roth, M., Grimmond, C. S. B., Masson, V., Oleson, K. W., Velasco, E., and Wouters, H.: Impact of urban canopy models and external parameters on the modelled urban energy balance in a tropical city, Quarterly, https://doi.org/10.1002/qj.3028, 2017.

Dickinson, R. E., Henderson-Sellers, A., and Kennedy, P. J.: Biosphere-atmosphere transfer scheme (BATS) version 1E as coupled to the NCAR Community Climate Model, Tech. Rep. NCAR/TN-387+STR, Natl. Cent. for Atmos. Res., Boulder, Colorado, 1993.

Dye, D. G.: Spectral composition and quanta-to-energy ratio of diffuse photosynthetically active radiation under diverse cloud conditions, Journal of Geophysical Research, 109, doi:10.1029/2003JD004251, 2004.

Eltahir, E. A. B. and Bras, R. L.: A Description of rainfall interception over large-areas, Journal of Climate, 6, 1002–1008, 1993.

Farouki, O. T.: The thermal properties of soils in cold regions, Cold Regions Science and Technology, 5, 67–75, 1981.

Farquhar, G. D., Caemmerer, S. V., and Berry, J. A.: A biochemical model of photosynthetic CO_2 assimilation in leaves of C3 species, Planta, 149, 78–90, 1980.

Fatichi, S. and Pappas, C.: Constrained variability of modeled T:ET ratio across biomes, Geophysical Research Letters, 44, 6795–6803, https://doi.org/10.1002/2017GL074041, 2017.

Fatichi, S., Ivanov, V. Y., and Caporali, E.: A mechanistic ecohydrological model to investigate complex interactions in cold and warm water-controlled environments : 1 . Theoretical framework and plot-scale analysis, Journal of Advances in Modeling Earth Systems, 4, 1–31, https://doi.org/10.1029/2011MS000086, 2012a.

Fatichi, S., Ivanov, V. Y., and Caporali, E.: A mechanistic ecohydrological model to investigate complex interactions in cold and warm water-controlled environments : 2 . Spatiotemporal analyses, Journal of Advances in Modeling Earth Systems, 4, 1–22, https://doi.org/10.1029/2011MS000087, 2012b.

Fatichi, S., Ivanov, V. Y., and Caporali, E.: Supplementary Material : A mechanistic ecohydrological model to investigate complex interactions in cold and warm water-controlled environments . 1 . Theoretical Framework, Journal of Advances in Modeling Earth Systems, pp. 1–73, 2012c.

Feddes, R. A., Hoff, H., Bruen, M., Dawson, T., de Rosnay, P., Dirmeyer, P., Jackson, R. B., Kabat, P., Kleidon, A., Lilly, A., and Pitmank, A. J.: Modeling Root Water Uptake in Hydrological and Climate Models, Bulletin of the American Meteorological Society, 82, 2797–2809, 2001.

Frank, A., Heidemann, W., and Spindler, K.: Modeling of the surface-to-surface radiation exchange using a Monte Carlo method, Journal of Physics: Conference Series, 745, https://doi.org/10.1088/1742-6596/745/3/032143, 2016.

Gao, Q., Xhao, P., Zeng, X., Cai, X., and Shen, W.: A model of stomatal conductance to quantify the relationship between leaf transpiration, microclimate, and soil water stress, Plant, Cell and Environment, 25, 1373–1381, 2002.

Garrote, L. and Bras, R. L.: A distributed model for real-time flood casting using digital elevation models, Journal of Hydrology, 167, 279–306, 1995.

Grimmond, C. S. B., Blackett, M., Best, M. J., Baik, J., Belcher, S. E., Beringer, J., Bohnenstengel, S. I., Calmet, I., Chen, F., Coutts, A., Dandou, A., Fortuniak, K., Gouvea, M. L., Hamdi, R., Hendry, M., Kanda, M., Kawai, T., Kawamoto, Y., Kondo, H., Krayenhoff, E. S., Lee, S., Loridan, T., Martilli, A., Masson, V., Miao, S., Oleson, K., Ooka, R., Pigeon, G., Porson, A., Ryu, Y., Salamanca, F., Steeneveld, G. J., and Tombrou, M.: Initial results from Phase 2 of the international urban energy balance model comparison, International Journal of Climatology, 272, 244–272, https://doi.org/10.1002/joc.2227, 2011.

Guan, D., Zhang, Y., and Zhu, T.: A wind-tunnel study of windbreak drag, Agricultural and Forest Meteorology, 118, 75–84, https://doi.org/10.1016/S0168-1923(03)00069-8, 2003.

Guan, D.-x., Zhu, T.-y., and Han, S.-j.: Wind tunnel experiment of drag of isolated tree models in surface boundary layer, Journal of Forestry Research, 11, 156–160, https://doi.org/10.1007/bf02855516, 2000.

Haghighi, E., Shahraeeni, E., Lehmann, P., and Or, D.: Evaporation rates across a convective air boundary layer are dominated by diffusion, Water Resour. Res., 49, 1602–1610, doi:10.1002/wrcr.20166, 2013.

Harman, I. A. N. N.: Radiative exchange in an urban street canyon, Boundary-Layer Meteorology, 110, 301–316, 2003.

Harshan, S., Roth, M., Velasco, E., and Demuzere, M.: Evaluation of an urban land surface scheme over a tropical suburban neighborhood, Theoretical and Applied Climatology, pp. 1–20, https://doi.org/10.1007/s00704-017-2221-7, 2017.

Hillel, D.: Environmental Soil Physics: Fundamentals, Applications, and Environmental Considerations, Academic Press, London, UK, 1998.

Hoff, S. J. and Janni, K. a.: Monte Carlo Technique for the Determination of Thermal Radiation Shape Factors, American Society of Agricultural Engineers, 32, 1023–1028, https://doi.org/10.13031/2013.31108, 1989.

Hu, Z. and Islam, S.: Prediction of ground surface temperature and soil moisture content by the force restore-method, Water Resources Research, 31, 2531–2539, 1995.

Ivanov, V. Y., Bras, R. L., and Vivoni, E. R.: Vegetation-hydrology dynamics in complex terrain of semiarid areas: 1. A mechanistic approach to modeling dynamic feedbacks, Water Resources Research, 44, doi:10.1029/2006WR005588, 2008a.

Ivanov, V. Y., Bras, R. L., and Vivoni, E. R.: Vegetation-hydrology dynamics in complex terrain of semiarid areas: 1. A mechanistic approach to modeling dynamic feedbacks, Water Resources Research, 44, doi:10.1029/2006WR005588, 2008b.

Jones, H. G.: Plants and Microclimate, Cambridge University Press, New York, 1983.

Kattge, J. and Knorr, W.: Temperature acclimation in a biochemical model of photosynthesis: a reanalysis of data from 36 species, Plant, Cell and Environment, 30, 1176–1190, doi: 10.1111/j.1365-3040.2007.01690.x, 2007.

Katul, G. G., Leuning, R., and Oren, R.: Relationship between plant hydraulic and biochemical properties derived from a steady-state coupled water and carbon transport model, Plant, Cell and Environment, 26, 339–350, 2003.

Kent, C. W., Grimmond, S., and Gatey, D.: Aerodynamic roughness parameters in cities: Inclusion of vegetation, Journal of Wind Engineering and Industrial Aerodynamics, 169, 168–176, https://doi.org/10.1016/j.jweia.2017.07.016, http://dx.doi.org/10.1016/j.jweia.2017.07.016, 2017.

Kirkham, M. B.: Principles of soil and plant water relations, Elsevier Academic Press, 2005.

Kondo, J. and Ishida, S.: Sensible Heat Flux from the Earth's Surface under Natural Convective Conditions, Journal of the Atmospheric Sciences, 54, 498–509, 1997.

Kot, S. C. and Song, Y.: An improvement of the Louis scheme for the surface layer in an atmopsheric modelling system, Boundary-Layer Meteorology, 88, 239–254, 1998.

Kusaka, H., Kondo, H., and Kikegawa, Y.: A simple single-layer urban canopy model for atmospheric models: Comparison with multi-layer and slab models, Boundary-Layer Meteorology, 101, 329–358, 2001.

Lee, H. S., Matthews, C. J., Braddock, R. D., Sander, G. C., and Gandola, F.: A MATLAB method of lines template for transport equations, Environmental Modelling & Software, 19, 603–614, doi:10.1016/j.envsoft.2003.08.017, 2004.

Leuning, R.: Modelling stomatal behaviour and photosynthesis of Eucalyptus grandis, Australian Journal of Plant Physiology, 17, 159–175, 1990.

Leuning, R.: A critical appraisal of a combined stomatal- photosynthesis model for C3 plants, Plant, Cell and Environment, 18, 357–364, 1995.

Leuning, R., Kelliher, F. M., Pury, D. G. G., and Schulze, E.-D.: Leaf nitrogen, photosynthesis, conductance and transpiration: Scaling from leaves to canopies, Plant, Cell and Environment, pp. 1183–1200, 1995.

Liu, X., Li, X.-x., Harshan, S., Roth, M., and Velasco, E.: Evaluation of an urban canopy model in a tropical city : the role of tree evapotranspiration Evaluation of an urban canopy model in a tropical city : the role of tree evapotranspiration, Environmental Research Letters, 12, 2017.

Maass, J., Vose, J., Swank, W., and Martínez-Yrízar, A.: Seasonal changes of leaf area index (LAI) in a tropical deciduous forest in west Mexico, Forest Ecology and Management, 74, 171–180, http://www.sciencedirect.com/science/article/pii/037811279403485F, 1995.

Macdonald, R. W., Griffiths, R. F., and Hall, D. J.: An improved method for the estimation of surface roughness of obstacle arrays, Atmospheric Environment, 32, 1857–1864, 1998.

Mahat, V., Tarboton, D. G., and Molotch, N. P.: Testing above- and below-canopy representations of turbulent fluxes in an energy balance snowmelt model, Water Resources Research, 49, 1107–1122, doi:10.1002/wrcr.20073, 2013.

Mahfouf, J.-F. and Jacquemin, B.: A study of rainfall interception using a land surface parameterization for mesoscale meteorological models, Journal of Applied Meteorology, 28, 1282–1302, 1989.

Mascart, P., Noilhan, J., and Giordani, H.: A Modified Parameterization of Flux-Profile Relationships in the Surface Layer using Different Roughness LengthValues for Heat and Momentum, Boundary-Layer Meteorology, 72, 331–334, 1995.

Masson, V.: A physically-based scheme for the urban energy budget in atmospheric models, Boundary-Layer Meteorology, 94, 357–397, 2000.

Meili, N. and Fatichi, S.: Urban Tethys-Chloris (UT&C v1.0) with the possibility of sub-houly timesteps, https://doi.org/10.5281/zenodo.3548147, 2019.

Monin, A. S. and Obukhov, A. M.: Dimensionless Characteristics of Turbulence in the Surface Layer of the Atmosphere, Trudy Geofiz. Inst. Akad. Nauk. SSSR, 24, 163–187, (In Russian), 1954.

Monteith, J. L.: Principles of Environmental Physics, Edward Arnold, London, 1973.

Mualem, Y.: A new model for predicting the hydraulic conductivity of unsaturated porous media, Water Resour. Res, 12, 513–522, doi:10.1029/WR012i003p00513, 1976.

Newman, E. I.: Resistance to water flow in soil and plant. I. Soil resistance in relation to amounts of root: theoretical estimate, J. Appl. Ecol., 6, 1–12, 1969.

Nice, K. A., Coutts, A. M., and Tapper, N. J.: Development of the VTUF-3D v1.0 urban micro-climate model to support assessment of urban vegetation influences on human thermal comfort, Urban Climate, pp. 1–25, https://doi.org/10.1016/j.uclim.2017.12.008, http://linkinghub.elsevier.com/retrieve/pii/S2212095517301141, 2018.

Nobel, P. S.: Physicochemical and Environmental Plant Physiology, Elsevier Academic Press, 2009.

Noilhan, J. and Mafhouf, J.-F.: The ISBA land surface parameterisation scheme, Global and Planetary Change, 13, 145–159, 1996.

Noilhan, J. and Planton, S.: A simple parameterization of land surface processes for meteorological models, Monthly Weather Review, 117, 536–549, 1989.

Núnez, C. M., Varas, E. A., and Meza, F. J.: Modelling soil heat flux, Theoretical Applied Climatology, 100, 251–260, doi:10.1007/s00704-009-0185-y, 2010.

Oleson, K. W., Dai, Y., Bonan, G., Bosilovich, M., Dickinson, R., Dirmeyer, P., Hoffman, F., Houser, P., Levis, S., Niu, G. Y., Thornton, P., Vertenstein, M., Yang, Z. L., and Zeng, X.: Technical Description of the Community Land Model (CLM), Tech. Rep. NCAR/TN-461+STR, Natl. Cent. for Atmos. Res., Boulder, Colorado, 2004.

Oleson, K. W., Bonan, G. B., Feddema, J., Vertenstein, M., and Grimmond, C. S. B.: An Urban Parameterization for a Global Climate Model . Part I : Formulation and, Journal of Applied Meteorology and Climatology, 47, 1038–1060, https://doi.org/10.1175/2007JAMC1597.1, 2007.

Oleson, K. W., Lawrence, D. M., Bonan, G. B., Drewniak, B., Huang, M., Kowen, C. D., Levis, S., Li, F., Riley, W. J., Subin, Z. M., Swenson, S. C., and Thornton, P. E.: Technical Description of version 4.5 of the Community Land Model (CLM), Tech. Rep. NCAR/TN-503+STR, Natl. Cent. for Atmos. Res., Boulder, Colorado, 2013.

Park, S.-h. and Lee, S.-u.: A Vegetated Urban Canopy Model for Meteorological and Environmental Modelling, Boundary-Layer Meteorology, 126, 73–102, https://doi.org/10.1007/s10546-007-9221-6, 2008.

Philip, J. R.: Evaporation, and moisture and heat fields in the soil, Journal of Meteorology, 14, 354–366, 1957.

Ramírez, J. A. and Senarath, S. U. S.: A Statistical-Dynamical Parameterization of Interception and Land Surface-Atmosphere Interactions, Journal of Climate, 13, 4050–4063, 2000.

Richards, L. A.: Capillary conduction of liquids through porous mediums, Physics, 1, 318–333, 1931.

Roth, M., Jansson, C., and Velasco, E.: Multi-year energy balance and carbon dioxide fluxes over a residential neighbourhood in a tropical city, International Journal of Climatology, https://doi.org/10.1002/joc.4873, 2016.

Rowley, F. B. and Eckley, W. A.: Surface coefficients as affected by wind direction, ASHREA Trans., 39, 33–46, 1932.

Rowley, F. B., Algren, A. B., and Blackshaw, J.: Surface conductance as affected by air velocity, temperature and character of surface, ASHREA Trans., 36, 429–446, 1930.

Rutter, A. J., Kershaw, K. A., Robins, P. C., and Morton, A. J.: A predictive model of rainfall interception in forests. 1. Derivation of the model from observation in a plantation of Corsican pine, Agricultural Meteorology, 9, 367–384, 1971.

Rutter, A. J., Morton, A. J., and Robins, P. C.: A predictive model of rainfall interception in forests. 2. Generalization of model and comparison with observations in some coniferous and hardwood stands, The Journal of Applied Ecology, 12, 367–380, 1975.

Ryu, Y.-H., Baik, J.-J., and Lee, S.-H.: A New Single-Layer Urban Canopy Model for Use in Mesoscale Atmospheric Models, Journal of Applied Meteorology and Climatology, 50, 1773–1794, https://doi.org/10.1175/2011JAMC2665.1, 2011.

Ryu, Y.-H., Bou-Zeid, E., Wang, Z.-H., and Smith, J. A.: Realistic Representation of Trees in an Urban Canopy Model, Boundary-Layer Meteorology, 159, 193–220, https://doi.org/10.1007/s10546-015-0120-y, 2016.

Sack, L. and Holbrook, N. M.: Leaf hydraulics, Annual Review of Plant Biology, 57, 361–381, 2006.

Sailor, D. J. and Lu, L.: A top-down methodology for developing diurnal and seasonal anthropogenic heating profiles for urban areas, Atmospheric Environment, 38, 2737–2748, https://doi.org/10.1016/j.atmosenv.2004.01.034, 2004.

Sailor, D. J., Georgescu, M., Milne, J. M., and Hart, M. A.: Development of a national anthropogenic heating database with an extrapolation for international cities, Atmospheric Environment, 118, 7–18, https://doi.org/10.1016/j.atmosenv.2015.07.016, http://dx.doi.org/10.1016/j.atmosenv.2015.07.016, 2015.

Saxton, K. E. and Rawls, W. J.: Soil Water Characteristic Estimates by Texture and Organic Matter for Hydrologic Solutions, Soil Science Society of America Journal, 70, 1569–1578, doi:10.2136/sssaj2005.0117, 2006.

Schenk, H. J. and Jackson, R. B.: The global biogeography of roots, Ecological Monography, 72, 311–328, 2002.

Sellers, P. J., Los, S. O., Tucker, C. J., Justice, C. O., Dazlich, D. A., Collatz, G. J., and Randall, D. A.: A revised land surface parameterization (SiB2) for atmospheric GCMs. 2. The generation of global fields of terrestrial biophysical parameters from satellite data, Journal of Climate, 9, 706–737, 1996a.

Sellers, P. J., Randall, D. A., Collatz, G. J., Berry, J. A., Field, C. B., Dazlich, D. A., Zhang, C., Collelo, G. D., and Bounoua, L.: A revised land surface parameterization (SiB2) for atmospheric GCMs. 1. Model formulation, Journal of Climate, 9, 674–705, 1996b.

Sellers, P. J., Dickinson, R. E., Randall, D. A., Betts, A. K., Hall, F. G., Berry, J. A., Collatz, G. J., Denning, A. S., Mooney, H. A., Nobre, C. A., Sato, N., Field, C. B., and Henderson-Sellers, A.: Modeling the Exchanges of Energy, Water and Carbon Between Continents and the Atmosphere, Science, 275, 502–509, 1997.

Shahraeeni, E., Lehmann, P., and Or, D.: Coupling of evaporative fluxes from drying porous surfaces with air boundary layer-Characteristics of evaporation from discrete pores, Water Resour. Res., 48, W09 525, doi:10.1029/2012WR011857, 2012.

Shampine, L. F. and Reichelt, M. W.: The MATLAB ODE Suite, SIAM Journal on Scientific Computing, 18, 1–22, 1997.

Shuttleworth, W. J.: Terrestrial hydrometeorology, John Wiley & Sons, Ltd, 2012.

Shuttleworth, W. J. and Gurney, R. J.: The theoretical relationship between foliage temperature and canopy resistance in sparse crops, Quarterly Journal of the Royal Meteorological Society, 116, 497–519, 1990.

Singsaas, E. L., Ort, D. R., and Delucia, E. H.: Variation in measured values of photosynthetic quantum yield in ecophysiological studies, Oecologia, 128, 15–23, 2001.

Song, J. and Wang, Z. H.: Interfacing the Urban Land–Atmosphere System Through Coupled Urban Canopy and Atmospheric Models, Boundary-Layer Meteorology, 154, 427–448, https://doi.org/10.1007/s10546-014-9980-9, 2015.

Sparrow, E. and Cess, R. D.: Radiation Heat Transfer, Chapters 3-4, Appendices A & B, Thermal Science Series, Brooks/Cole, 1970.

Sperry, J. S., Stiller, V., and Hacke, U. G.: Xylem Hydraulics and the Soil-Plant-Atmosphere Continuum: Opportunities and Unresolved Issues, Agronomy Journal, 95, 1362–1370, 2003.

Su, Z.: The Surface Energy Balance System (SEBS) for estimation of turbulent heat fluxes, Hydrology and Earth System Sciences, 6, 85–99, 2002.

Tuzet, A., Perrier, A., and Leuning, R.: A coupled model of stomatal conductance, photosynthesis and transpiration, Plant, Cell and Environment, 26, 1097–1116, 2003.

van den Hurk, B. J. J. M. and Holtslag, A. A. M.: On the bulk parameterization of surface fluxes for various conditions and parameter ranges, Boundary-Layer Meteorology, 82, 119–134, 1997.

van Genuchten, M. T.: A closed-form equation for predicting the hydraulic conductivity of unsaturated soils, Soil Science Society of America Journal, 44, 892–898, 1980.

Velasco, E., Roth, M., Tan, S. H., Quak, M., Nabarro, S. D. A., and Norford, L.: The role of vegetation in the CO 2 flux from a tropical urban neighbourhood, Atmospheric Chemistry and Physics, 13, 10 185–10 202, https://doi.org/10.5194/acp-13-10185-2013, 2013.

Verbeeck, H., Steppe, K., Nadezhdina, N., DeBeeck, M. O., , Deckmyn, G., Meiresonne, L., Lemeur, R., Čermák, J., Ceulemans, R., and Janssens, I. A.: Stored water use and transpiration in Scots pine: a modeling analysis with ANAFORE, Tree Physiology, 27, 1671–1685, 2007.

Vico, G. and Porporato, A.: Modelling C3 and C4 photosynthesis under water-stressed conditions, Plant Soil, 313, 187–203, doi:10.1007/s11104-008-9691-4, 2008.

Villar, R., Held, A. A., and Merino, J.: Dark leaf respiration in light and darkness of an evergreen and a deciduous plant species, Plant Physiology, 107, 421–427, 1995.

Viterbo, P. and Beljaars, A. C. M.: An improved land surface parameterization scheme in the ECMWF model and its validation, Journal of Climate, 8, 2716–2748, 1995.

Volo, T. J., Vivoni, E. R., Martin, C. A., Earl, S., and Ruddell, B. L.: Modelling soil moisture, water partitioning, and plant water stress under irrigated conditions in desert Urban areas, Ecohydrology, 7, 1297–1313, https://doi.org/10.1002/eco.1457, 2014.

von Caemmerer, S. and Farquhar, G. D.: Some relationships between the biochemistry of photosynthesis and the gas exchange of leaves, Planta, 153, 376–387, 1981.

Wang, Y.-P. and Leuning, R.: A two-leaf model for canopy conductance, photosynthesis and portioning of available energy I: Model description and comparison with a multi-layered model, Agricultural and Forest Meteorology, 91, 89–111, 1998.

Wang, Z.-h.: Geometric effect of radiative heat exchange in concave structure with application to heating of steel I-sections in fire, International Journal of Heat and Mass Transfer, 53, 997–1003, https://doi.org/10.1016/j.ijheatmasstransfer.2009.11.013, http://dx.doi.org/10.1016/j.ijheatmasstransfer.2009.11.013, 2010.

Wang, Z.-h.: Monte Carlo simulations of radiative heat exchange in a street canyon with trees, SOLAR ENERGY, 110, 704–713, https://doi.org/10.1016/j.solener.2014.10.012, http://dx.doi.org/10.1016/j.solener.2014.10.012, 2014.

Wang, Z.-h., Bou-Zeid, E., and Smith, J. A.: A Spatially-Analytical Scheme for Surface Temperatures and Conductive Heat Fluxes in Urban Canopy Models, Boundary-Layer Meteorology, 138, 171–193, https://doi.org/10.1007/s10546-010-9552-6, 2011.

Wang, Z.-h., Bou-zeid, E., and Smith, J. A.: A coupled energy transport and hydrological model for urban canopies evaluated using a wireless sensor network, Quarterly Journal of the Royal Meteorological Society, 139, 1643–1657, https://doi.org/10.1002/qj.2032, 2013.

Warren, C. R.: Why does photosynthesis decrease with needle age in Pinus pinaster?, Trees, 20, 157–164, doi: 10.1007/s00468-005-0021-7, 2006.

Wieringa, J.: Representative roughness parameters for homogeneous terrain, Boundary-Layer Meteorology, 63, 323–363, 1993.

Yang, J., Wang, Z. H., Chen, F., Miao, S., Tewari, M., Voogt, J. A., and Myint, S.: Enhancing Hydrologic Modelling in the Coupled Weather Research and Forecasting–Urban Modelling System, Boundary-Layer Meteorology, 155, 87–109, https://doi.org/10.1007/s10546-014-9991-6, 2015.